X-ray investigation of Nb/O interfaces

Mélissa Delheusy
Paris, 2008

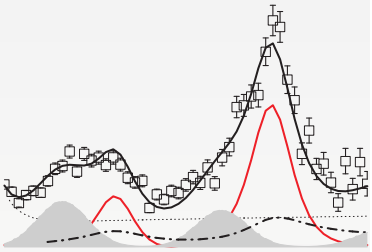

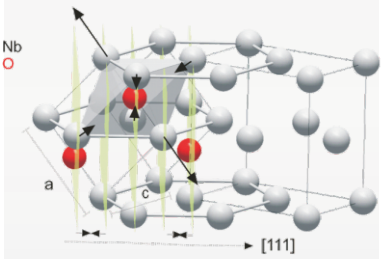

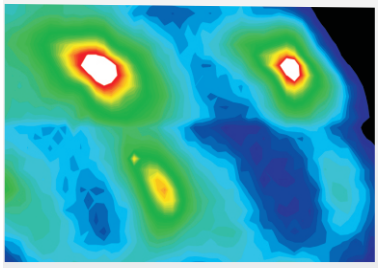

Institut de Recherche sur les
lois Fondamentales de l'Univers
Commissariat à l'énergie atomique

Université Paris-Sud XI
UFR scientifique d'Orsay

Max-Planck-Institut
für Metallforschung
in Stuttgart

Universität Stuttgart,
Fakultät Mathematik und Physik

X-ray investigation of Nb/O interfaces

UNIVERSITE PARIS-SUD XI
UFR SCIENTIFIQUE D'ORSAY

UNIVERSITÄT STUTTGART
FAKULTÄT MATHEMATIK UND PHYSIK

Thèse présentée pour obtenir le grade de Docteur
en Sciences de l'Université Paris XI Orsay

Zur Erlangung der Würde eines Doktors der
Naturwissenschaften (Dr. rer. nat.) genehmigte Abhandlung

Par / Vorgelegt von

Mélissa DELHEUSY

Soutenue publiquement le: / Tag der mündlichen Prüfung: 07.07.2008

Composition du jury :

Prof. Dr. H. Dosch	Directeur de thèse
Prof. Dr. L. Priester	Directeur de thèse
Prof. Dr. D. Seidman	Rapporteur
Prof. Dr. H. Over	Rapporteur
Dr. A. Stierle	Examinateur
Dr. C. Antoine	Examinateur

Contents

Chapter 1

Introduction

The 20th century is often referred to as the age of physics, while nano and biotechnology sciences are expected to dominate the progress of the 21st century. Crucial for the progress in these fields are suitable research tools, capable of providing minute information on disordered and complex systems at the nanoscale. The forthcoming new generation of particle accelerators, such as the International Linear Collider (ILC) or X-ray free electron lasers, will open new scientific frontiers, offering opportunities for revolutionary scientific breakthroughs. X-ray free electron lasers will provide photon pulses shorter than 100 femtoseconds and a billion times brighter than what can be produced by any other X-ray source available now. Combining the intensity and coherence of a laser with the short X-ray wavelength available in a synchrotron, and the penetrating power and atomic sensitivity of X-rays, they will assure the supremacy of light as one of the most important research tool for science.

Niobium superconducting radio-frequency (rf) cavities are fundamental components of future high-energy particle accelerators, such as X-ray free electron lasers or the ILC. Preliminary estimations contemplate more than ten thousand niobium rf cavities to achieve the required energy range of the ILC, up to 500 billion electron volts. The quest for high accelerating fields and an affordable superconducting rf technology has revolutionized accelerator applications. Considerable efforts have been devoted in the past years in order to enhance the performance of niobium cavities. A remarkable increase of the rf accelerating field has been achieved applying a low-temperature annealing (below 150°C for several hours) [1–3]. It has been argued that a redistribution of subsurface interstitial oxygen within the penetration depth of the rf field into niobium (typically 50 nm) is involved in this effect [4]. Interstitial oxygen has indeed a strong influence on the properties of niobium, e.g. it decreases its superconducting critical temperature by 0.93K/at.% O [5,6].

The interest on niobium and its oxide extends beyond rf cavities, including tunnel barrier in nanolelectronic devices, stainless steel alloys and superalloys, or heterogeneous catalysis [7–14]. Recent investigations have reported high concentrations of interstitial oxygen at the niobium/oxide interface, for Nb(110) films oxidized above 100°C in air [15], for a Nb(110) single crystal after high-temperature ultrahigh vacuum annealing [16], and for high residual resistivity ratio niobium samples in a recent atom probe tomography study [17]. The progressive dissolution of the niobium oxide layer has been observed by core-level spectroscopy studies on polycrystalline samples [18–20] and Nb(100) single crystals [21]. However, these studies have focused on the chemical analysis of the near surface region. The microscopic mechanism of the oxide layer dissolution, its influence on the superconducting behavior of the surface region of niobium, and the simultaneous formation of subsurface interstitial oxygen are not yet well understood.

In this work, a systematic, non-destructive, *in-situ* X-ray investigation of the near surface structure of oxidized niobium single crystals has been undertaken. Particular interest has been dedicated on analyzing the impact of different thermal treatments on the oxidation process on Nb(110) and Nb(100), and on the simultaneous behavior of the interstitial oxygen dissolved underneath. To this aim, grazing incidence X-ray oxygen-induced diffuse scattering, X-ray reflectivity, crystal truncations rods and high resolution core-level spectroscopy, have been combined. The three last methods have been proved in the previous years to be powerful tools for the determination of surface structures. The use of the first method is on the contrary nonstandard. Combining intrinsic properties of the *bcc* lattice of niobium to the power of grazing incidence X-ray scattering, a non-destructive way of investigation of the interstitial oxygen dissolved in the near surface region on the atomistic scale is proposed for the first time.

For the unambiguous monitoring of subsurface interstitial oxygen, one exploits the fact that interstitial oxygen gives rise to strong local distortions of the host lattice [22]. Niobium exhibits an intrinsic instability towards the ω phase, which is manifested in the deep minimum of the phonon dispersion curve at $\mathbf{Q}^*=\frac{2}{3}(1,1,1)$. It has been shown that the strong oxygen-induced local lattice distortions couple to this anisotropic softness of the lattice, thereby producing pronounced maxima of the distortion-mediated diffuse X-ray scattering at $\mathbf{Q}^*$ [22, 23]. As it will be demonstrated in this work, the monitoring and quantitative analysis of these diffuse maxima by grazing incidence diffuse X-ray scattering allow us to obtain a detailed picture on the emergence of interstitial oxygen close to the niobium surface.

This combination of surface sensitive X-ray methods offers a unique opportunity to unambiguously determine the near surface structure of niobium and its oxide, providing

structural, and chemical information.

A multitechnique approach demands often a collaborative effort between several research groups and facilities. In our case, this has been achieved by the joint effort of Max Planck Institute for Metals Research, Stuttgart, and the Département d'astrophysique, de physique des particules, de physique nucléaire et instrumentation associée, DAPNIA, CEA, Gif-sur-Yvette. Most of the features associated to the natural oxides layers on niobium surfaces, and the weak surface sensitive oxygen-induced diffuse scattering used for the characterization of the subsurface oxygen profiles, require the high brilliance offered only by synchrotron radiation. The synchrotron experiments performed in this work, have been carried out at the MPI-MF beamline at ANKA, Karslruhe, on ID32 and ID03 at the European Synchrotron Radiation Facility, Grenoble, and at the I311 beamline of the Max-Lab synchrotron source, Lund.

This dissertation is organized as follows : Chapter 2 introduces niobium superconducting radio-frequencey cavities, their technology and problematic. The third chapter introduces niobium and its interaction with oxygen. The main and relevant results available in literature about the properties of niobium and its oxide are discussed. In Chapter 4, the theoretical background for the X-ray surface sensitive methods exploited in this work are presented. Followed in Chapter 5 by the description of the experimental set-ups and the *in-situ* high-temperature set-up (>1800°C) developed in the framework of this study. The first part of the experimental results on the Nb(110) surface oxidized in air are presented in Chapter 6. The natural oxide layer, its structure and its progressive dissolution upon thermal treatments are characterized by mean of X-ray reflectivity, core-level spectroscopy and grazing incidence X-ray diffraction. The second part of the results on the Nb(110) surface oxidized in air concerns the determination of the interstitial oxygen depth-distribution beneath the oxide layer and its evolution upon heating, in parallel to the oxide dissolution. This part is described in Chapter 7, together with a comprehensive description of the depth-resolved oxygen-induced diffuse scattering analysis developed in this work. Chapter 8 comprises complementary experimental results on Nb(100) surfaces oxidized under atmospheric and wet conditions, and on the Nb(110) oxidized in water. Discussion are given in respective Chapters and the thesis is concluded with a summary in Chapter 9.

Chapter 2

Niobium superconducting radio-frequency cavities

Niobium superconducting radio-frequency (rf) cavities are a key component of modern high-energy particle accelerators, as they are the devices which impart their energy to the charged particles ("cold technology"). Niobium has been the material of choice for superconducting rf cavities for several decades mainly because of its relatively high critical temperature, the highest lower critical magnetic field, but also its good mechanical properties (see chapter 3). The fundamental advantage of superconducting niobium cavities is the extremely low surface resistance, of a few nano-ohms at 2 K, as compared to several milli-ohms in copper cavities. In this chapter, a brief introduction to the niobium superconducting rf cavities, their technology, properties and open questions that have motivated the present work is given.

Cavity performances

The two main characteristics describing a superconducting accelerating cavity are its average accelerating field E_{acc}, and the quality factor Q_0 ($2\ \pi$ times the ratio of stored energy to the energy loss per cycle) which is inversely proportional to the surface resistance. The quest of high accelerating fields and an affordable superconducting rf technology requested for X-ray Free Electron Lasers and the future International Linear Collider project, which will use more than 500 tons of niobium in building over 20000 superconducting cavities, has revolutionized accelerator applications. Considerable efforts have been made in the past years for the understanding of the limiting factors of the performance achieved by rf cavities. The actual challenge is the understanding of the sharp degradation, the so-called *Q-drop*, of the quality factor at high magnetic field and in the absence of field emission[1] [3]

[1] Field emission of electrons from sharp tips is the most severe limitation in high-gradient superconducting cavities.

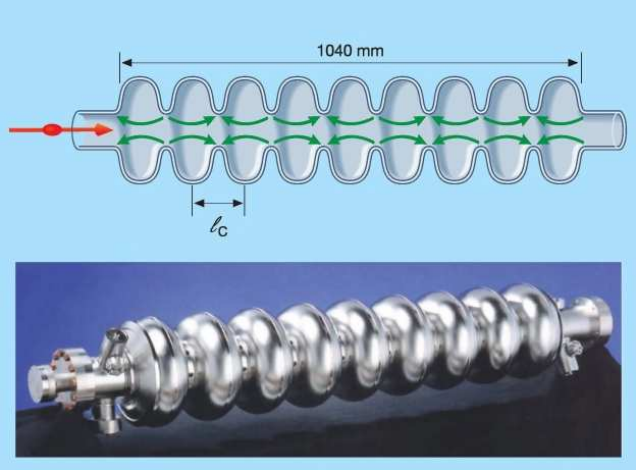

Figure 2.1: Longitudinal cut and picture of a nine-cell superconducting cavity made from pure niobium and cooled by superfluid helium of 2 K. The resonance frequency is $f_0 = 1.3$ GHz. The electric field lines are shown at the instant when an electron bunch has just entered the first cell. The length of a cell is chosen such that the field direction is inverted when the relativistic bunch has moved to the next cell. This is fulfilled for a cell length equal to half the radio-frequency wavelength, $l_0 = c/(2f_0)$. Thereby it is ensured that the particles receive the same energy gain in each cell [24].

(see Fig. 2.4). A remarkable increase of the rf accelerating field has been achieved by low-temperature annealing (below 150°C for several hours), although the microscopic origin of this effect has up to now remained unclear. But before discussing this point, let's first introduce some basic knowledge about rf superconductivity.

rf superconductivity

Niobium is a type II superconductor, characterized by two critical fields, H_{c1} and H_{c2}. For magnetic fields lower than the first critical magnetic field H_{c1}, the Meissner state is observed, where the magnetic field is expelled from the material when cooled below T_c, except inside the penetration depth at the surface of the material. The niobium penetration depth is about 30-50 nm under the native oxide layer. In the range $H_{c1} < H < H_{c2}$, the superconductor is in the so-called "mixed state", in which the magnetic field penetrates the bulk material in the form flux lines (vortices). At higher field than the second critical magnetic field H_{c2} the transition to the normal conducting state occurs as illustrated in Fig. 2.2. The dc superconductivity of niobium is relatively well predicted by the BCS theory[2]. In the rf regime, the behavior of superconductors is slightly different and the Meissner state (expulsion of magnetic field) is observed at higher field than the first critical

[2]The BCS theory for superconductivity was developed in 1957 by John Bardeen, Leon Cooper, and Robert Schrieffer and is based on the assumption that the supercurrent is not carried by single electrons but rather by pairs of electrons of opposite momenta and spins, the so-called *Cooper pairs*.

magnetic field. A superheating field H_{sh} was introduced to describe this behavior. Surface energy considerations lead to an estimation of the superheated critical field values. In type II superconductors the dependence of the superheating fiel has been calculated [25]. The phase diagram, including all critical fields, is plotted in Fig. 2.2 as a function of the Ginsburg-Landau parameter κ. The maximum accelerating field achieved by a cavity is a function of the electric/magnetic field ratio related to the specific shape of the cavity and is reached when the local magnetic field inside the cavity exceeds the transition magnetic field of the superconductor. The critical rf magnetic field of niobium is close to H_{sh} [25].

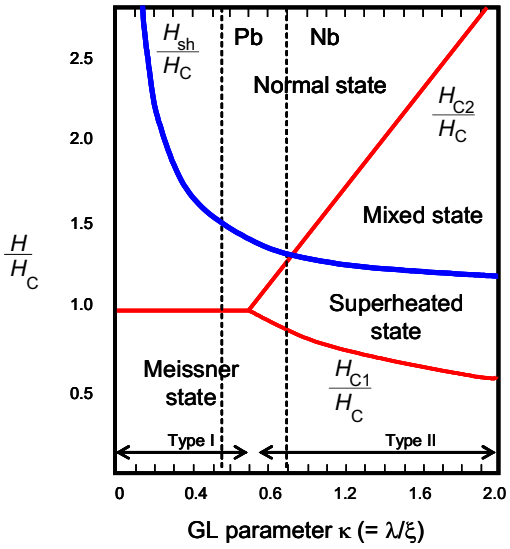

Figure 2.2: Phase diagram showing the Meissner, normal, mixed, and superheated states [25].

Surface resistance

In the case of alternating rf currents, dissipation does occur for all $T > 0$ K. The reason is that the high-frequency magnetic field present in the skin layer induces oscillations of the electrons which are not bound in Cooper pairs, leading to dissipation. The rf surface resistance R_s is in general described by the following expression,

$$R_s = R_{BCS} + R_{Res} \tag{2.1}$$

with

$$R_{BCS} = A(\lambda_L^4, \xi_F, l, \sqrt{\rho_n})\frac{\omega^2}{T}e^{-\Delta/kT} \tag{2.2}$$

where A is a constant dependent on the material parameters of the superconductor, such as the penetration depth λ_L, the Cooper pairs coherence length ξ, the Cooper pairs mean free

path l, the normal state conductivity ρ_n, the rf frequency ω, and the superconducting gap Δ. R_{BCS} is the well know BCS term and R_{res} that describes residual losses, is temperature independent and caused by several factors: surface imperfections and inclusions, impurities, residual dc magnetic field, lattice distortions, etc. [25, 26]. R_{res} is equal to a few nΩ for a clean niobium surface but can sensibly increase if the surface is contaminated. Typical R_s values for niobium cavities are in the range from 100 to few nΩ (see Fig. 2.3). Any defect that locally enhances the magnetic field or the surface resistance decreases the cavity performance due to local heating of the material.

In the case of superconducting cavities, the purity of purchased niobium is important, in terms of bulk impurity content as well as inclusions from manufacturing steps. Dissolved impurities serve as scattering sites for the electrons which are not condensed into Cooper pairs. These impurities lower the thermal conductivity and thereby limit the maximum tolerable surface magnetic field before onset of thermal breakdown [25]. Among the light, interstitially dissolved impurities, oxygen is dominant due to the high affinity that niobium has for oxygen (see chapter 3). Interstitial impurities such as oxygen have a bigger effect than substitutional impurities such as tantalum, as for example, oxygen decreases the T_c of niobium by 1°C/at. %, whereas tantalum decreases T_c by 0.1°C/at. %

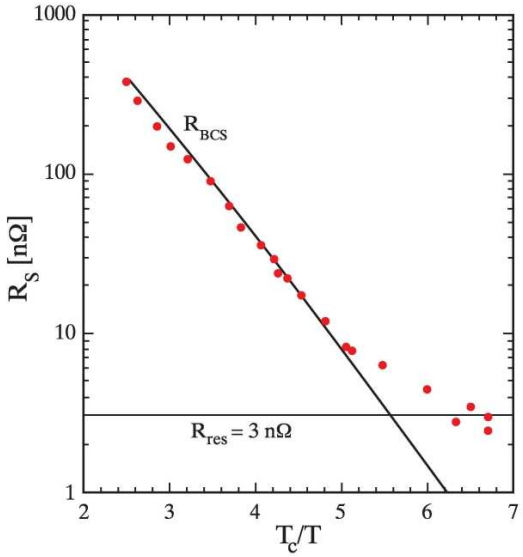

Figure 2.3: The surface resistance of a 9-cell superconducting cavity plotted as a function of T_c/T. The residual resistance of 3 nΩ corresponds to a quality factor $Q_0 = 10^{11}$ [24].

Therefore high purity material with high thermal conductivity is preferred for the fabrication of the cavities because it allows thermal stabilization of minor defects. The purity of the material is expressed through the residual resistivity ratio (RRR), which is the ratio

of the resistivity at room temperature to that at T_c. Typical niobium used for cavities exhibit a RRR about 300, which corresponds to 99.98 % - 99.99 % purity[3]. Until now, no other superconductor has been able to break the niobium 30 years old monopoly in high field applications. Niobium itself exhibits limitations undoubtedly related to the behavior of the first few nanometers of its surface. In particular, a strong degradation at high field is observed, which can be somehow recovered with a low temperature treatment, as discussed in the following.

Low temperature annealing and cavities performances

Cavities performances are generally expressed in a graph where the accelerating gradient E_{acc} (proportional to the magnetic field), is plotted with respect to the quality factor Q_0 (inversely proportional to the overall dissipations). Without baking, cavities exhibit a strong dissipation at high field, the so called "Q-slope", which was found to be drastically improved when a low temperature baking, (100-140°C) *in-situ* baking of the cavity in ultrahigh vacuum for several hours, is applied [1–3] (see Fig. 2.4). It has been established that this phenomenon is related to the behavior of the first 10-30 nm of the surface [2, 4, 27, 28]. It is believed that the Nb_2O_5 oxide layer present at the niobium surface does not play a direct role in rf dissipation. Nevertheless, the role of the oxide species such as NbO_2 and the metallic NbO at its interface with the metallic niobium is still unclear, and the

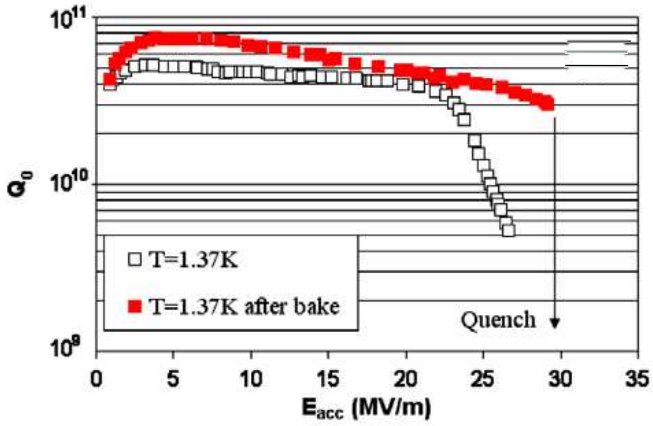

Figure 2.4: Illustration of the performances of rf cavities before and after low temperature *in-situ* baking of a cavity in ultrahigh vacuum for several hours. The accelerating gradient E_{acc} is proportional to the magnetic field inside the cavity, and the quality factor Q_0 is inversely proportional to thermal dissipation, thus to the surface resistance. In this case, Q_0 vs. E_{acc} is measured on a 1.47 GHz single cell cavity before and after baking at 120°C for 48 h from [26].

[3]Below RRR 800, interstitials atoms mainly influence this ratio whereas at higher value, substitutional atoms (metals) and crystallographic defects are the main contributors. Commercial niobium is RRR 30 whereas theoretical value for an infinite defect less monocrystals would be 33 000.

different oxide modifications upon surface and/or thermal treatments might influence the overall superconducting behavior of the niobium surface. The aim of the present work is to respond to the crucial need of a better atomistic understanding of the near surface region and its evolution upon thermal treatments. This implies the investigation of the niobium oxidation, the thermal stability of niobium oxides upon annealing, but also the interstitial oxygen distribution below the oxide layer before and after thermal treatments.

Indeed, one of the scenarios proposed to explain the baking effect involves interstitial diffusion toward the bulk of the material, i.e. a redistribution of subsurface interstitial oxygen within the penetration depth of the rf field into niobium (typically 50 nm) [3, 4, 29]. Oxygen, reported in high concentrations at the niobium/oxide interface [3, 16, 17, 29], is known to decrease superconducting properties like the critical temperature [5, 6] or the superconducting gap, which in turn increases the surface resistance [30, 31]. By diluting the oxygen "contamination" layer, one can expect the superconducting gap to increase back to the bulk value and recover a good surface resistance.

To confirm or infer such a hypothesis one needs to establish with a very high precision the oxygen distribution before and after thermal treatments, and to investigate how it balances between the oxide layers and the underlying superconductor. This will be discussed in details in chapters 6 and 7. In parallel to this work, attempts have been made to measure the superconducting gap. Very recent results in this field are consistent with the results presented here [32, 33]. As we will see no evidence of oxygen depletion underneath the interface has been found for temperatures below 300°C for the surface preparations investigated in this work.

Chapter 3

Niobium and its oxide

In this chapter, the main and relevant results for the present work available in literature about niobium, niobium oxides, the oxidation process of niobium and the subsequent dissolution of its oxide layers upon heating, are reviewed.

3.1 Niobium

Niobium[1] has been discovered in 1801 by C. Hatchett, nearly in the same time as Tantalum as both occur nearly always together in nature. Niobium derived its name from *Niobe*, mythological Goddess of Tears, daughter of the Greek mythological character Tantalus who gave his name to Tantalum because of the "tantalizing" difficulty in dissolving the oxide of the new metal in acids [34]. Niobium and Tantalum show very similar chemical properties and are never found in a free state in nature, usually occurring in combination with oxygen and one or more other metals[2].

Niobium is a ductile transition metal characterized by an incomplete *d* sub-shell, which crystallizes in the *bcc* cubic structure. As other refractory metals, niobium has a rather elevated melting point, and presents a high strength at elevated temperatures. Its metallurgy has been thoroughly studied because of its use as an alloying element in stainless steels, main commercial application of niobium, and superalloys for aerospace applications [34,35]. The addition of niobium to stainless steel generally forms carbide precipitates, which bring about a beneficial hardening effect in the matrix.

Niobium and its oxides have also been extensively investigated in the past because of its technological importance as a superconducting material. Niobium has indeed the highest

[1]The original name of the 41^{st} element was *columbium* given by Hatchett in honor of the country of its origin. The International Union of Pure and Applied Chemistry adopted *niobium* as official name in 1950.

[2]Most of industry's demands are supplied by the minerals tantalite and columbite which cover the range of tantalates and niobates of iron and manganese $(FeMn)O.(NbTa)_2O_5$.

critical temperature of all elements, $T_c \cong 9.25$ K, allowing operation of the devices at 4.2 K, where He I boils, but also the highest first critical magnetic field B_{c1} ($\sim$170mT) [36]. Niobium is one of the three elemental superconductors that are of Type II (the others being vanadium and technetium). Niobium is used in nanoelectronic devices as Josephson junction or tunnel barrier, applications for which a good control of the oxide layer is needed ; as niobium-tin and niobium-titanium alloys in wires for superconducting magnets ; and in its pure form as the most commonly used material for the rf superconducting cavities in particles accelerators (see section 2).

The high chemical reactivity of niobium makes that it gets easily polluted by impurities like oxygen, nitrogen, or carbon, but also makes of it a good candidate for its use in heterogeneous catalytic systems [7–14]. Catalysts containing molybdenum and vanadium, neighbors of niobium in the periodic table, are very important and their catalytic properties have been studied extensively, in contrast to niobium. However, in some cases, if the catalysts are applied in liquid phase reactions or have to work at very high temperatures during the reaction, the higher stability of niobium species protects the catalysts from leaching of the active phase [9]. Niobium oxides remarkably enhance the catalytic activity and prolong catalyst life when added in small amounts to known catalysts [8]. Moreover, niobium oxides exhibit a pronounced effect as supports of metal and metal oxide catalysts. Further catalytic applications of niobium are expected and for this purpose, a fundamental knowledge about the niobium oxidation behavior and the properties of the different niobium oxides is also required.

Note that because of its low neutron capture cross section, niobium is also used as cladding material for nuclear fuel elements. And adding niobium to glass has been demonstrated to provide a higher rate of refraction, which in turn makes it possible to create thinner and lighter corrective lenses.

Physical properties and in particular superconducting properties of materials are strongly influence by impurities, surface and interface effects. The electronic, vibrational, and structural properties of bulk niobium [37], and niobium surfaces [38–41], have been explored by numerous *ab-initio* calculations. The surface properties of Nb(100) have attracted a special interest due to the hydrogen adsorption and/or desorption behavior manifested by this surface, and attributed to subsurface hydrogen sites [42, 43]. The Nb(100) surface has been investigated by numerous photoemission studies [44–46].

All transition metals of group III-VI exhibit a stable *bcc* phase in a certain temperature range and at normal pressure. For group V elements, such as niobium and tantalum, the *bcc* phase β is stable over the whole range of temperatures. Transition elements may have multiple stable oxidation states, since they can lose d electrons without a high energetic

penalty.

The following sections will concentrate on the interaction of niobium with its main impurity, i.e. oxygen. Before discussing the oxidation of niobium and the properties of its oxides, the striking features of interstitial oxygen in niobium are described. Note that the solubility and mobility of other light elements that dissolve as interstitials in niobium such as hydrogen [47–50], or nitrogen [51–53], have been investigated in various works. The interaction of carbon with niobium is shortly discussed in 3.2.

The main physical properties of niobium are summarized in Tab. 3.2 and 3.3.

3.2 Interstitial oxygen in niobium

Interstitial oxygen impurities are known to have a strong influence on the physical properties of niobium [34, 54], in particular its superconducting properties [5, 6]. The superconducting critical temperature of niobium decreases almost linearly by 0.93K/at.% O. The lower critical field H_{c1} and the electronic density of states at the Fermi level decrease with increasing oxygen content, while the superconducting upper critical field H_{c2} and the normal-state resistivity ρ_n are increasing with increasing the oxygen concentration.

The main features of the Nb-O phase diagram have been established by Elliott [55], showing the *bcc* structure of niobium, the three main niobium oxides NbO, NbO_2 and Nb_2O_5, and determining the solubility of oxygen in niobium in between 1 at.% at 500°C and 4.04 at.% at 1915°C (see Fig. 3.5), extending thereby the work of Seybolt [56], who reported a solubility between 1.38 to 5.52 at.% from 775°C to 1100°C. The dependence of the unit cell parameter a with respect to the oxygen concentration c is given at room temperature by

$$a = 3.3001 + 0.0041 \ \times c \quad (\text{Å})$$

where c is in the range 0-4.2 at.% [57].

Two types of interstices are found in cubic lattices : octahedral and tetrahedral sites. The interstitial solubility of an element in a metal depends on the stability of the phase acting as a source of the interstitial atoms and on the total electronic interaction energy (enthalpy) between the element in solution and the metal (electronegativity and valence). These chemical factors have been shown to be of greater importance than the size factor (strain energy) of the interstitial with respect with the interstices. Different works have shown that interstitial oxygen occupies the octahedral sites in the *bcc* lattice of niobium [22, 58, 59]. Three groups of octahedral sites in equal numbers can be distinguished, as x, y and z sites conforming to their location between two nearest-host-neighbor atoms along the x, y and z axes of the cubic unit cell. This is illustrated in Fig. 3.1.

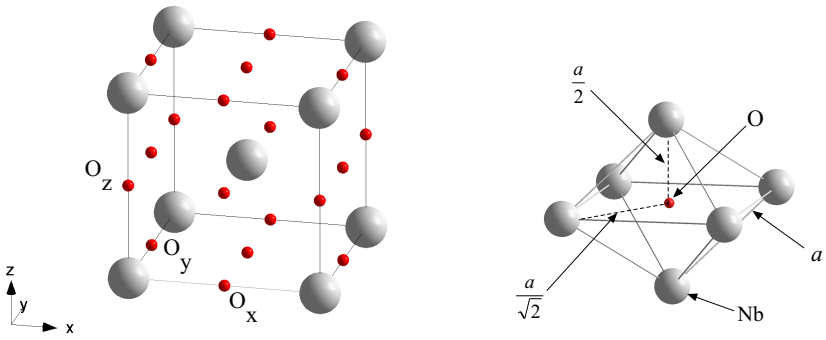

Figure 3.1: Octahedral interstitial sites in the niobium *bcc* lattice of lattice parameter a.

The diffusion of oxygen in niobium has been the subject of various studies [57,60]. The expression of Powers et. al [60] for the diffusion coefficient D is[3]

$$D(T) = 0.0212 \ \exp\left(-\frac{26910}{RT}\right) \quad (cm^2/s) \tag{3.1}$$

where T is the temperature in Kelvin and $R = 1.987\, cal.K^{-1}.mol^{-1}$ the ideal gas constant, the frequency factor is equal to $0.0212\, cm^2/s$ and the activation energy $26910\, cal.mol^{-1}$. Following Eq. (3.1), the diffusion length $2\sqrt{Dt}$ of oxygen in bulk niobium is equal to 350 Å for 5 hours at 145°C, while it reaches the μm range for 50min. at 300°C.

Several studies performed under ultra high vacuum have underlined the oxygen segregation at the niobium surface after annealing at temperatures above already 300°C [61–66]. After cooling to room temperature an oxygen-rich layer, typically about 10-15Å was found [64]. Oxygen redistributes reversibly between bulk and surface as a function of temperature, and equilibrium between the oxygen diffusion and segregation is established around 800°C. If the driving force for surface segregation is the lowering of the surface free energy, equilibrium conditions provide information on how much the surface energy is reduced by oxygen segregation. The estimated segregation enthalpy is 11-17 kcal/g.atom depending on the bulk concentration in oxygen (resp. 2-0.1 at. %) [64]. Oxygen in niobium prefers to segregate toward the crystal surface in relatively high concentration although the solubility limit in the bulk is not reached. High concentrations of interstitial oxygen have been reported at the niobium/oxide interface for : Nb(110) films oxidized above 100řC in air [15], due to surface segregation after high temperature UHV annealing of a Nb(110) single crystal [16], and for polycrystalline, high residual resistivity ratio samples in a recent atom probe tomography study [17]. Desorption of oxygen becomes relevant only at

[3] D indicates the amount of dissolved substance diffusing in unit time through a plane of unit area in a unit of concentration gradient.

elevated temperature > 1600 °C, and mainly occurs by evaporation of niobium monoxide and dioxide [57, 67, 68]. Segregated oxygen-induced reconstructions have been recently investigated by several authors [16, 66, 69, 70] (see also section 3.4).

The dissolution of interstitial oxygen in the metal core plays an important role in the oxidation of niobium as often pointed out [71,72]. As mentioned above niobium may take up under certain conditions more oxygen than its saturation value [71]. This supersaturation is one of the determining factors in the formation of suboxides. The initial incorporation of subsurface O has been referred to as the "bottleneck" in the oxidation sequence of transition metals. The stability of subsurface oxygen was shown to depend strongly on the lattice deformation properties, implying correlations between the oxidation behavior and properties such as the cohesive energy or bulk modulus [73].

Omega (ω) phase

The β phase of pure niobium exhibits an intrinsic instability toward the ω-phase, manifested in the deep minimum of the phonon dispersion curve at $\mathbf{Q}^*_\omega = \frac{2}{3}(1,1,1)(2\pi/a_{bcc})$. In this section, the characteristic of the ω-phase are presented. The strong oxygen-induced local distortions in niobium couple to this anisotropic softness of the lattice, such that *single* oxygen impurities in niobium bulk are nuclei for the local formation of trigonal ω-phase embryo, embedded into the natural *bcc* lattice [22].

The precipitation of the metastable omega (ω) phase in transition metal elements has attracted considerable interest, initially motivated by the effect of the phase on the mechanical properties of the material, and later on by the discovery of the marked improvement in the superconducting properties in alloys[4] [74] [and references therein]. The crystallographic aspects of the displacive *bcc* $\rightarrow$ ω phase transition have been reviewed in various works [74, 75].

The β to ω transformation can be described by referring to an hexagonal description of the parent β phase, with lattice parameters $a_{\beta hex} = \sqrt{2}a$ and $c_{\beta hex} = a\sqrt{3}/2$ where a is the lattice parameter of the β phase. In this representation, one has three atoms per cell at $(0,0,0)$, $(1/3,2/3,1/3)$ and $(2/3,1/3,2/3)$, the [0001] hexagonal axis is parallel to the $[111]_\beta$ cubic direction, and the $[11\bar{2}0]$ hexagonal direction is parallel to the $[1\bar{1}0]_\beta$ cubic direction, as illustrated in Fig. 3.3 (a). When the ω phase is created, two neighboring (111) planes move toward each other by a displacement in the [111] direction, while each third (111) plane remains unmoved. The fully collapsed ω phase is described by a displacement $\mathbf{u}^* = \pm a(\sqrt{3}/12)(1,1,1)$ and gives rise to superlattice reflections at $\mathbf{Q}_\omega*$. If the displacement

[4] ω phase precipitates act as pinning sites for magnetic flux and prevent Lorentz-force induced motion with simultaneous energy dissipation.

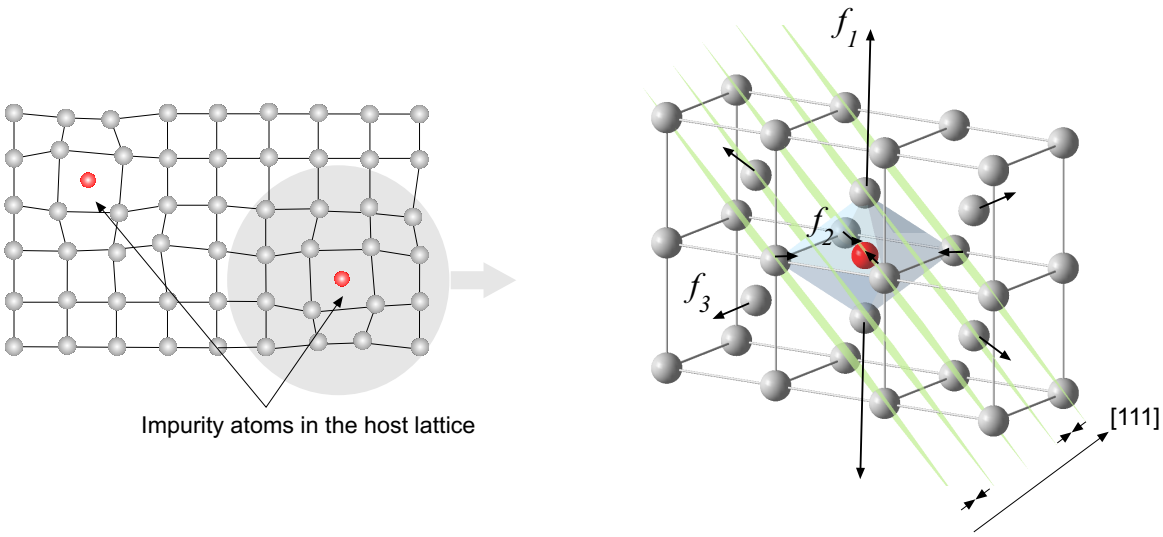

Figure 3.2: Left : Schematic view of the lattice distortions induced by point defects. Right: Niobium lattice distortions in the local neighborhood of an interstitial oxygen located on an octahedral site, (111) planes (green planes), and Kanzaki forces f_i around it up to the third nearest-Nb-neighbor atoms (note that only four third nearest-Nb neighbor atoms are shown). The strong oxygen-induced distortions couple to the intrinsic instability of the *bcc* lattice in the [111] direction, such that every single oxygen defect are nuclei for the formation of the trigonal ω phase [22] (see text for details).

u_{111} is inferior to $u*$, the structure is then called the "rumpled" ω phase. The $\beta \rightarrow \omega$ transformation is illustrated in these two cases in Fig. 3.3. The "ideal" ω phase has an hexagonal symmetry ($P6/mm$), while the rumpled ω phase present a trigonal symmetry described by the space group ($P\bar{3}m1$).

Kanzaki [76] introduced a powerful concept which models the deformation of the host lattice by a set of virtual forces which would have the same effect on the position of the neighboring defect atoms as the defect (see section 4.2.1). It has been shown that for oxygen (and nitrogen) in niobium, radial Kanzaki forces extending up to the third-nearest niobium neighbor around the defect are needed in order to describe the diffuse scattering intensities recorded in neutron scattering experiments [22, 23]. This is illustrated in Fig. 3.2. The Kanzaki forces and the distortions of the first four niobium shells around the oxygen atoms (see section 4.2) are given in Tab. 3.1.

As it will be demonstrated in this work (see section 4.2 and chapter 7), the monitoring and quantitative analysis of the pronounced maxima of the distortion-mediated diffuse X-ray scattering at $\mathbf{Q}^*$, by means of grazing incidence diffuse X-ray scattering, allows to obtain a detailed picture on the emergence of interstitial oxygen close to the niobium surface and its depth-distribution profile.

Metals such Ti or Zr, with a large oxygen solubility, present ordered structure of the

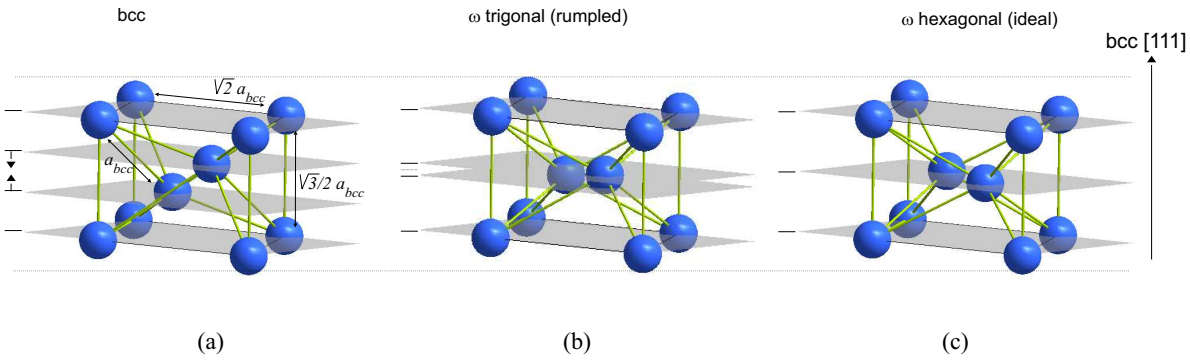

Figure 3.3: The $\beta \rightarrow \omega$ transition. When the ω phase is created, two neighboring (111) planes (grey planes) of the β bcc phase move towards each other by a displacement in the [111] direction, while each third (111) plane remains unmoved. (a) (111) planes in the hexagonal representation of the bcc lattice. (b) The "rumpled" (trigonal) ω phase. (c) The fully collapsed ideal (hexagonal) ω phase (see text for details).

solid solution. In the case of oxygen in niobium however, with a relative moderate oxygen solubility, ordering has been only rarely reported in literature. At low concentrations, interstitial oxygen is disordered in the niobium lattice. A recent work has described various sequences of oxygen ordering above a certain concentration [15, 77]. A possible ordering force is mediated by the static lattice distortions around the oxygen defect as discussed theoretically in [78].

Kanzaki forces (eV Å^{-1})	Lattice distortions (Å)
$f_1 = 2.8$	$u_1 = 0.42$
$f_2 = -0.27$	$u_2 = -0.13$
$f_3 = 0.54$	$u_3 = 0.06$
	$u_4 = 0.07$

Table 3.1: Kanzaki forces f_i $(i = 1, 2, 3)$ and lattice distortions u_j $(j = 1, 2, 3, 4)$ for oxygen in niobium from [22].

Carbon in niobium The solubility of carbon in niobium is very limited [79], and carbon interstitials have been predicted to occupy the tetrahedral sites of the niobium lattice [80]. The heat of formation of NbC at room temperature is -30 kcal/mole [34]. NbC crystallizes in the rock-salt structure (B_1). The lattice constant is $a = 4.467$ and the density equal to 7.8 gr/cm^3 are close to the NbO values. Depending on the relative surface coverages of oxygen and carbon, the decarburization may occur either via carbon monoxide and/or the formation of volatile oxides (NbO, NbO_2).

3.3 Niobium oxides

The process of oxidation of metal surfaces is of considerable technological importance as many applications are determined by the properties of the thin oxide layer which covers them. Corrosion and passivation are just two examples of either destructive or useful processes directly linked to this phenomenon. The oxide crystal structure, its stability with respect to temperatures, and its epitaxial relationship with the metal substrate are then issues of crucial importance for the material properties, especially when the thin layer near the surface is conductive and might play a crucial role for superconducting applications as niobium cavities. Before describing the different niobium oxides and their properties, a short introduction to the theory of metal oxidation is given.

3.3.1 Oxidation theory

The initial stage of the oxidation process of a clean metal surface immersed in an oxygen atmosphere involves adsorption of the oxygen on the metal surface. Two main adsorption mechanisms can be distinguished: *physisorption* and *chemisorption*. In physisorption, the oxygen molecules are bound to the metal surface via weak *Van der Waals* interactions. Chemisorption on the other hand involves a rearrangement of the valence electrons of the metal and adsorbate, and the formation of a chemical bond. Chemisorption is often accompanied by a dissociation of the O_2 molecules into atomic oxygen.

As soon as the critical oxygen concentration is reached on the surface [81], oxide clusters are nucleating and coalesce until a close oxide layer is formed. Further oxide growth proceeds in the direction perpendicular to the surface.

Assuming that the oxygen molecules are dissociated and charged at the oxide surface, the continuation of the oxidation reaction requires the diffusion of either oxygen, either metal ions (or both) through the existing oxide layer which acts as a barrier. The driving force for this diffusion is the so-called *Mott-potential* existing in between the negatively charged surface and the positively charged interface. The Mott-potential depends therefore on the difference in electronegativity between the metal and the electronegative oxygen. If the potential is strong enough, one of the species (the metallic ions, the oxygen ions, or both) will then diffuse through the existing oxide layer and continue the growth of the oxide layer. Otherwise the oxidation stops and the oxide acts as a passivating layer. Depending of the diffusing species the oxidation reaction takes place at the surface (metallic ions diffusing from the interface to the oxide surface) or at the metal/oxide interface (oxygen ions diffusing from the surface to the interface). In some cases both species are diffusing simultaneously and the oxidation process can therefore occur in principle anywhere in the

oxide. The driving force of this reaction is the change of the free energy associated to the formation of the oxide from the reactants, while the reaction rate is a question of kinetics and is influenced by the energy barriers involved in the reaction.

A quantitative theory of the oxidation process in atomistic terms has been developed by Cabrera and Mott [82] and continued by Fromhold and Cook [83], describing the oxide growth perpendicular to the surface with respect to the thickness limiting factor (up to oxide layer thicknesses of about a micrometer). The individual oxide growth is usually determined by one of the following processes : electron transfer associated to the chemisorption step, electron transport by electron tunneling or by thermoemission, or ion diffusion of either metallic cations or oxygen anions through the oxide layer. Usually only one of these processes, depending on the oxidation conditions such as temperature and oxide thickness and the material, is predominantly limiting the oxide formation and determines the oxide growth. According to the Cabrera and Mott model, the oxide growth rate is limited in the early phase by ion diffusion and in the later phase by electron tunneling through the oxide, with a transition film thickness about 30-40Å. As the film thickens, the electron current drops considerably and becomes rate-limiting. A number of books and reviews have discussed the details of the oxidation theory of metals to which the interested

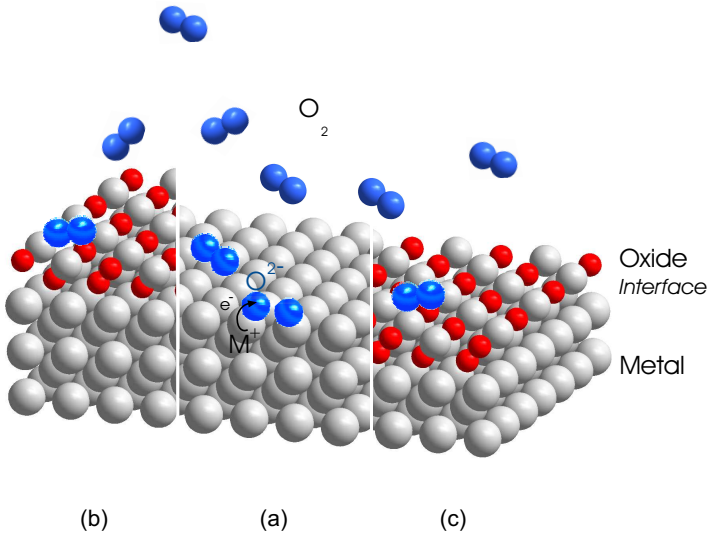

Figure 3.4: (a) First steps of the metal oxidation process, the O_2 molecules are *physisorbed* at the surface via Van der Waals interaction, and then *chemisorbed* with a charge transfer from the metal to the oxygen giving rise to n O^{2-} ions and $2n$ metallic cations. As soon as the critical oxygen concentration is reached on the surface, oxide clusters are nucleating and coalesce until a close oxide layer is formed. Further oxide growth proceeds in the direction perpendicular to the surface. Depending on the diffusing species, the oxide growth perpendicular to the surface occurs either (b) at the surface of the oxide layer, if the metal ions are diffusing, or (c) at the metal/oxide interface if the oxygen ions are diffusing.

reader is invited to refer [82–86].

Note that following the physisorption, oxygen dissolution in the metals can take place if the potential energy for an oxygen ion on an interstitial site within the metal lattice is similar to the chemisorption potential. For some metals (Ta, Nb, Ni) many oxygen monolayers are taken up at room temperature prior to the observance of any oxide formation, leading to an oxygen solution beneath the surface. The precipitation from a metal layer saturated or supersaturated with oxygen plays then an important role in the initial formation of isolated nuclei [84].

The reactivity of oxygen and/or mass transport through the oxide are often increased by the presence of impurities, especially water, in the oxidizing environment. The oxide structure depends directly on the oxidation temperature, the oxygen pressure, the state of the surface, and also on the orientation of the surface. The formation of epitaxial oxide layers depends strongly on the symmetry and on the lattice mismatch between the oxide and the underlying metal. Oxide films formed at low temperatures tend to be amorphous, some of these such as Nb_2O_5 form network structures, where an oxygen ion can move more easily through the channels of the network than a tightly bound though smaller cation. These oxide films grow therefore by oxygen-ion diffusion. The effect of water can result in an increase of the oxidation rate, and it is suggested that the increase of the ion-transport might be caused by the incorporation of hydrogen in the oxide which can change its defect-dependent properties.

Single crystals and amorphous layers differ from polycrystalline material in that sense that no grain boundaries are present. Impurities often concentrate at grain boundaries, leading to defect regions in the oxide grown from the polycrystalline metal. These regions provide paths for easy-ion diffusion and thus, fast oxide growth. Single crystals and amorphous materials minimize such defects and should therefore produce more perfect oxides with a slower oxidation rate [86]. A comparison of different diffusion types results in a difference of the diffusion velocity by a factor of $10^2 - 10^5$ between diffusion along grain boundaries and bulk diffusion in a high quality single crystal [58].

3.3.2 Niobium oxidation

The main features of the Nb-O phase diagram have been established by Elliott [55], showing aside the solubility region, three niobium oxides: NbO, NbO_2 and Nb_2O_5 (see Fig. 3.5). Nb_2O_5 is the most stable of them but all three have a large negative free energy of formation [87]. Before describing the main properties of these oxides, and other suboxide species reported in literature, lets review shortly the relevant results available on the niobium oxidation process.

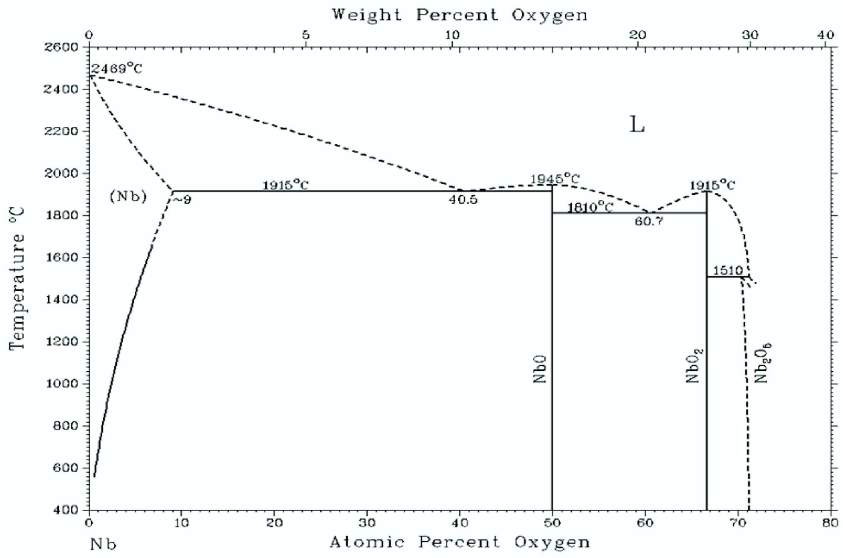

Figure 3.5: Nb-O phase diagram

The initial stages of niobium oxidation have been studied by Lindau and Spicer [72] by means of ultraviolet photoemission spectroscopy (UPS). They reported the initial formation of a thin layer of NbO, followed for larger oxygen exposures and/or higher temperatures by the formation of NbO_2, and after heavy exposure by the formation of Nb_2O_5. Their suggestion that the dissolution of interstitial oxygen into the niobium matrix acts a precursory stage before the oxide starts growing is supported by different works [15, 58, 84, 88, 89].

The study of Halbritter in direct connection with rf superconductivity, focused on the interfacial properties in between niobium and its oxide [89–91]. In his model, the oxide formation is initiated by oxygen dissolution in niobium and subsequent Nb_6O segregation to relax strain. The Nb_2O_5 nucleation strains the interface and generates defects underneath. Halbritter reports on both oxidation in an atmosphere of H_2O and O_2, studying the growth of Nb_2O_5 layers up to a passivating thickness of about 60Å. The growth of the insulating Nb_2O_5 is well described by the Cabrera-Mott theory in the extension given by Fromhold and Cook [83]. Cation diffusion within the oxide film is insignificant compared with the anion diffusion, therefore, the new oxide layers are formed at the oxide-metal interface [92, 93]. The dry oxidation is shown to proceed much slower than in H_2O, as well as the oxidation of polycrystalline samples is much faster than on single crystals.

As mentioned before, niobium oxidation has been extensively studied by mean of various methods including mostly low energy electron diffraction (LEED) [94, 95], auger electron spectroscopy (AES) [62, 66, 94–98], secondary ion mass spectroscopy (SIMS) [66, 97], electron energy loss spectroscopy (EELS) [66, 94], XPS [16, 18, 19, 21, 90, 91, 99–106] and UPS [72, 104]. Such surface sensitive methods provide limited information about the struc-

ture and the morphology of the system, and mainly focus on its chemical properties.

The oxidation of niobium appears to be very complex, and the oxide species and structures obtained very sensitive on the oxidation conditions, the orientation of the surface, and the preparation of the surface. The study of initial oxide formation is complicated owing to difficulties in producing clean niobium surfaces as mentioned before (see also section 5.4), and the stringent high-vacuum requirements needed for maintaining them. Several works have studied the adsorption of oxygen on clean Nb(110) surfaces [62, 96, 107, 108] at room temperature and low exposure mainly with low energy electron diffraction (LEED). Complex LEED patterns reported for the (110) surface annealed at temperatures below 2000°C [66, 94], suggest the formation of an epitaxial overlayer on the surface. The morphology of oxygen-induced structures on Nb(100) [95, 96, 105, 108, 109] and Nb(111) [96] surfaces has been investigated by LEED. Farrell and Strongin [108] reported that the structure of the Nb(001) surface changes from facetted to (1×1) of the clean surface via a c(2×2) as the annealing temperature is increased to 2000°C. Recently the atomic structures of annealed surfaces have been investigated by scanning tunneling microscopy (STM) on Nb(100) [95, 110, 111] and on Nb(110) [69, 112]. Amorphous NbO and NbO_2 oxides were reported on Nb(100) surfaces during oxidation at room temperature and low pressure due to difficult oxygen diffusion, while at elevated temperatures (600°C, UHV) the oxide crystallizes into epitaxial NbO(100) nanocrystals via dissolution of oxygen into the bulk metal [95].

A theoretical study of the effect of the initial formation of an oxide layer on the metal surface have been performed by Ronay and Nordlander [113, 114]. They calculated the potential energy barrier for both Nb(110) and NbO(110), showing that the formation of NbO on a niobium surface dramatically increases the potential barrier for oxygen incorporation. They refer to the experimental data from R. Pantel et al [96] and I. Lindau [72] who reported a dramatic slowing down of the niobium oxidation process once NbO is formed on the surface.

The difference between dry and atmospheric oxidation of Nb(110) films on sapphire has been recently investigated by X-ray diffraction [115, 116]. XPS, UPS, AES and EELS studies for H_2O exposure [117, 118], show that the uptake of oxygen atoms is much more efficient when the surface is exposed to H_2O than to O_2.

Note that the presence of NbO and/or NbO_2 at the interface between Nb_2O_5 and the metal is of fundamental importance for niobium applications such as tunnel-barrier material in superconductive Josephson junctions and has often been subject to controversy. Unlike the presence of NbO which has been reported together with the stable Nb_2O_5 by various works, the existence of NbO_2 appeared to be more hypothetical.

Some further XPS works showed that the air oxidation of niobium could be stopped by the use of a thin aluminum, Yttrium or Mg overlayers, while a thin layer of Cerium enhanced the oxidation [119], which was proposed as the first observation of the "catalytic oxidation" of a solid.

The thermal stability of niobium oxides and the epitaxial relationships observed between the niobium oxides with the underlying metal substrate are discussed in sections 3.3.7 and 3.4. The following sections are dedicated to the main properties of the different niobium oxide species mentioned above.

3.3.3 NbO

Unlike most oxides of transition metals of the two first groups having a simple close-packed structure of rock-salt type, the structure of the niobium monoxide is an ordered defective rock-salt structure where one-fourth of both fcc sublattices of niobium and oxygen atoms, corresponding to (0,0,0) and (1/2,1/2,1/2) sites, are unoccupied. This corresponds to 25% vacancies as illustrated in Fig. 3.6. The space group is $Pm\bar{3}m$ with a structural parameter $a = 4.21$Å. NbO forms in a very narrow stoichiometry range NbO_x 0.96 $\leq$ x $\leq$ 1.02 [55, 120, 121]. The niobium atoms can be seen in the NbO structure as a three dimensional network of octahedra coupled with each other by vertices, with oxygen atoms located between them. The strong metal-metal bonding inside the octahedra, and the metal-oxygen π bonding are both important in stabilizing this structure [122, 123]. NbO has a metallic type conductivity and becomes superconducting around 1.4K [120, 124], which distinguishes it from other transition metal oxides and other niobium oxides. The core-level binding energies of NbO reported in literature are summarized in Tab. 4.2.

As mentioned before, NbO is the first oxidation step after oxygen adsorption in vac-

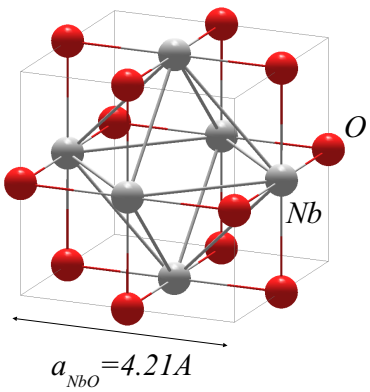

Figure 3.6: Defective ordered rock-salt crystal structure of NbO (space group $Pm\bar{3}m$).

uum [34, 66, 72, 94, 97, 104] and its presence at the interface with the Nb_2O_5 formed after higher oxygen exposure has been reported in different studies [17, 19, 89]. Segregated oxygen-induced NbO structures have been described after annealing of samples at elevated temperatures in various recent studies [16, 69, 95]. The epitaxial relationships of these structures with respect to the underlying metal are discussed in section 3.4.

3.3.4 NbO_2

NbO_2 undergoes a semiconductor-metal transition at approximately 800°C accompanied by a change in the crystal structure [125–128]. The structure of the low-temperature (LT) semiconducting phase was determined by X-ray and neutron diffraction [128–130] as a distorted rutile and the space group $I4a_1/a$. The lattice parameters of the tetragonal supercell are related to the parameters of the ideal rutile structure observed at high temperatures a_r and c_r, with $a = 2\sqrt{2}a_r = 13.70$Å and $c = 2c_r = 5.987$Å. The LT structure can be described by chains of edge-sharing NbO_6 octahedra, cross-linked by edges and corner-sharing as in the ideal rutile structure. The Nb-Nb distances along the c direction, i.e. the edge-sharing chains, are alternately 2.80 and 3.20Å corresponding to pairing of metal atoms. This is illustrated in Fig. 3.7(b). This metal atoms pairing is very likely to be the result of a Peierls instability [131, 132]. The Nb-O bond lengths in the distorted NbO_6 octahedra are comprised between 1.91 and 2.25Å.

NbO_2 is usually observed as the second oxidation step of niobium following the initial formation of NbO, and preceding the formation of the stable Nb_2O_5. Some works using angle-resolved X-ray photoemission spectroscopy [21, 89] have suggested that NbO_2 exists at room temperature predominantly under the Nb_2O_5 layer, rather than as point defects in the Nb_2O_5 matrix. The core-level binding energies of NbO_2 reported in literature are

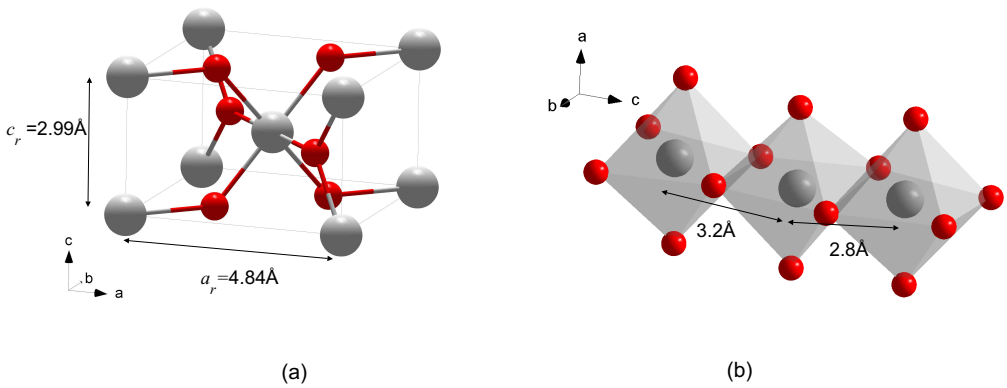

Figure 3.7: (a) High-temperature undistorted rutile structure of NbO_2. (b) NbO_6 octahedra chains in the low-temperature distorted rutile structure NbO_2 (see text for details).

summarized in Tab. 4.2.

3.3.5 Nb_2O_5

The most thermodynamically stable oxide of niobium in atmospheric conditions is the pentoxide, Nb_2O_5 [87, 89]. This insulating oxide forms on the metal heated in air or in the hydrated form as the result of hydrolisis of niobium salts. Nb_2O_5 exists in several polymorphic forms which have been subject to controversy for many years [133]. Amorphous at first, it becomes crystalline at higher temperature, and three main modifications appear successively called after Brauer [134] the L, M and H Nb_2O_5 forms, or the Nb_2O_5 - γ, β, α forms. The different niobium pentoxides Nb_2O_{5-y} are built on a volumic arrangement of NbO_6 coordinated octahedra where the niobium positions are about 3.9Å apart, which allows changes in stoichiometry to be accommodated while retaining a high degree of local order [89, 135, 136]. The crystalline monoclinic γ phase (a=7.31Å, b=15.72Å, c=10.75Å and β=120.42°) appears just after heating at about 500°C. After 1000°C the second modification to the β form, is produced. Heating above 1100°C gives rise to the α form which is irreversible. The α form is also monoclinic with a=21.34Å, b=3.816Å, c=19.47Åand β=120.20°. The melting point of Nb_2O_5 is reported to be 1460 ± 5°C [34]. The density of the Nb_2O_5 at room temperature is 4.36 g/cm^3 for the amorphous Nb_2O_5, 5.17 g/cm^3 for Nb_2O_5- γ and 4.55 g/cm^3 for Nb_2O_5-α [133, 137].

Nb_2O_5 is a typical strong metal-support interaction oxide and well-known to exhibit a pronounced effect as a support for metal and metal oxide catalysts [138]. The oxygen solubility in Nb_2O_5 and the corresponding change in resistivity has been investigated for oxygen sensors applications [139, 140].

The main properties of niobium and niobium oxides are summarized in Tab. 3.2 and 3.3. Their thermal stability will be discussed in section 3.3.7.

3.3.6 Suboxides

The existence of several niobium suboxides such as Nb_2O or Nb_2O_3 reported in different works has been subject to controversy owing to different sample preparation or poor experimental resolution. Norman [71, 141] has confirmed the existence of two suboxide forms of niobium, NbO_X and NbO_Z. The NbO_X phase observed after heating of a laminated niobium sheet in air at about 300-400°C is tetragonal with the lattice parameters $a = 3.38$ Å and $c = 3.27$ Å. The structure has been attributed by Brauer [142] and Norman to the Nb_2O composition, while other studies assigned it to Nb_6O or Nb_5O after a weight measurement of the oxygen quantity in the specimen. The occurrence of the NbO_X phase

has been reported in niobium powder after heating in air during 5-6h at 350°C, and under vacuum at around 400-500°C [133]. The partial transformation of the sample in NbO_X occurs after the existence of a solid solution of oxygen in niobium. Further annealing of the sample in air leads to the successive formation of the different forms of Nb_2O_5. Under vacuum conditions, further annealing leads to the NbO_Z phase first, which is also tetragonal with $a = 6.64$ Å and $c = 4.8$ Å. Further annealing then leads at about 550-600°C to NbO. The tetragonal Nb_2O structure proposed on the basis of X-ray analysis by Brauer [142] is represented in Fig. 3.8. The oxygen atoms are organized on the x-y interstitial sites of the niobium lattice with an occupancy of 25%. This structure, which corresponds to an alternance of oxygen and niobium planes in the [110] direction, was suggested by analogy to the V_4O structure observed in vanadium. The existence of Nb_2O has been reported in various X-ray photoemission spectroscopy studies [19–21, 90, 109], where a chemical shift of the binding energy of about 1±0.2eV was attributed to the Nb_2O state by extrapolation of the relationship between the valence of niobium oxide states and the corresponding chemical shifts (see Fig. 6.3).

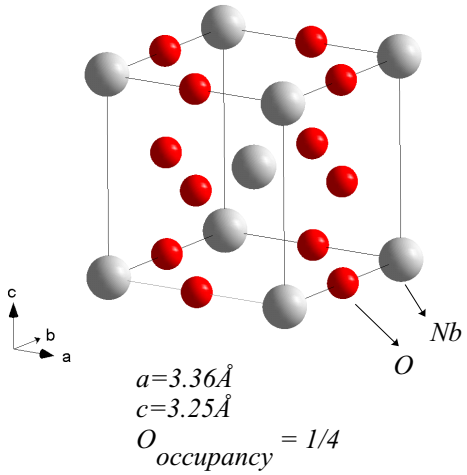

Figure 3.8: The tetragonal Nb_2O lattice [142]. The oxygen atoms are organized on the $x - y$ interstitial sites of the niobium lattice with an occupancy of 25%.

Properties	Nb	NbO	NbO_2	Nb_2O_5
Electronic structure	Z=41 [Kr]$4d^4$ $5s^1$	-	-	-
Crystal structure	bcc	NaCl (25% vacancies)	rutile	polymorph
Structural parameter (Å)	3.3001	4.21	a= 13.7, c=5.98 (LT)	
			a= 4.841, c=2.992 (HT)	
	metallic	metallic	semiconductor (LT)	dielectric
			metallic (HT)	
Density (g/cm^3)	8.57	7.26	5.9	4.36 -5.17
Atomic density (at./cm^3):				
Nb	5.5×10^{22}	4×10^{22}	2.83×10^{22}	2×10^{22}
O	-	4×10^{22}	5.67×10^{22}	5×10^{22}
Melting temperature T_m(°C)	2468	1945	1915	1770

Table 3.2: Properties of niobium and its oxides. For more details refer to the respective sections.

Properties	Nb
Critical temperature T_c	9.2 [K]
Bulk energy gap	1.86 [meV]
Penetration depth	360 [Å]
Coherence length	640 [Å]
H_{c1} (0K)	170 [mT]
H_c (0K)	200 [mT]
H_{c2} (0K)	240 [mT]
H_{sh} (0K)	240 [mT]
Mean free path	500 [Å]

Table 3.3: Superconducting properties of niobium [25].

3.3.7 Thermal stability of niobium oxides

In his early review Terao [133] showed how heating under reduced oxygen pressure can considerably change the oxides observed, as well as the transformation paths during the oxidation of niobium. The thermal stability of niobium oxide layers on niobium have been investigated by several X-ray photoemission spectroscopy works [18, 19, 21, 106]. During ultra-high vacuum annealing Nb_2O_5 films on niobium were shown to reduce to NbO with dissolution of oxygen into the bulk metal at temperatures above 300°C [18]. The following reaction scheme for the reduction process was established:

$$Nb_2O_5 \xrightarrow{k_1} NbO_2 \xrightarrow[k]{k_2} NbO \tag{3.2}$$

where k is the rate constant for the overall reduction process following an Arrhenius equation generally expressed as $k_i(T) = A_i\, e^{-E_{ai}/RT}$ with the frequency factor A_i and the activation energy E_a. One has $-\frac{d[A]}{dt} = k\,[A]$ and therefore the concentration of the species A is given by $[A] = [A]_0 e^{k.t}$.

The dissolution process was shown to be independent of the initial oxide thickness and controlled by reaction at the metal-oxide interface (i.e. not by the migration of the transport species within the overlayer). Since each step of the serie conversion (3.2) involves oxygen removal, the rate of the oxygen release is the sum of all processes and is limited by the kinetics of the slowest step. The rate constant involved in (3.2) was determined:

$$k = 8.9 \times 10^{10}\ \exp(-174/RT) s^{-1} \tag{3.3}$$

$$k_1 = 8.0 \times 10^{7}\ \exp(-134/RT) s^{-1} \tag{3.4}$$

$$k_2 = 1.0 \times 10^{11}\ \exp(-176/RT) s^{-1} \quad \text{rate-limiting step} \tag{3.5}$$

All reduction steps were shown to be first-order irreversible with the NbO_2 to NbO transition being the slowest and, hence, the rate-limiting step.

The effect of thermal annealing on the natural oxide has been studied in the framework of superconducting r.f. cavity applications on polycrystalline niobium [19], and Nb(100) single crystal [21] surfaces. For the polycrystalline sample (250°C, UHV), the reduction of the native oxide layer (43h in air) from Nb_2O_5 to a stable metallic Nb_2O-dominated layer was observed. On the polycrystalline and Nb(100) sample surface the average oxide layer thickness remains unchanged up to about 250°C. The re-oxidation at room temperature of their annealed surfaces regenerate the Nb_2O_5 layer by inward oxygen diffusion. The released oxygen is assumed to diffuse into the metal where it will react with the metal.

The equilibrium state in a system is attained when the Gibbs free energy G is minimum. The change in the free energy ΔG of a system associated to a reaction must therefore

become equal to zero

$$\Delta G = \Delta H - T\Delta S = 0$$

where ΔH is the energy quantity exchanged, the reaction enthalpy, and ΔS is the entropy change. The heat of formation and of dissociation of niobium oxides are summarized in Tab. 3.4 and 3.5.

Oxide	$\Delta H^0_{298}(kJ/mol)$
NbO	-418,261
NbO_2	-792,147
Nb_2O_5	-1905,831

Table 3.4: Heat of formation for the different niobium oxides [87].

Reaction		Heat of decomposition $(10^{-3}J)$
2NbO	$\longrightarrow$ 2 Nb + (O_2)	$\Delta H_{298} = +816.426$
$2NbO_2$	$\longrightarrow$ 2 NbO + (O_2)	$\Delta H_{298} = +782.932$
$2Nb_2O_5$	$\longrightarrow$ 4 NbO_2 + (O_2)	$\Delta H_{298} = +614.622$

Table 3.5: Heat of decomposition for the different niobium oxides. The heat of decomposition refers to the formation of one mole of oxygen and a solid phase in the next lowest oxidation state [87].

3.4 Epitaxial relationships at the metal-oxide interface

The structural properties of epitaxial niobium films have attracted much interest because of their wide use as buffer layers for the growth of single crystalline rare-earth films and multilayers. Niobium can be grown on sapphire substrates in different orientations due to a strong correspondence between the orientation of the substrate and the film ([143], and references therein.). Several recent studies have reported segregated oxygen-induced structures on niobium surfaces presenting high epitaxial order [16, 66, 69, 70]. The effect of epitaxy on superconducting properties of evaporated niobium films has been studied [144].

For fcc-(111)/bcc-(110) interfaces, three orientations are basically predicted by the rigid-lattice theory and observed for many metal on metal system, the Nishiyama-Wassermann (NW) [145, 146], the Kurdjumov-Sachs (KS) [147], and the R30°C [148] orientations, depending on the ratio of the nearest neighbor distances [148, 149]. Orientations preferred

are those in which the most densely packed rows in the fcc-(111) plane are parallel to one of the densely packed rows in the bcc-(110) plane [150]. Presumably, they are most likely when the distances between the corresponding densely packed rows, d_{bcc} and d_{fcc}, are the same in the two crystals (see Fig. 3.9). In the NW case the rows are oriented either $[10\bar{1}]_{fcc} \parallel [001]_{bcc}$ (NW_x), with $\frac{1}{2}\sqrt{3}b = (\frac{2}{3})^{1/2}a$ and

$$r \equiv \frac{b}{a} = 0.9428 \equiv r_{NW_x}$$

or equivalently, $[1\bar{2}1]_{fcc} \parallel [1\bar{1}0]_{bcc}$ (NW_y) with $r_{NW_y} = 1.1547$. In the KS case, the rows are oriented $[1\bar{1}0]_{fcc} \parallel [1\bar{1}1]_{bcc}$ whereas the $[10\bar{1}]_{fcc}$ rows are rotated by 5.26° with respect to the $[001]_{bcc}$ with $\frac{1}{2}\sqrt{3}b = \frac{2}{3}\sqrt{2}a$ or

$$r = 1.0887 \equiv r_{KS}$$

With increasing r, the orientation changes from NW-x to KS to NW-y. The NW, the KS and the R30° orientations relationships are illustrated in Fig. 3.10.

For a NbO(111) layer on Nb(110) the parameter $r = 1.042$ is smaller than the ideal $r_{KS} = 1.0887$ for which the interaction between the substrate and the overlayer atoms is minimal but is very different from the optimal value of the NW orientation. However, simple rigid-lattice model does not take into account the role of oxygen, in particular the different bonding strengths between niobium and oxygen. The presence of an epitaxial oxide layer on top of Nb(110) has been discussed in some studies. The NW orientation has been previously reported on Nb(110) thin films oxidized in dry oxygen atmosphere (∼ 300°C) [116], and on Nb(110) single crystals annealed at high temperatures [69]. Arfaoui et *al.*, in contrast, observed a side to side arrangement of NbO nanocrystals (111) on Nb(110) with a Kurdjumov-Sachs-type epitaxial relationship [112]. Various studies on different systems have reported the coexistence of the KS to the NW orientation relationships, or transitions between both, depending on film thickness or the growth temperature [151]. For further discussions see also 6.3.

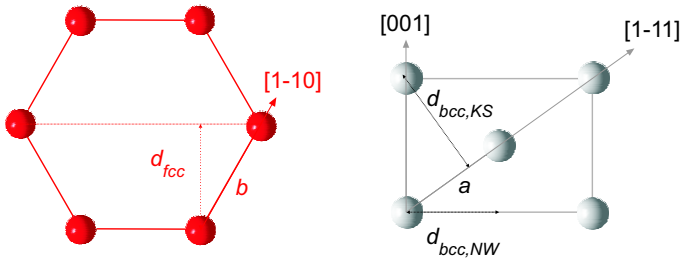

Figure 3.9: Nearest-neighbor distances a and b in the fcc (111) plane (left), and in the bcc (110) plane (rigth). Corresponding densily-packed row distances for the Nishiyama-Wassermann ($d_{bcc,NW}$) orientation and Kurdjumov-Sachs ($d_{bcc,KS}$) orientations.

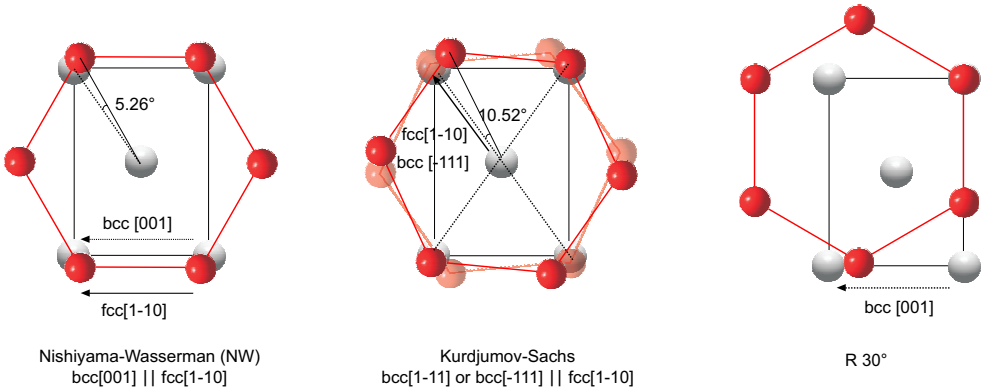

Figure 3.10: Possible in-plane orientation relationships at the fcc(111)/bcc(110) interface.

For the Nb(100) surface, oxygen-induced NbO(100) epitaxial nanocrystals with $[011]_{fcc} \parallel [010]_{bcc}$ have been observed during cleaning of the surface at elevated temperatures by means of LEED, AES and STM [95].

Chapter 4

Surface sensitive x-ray methods

Since their discovery in 1895 by W. C. Röntgen, X-rays have been extensively used for structural investigations not only by physicists but also by chemists and biologists, playing for example a decisive role in the discovery of the structure of the DNA in 1953. Dramatic improvements in the quality of the beam offered by X-ray facilities has been continuously achieved, enlarging progressively new scientific frontiers. The forthcoming fourth generation source X-ray free-electron lasers are going to open a new era in science, combining the high intensity and coherence of a laser with the short wavelength of X-ray light available in a synchrotron, its penetrating power and atomic sensitivity.

X-rays are electromagnetic waves with wavelengths of the order of inter-atomic distances in solid crystals (Å), and energies similar to core-level electrons (keV), which makes them particularly suitable for the investigation of various properties of condensed matter on the atomic length scale. Their wavelength and energy are related through

$$\lambda(\text{Å}) = \frac{12.398}{E\ (\text{keV})} \tag{4.1}$$

X-rays interact with atoms via their electrons[1] in two different ways: they may be scattered, or they may be absorbed [152]. Both processes are exploited in this work. Scattered intensities can be recorded in different regions of the reciprocal space using different scattering geometries, offering thereby complementary structural information about the material.

Four surface sensitive X-ray techniques have been combined in this work: X-ray reflectivity (XRR) probes the electron density profile normal to the surface on an atomic scale ; the depth-distribution of interstitial oxygen is investigated with a nm-resolution by depth-resolved grazing incidence diffuse X-ray scattering (GIDXS) ; the atomic structure at surface and interface is characterized by crystal truncation rods (CTR) measurements ; and finally an overview of chemical states in the near surface region is given by

[1] The scattering process involves the mass to the power of two of the scattering particle in denominator, which for a proton is (1840^2) smaller than for an electron.

high-resolution core-level spectroscopy analysis (HRCLS). X-ray methods are extensively covered in textbooks [152–154] (other references are given in the text). In this chapter, a rapid introduction to the aforementioned techniques, the origin of their surface sensitivity, and the formalism used in this work necessary for the understanding of the experimental results is given.

X-ray methods present various advantages with respect to other conventional surface techniques. The weak scattering cross-section of X-rays as compared with electrons for example, implies a large penetration depth into the material, or the possibility of applying the so-called *kinematical* approximation[2], where multiple diffraction events are neglected. X-rays are well suited for *in-situ* atomic structural studies at elevated gas pressures and temperatures.

Kinematic Bragg, diffuse or CTR scattering is proportional to the number of atomic layers involved and the ratio of the grazing incidence intensity to bulk intensity of the order of 10^{-4}. Due to this severe intensity problem, the observation of scattering intensity in combination with total external reflection has not been feasible until the availability of the highly brilliant synchrotron radiation. All measurements presented in the present work have been performed with synchrotron radiation. Details about the synchrotron beamlines and beamtimes are given in chapter 5.

4.1 Introduction to X-ray Diffraction

In a classical picture, the oscillating electric field of an incident X-ray wave impinging on a material exerts a force on any single electron on its path. The electron then accelerates with the same frequency and radiates the *scattered* wave. The scattered intensity detected in a solid angle $\Delta\Omega$ subtended by the detector for an incoming beam intensity I_0 is given by,

$$I = \frac{I_0}{A_0}\ \Delta\Omega\ \frac{d\sigma}{d\Omega} \tag{4.2}$$

where A_0 is the cross-sectional area of the incident beam, and $(d\sigma/d\Omega)$ the differential cross-section defined as the number of X-rays scattered per second into the solid angle element $d\Omega$ divided by the incident photon flux and $d\Omega$. In the case of a single free electron,

$$\left(\frac{d\sigma}{d\Omega}\right)_e = r_0^2\ P \tag{4.3}$$

where $r_0 = \left(\frac{e^2}{4\pi\epsilon_0 mc^2}\right) = 2.82\ ^{-5}$Å is the Thomson scattering length, also called classical electron radius, which described the scattering ability of the electron. P is the *polarization*

[2]By opposition to the dynamical theory.

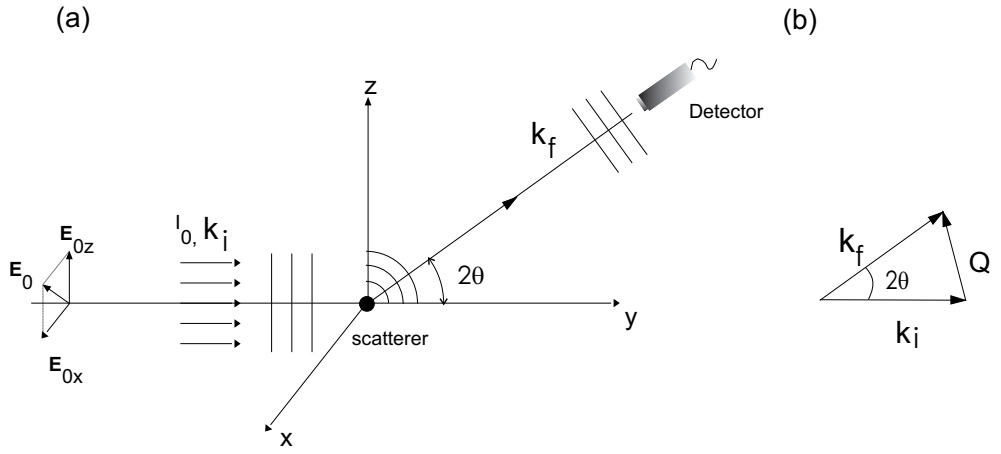

Figure 4.1: (a) Scattering of an incident X-ray beam of wave vector $\mathbf{k}_i$ by an electronic charge in the direction specified by $\mathbf{k}_f$. (b) Definition of the scattering vector $\mathbf{Q} = \mathbf{k}_f - \mathbf{k}_i$.

factor, with for an unpolarized X-ray source $P = \frac{1+\cos^2 2\theta}{2}$, where 2θ is the scattering angle between the wave vectors $\mathbf{k}_i$ of the incident wave and the wave vector $\mathbf{k}_f$ of the scattered wave respectively (see Fig. 4.1). The vector $\mathbf{Q}$ known as *scattering vector*, or *momentum transfer*, is the variable of choice to describe any scattering process and is defined as,

$$\mathbf{Q} = \mathbf{k_f} - \mathbf{k_i} \tag{4.4}$$

with in the case of elastic scattering, $|\mathbf{k}_i| = |\mathbf{k}_f| = |\mathbf{k}|$ and $Q = 2|\mathbf{k}|\, sin\theta = (4\pi/\lambda)\sin\theta$.

The X-ray scattering amplitude of a given distribution of electrons is the superposition of contributions from different elements of the charge distribution, including phase shift due to the different path length which, in other words, is the Fourier transform of the electronic density of the scattering object. The X-ray scattering amplitude of a single atom with an electron density $\rho(r)$ is therefore,

$$f_0(\mathbf{Q}) = \int_{atom} \rho(\mathbf{r}) e^{i\mathbf{Q}.\mathbf{r}}\, d\mathbf{r} \tag{4.5}$$

where $f_0(\mathbf{Q})$ is the so-called *atomic form factor*. If the incoming photons have an energy close to the absorption edges in the atom, the electrons can no longer be considered as free, and resonance effects have to be taken into account by introducing the *dispersion* correction to the atomic form factor such that the corrected scattering factor f is

$$f(\mathbf{Q}, \lambda) = f_0(\mathbf{Q}) + f'(\lambda) + if''(\lambda) \tag{4.6}$$

where $f'(\lambda)$ and $f''(\lambda)$ are the real and imaginary parts of the dispersion correction, and are energy dependent.

A crystalline structure is characterized by the periodic repetition of a structural unit, the *unit cell* on the node of a three-dimensional Bravais *lattice* that can be described by a set of vectors $\mathbf{R}_n$ with the crystal axes $\mathbf{a}_1, \mathbf{a}_2$ and $\mathbf{a}_3$:

$$\mathbf{R}_n = n_1\mathbf{a}_1 + n_2\mathbf{a}_2 + n_3\mathbf{a}_3 \tag{4.7}$$

where n_1, n_2 and n_3 are integer. The scattered amplitude by a crystal is therefore given by a contribution due to the unit cell, called the *unit cell structure factor* and one contribution due to the crystal structure, called the *lattice sum*,

$$F_{\text{Crystal}}(\mathbf{Q}) = \underbrace{\sum_{\mathbf{r}_j} f_j(\mathbf{Q})\ e^{i\mathbf{Q}.\mathbf{r}_j}}_{\text{Unit cell structure factor}} \underbrace{\sum_{\mathbf{R_n}} e^{i\mathbf{Q}.\mathbf{R}_n}}_{\text{Lattice sum}} \tag{4.8}$$

where $\mathbf{r} = \mathbf{R}_n + \mathbf{r}_j$, is the position of one atom in the crystal, $\mathbf{R}_n$ is the position of the origin of the unit cell, and $\mathbf{r}_j$ the position of the j^{th} atom in the unit cell.

The lattice sum, $S(\mathbf{Q}) \simeq 0$, unless all the phase factors $\mathbf{Q}.\mathbf{R_n}$ equal an integer multiple of $2\,\pi$, in which case it becomes of order N, the number of unit cells. A unique solution for that is found by introducing the concept of *reciprocal lattice* so that any lattice sites is given by,

$$\mathbf{G} = h\mathbf{a}_1^* + k\mathbf{a}_2^* + l\mathbf{a}_3^* \tag{4.9}$$

where hkl are integers know as the Miller indexes, and $\mathbf{a}_1^*, \mathbf{a}_2^*, \mathbf{a}_3^*$ the reciprocal vectors, defined such that $a_i a_j^* = 2\pi\delta_{ij}$. The diffraction maxima, so-called *Bragg peaks*, are described through the *Laue condition*

$$\mathbf{Q} = \mathbf{G} \tag{4.10}$$

One can demonstrate that $|S(\mathbf{Q})|^2 \rightarrow N v_c^* \delta(\mathbf{Q} - \mathbf{G})$, where N is the total number of unit cells and v_c^* the volume of the reciprocal unit cell. For a finite size crystal this condition relaxes and the scattering extends over a volume in reciprocal space inversely proportional to the size of the crystal. The scattered intensity, proportional to the square of the structure factor 4.8, is then,

$$I(\mathbf{Q}) = I_0 r_0^2 P\,|F(\mathbf{Q})|^2\,\frac{\sin^2(N_1\mathbf{Q}\mathbf{a_1}/2)}{\sin^2(\mathbf{Q}\mathbf{a_2}/2)}\frac{\sin^2(N_2\mathbf{Q}\mathbf{a_2}/2)}{\sin^2(\mathbf{Q}\mathbf{a_2}/2)}\frac{\sin^2(N_3\mathbf{Q}\mathbf{a_3}/2)}{\sin^2(\mathbf{Q}\mathbf{a_3}/2)} \tag{4.11}$$

The Laue condition (4.10) is equivalent to the well known Bragg's law $n\,\lambda = 2\,d_{hkl}\,\sin\theta$, where d_{hkl} is the interplanar distance of the family of planes hkl. The family of planes hkl is defined such that considering a set of parallel equidistant planes, one of them passes through the origin, and the next nearest intercepts $(a_1/h,\ a_2/k,\ a_3/l)$ on the three crystallographic axes. For the cubic *bcc* lattice of niobium,

$$d_{hkl} = \frac{a}{\sqrt{h^2 + k^2 + l^2}}$$

where a is the unit cell parameter, with in the case of niobium $a = 3.001$ Å.

The unit cell structure factor of the *bcc* lattice of niobium is given by

$$\begin{aligned} F_{hkl}^{Nb} =& f_{Nb}\ (1 + e^{i\pi(h+k+l)} \\ =& f_{Nb} \begin{cases} 2f & h,k,l \ \text{ even} \\ 0 & h,k,l \ \text{ odd} \end{cases} \end{aligned} \tag{4.12}$$

In this section it was tacitly assumed that the interaction between the X-rays and the crystal is weak, and no multiple scattering of the scattered beam, this assumption leads to considerable simplicity and is known as the *kinematical* approximation.

Crystal Truncation Rods

The sharp truncation of a crystal surface breaks the translational symmetry of the crystal lattice in the direction normal to the surface. This relaxes the Laue condition (4.10) and produces streaks in reciprocal space extending perpendicular to the surface and connecting bulk Bragg peaks, known as *Crystal Trunction Rods* (CTRs) [155–157]. The surface of a clean material kept under ultrahigh vacuum conditions is never the exact truncation of the bulk atomic configuration. The atoms at the surface present a different scheme of bounds which gives rise to various effects as relaxation, i.e. displacements perpendicular to the surface normal modifying the spacing in between crystalline planes, or reconstruction, i.e. displacements parallel to the surface giving rise to a new symmetry for the unit cell. The intensity distribution between the Bragg peaks along the CTRs is very sensitive to the structure of the crystal termination. CTR measurements have proved over the last decade to be a powerful tool for investigating surfaces or interfaces structure.

Scattering events in the case of a three-dimensional infinite crystal are restricted by the Laue condition introduced in (4.10), which leads to delta functions. For a truncated crystal, the intensity distribution along the CTR, i.e. in the direction of the surface normal $\mathbf{a}_3$, relaxes, while the sum over the two other directions produces the usual product of delta functions. From (4.8), one can write

$$I(\mathbf{Q}) = I_0 r_0^2 P \left|F(\mathbf{Q})\right|^2 N_1^2 N_2^2 \delta(\mathbf{Q}_{||} - \mathbf{G}) \frac{\sin^2(N_3 \mathbf{Q}.\mathbf{a_3}/2)}{\sin^2(\mathbf{Q}.\mathbf{a_3}/2)} \tag{4.13}$$

$$\propto \frac{1}{2\sin^2(\mathbf{Q}.\mathbf{a_3}/2)} \quad \text{as } N_3 \to \infty \quad \text{for } \mathbf{Q}.\mathbf{a_3} \neq 2\pi l \tag{4.14}$$

where $\mathbf{Q}_{||}$ is the component of the scattering vector in the plane of the surface. Fig. 4.2 illustrates the influence of the crystal termination on the intensity profile of the CTRs as a function of the reciprocal lattice coordinate l. This includes reduced occupancy, or strain

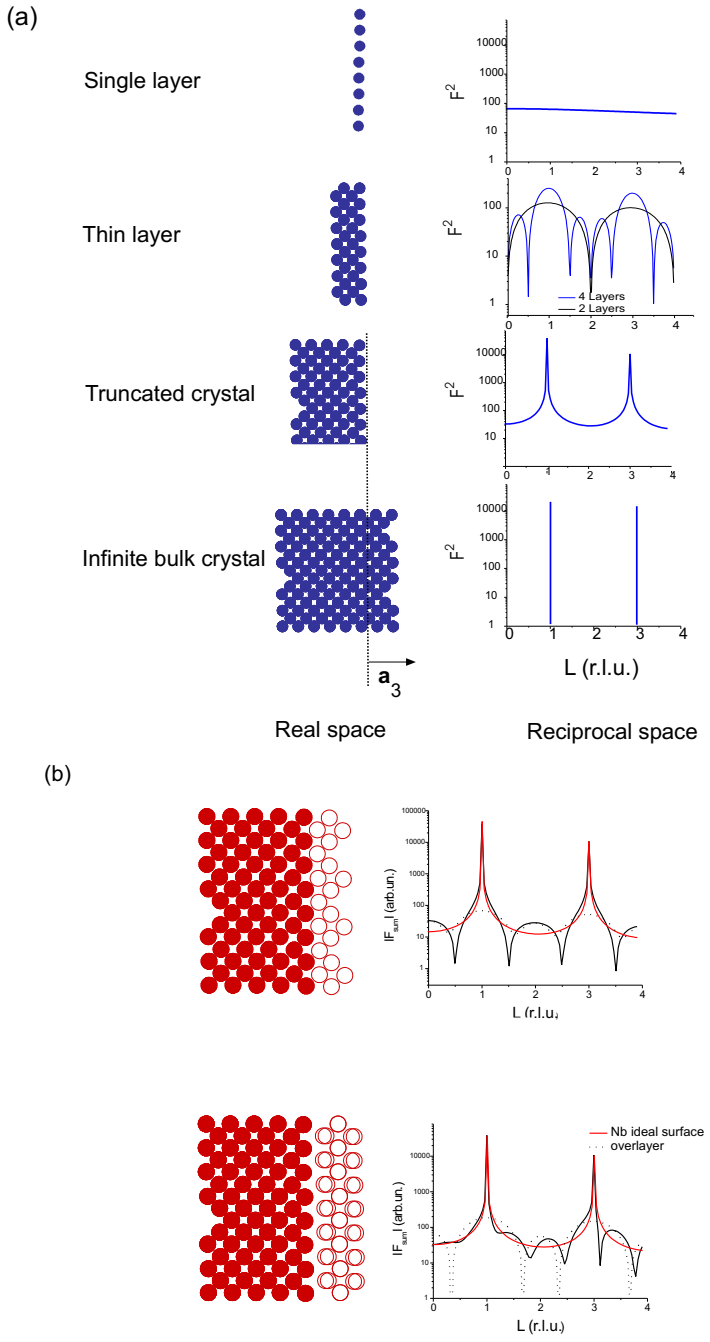

Figure 4.2: (a) Scattering events are restricted by the Laue condition (4.10). In the case of a three-dimensional infinite crystal delta peaks are observed at the Bragg positions. For a truncated surface, the condition relaxes and streaks are observed in reciprocal space extending perpendicular to the surface normal between the Bragg peaks. (b) Different surface termination and their influence on the intensity profile normal to the surface: crystal truncation rod from an ideal surface surface (red line) and with an overlayer (solid line), the surface contribution is indicated (dotted line).

effects at interfaces that can extend over several atomic layers and lead to asymmetric intensity distributions in between the Bragg reflections. Numerous other examples are found in literature [156–160]. The ratio in intensity between the Bragg peaks and the minimum of the CTR is typically 10^5, such that in order to perform CTR measurements with a reasonable statistics the use of highly brilliant synchrotron radiation is required.

4.2 Diffuse X-ray scattering

In a general way, disorder or displacements of atoms regarding their ideal rigid positions in the crystal give rise to diffuse scattering, in addition to the Bragg scattering described in the previous section. The presence of point defects in the crystal such as substitutional atoms, interstitial atoms, vacancies etc... induces *static* distortions u_m of the crystal lattice, while thermal motion as most important *dynamic* effect gives rise to Thermal Diffuse Scattering (TDS).

The fundamental theory of diffuse scattering from defects in crystals has been treated by several authors [161–163]. Only parts of the theory relevant for the understanding of our experimental measurements are outlined in the following.

4.2.1 Interstitial oxygen induced diffuse scattering

If defects are particles of a new phase whose lattice differs from the host lattice, peaks appear in the vicinities of the points $\mathbf{G}^*$ of the reciprocal lattice of the new phase, as observed for interstitial oxygen defects dissolved into the niobium lattice. It has been demonstrated that *single* interstitial oxygen impurities in niobium bulk are nuclei for the local condensation of the trigonal ω-phase embedded in the *bcc* Nb lattice [22]. The properties of the ω-phase have been introduced in section 3.2. The strong oxygen-induced lattice distortions couple to the anisotropic softness of the *bcc* lattice in the [111] direction, thereby producing pronounced maxima of the diffuse X-ray scattering at $\mathbf{Q}^* = \frac{2}{3}(1,1,1))$. Fig. 4.3 illustrates the calculated diffuse scattering pattern of a dilute solution of interstitial oxygen in niobium bulk in the Nb$(1\bar{1}0)$ plane. The theoretical calculation of the oxygen-induced X-ray diffuse scattering as well as of the thermal diffuse scattering used in this work, have been performed as described hereafter by R. P. Kurta in the framework of his PhD thesis [164].

The defect distribution in the crystal is described by the binary occupation parameter $c_{\mathbf{R}}$, which equals 1 or 0 depending on the presence of a defect at the position $\mathbf{R}$. When macroscopic parameters such as the scattering intensities have to be determined, the numbers $c_{\mathbf{R}}$ must be regarded as random quantities and averaged for the given defect concentration $c = \langle c_{\mathbf{R}} \rangle$, and the given correlation function $\langle c_{\mathbf{R}} c_{\mathbf{R}'} \rangle$, $\langle c_{\mathbf{R}} c_{\mathbf{R}'} c_{\mathbf{R}''} \rangle$, ... for

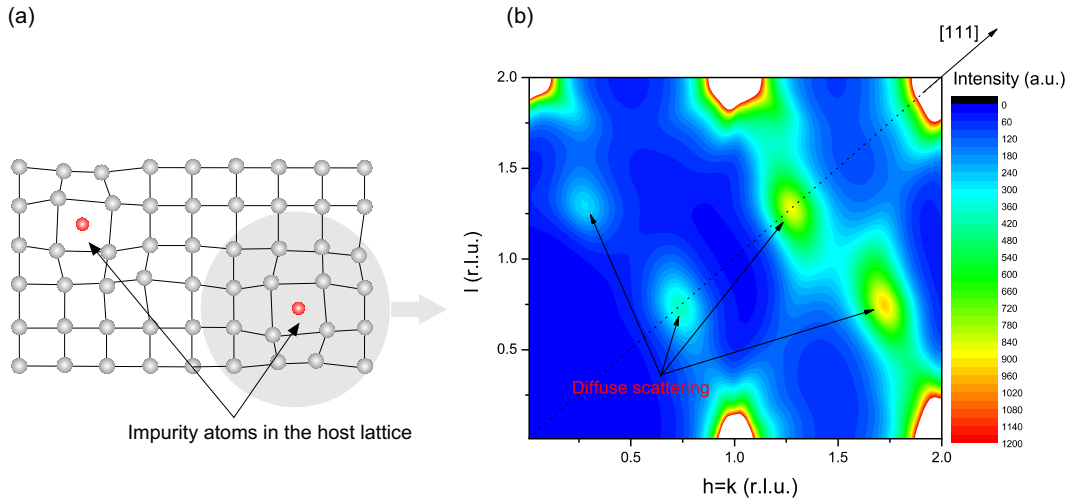

Figure 4.3: Defects which are particles of a new phase whose lattice differs from the host lattice, give rise to scattering peaks in the vicinities of the reciprocal lattice points of the new phase. (a) Sketch of static distortions induced by impurities in a host lattice. (b) Scattering pattern for a dilute solution of interstitial oxygen in the Nb($1\bar{1}0$) plane showing aside the niobium Bragg peaks, diffuse scattering at $\mathbf{Q}^*=\frac{2}{3}(1,1,1)$ and equivalent positions [164]. *Single* interstitial oxygen impurities in niobium bulk are nuclei for the local condensation of the trigonal ω-phase embedded in the *bcc* Nb lattice [22]. The strong oxygen-induced lattice distortions couple to the anisotropic softness of the *bcc* lattice in the [111] direction, thereby producing pronounced maxima of the diffuse X-ray scattering at $\mathbf{Q}^*$ (see text for details).

small defects concentration, defects correlation can reasonably be neglected [162]. Assuming dilute and randomly distributed defects, the scattered intensity is proportional to the defect concentration c through the following expression [162, 165]:

$$I(\mathbf{Q}) \propto c(1-c)S_D(\mathbf{Q}) \tag{4.15}$$

where $S_D(\mathbf{Q})$ is the scattering factor associated to one single defect and is discussed hereafter. Regardless of the presence of the ω phase, the diffuse scattering can be ascribed to the lattice static distortions $\mathbf{u}_m$, such that the positions of atoms have to be described by $\mathbf{r}_m = \mathbf{R}_m + \mathbf{u}_m$, where $\mathbf{R}_m$ is their ideal position. The scattering factor can be derived from the general equation Eq. (4.8) [161–163] as,

$$S(\mathbf{Q}) = \left\langle \left| \sum_m f\ e^{i\mathbf{Q}.(\mathbf{R}_m+\mathbf{u}^p_{\mathbf{R}_m})} + f_D\ e^{i\mathbf{Q}.\mathbf{R}_p} \right|^2 \right\rangle_p \tag{4.16}$$

where $\mathbf{u}^p_{\mathbf{R}_m}$ is the static displacement of the host lattice atom at the site $\mathbf{R}_m$ (with a scattering factor f) due to the action of a defect located at $\mathbf{R}_p$ (with a scattering factor f_D). The summation has to be performed over the entire long-ranged displacement field around the defect. $\langle\rangle_p$ represents the average over all possible defect sites $\mathbf{R}_p$. The second part of

(4.16) can be in first approximation neglected due to the weak value of f_D for the interstitial oxygen impurity. If one assumes a random defect distribution, the diffuse intensity is ruled by the lattice deformation $\mathbf{u}^p_{\mathbf{R}_m}$ around on individual defect at $\mathbf{R}_p$. Excluding the Bragg reflections from (4.16) one has,

$$S_{\mathrm{D}}(\mathbf{Q}) = \left\langle \left| \sum_m f_{\mathrm{Nb}}\; e^{i\mathbf{Q}.\mathbf{R}_m} (e^{i\mathbf{Q}.\mathbf{u}^p_{\mathbf{R}_m}} - 1) \right|^2 \right\rangle_p \tag{4.17}$$

which can be rewritten as,

$$S_{\mathrm{D}}(\mathbf{Q}) = \left\langle \left| \sum_m f_{\mathrm{Nb}}\; e^{i\mathbf{Q}.\mathbf{R}_m} (e^{i\mathbf{Q}.\mathbf{u}^p_{\mathbf{R}_m}} - 1 - i\mathbf{Q}.\mathbf{u}^p_{\mathbf{R}_m}) + f_{\mathrm{Nb}}\, i\, \mathbf{Q}.\mathbf{u}_{\mathbf{Q}} \right|^2 \right\rangle_p \tag{4.18}$$

with

$$\mathbf{u}_{\mathbf{Q}} = \sum_m \mathbf{u}_{\mathbf{R}_m}\, e^{i\mathbf{Q}.\mathbf{R}_m} \quad \text{and} \quad \mathbf{u}_{\mathbf{R}_m} = \frac{1}{N} \sum_{\mathbf{Q}} \mathbf{u}_{\mathbf{Q}}\, e^{-i\mathbf{Q}.\mathbf{R}_m} \tag{4.19}$$

The first part of the Eq. (4.18) can be approximated by a finite summation over the local environment, easily calculated in real space since,

$$\sum_{\text{Local}}^{\text{Long range}} C(e^{i\mathbf{Q}.\mathbf{u}^p_{\mathbf{R}_m}} - 1 - i\mathbf{Q}.\mathbf{u}^p_{\mathbf{R}_m}) \to 0$$

since the lattice is strongly distorted only in the immediate neighborhood of the defect and for the long-range part $\mathbf{u}^p_{\mathbf{R}_m} \ll 1$ and $e^{i\mathbf{Q}.\mathbf{u}^p_{\mathbf{R}_m}} = 1 + i\mathbf{Q}.\mathbf{u}^p_{\mathbf{R}_m} + \Theta(...)$. The second part of (4.18) is evaluated in reciprocal space, where the extended contributions of $\mathbf{u}_{\mathbf{R}_m}$ become localized.

The calculation of the diffuse intensity (4.18) requires the knowledge of the static displacements $\mathbf{u}^p_{\mathbf{R}_m}$ in the niobium lattice[3]. Kanzaki [76] introduced a powerful concept which models long-ranged displacements, such as strain interaction, by a set of short-ranged external forces $(\mathbf{f}^m_p)_j$ (applied at the host lattice atoms m around the occupied defect site $\mathbf{R}_p$) defined as the forces necessary to be applied to an ideal crystal without defect in order to create the same displacements as the defect, and the lattice Green's functions tensor $\hat{G}_{\mathbf{Q}}$ such that,

$$\mathbf{u}_{\mathbf{Q}} = \hat{G}_{\mathbf{Q}}.\mathbf{F}_{\mathbf{Q}} \tag{4.20}$$

The lattice Green's functions tensor,

$$\hat{G}_{\mathbf{Q}} = \hat{D}^{-1}_{\mathbf{Q}} \tag{4.21}$$

[3]Defect-induced static distortions are very strong in the local neighborhood, typically 0.1-0.5 Å, and exhibit a long ranging power-law decay $(1/r^2)$ with the distance r.

is the inverse of the dynamical matrix $\hat{D}_{\mathbf{Q}}$, Fourier transform of the Born-von-Kárman tensor $\hat{\Phi}_{\mathbf{R}_m}$,

$$\hat{D}_{\mathbf{Q}} = \sum_m \hat{\Phi}_{\mathbf{R_m}} \, e^{i\mathbf{Q}.\mathbf{R}_m} \tag{4.22}$$

Quantitative values of $\widehat{G}_{\mathbf{Q}}$ are obtained via a fit of phonon dispersion curves [166] and are found for niobium in [167]. $\mathbf{F_Q}$ is the Fourier transform of the Kanzaki forces,

$$\mathbf{F}^p_{\mathbf{Q}} = \sum_m \mathbf{f}^m_p \, e^{i\mathbf{Q}.\mathbf{R}_m} \tag{4.23}$$

Kanzaki's formalism limits considerably the amount of parameters necessary to describe the displacement field. The Kanzaki forces are material constants, describing the ability of the defect atom to distort the environmental host lattice at a given distance. Their directions is parallel to the vector binding the two atoms and their strength depends on the coordination distance and is therefore constant for a given shell. Oxygen atoms occupy octahedral sites in the *bcc* lattice of niobium [22,58,59]. Possible sets of short-range Kanzaki forces can be found from the measured dipole moment [22]

$$\widehat{P}_p = \sum_m R_m(\mathbf{f}^m_p) \tag{4.24}$$

determined experimentally by Huang diffuse X-ray scattering [168] :

$$P_{ij} = \begin{pmatrix} 12.4 & 0 & 0 \\ 0 & 5.1 & 0 \\ 0 & 0 & 5.1 \end{pmatrix} \text{eV} \tag{4.25}$$

In a detailed experimental and theoretical study of the diffuse neutron scattering of dilute solution of oxygen in niobium bulk, the very local lattice distortions around interstitial oxygen were determined [22]. Within the Kanzaki force approach, these ω-like local distortions were found to require elastic forces up to the third neighbor shell. The corresponding Kanzaki forces f_i $(i = 1, 2, 3)$ are summarized in Tab. 3.1.

Note that the ω-phase domains formed around the oxygen impurities are coherently embedded in the *bcc* matrix through a long-ranging static displacement field which itself gives rise to *Huang scattering* around Bragg reflections [162, 169]. The *bcc*/ω interface as well as the Huang diffuse scattering are naturally included in the model discussed above.

Since the intensity of diffuse scattering is several orders of magnitudes smaller than the one of Bragg scattering, an intense synchrotron source is necessary to perform this type of experiments.

4.2.2 Thermal diffuse scattering

At finite temperatures, the thermal vibrations of the atoms around their average position in the crystal induce *dynamic* displacements in the lattice. This has two effects on the scattering pattern: the Bragg reflections are weakened through the Debye Waller factor and an additional diffuse intensity, the Thermal Diffuse Scattering (TDS), appears. These effects are increasing with increasing temperature.

If one considers the instantaneous displacement $\mathbf{u}_n$ of an atom from its mean position R_n, one has by definition $\langle \mathbf{u}_n \rangle$=0, where $\langle \ldots \rangle$ indicates a temporal average. The scattering intensity in electronic units is then expressed as

$$I_{eu}(\mathbf{Q}) = \sum_{mn} f^2 e^{i\mathbf{Q}(\mathbf{R}_m - \mathbf{R}_n)} \left\langle e^{i\mathbf{Q}(\mathbf{u}_{\mathbf{R}_m} - \mathbf{u}_{\mathbf{R}_n})} \right\rangle \tag{4.26}$$

where f is the average atomic form factor. This expression can be simplified according to the Baker-Hausdorff theorem to,

$$I_{eu}(\mathbf{Q}) = \sum_{mn} f^2 e^{i\mathbf{Q}(\mathbf{R}_m - \mathbf{R}_n)} e^{-\frac{1}{2}\left\langle [\mathbf{Q}(\mathbf{u}_{\mathbf{R}_m} - \mathbf{u}_{\mathbf{R}_n})]^2 \right\rangle} \tag{4.27}$$

which can be decomposed in two terms as,

$$I_{eu}(\mathbf{Q}) = \sum_{mn} f^2 e^{-\frac{1}{2}\mathbf{Q}^2 \left\langle u^2_{\mathbf{Q}_m} \right\rangle} e^{i\mathbf{Q}(\mathbf{R}_m - \mathbf{R}_n)} + \sum_{mn} f^2 e^{i\mathbf{Q}(\mathbf{R}_m - \mathbf{R}_n)} \left\{ e^{\mathbf{Q}^2 \langle \mathbf{u}_{\mathbf{R}_m} \mathbf{u}_{\mathbf{R}_n} \rangle} - 1 \right\} \tag{4.28}$$

The first term of this expression can be recognized as the elastic scattering from the lattice where the atomic form factor is replaced by

$$f_{atom} = f(\mathbf{Q})\ e^{-\frac{1}{2}\mathbf{Q}^2 \left\langle u^2_{\mathbf{Q}_m} \right\rangle} \equiv f(\mathbf{Q})\ e^{-2M} \tag{4.29}$$

the exponential term e^{-2M} is known as the Debye-Waller factor. This shows that the elastic Bragg scattering is reduced in intensity by the atomic vibrations without any change in the width of the peaks. The contribution from the second term in (4.28) has a distinct character. The corresponding intensity increases as the mean-squared displacements increases, and has a width determined by the correlations between the displacements of different atoms. The latter are significant only over short distances so that the lattice sum extends over a few lattice sites and the scattering presents a considerable width, much greater than the width of the Bragg peaks. Except from these two factors, (4.28) is equivalent to (4.8). The derivation of the thermal effects discussed so far can be found in more details in [152,154] and other textbooks. The Debye-Waller factor in (4.29) can be written

$$2M = \mathbf{Q}^2 \left\langle u^2_{\mathbf{Q}} \right\rangle = \left(\frac{4\pi}{\lambda} \right)^2 \sin^2\theta \left\langle u^2_{\mathbf{Q}} \right\rangle = B_T \left(\frac{\sin\theta}{\lambda} \right)^2 \tag{4.30}$$

with $B_T = 8\pi^2 \left\langle u_Q^2 \right\rangle$. The Debye Waller factor and the TDS intensity can be expressed in terms of the Fourier components of the lattice Greens functions at $\mathbf{Q}\, \hat{G}_{\mathbf{q}}$

$$I_{eu}^{TDS}(\mathbf{Q}) = NK_BTe^{-2M} f^2 \mathbf{Q}\, \hat{G}_{\mathbf{q}}\, \mathbf{Q} \tag{4.31}$$

with the Debye-Waller factor

$$2M = k_BT \sum_{\mathbf{q}} \mathbf{Q}\, \hat{G}_{\mathbf{q}}\, \mathbf{Q} \tag{4.32}$$

For the inelastic TDS process, the change in photon energy due to phonons, of the order of k_BT (25meV), is much lower than the X-ray photons energy typically of the order of keV. As it will be shown in section 7, the TDS contribution to the signal is of the order of magnitude of the diffuse X-ray scattering due to oxygen impurities of interest in the present work.

4.3 X-ray refraction and reflection from interfaces

When an X-ray beam impinges on a mirrorlike surface, part of the incoming beam is reflected and part of it is transmitted through the material, as commonly observed for visible light, carrying information about the surface studied. The refractive index n that characterizes the X-ray optical path in a medium is given by

$$n = 1 - \delta + i\beta \tag{4.33}$$

with the dispersion δ, and absorption β terms,

$$\delta = \frac{\lambda^2}{2\pi} r_0 \sum_j \rho_j \ (f_0(0) + f'(\lambda))_j \tag{4.34}$$

$$\beta = \frac{\lambda^2}{2\pi} \ r_0 \sum_j \rho_j \ f''_j(\lambda) = \frac{\lambda}{4\pi}\mu \tag{4.35}$$

where r_0 is the classical electron radius, λ the X-ray wavelength, ρ_j the atomic density of the component j, and μ the linear photoabsorption coefficient of the material. The corrected atomic form factor $f(\mathbf{Q}, \lambda) = f_0(\mathbf{Q}) + f'(\lambda) + f''(\lambda)$ is given by (4.6), with $f_0(0) \approx Z_j$ (Z_j is the atomic number). The deviation of n from unity, δ, is related to the scattering properties of the medium. Each electron scatters the X-ray beam with the Thomson amplitude r_0 and, far from the absorption edges, δ is then proportional to the product of r_0 and the electron density ρ_e,

$$\delta = \frac{\lambda^2}{2\pi} \ r_0 \rho_e \tag{4.36}$$

Typical values for δ and β are of the order 10^{-5} such that n is slightly less than 1 (typical value of δ and β for niobium and its oxides are given in table 7.1). Total external reflection from a crystal surface occurs when the X-ray beam hits the surface under an angle α_i inferior to the critical angle α_c, defined through the Snell's law $\cos\alpha_c = n$, which for small α leads to

$$\alpha_c = \sqrt{2\delta} \tag{4.37}$$

α_c is typically of the order of some milli-radian ($\alpha_c^{Nb}(10 \text{ keV})$=0.32°).

Let's consider an incoming X-ray wave $\mathbf{E}_i(r) = \mathbf{E}_i e^{i\mathbf{k}_i.\mathbf{r}}$ with a wave vector $\mathbf{k}_i$ impinging on the surface at an angle α_i, the reflected beam goes out in the specular geometry with an exit angle equal to α_i and a wave vector $\mathbf{k}_r$, while the refracted wave is transmitted with $\mathbf{k}'_i = n\mathbf{k}_i$, as illustrated in Fig. 4.4. The prime denotes quantities inside the material. The amplitude of the refracted and reflected waves are described by the Fresnel coefficients of transmission T, and of reflection R, derived from the Helmholtz equation under the

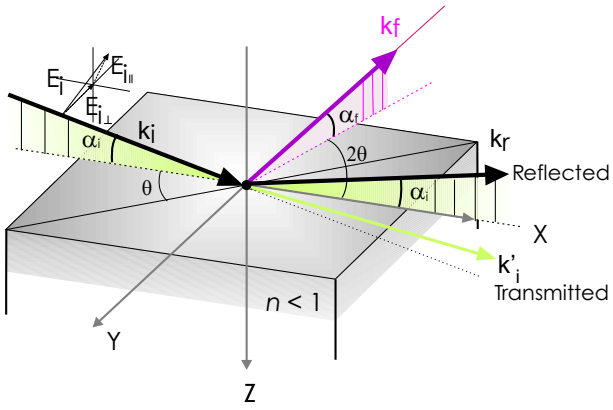

Figure 4.4: An incident X-ray beam of wave vector $\mathbf{k}_i$ impinging on a mirrorlike surface can be reflected with $\mathbf{k}_r$ in a direction symmetric to the incident one in the *specular* geometry, or transmitted through the material with $\mathbf{k'}_i$. If the incident angle is smaller than the critical angle total external reflection occurs and an evanescent wave field traveling parallel to the surface is induced into the surface. Grazing incidence X-ray scattering experiments can be performed using the evanescent wave field as incident wave and the scattered wave exits at an angle α_f and a wave vector $\mathbf{k}_f$.

boundary conditions that the tangential components of the electric and magnetic field vectors are continuous across the interface, which gives,

$$\begin{aligned} R &\equiv \frac{E_r}{E_i} = \frac{k_{i,z} - k'_{i,z}}{k_{i,z} + k'_{i,z}} \\ T &\equiv \frac{E_t}{E_i} = \frac{2k_{i,z}}{k_{i,z} + k'_{i,z}} \end{aligned} \tag{4.38}$$

where $k_{i,z}$ and $k'_{i,z}$ are the vertical component of, respectively, the incident and transmitted wave vectors. $k'_{i,z}$ is a complex quantity given by,

$$k'_{i,z} = \frac{2\pi}{\lambda}(\sin^2\alpha_i - 2\delta + 2i\beta)^{1/2} \tag{4.39}$$

that can be verified easily by applying the Snell's law to $\mathbf{k}_i$.

The transmitted electromagnetic field in the medium takes the form

$$E_t(\mathbf{r}') \propto e^{i\mathrm{Re}(\mathbf{k}'_i).\mathbf{r}'}\, e^{-z/l_i} \quad \text{with} \quad l_i \equiv |\mathrm{Im}(k'_{i,z})|^{-1} \tag{4.40}$$

where l_i is the penetration depth, which describes the depth where the intensity of the wave drops by $1/e$. The reflected and transmitted intensity, given by $|R|^2$ and $|T|^2$ respectively, are plotted as a function of α_i/α_c and for various β/δ in Fig. 4.5. The reflected wave can be used to study the electron density profile normal to the surface and provides information about the thickness and interfacial properties, irrespective of the structural order. X-ray reflectivity is discussed in section 4.3.1.

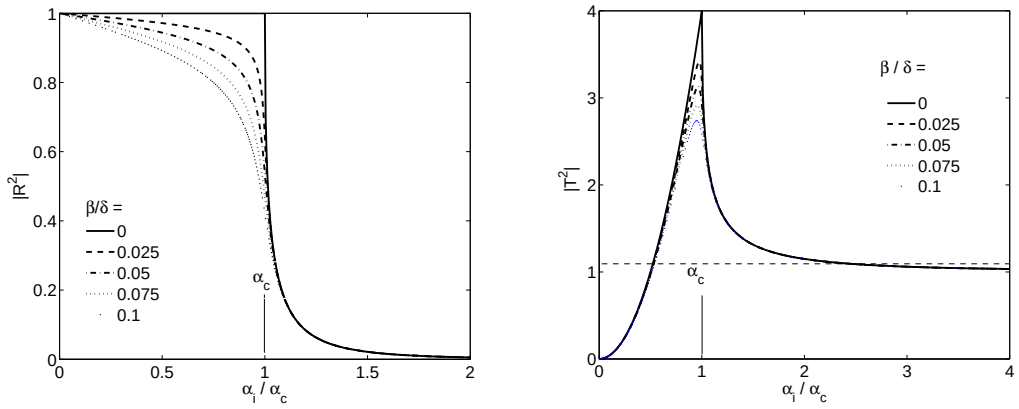

Figure 4.5: Left: X-ray reflectivity $|R|^2$ as a function of α_i/α_c and for various β/δ. Right : Transmission coefficient $|T|^2$ versus α_i/α_c for various β/δ.

In the regime of total external reflection, i.e. for incidence angles less than the critical angle, a so-called *evanescent* X-ray wave field forms inside the less dense medium and propagates parallel to the surface (in real system $\beta \neq 0$ and a small oscillatory component perpendicular to the surface has to be taken into account), and decaying exponentially into the material. The wave amplitude decay does not imply absorption of the wave energy because an examination of the Poynting vector shows that no energy enters into the medium. Evanescent waves are therefore an example of a wave in which exponential decay of the amplitude does not imply that dissipation is taking place. At the critical angle, the phases of the two external waves match at the surface allowing the maximum evanescent field into the material ($|T_c|^2 = 4$). The use of the evanescent wave field as incident wave to probe the *in-plane* structural properties (parallel to the surface), establishes the basis of Grazing-Incidence X-ray Diffraction (GIXD) experiments described in more detail in

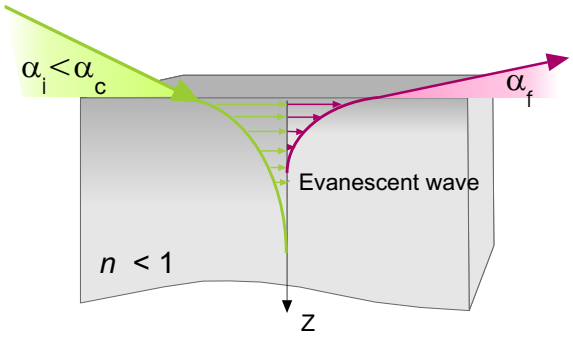

Figure 4.6: Total external reflection from a crystal surface occurs when the X-ray beam hits the surface under an angle α_i inferior to the critical angle α_c. In the regime of total external reflection a specularly reflected intensity occurs, while inside the less dense medium an X-ray *evanescent* wave field is formed that propagates parallel to the surface and decays exponentially into the material (see text for details).

section 4.3.2. A non zero photoelectric absorption affects the transmission function and the reflectivity essentially at the critical angle as illustrated in Fig. 4.5.

4.3.1 X-ray Reflectivity

X-ray Reflectivity (XRR), is a powerful tool to study multilayers or thin films irrespective of their structural order, as the reflected intensity depends only on the optical properties of the layers via their electron density. If the surface of the reflecting material is flat, the reflected intensity is confined in a direction symmetric from the incident one, called the *specular* geometry illustrated in Fig. 4.4, where both incident angle α_i and exit angle α_f are equal[4]. The Fresnel reflectivity $R_F = |R|^2$ introduced in (4.38) is illustrated in Fig. 4.5 (left). R_F is equal to 1 for $\alpha_i < \alpha_c$, and drops as $\sim 1/\alpha^4$ for $\alpha_i >> \alpha_c$.

If the system presents multiple interfaces, in the case of multilayers, or oxide layers on the surface, the scattering from all interfaces has to be taken into account. The properties of reflected intensity for multiple interfaces have been studied in details by Parrat [170] who developed a rigorous recursion formalism[5]. The medium is composed of N layers, sitting on an infinitely thick substrate as illustrated in Fig. 4.7. Each layer j has an refractive

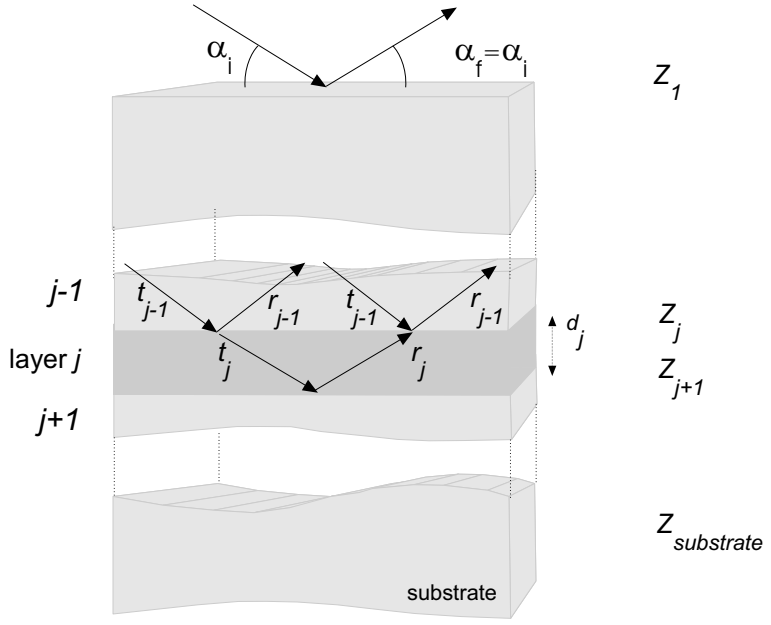

Figure 4.7: Scheme of a layered material. The medium is composed of N layers, sitting on an infinitely thick substrate. Each layer j has an refractive index $n_j = 1 - \delta_j + i\beta_j$ and the thickness d_j, the interfaces are located at z_j. At each interface, a reflected wave r_j and transmitted wave t_j are created and a recursive approach allows to calculate the reflectivity (see text for details).

[4]Non-specular reflectivity is produced by rough surfaces and won't be discussed here

[5]The Parratt formalism takes into account multiple scattering effects and therefore dynamical effect neglected in the kinematical theory of scattering presented in the previous sections.

index $n_j = 1 - \delta_j + i\beta_j$ and the thickness d_j, the interfaces are located at z_j. At each interface, a reflected wave r_j and transmitted wave t_j are created and related through,

$$X_j = \frac{r_j}{t_j} = e^{-2ik_{z,j}z_j} \frac{r_{j,j+1} + X_{j+1}\ e^{2ik_{z,j}z_j}}{1 + r_{j,j+1}\ X_{j+1}\ e^{2ik_{z,j}z_j}} \tag{4.41}$$

where

$$r_{j,j+1} = \frac{k_{z,j} - k_{z,j+1}}{k_{z,j} + k_{z,j+1}} \tag{4.42}$$

is the Fresnel coefficient of the interface between the layer j and $j+1$, and $k_{z,j}$ the $z-$component of the wave vector in layer j. The recursion is solved using $t_1 = 1$ (incident wave normalized to unity) and $r_{N+1} = 0$ (no reflection from the substrate, i.e., from below the substrate surface). The reflected intensity presents interference oscillations known as Kiessig fringes. These oscillations have their origin only in the electron density profile regardless of the crystallinity, and their periodicity in Q_z can be related to the thickness d of the layer via

$$\Delta Q_z \sim \frac{2\pi}{d} \tag{4.43}$$

Arbitrary electron density profiles can be treated with the Parratt formalism by slicing the profile into a given number of thin layers of thickness d with constant δ in each layer and sharp interfaces. Uncorrelated surface roughness may be included by [171],

$$r = r_{ideal}\ e^{-2k_{z,j}k'_{z,j}\sigma^2_{j,j+1}} \tag{4.44}$$

where $\sigma = \sqrt{\langle z \rangle^2}$ represents the root mean square roughness. The usual approach for analyzing reflectivity data is thus to assume a model of the electron density profile (incorporating all knowledge about the system) and fit the free parameters of the model to the

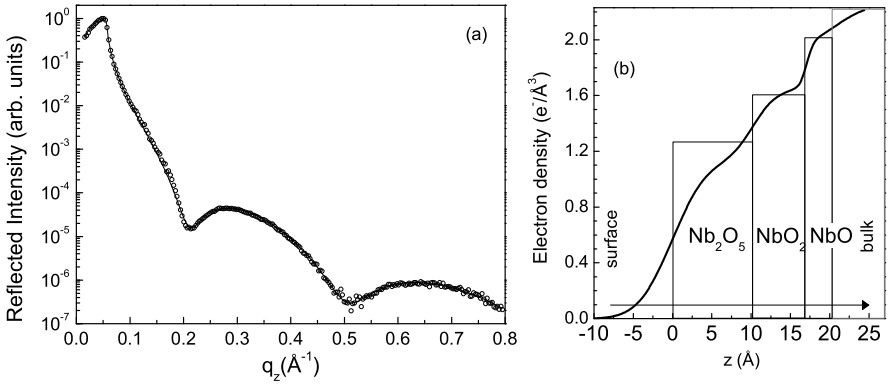

Figure 4.8: (a) X-ray reflectivity data (open circles) and fit (solid lines) from a Nb(110) single crystal oxidized 10h in air at RT. (b) Corresponding electron density profile using a three layer model in the Parrat formalism (see text for details).

measured data. Fig. 4.8 illustrates an example of X-ray reflectivity data measured on a Nb(110) single crystal oxidized 10h in air at RT. The corresponding electron density profile is extracted from the fit using a three layer model in the Parrat formalism. These results are discussed in details in section 6. At small angles geometric effects due to the finite size of the incident beam have to be accounted for, either by correcting the measured data, or by including it in the calculation of the reflected intensities (see section 4.4).

4.3.2 Grazing incidence X-ray scattering : depth-resolution

A description of the grazing incidence X-ray diffraction in the framework of conventional kinematic theory, as applied in section 4.1, can not account for the strong optical effects in this regime [6]. However, a pseudo-kinematic description of the scattering phenomena can be retained if the evanescent wave field inside the material, the "distorted-wave", is taken as incident wave field, instead of the incident wave in vacuum as usually considered. This is the so-called "distorted-wave Born approximation" (DWBA) [22, 172]. In other words, the evanescent wave field that forms at the surface of a material under total external reflection conditions, can be used as an incident wave parallel to the surface in order to probe the structural properties of the material. Depth-resolved diffraction, diffuse scattering, or fluorescence experiments can be achieved as demonstrated hereafter, by varying either the incident either the exit angle.

Within the distorted-wave Born approximation, any kinematic scattering intensity I_{GIXS}

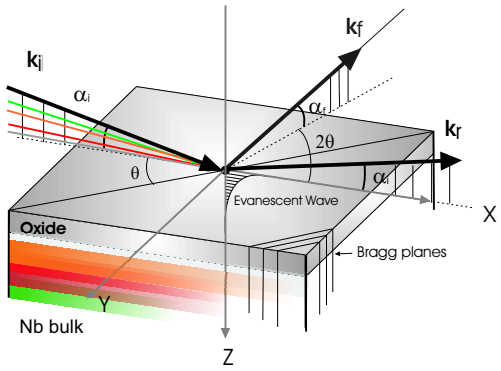

Figure 4.9: Depth-resolved grazing incidence X-ray scattering measurements are performed controlling the information depth, the so-called *scattering depth* Λ, by varying either the incident angle α_i either the exit angle α_f. Λ increases with increasing angle. In the evanescent regime Λ is small, while for angles above α_c, the scattering depth is determined by the absorption coefficient of the material (see text for details).

[6] As multiple scattering is neglected and the X-ray refraction n index is considered to be 1

near the condition of total external reflection can be expressed as [173]

$$I_{\mathrm{GIXS}}(\mathbf{Q}') = I_0\ r_e^2\ |T_i|^2 |T_f|^2\ S(\mathbf{Q}') \tag{4.45}$$

where $S(\mathbf{Q}')$ is the structure factor of the scattering process under consideration, as in our case, oxygen-induced diffuse scattering, thermal diffuse scattering or Bragg scattering. $T_{i,f}$ are the Fresnel transmission coefficients for the incident and exit beam. $\mathbf{Q}' = k'_f - k'_i$ represent the scattering vector into the material and its $z-$component Q'_z is, in contrast to conventional bulk scattering, a complex quantity into the sample

$$Q'_z = k'_{fz} - k'_{iz} \equiv q'_z + i/\Lambda \tag{4.46}$$

where $(k'_{i,f})_z$ are the z-component of the transmitted wave vectors given by Eq. (4.39) and,

$$k'^{(z)}_{i,f} = \pm\frac{2\pi}{\lambda}(\sin^2\alpha_{i,f} - 2\delta + 2i\beta)^{1/2} \tag{4.47}$$

When $\alpha_{i,f}$ are below the critical angle α_c, the imaginary part of Q'_z dominates and leads to a strong exponential damping of the transmitted wave field, leading to the "evanescent wave" regime. The real part of the momentum transfer $q'_z = Re(Q'_z)$ vanishes to a small remaining value only due to photoelectric absorption through β.

The relevant depth describing the grazing incidence intensity is the so-called *scattering depth*[7] Λ, defined as the depth for which the scattered intensity is reduced by $1/e$. Λ is related to Q'_z through

$$\Lambda \equiv Im(Q'_z)^{-1} = \frac{\lambda}{2\pi(l_i + l_f)} \tag{4.48}$$

with

$$l_{i,f} = 2^{-1/2}\{(2\delta - \sin^2\alpha_{i,f}) + [(\sin^2\alpha_{i,f} - 2\delta)^2 + 4\beta^2]^{1/2}\}^{1/2} \tag{4.49}$$

Equations (4.48) and (4.49) explicitly show the symmetric influence of the incident and exit angle on the scattering depth. The scattering depth of a niobium surface is plotted as an example in Fig. 4.10 as a function of α_f for different α_i. The scattering depth increases with increasing angles. In the evanescent regime Λ remains small, while for angles above α_c, Λ is determined by the absorption coefficient of the material. *Depth-resolved* grazing incidence X-ray scattering measurements can therefore be performed controlling the scattering depth by tuning either α_i either α_f, as illustrated in Fig. 4.6 and 4.9. The scattering depth of niobium at a photon energy of 10 keV can for example, be tuned from ~ 2 nm to few μm with a nanometer scale resolution.

Let's present two opposite types of scattering laws that will be encountered under grazing incidence in the following of this work: the kinematic Bragg scattering with a very

[7] To distinguish from the penetration depth (4.40) which only depends on the incident angle α_i.

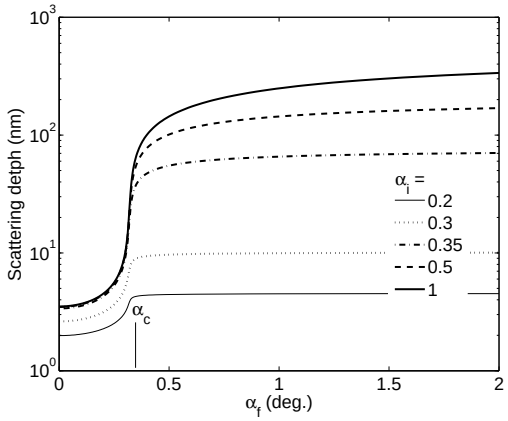

Figure 4.10: Niobium scattering depth Λ as a function of the exit angle α_f for different α_i ($\lambda = 0.1239$ nm).

pronounced Q-dependence, and the incoherent scattering with neglectible Q-dependence. The semi-infinite kinematic sum for Bragg scattering of a truncated surface is simply given by,

$$\begin{aligned} S_{\text{Bragg}}(Q_{\parallel}, Q'_z) &= \sum_{m,n=0}^{\infty} F_m F_n^* \, e^{iQ_{\parallel}\cdot(\mathbf{r}_m - \mathbf{r}_n)} e^{-i(Q'_z z_m - Q'^*_z z_m)} \\ &= |F_{hkl}|^2 \delta(Q_{\parallel} - G_{hkl}) \, \frac{1}{|1 - e^{-2Q'_z a_{\perp}}|^2} \end{aligned} \tag{4.50}$$

where the scattering vector Q' has been divided into the in-plane component $Q_{\parallel}$ and the normal component Q'_z, $a_{\perp}$ is the lattice constant normal to the surface, $|F_{hkl}|$ the unit cell structure factor and G_{hkl} the associated reciprocal lattice vector. In (4.50) it is tacitly assumed that the Bragg condition parallel to the surface is not violated by moving along Q_z. For totally incoherent scattering one has [173],

$$S_{inc}(Q'_z) = \sum_{m=0}^{\infty} \left| f_{\text{inc}} e^{-iQ'_z z_m} \right|^2 = \frac{f_{\text{inc}}^2}{1 - e^{-2a\perp/\Lambda}} \propto f_{inc}^2 \Lambda \tag{4.51}$$

The latest will be particularly important in our analysis, as it will be the one used for describing the oxygen induced diffuse scattering and the thermal diffuse scattering, for which the Q-dependence can be in first approximation neglected. See also the discussion in chapter 7.

Kinematic Bragg or diffuse scattering is proportional to the number of atomic layers involved, in turn, the ratio of the grazing incidence intensity to bulk intensity is of the order of 10^{-4}. Due to this intensity problem, the observation of scattering intensity in combination with total external reflection has not been feasible until the availability of the highly brilliant synchrotron radiation [173].

4.4 Correction factors

In order to compare measured intensities to the theoretical structure factor $S(q)$ discussed in the previous sections, various corrections factors have to be accounted for. The use of the corrections described hereafter will be mentioned on a case by case basis in the experimental results parts. For the Z-axis geometry described in section 5, the geometrical corrections that occur in the measurement of the integrated intensities of surface diffraction rods have been reviewed in [174].

Compton scattering

The Compton scattering is due to the inelastic collision, i.e. with energy and momentum exchange, between the incident photon of wavelength λ and one electron. The expelled electrons during this process originate from the external energy levels of the atom and the scattered photons keep therefore a energy close to the incident photon energy. The corresponding wavelength λ' of the scattered photons becomes slightly superior to λ and

$$\Delta\lambda = \lambda' - \lambda = \frac{h}{mc}(1 - \cos 2\theta) \tag{4.52}$$

with $h/mc = 0.0242$Å and m is the mass of the electron. The wavelength change $\Delta\lambda$ is therefore independent of the incident wavelength λ. The Compton scattering is a smooth background increasing with the scattering angle 2θ, i.e. the scattering vector. Analytical functions of the incoherent scattering intensity for individual atoms are available in literature [175–177].

Geometrical corrections

Polarisation factor The polarization of the incident X-ray beam influence the measured scattered intensity and has to be corrected through the following expression :

$$P = p_h P_{hor} + (1 - p_h) P_{ver} \tag{4.53}$$

$$P_{hor} = 1 - (\sin\alpha_i \cos\delta \cos\gamma + \cos\alpha_i \sin\gamma)^2 \tag{4.54}$$

$$P_{ver} = 1 - \sin^2\delta \cos^2\gamma \tag{4.55}$$

where P_{hor} is the horizontal polarization factor, P_{ver} the vertical polarization factor, and p_h the proportion of horizontal polarization. In the case of synchrotron radiation experiments the polarization is almost completely horizontal. In our case $p_h \sim 95\%$. In our measurements, the samples surface were mounted horizontally thus, the incident beam is polarized perpendicular to the plane of incidence.

Lorentz factor The geometrical correction for the integration volume is usually called the Lorentz factor, and can be expressed in the common case of a rocking-scan through

$$L = 1/\sin\delta\cos\alpha_i\cos\gamma \tag{4.56}$$

or in stationnary geometry as, $L = 1/\sin\gamma$. Further discussions about the Lorentz factor for various geometries and scans directions can be found in [174].

Beam footprint The footprint F of an incident beam of vertical size S is given by $F = S/\sin\alpha_i$, as illustrated in Fig. 4.11. At small incident angles the sample gets fully flooded. If $F \geq L$, only the part of the beam intercepted by the sample contributes to the reflected intensity and the measured intensity has to be corrected by

$$R = R_{\text{mes}}.\begin{cases} S/(L\sin\alpha_i) & \text{for} \quad F \geq L \\ 1 & \text{otherwise} \end{cases}$$

For $F < L$, the whole beam is intercepted by the surface sample, and for Bragg or diffuse X-ray scattering correction must be applied to get the true active area, and $C_f = S/L\sin\alpha_i$.

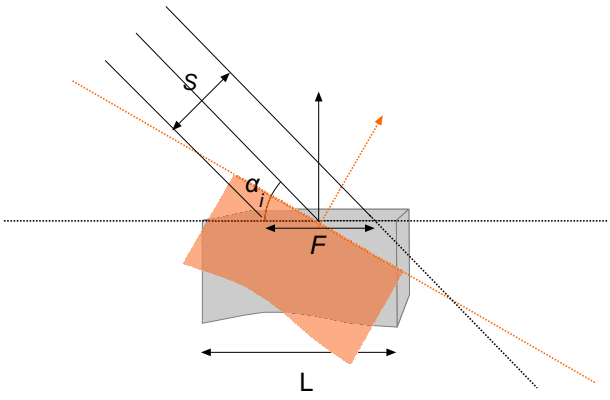

Figure 4.11: Schematic illustration of the footprint F of a incident beam of size S on a sample of size L as a function of the incident angle α_i.

Active area correction The illuminated area of the sample depends on the size of the incident beam s_1 and the opening of the detector slits s_2. The variation of this active area as a function of the position of the detector is corrected via the following factor

$$C_{Area} = s_1 s_2/\sin\delta \tag{4.57}$$

Total correction factor The total correction factor is therefore given by

$$C_{tot} = PLC_{Area}C_f \tag{4.58}$$

The measured intensities are corrected by dividing them by the total correction factor.

4.5 High-resolution core-level spectroscopy

High-resolution core-level spectroscopy (HRCLS) has its origin in the photoelectric effect discovered by Hertz in 1887, in which a photon of an exciting source shining on matter can be absorbed and its energy used to emit an electron. Also designated as X-ray Photoelectron Spectroscopy (XPS) as a reference to the soft X-ray ($\sim$ 100-2000 eV) radiation used to examine core-levels, in contrast to the Ultraviolet Photoelectron Spectroscopy (UPS) using ultraviolet (10-45 eV) radiation to examine valence levels, XPS[8] has been developed from the fifties by Professor K. Siegbahn, whose work has been awarded by the Physics Nobel Prize in 1981 [178]. Core level spectroscopy provides nowadays a key tool for the investigation of surface chemical state [179, 180]. The method takes advantage of the fact that core levels binding energies, although they are not directly involved in the chemical bonding like valence electrons, have small *chemical shifts* depending on the chemical environment of the atom which is ionized, allowing the determination of the chemical state. XPS is highly surface specific due to the short range of the photoelectrons that are excited from the solid. The development of synchrotron radiation sources has enabled high resolution studies to be carried out, with radiation spanning a more complete energy range.

In contrast to the Thomson scattering, exploited in the previous sections, photoelectric absorption can not be explained by classical physics, and a quantum mechanical description of both X-ray field and the photoelectron. The photoemission process can be described energetically by

$$E_i + h\nu = E_f + E_{kin} \tag{4.59}$$

where E_i and E_f are the initial and final energies of the system, $h\nu$ is the photon energy, and E_{kin} the kinetic energy of the emitted photoelectron. To recover from this ionized state, the atom can emit another photon (fluorescence) or undergo an Auger transition. The basic principle of the core-level photoemission is described in Fig. 4.12. The kinetic energy of the emitted electrons depends therefore on the incident photon energy and on their binding energy E_b with

$$E_b = h\nu - E_{kin} = E_f - E_i \tag{4.60}$$

[8] Also known as ESCA (Electron Spectroscopy for Chemical Analysis)

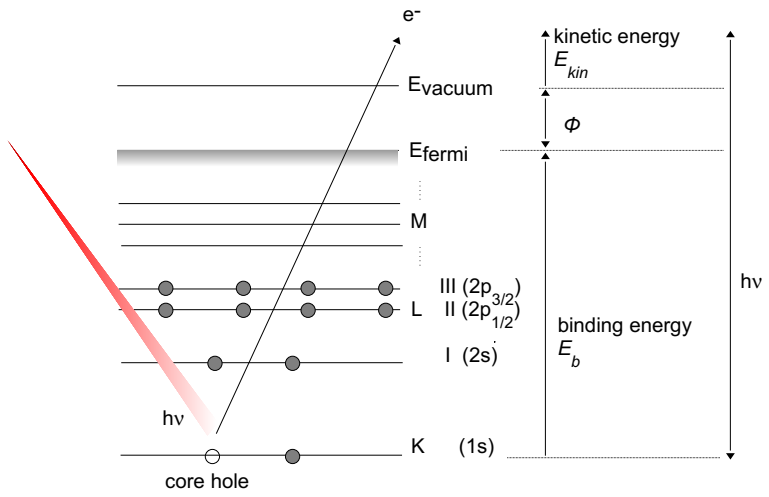

Figure 4.12: Schematic illustration of the core-level photoemission process. The K, L, and M shells are represented, and the first levels labeled as nl_j, where n, l and j are the principal, orbital angular momentum, and total angular momentum quantum numbers, respectively of the single-electron states.

In practice, the experimentally measured energies of the photoelectrons are given by : $E_b = h\nu - E_{kin} - \phi$ where ϕ is the work function of the spectrometer (not the material). By recording the kinetic energy of the photoelectrons the spectrum of the binding energies, i.e. the energy differences between the final and initial states, is obtained. For the determination of the elemental composition of the surface, measurements do not require high-energy resolution as the core-level binding energies of different elements normally differ substantially. However, the chemical shift of a given element associated to different surrounding, such as different oxidation states for example, are small and might require the high energy resolution offered by synchrotron sources.

After escape from an atom, a photoelectron travels some distance inside the solid before it escapes to vacuum or it relaxes. On the way it collides elastically or inelastically with lattice atoms.

Surface sensitivity

The surface sensitivity of the core-level spectroscopy is provided by the relatively small inelastic mean free path (IMFP) of the photoelectron (and not due to the incoming soft X-ray photons, which penetrate the sample over a few hundred nanometers). The inelastic mean free path (IMFP), λ, defined as the average distance that an electron travels between successive inelastic collisions, depends mainly on the kinetic energy of the electron and to a smaller extend on the material. Fig. 4.13 illustrates the IMFP in different materials as a function of the kinetic energy. As one sees, depth-sensitive measurements can be realized by tuning the incident photon energy, and therefore the kinetic energy. A minimum depth

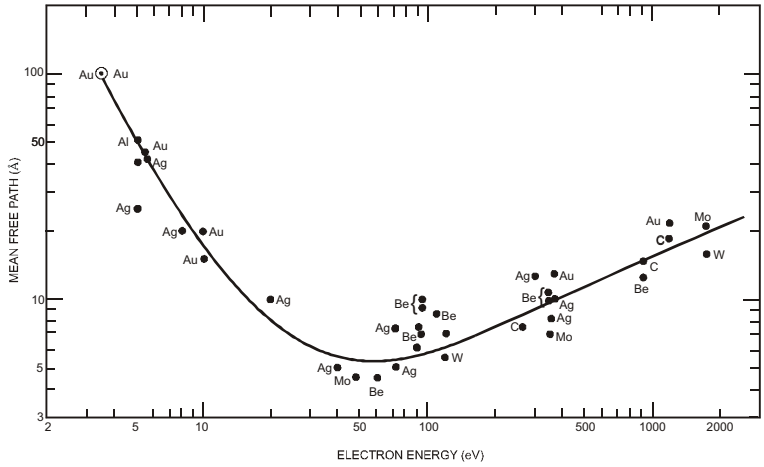

Figure 4.13: Electronic inelastic mean free path (IMFP) as a function of the kinetic energy.

of ~ 5 Å is reached for electrons of kinetic energy between 50 and 200eV.

Spin-orbit splitting

Energy levels with a non-zero value of the orbital angular momentum quantum number,l, show spin-orbit splitting. Two possible states characterized by the quantum number j, the total angular momentum, $j = l \pm s$, arise when $l > 0$. The magnitude of the energy difference ΔE_j is proportional to the spin-orbit coupling constant which depends on the expectation value $< 1/\mathbf{r} >$ of the particular orbital [181]. The separation can be many electronvolts, and is therefore expected to increase as Z increases for a given subshell. The relative intensities of the doublet peaks are given by the ratio of their respective degeneracies $(2j+1)$. Therefore the ratio for the $3d_{5/2} - 3d_{3/2}$ doublet is equal to $3/2$. The area ratio and designations are given in Tab. 4.1.

Subshell	j values	Area ratios
s	$1/2$	-
p	$1/2$, $3/2$	1:2
d	$3/2$, $5/2$	2:3
f	$5/2$, $7/2$	3:4

Table 4.1: Spin-orbit splitting parameters for various shells.

Core-level line shape

The width of a core line is determined by various factors : the intrinsic lifetime width of the core hole, the bandwidth of the photon source, the resolution of the photoemission spectrometer, i.e. the experimental broadening, but also the creation of phonons. The line shape of core-level spectrum can be, for most metals, described by a Doniach-Sunjic line shape convoluted with Gaussian functions. The Doniach and Sunjic line shape [182] itself is the convolution of a Lorentzian and an asymmetric function :

$$I(E) = \frac{\Sigma(1-\alpha)}{(E^2+\gamma^2)^{(1-\alpha)/2}} \cos\left(\frac{\pi\alpha}{2} + (1-\alpha)\arctan(E/\gamma)\right) \tag{4.61}$$

where α is known as the asymmetry parameter, Γ is the Gamma function, 2γ is the full width of half maximum (FWHM) of the Lorentzian function. The Lorentzian accounts for the broadening due to the finite life-time of the core-hole. The inherent line width of a core level is a direct reflection of the uncertainty in the lifetime of the ionized state remaining after photoemission. From the uncertainty principle, the line width can be expressed as $\gamma = \frac{h}{\tau}$, where Planck's constant $h = 4.1 \times 10^{-15}$ eV.s, and τ is the core-hole lifetime. The asymmetry of the line shape characterized by α, is associated with the creation of electron-hole pairs during the photoemission process in metals. Note that when α goes to zero, Eq. (4.61) reduces to a simple Lorentzian expression. The higher the density of states at the Fermi level the more likely is this effect to be observed. The instrumental resolution function has to be included into the theoretical line shape by convolution of expression (4.61) with a Gaussian function including many independent contributions. The Gaussian function also accounts for phonons, disorder broadenings.

In practice, peak widths in the range 0.01-0.5 eV are often encountered, while conventional instruments have energy resolutions which are not better ∼0.25eV. The energy resolution achieved with synchrotron radiation is two order of magnitude higher. Note that the energy resolution decreases as the photon energy increases.

The analysis of the data presented in this work is performed with the program FitXPS [183]. If several components, corresponding to different chemical surroundings, such as different oxidation states, the total line shape is achieved by the sum of them. The fitting parameters are for each peak, the peak energy position, the peak height, the Lorentz full width at half maximum (LFWHM) Γ, the asymetry parameter α, and the Gaussian full width at half maximum (GFWHM) σ. Constrains and correlations between the different peak parameters can be introduced. A simple polynomial background can be included, with up to 3 polynomial coefficients.

Tab. 4.2 gives a non-exhaustive list of reported binding energy positions in literature for the $3d_{3/2-5/2}$ doublets for the main niobium oxides.

Nb_{5+} (Nb_2O_5)		Nb_{4+} (NbO_2)		Nb_{2+} (NbO)		Nb_0 (metal)		Ref.
$3d_{3/2}$	$3d_{5/2}$	$3d_{3/2}$	$3d_{5/2}$	$3d_{3/2}$	$3d_{5/2}$	$3d_{3/2}$	$3d_{5/2}$	
210.0	207.3	208.8	206.0	206.8	204.0	205.0	202.2	[102]
209.9	207.2	208.6	205.9	206.6	203.9	204.7	202.0	[103]
-	207.5	-	205.9	-	203.0	-	202.2	[91]
210.2	207.4	208.8	206.0	207.0	204.2	205.1	202.3	[99]
-	207.4	-	205.9	-	204.0	-	202.3	[100]
-	-	-	-	206.5	203.7	205.1	202.3	[16]
	207.4		205.9		204		202.2	average
	5.1 - 5.3		3.6-3.9		1.4-1.9			CS range

Table 4.2: Non-exhaustive list of reported binding energy positions of the $3d_{3/2-5/2}$ doublets for the main Nb oxides. The average value and the chemical shift (CS) range are indicated.

Chapter 5

Experimental details

This chapter is devoted to the description of the experimental set-ups, synchrotron light sources, and experimental end-stations used in this thesis. A high-temperature *in-situ* setup developed in the framework of this work is presented in section 5.2.

5.1 Synchrotron radiation and synchrotron beamlines

The different aspects of an X-ray source, which determine the quality of the produced X-ray beam, are combined in a single quantity, the so-called *brilliance*. For a given energy, the brilliance is defined as,

$$\text{Brilliance} = \frac{\text{Photons/second}}{\text{mrad}^2 \times (\text{source area in mm}^2) \times 0.1\%\text{bandwidth}} \tag{5.1}$$

which depends on the number of photons emitted per second, the collimation of the beam given in mrad for both horizontal and vertical direction, the area of the source, and a fixed relative energy bandwidth chosen at 0.1%. Fig. 5.1 represents the evolution of the brilliance of the different X-ray sources along the time, from the X-ray tubes to the synchrotron of first, second and third generation. As one can see, the brilliance offered by synchrotron radiation is about 10 orders of magnitudes higher than for the most powerful rotating anode set-up in an usual laboratory. The ESRF has been the first third generation synchrotron in the world and has entered in service in 1994. Since numerous similar sources have been build, and among them ANKA and Max-Lab II. The dramatic improvement of the brilliance achieved by X-ray sources has in many ways led to a paradigm shift in experimental X-ray science. Experiments inconceivable only 10 to 20 years ago are now performed on almost a routine basis [154].

The relativistic electrons (or positrons) in modern storage rings (the first 'synchrotron' radiation was observed with a cyclotron, but modern light sources are based on the concept of an electron storage ring) are forced on a circular orbit by bending magnets. The bending,

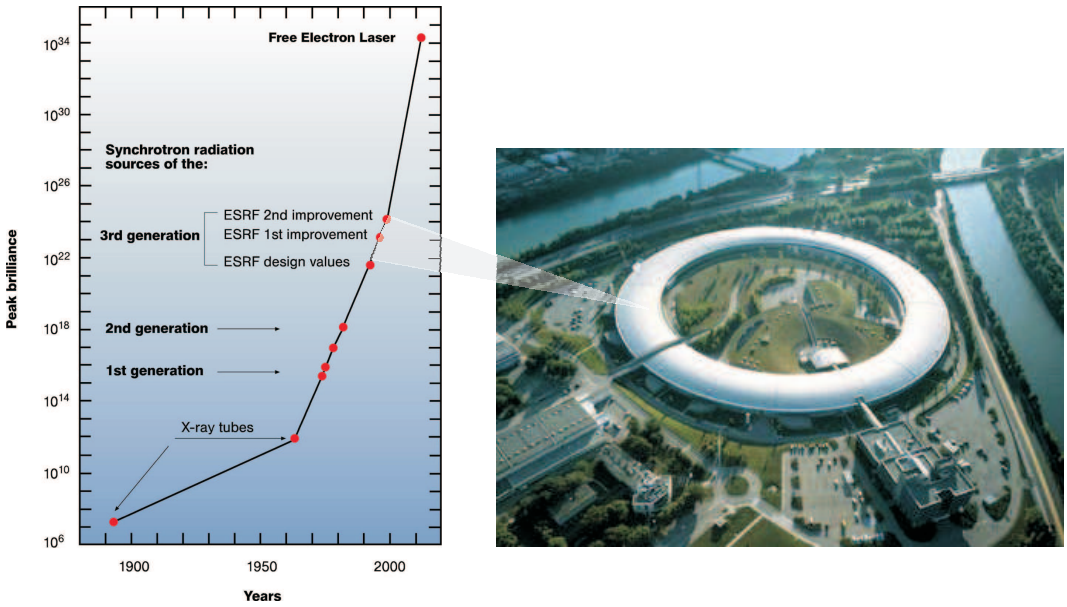

Figure 5.1: Advances of the X-ray sources. The development of the X-ray sources shows a tremendous improvement of brilliance after the discovery of synchrotron radiation at particle accelerators. The development carried on at free electron lasers opens new unexpected prospects [184]. Right : European Synchrotron Radiation Facility (ESRF) in Grenoble.

due to the centripetal acceleration, causes the emittance of photons with a continuous spectrum dependent on the energy of the ring electrons. Because of the relativistic speed of the electrons (e.g. E=6 GeV for the ESRF, i.e. approximatly 10^4 times the electron rest mass m_e of 511 keV), the calculations for the characteristics of the emitted spectrum have therefore to be based on the Lorentz transformation known from Einstein's special theory of relativity. Besides the radiation from simple bending magnets one can obtain higher flux and much higher brilliance with insertion devices, i.e. wigglers and undulators, that contain a periodic array of magnets. For a wiggler the intensity is multiplied by the number of periods N. This is different in an undulator, where the design parameters are chosen so that the emission of new photons from each 'wiggle' of the electrons occurs in phase with the emerging photon beam [154].

All measurements presented in this thesis have been performed using synchrotron radiation from three different third generation synchrotron radiation sources : at the dedicated beamline for the Max-Planck-Institut for Metals Research at the Angstromquelle Karlsruhe (ANKA), Germany ; at the European Synchrotron Radiation Facility (ESRF), France, at the beamline ID32 ; and at the beamline I311 at MAX-Lab in Lund, Sweden [185]. The experimental details about the different beamlines are shortly presented in the following.

5.1.1 MPI-MF beamline at ANKA

The Max Planck Institute for Metals Research (MPI-MF) runs a beamline at the ANKA synchrotron dedicated for surface and interface investigations [186]. ANKA (Angstromquelle Karlsruhe) is a third generation synchrotron located on the site of the Research Center Karlsruhe. The energy of the storage ring is 2.5 GeV with a current of 200 mA.

The MPI-MF beamline utilizes the synchrotron radiation produced by a bending magnet (1.5 T). To discriminate the energy of the photons (6-20 keV), a fixed exit height double crystal monochromator, consisting of a flat Si(111) single crystal and a sagittal Si(111) crystal bender for additional horizontal focusing is used. An energy resolution of (dE/E) 3.10^{-4} is achieved at 9 keV. A Rh coated mirror serves for harmonic rejection and focusing in the vertical plane. Several pairs of slits allow setting a convenient beam size at the sample position. The latter can be focused to 0.5 mm (h) x 0.3 mm (v). The typical divergence at the sample position is 0.3 mrad horizontally and 0.03 mrad vertically with a flux of $\sim 10^{12}$ ph/s/mm^2. For all measurement presented in this thesis, a conventional scintillation detector has been used.

The heavy duty HUBER diffractometer is a special design, implementing both a six-circle and a (2+3) diffractometer, which can be used with heavy load in the horizontal and vertical geometry (up to 200 kg). A sketch of the diffractometer circles is shown in Fig. 5.2. A detailed description of the beamline and the different diffractometer configurations can be found in [186].

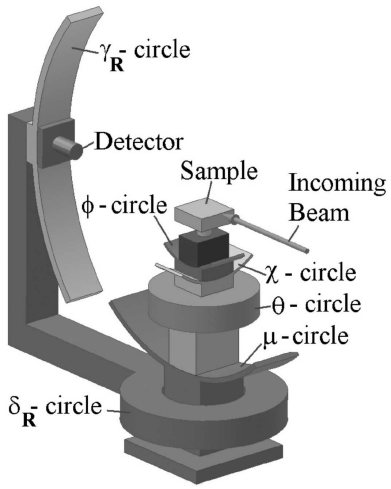

Figure 5.2: HUBER diffractometer at the MPI-MF beamline at ANKA [186].

5.1.2 ID32 beamline at the ESRF

The ESRF (European Synchrotron Radiation Facility) is the first 3rd generation synchrotron and up to now among the three largest and most powerful synchrotrons in the world, situated in Grenoble, France. The storage ring is filled with an electron current of 200 mA and Energy of 6 GeV in 'normal' operation mode.

The beamline ID32 at the ESRF is focusing amongst others on surface and interface studies by X-ray diffraction. Located on a high beta section (undulator), ID32 offers a highly brilliant beam. The optical elements are: a liquid nitrogen cooled primary silicon monochromator and alternatively a mirror for harmonic energy photon rejection or a high resolution post-monochromator. The Energy of the beam can be set from 2.5-30 keV with a resolution dE/E better then 10^{-4}. At the sample position the beam size is 2(v)x1(h) mm^2 with a flux of 10^{12}-10^{13} ph/s(10^{-4} bw, 0.1A). The experimental end-station is equipped with a six-circle HUBER diffractometer, which can accommodate the portable UHV sample chamber used for the experiments presented hereafter (see Fig. 5.2 and 5.3). A more detailed description of the beamline characteristics can be found in [187].

5.1.3 I311 beamline at MaxLab

MAX-lab is a Swedish national laboratory which supports amongst others research based on the use of synchrotron radiation. MAX II is a third generation storage ring and runs with an electron current of 200 mA with an Energy of 1.5 GeV.

The Beamline I311 [185] is an undulator based VUV, soft X-ray beamline with two end-stations. The end-station used in the frame of this work is aimed at high resolution X-ray Photoemission Spectroscopy (XPS) and X-ray Absorption Spectroscopy (XAS) on clean and adsorbate covered surfaces. A horizontally focusing spherical mirror serves as pre-focusing optics followed by a modified SX-700 monochromator with 1220 l/mm grating, a spherical focusing mirror and movable exit slits. This allows a high flexibility concerning the interplay between photon flux, resolving power and higher order suppression. The accessible energy range is 30 - ∼1500 eV with a resolution dE/E 5.10^{-3}-2.10^{-4}. The photon flux on the sample is 10^{11}-10^{13} photons/s. A hemispherical electron energy analyzer (SCIENTA SES200) is used for photoelectron spectroscopy.

5.2 Oxidation chamber and high temperature setup

A portable UHV diffraction chamber allowing $in-situ$ annealing and oxidation experiments at pressure up to 1 bar of oxygen has been used for the grazing incidence X-ray scattering

and X-ray reflectivity experiments described in this work. The chamber, mounted on the diffractometer at the MPI-MF beamline at ANKA, is shown in Fig. 5.3 (Left). The chamber is equipped with a beryllium window (thickness 2 mm). Ultra-high-vacuum in the 10^{-9} mbar regime is achieved after baking the chamber at temperatures around 120°C. The vacuum is maintained by a Varian turbo molecular pump (Turbo-V 70LP) and a Varian ion getter pump (Star Cell). The pressure is measured via two different types of gauges, the cold cathode ionization gauges (for pressures between 10^{-2}-10^{-10} mbar) and capacitive gauges (from atmospheric pressure up to $\sim 10^{-3}$mbar).

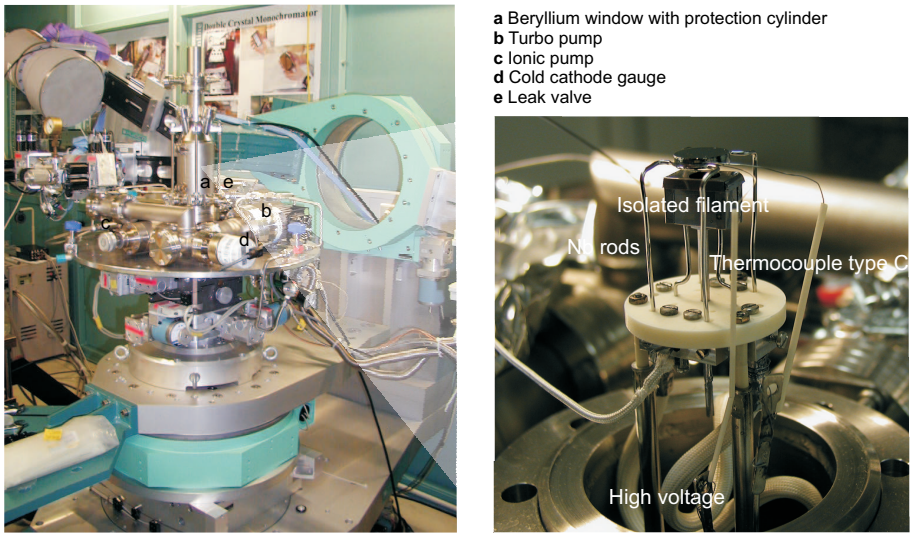

Figure 5.3: Left : Portable UHV diffraction chamber mounted on the diffractometer at the MPI-MF beamline at ANKA. Right : High temperatures setup (up to 2000°C) developed in this work, compatible with the portable UHV chamber.

High temperature setup

In order to perform $in-situ$ experiments on niobium clean surfaces, a high-temperature setup has been developed in the framework of this work, allowing annealing up to 2000°C. The setup is shown in Fig. 5.3 (right panel). The sample is supported by two parallel niobium rods purified by annealing cycles above 2100°C in ultrahigh vacuum (UHV). The heating is performed by electron bombardment obtained by applying high voltage to the filament. The high voltage elements are directly connected to the supporting rods isolating from the foundation of the sample holder by a purified ceramic plate. The temperature is measured directly at the sample by a type C thermocouple (W/Re (5%), W/Re (26%)) The different elements are mounted and fixed using purified molybdenum elements.

5.3 The beamtimes

The data presented in this thesis were recorded during six experimental beamtimes at the aforementioned MPI-MF beamline at ANKA, Karslruhe, on ID32 at the European Synchrotron Radiation Facility, Grenoble, and at the I311 beamline of the Max-Lab synchrotron source, Lund. During these different beamtimes, various experimental parameters have been varied, and the high-temperature setup described above improved. A list of the beamtimes is given in Tab. 5.1.

Beamtime	Sample	Oxidation conditions	Beamline	Energy	Time
A1	Nb(110)	air (3 h, RT)	MPI-MF	10 keV	September 04
A2	Nb(100)	air (14 days, RT)	MPI-MF	10 keV	May 05
A3	Nb(110)	air (10 h, RT)	MPI-MF	10 keV	August 05
		+ pure water (10 h, RT)			
A4	Nb(110)	air (10 h, RT)	MPI-MF	9 keV	September 06
E1	Nb(110)	air (3 h, RT)	ID32	12.83 keV	April06
L1	Nb(110)	air (10 h, RT)	I311		December 05

Table 5.1: Synchrotron beatimes carried out in the framework of this work.

5.4 Sample preparation

The Nb(110) and Nb(100) single crystals (see Fig. 5.4) were oriented with an accuracy better than 0.1°, chemically polished (HF:1, HNO_3:2, HCl_2:2, H_2O:2, in vol.), mechanically polished, and subsequently annealed above 2100°C in ultrahigh vacuum (UHV) (in-house furnaces). At the end of the heating cycles, the pressure was $\leq 10^{-9}$ mbar, which results in an interstitial oxygen concentration of a few ppm [188]. The samples were then oxidized and mounted horizontally in the dedicated UHV chamber presented in section 5.2 allowing *in-situ* annealing and oxidation under controlled environment.

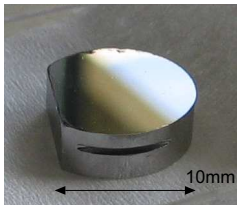

Figure 5.4: Nb(110) single crystal after polishing.

Chapter 6

Results on the atmospheric oxidation of Nb(110)

The atmospheric oxidation of niobium and the thermal stability of its natural oxide layer are of first importance for numerous technological applications of niobium, such as tunnel barrier in nanolelectronic devices, radiofrequency superconducting cavities, or heterogeneous catalysis, as seen in chapter 3. In this work, a systematic, non-destructive study of the niobium near surface region behavior upon annealing, including the simultaneous characterizations of the oxide layer structure and the interstitial oxygen, has been undertaken by means of complementary surface sensitive X-ray methods. The depth distribution of interstitial oxygen dissolved in niobium underneath the oxide layer, will be investigated by depth-resolved grazing incidence X-ray diffuse scattering in chapter 7.

In this chapter, the experimental results on the natural oxide layer on Nb(110) single crystals and its evolution upon vacuum annealing are presented. The results are organized as follows. In the two first sections, X-ray reflectivity (XRR) and high-resolution core-level spectroscopy analysis (HRCLS) will be used in turn to determine respectively the electron density profiles in the direction normal to the surface, and the chemical environment of the niobium atoms in the near-surface region. The natural oxide will be characterized in section 6.1. Its progressive dissolution as a function of the temperature will be discussed in section 6.2. Grazing incidence X-ray diffraction (GIXD) measurements will be used to characterize the in-plane and out-of-plane crystalline structure of the thin NbO layer in section 6.3, as well as the structure of the Nb(110)/oxide interface (section 6.4). A model of the oxidation process induced by the interstitial oxygen into the niobium lattice will be proposed in section 6.3. The chapter will be concluded by a summary of the results. Note that complementary results on the less dense Nb(100) surface oxidized in air, on Nb(110) surfaces oxidized in dry oxygen atmosphere, and in clean water, will be discussed in chapter 8.

The X-ray reflectivity and grazing incidence X-ray diffraction measurements discussed in this chapter (unless indicated[1]), were carried out at the MPI-MF beamline at the Angstromquelle Karlsruhe (ANKA), Germany [186], at a photon energy of 8.984 keV (beamtime A4). The core-level measurements were conducted at the beamline I311 at MAX-Lab in Lund, Sweden [185]. The different methods and experimental details have been discussed in chapters 4 and 5 respectively.

6.1 Natural oxide layer

Because of its high chemical reactivity, a clean niobium surface immersed in an atmospheric environment immediately forms a rather complex oxide layer [62, 66, 72, 94–98] (see section 3.3.2). Thin Nb(110) films oxidized in air at RT form a 20-50 Å amorphous Nb_2O_5 layer depending on the time they were exposed to air [15, 116]. Passivating oxide layer on niobium are typically observed at ∼50 Å [15, 90]. The occurrence of NbO or NbO_2 at the Nb_2O_5/substrate interface has been controversial and is of critical importance for superconducting devices, as they influence drastically the performances of the material.

Nb(110) single crystals with a diameter of 11 mm and a thickness of 3 mm were oriented with an accuracy better than 0.1°, mechanically polished and subsequently annealed above 2100°C in ultrahigh vacuum (UHV) [2]. The samples were then oxidized in air during 6-10h at RT and mounted in a dedicated UHV chamber allowing *in-situ* annealing (see section 5).

In this section, the XRR and HRCLS results on the natural oxide layer are presented in turn.

XRR results

The specular X-ray reflectivity spectra of the Nb(110) single-crystal oxidized 10h in air at room temperature is shown in Fig. 6.1 (a). The data were fitted using the Parratt formalism, where the thicknesses, roughnesses and density of the layers were in principle free parameters [3]. The best fit was obtained with a three layer model compatible with the following sequence of oxide layers : Nb_2O_5, NbO_2, NbO, from the surface to the metal/oxide interface. Attempts assuming only two oxide layers could not reproduce properly the

[1] Some of the results given in Sec. 6.3 refer to the *E1* beamtime at ESRF and *A1* beamtime at ANKA. For more details refer to chapter 5

[2] At the end of the heating cycles, the pressure was $\leq 10^{-9}$ mbar, which results in an interstitial oxygen concentration of a few ppm. For more details about the samples preparation please refer to chapter 5

[3] The data were fitted using the program FEWLAY developed by A. Stierle [189]. The method and the analysis procedure have been described in section 4.3. The fitting parameters are given in Appendix A

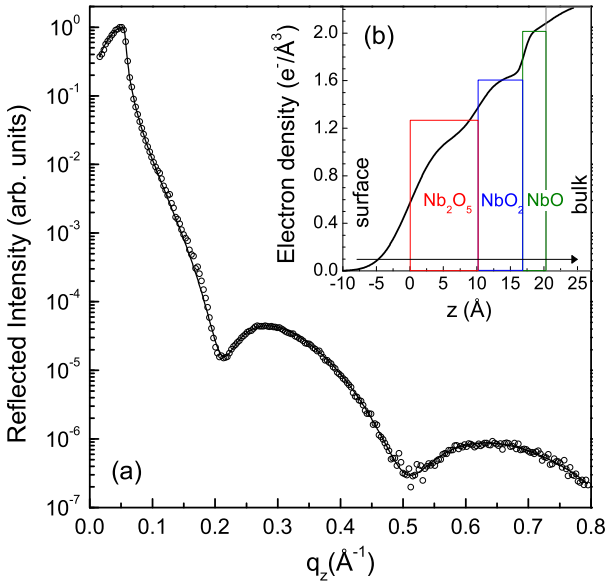

Figure 6.1: (a) X-ray reflectivity data (open circles) with fit (solid lines) from a Nb(110) single crystal oxidized 10h in air at RT. (b) Corresponding electron density profile using a three layer model in the Parratt formalism compatible with the following sequence : Nb_2O_5, NbO_2, NbO, from the surface to the metal/oxide interface (see text for details).

features of the data. The corresponding electron density profile is shown in Figure 6.1(b). Thin Nb(110) films oxidized in air at RT, typically show a 20-40 Å oxide layer depending on the time they were exposed to air [15]. After 10h in air, the total thickness of the oxide is 20.3±1 Å, with individual Nb_2O_5, NbO_2 and NbO thicknesses respectively equal to 10.2 Å, 6.7 Å and 3.4 Å (error bar of ± 1 Å). The respective roughnesses from the surface to the metal/oxide interface are 3.4, 2.2, 0.7 and 3.7 Å. All results are summarized in Tab. 6.1. The dispersion and absorption parameters are given in Appendix A. Nb_2O_5, highest oxidation state of niobium, is the most stable oxide under ambient conditions and predominates in the native oxide. Its presence as the outermost layer of the oxide is confirmed by the HRCLS results presented in the following. LEED measurements (not shown) also indicate a disordered oxide layer at the surface, typical for the presence of the amorphous Nb_2O_5 phase, as reported for the Nb_2O_5 RT oxide grown on Nb(110) films [15].

Note that similar measurements realized using a conventional Cu X-ray source (rotating anode) do not allow to resolve the multi-layers system, due to a insufficient signal to noise ratio.

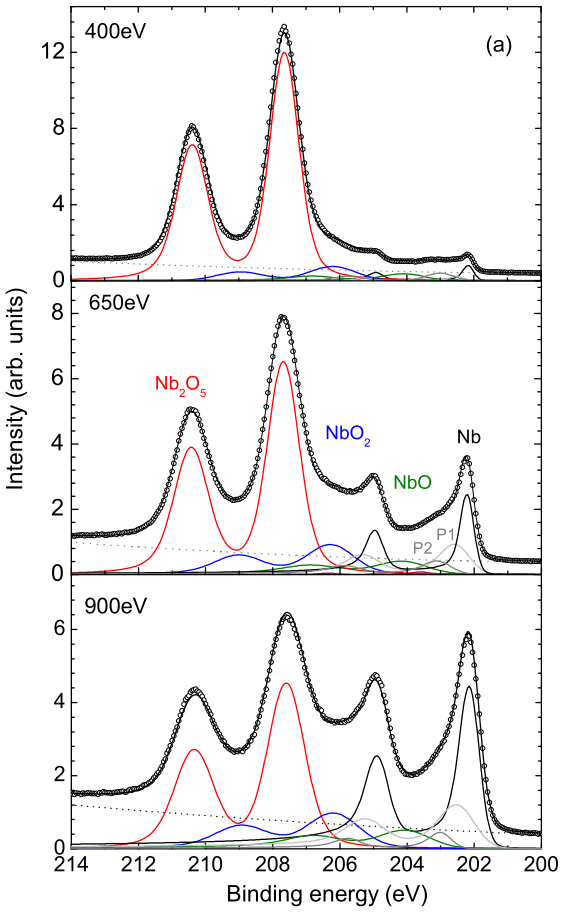

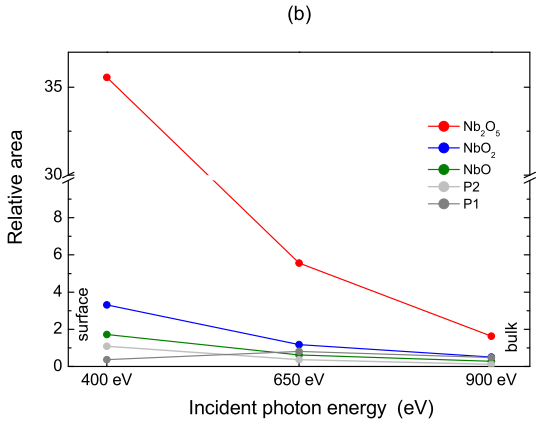

Figure 6.2: (a) Core-level Nb $3d_{3/2-5/2}$ spectra (open circles) measured on a Nb(110) single crystal oxidized 6h in air (RT) for $h\nu$ = 400, 650 and 900 eV (normal emission angle) and fits (solid lines). The major components assigned to Nb_2O_5, NbO_2, NbO and the Nb doublets are indicated. (b) Relative area of the oxygen-induced components with respect with the bulk component as a function of the photon energy.

High-resolution core-level results

Additional information about the chemical environment of the niobium atoms in the native oxide layer were obtained by core-level spectroscopy measurements. The technique has been presented in section 4.5. For each oxidation (valence) state, the niobium atoms give rise to a component with distinct energy shift with respect with the niobium atoms in the pure metal.

Due to spin-orbit interaction, each of these component splits into a doublet Nb $3d_{3/2-5/2}$, where the angular momentum state $j = 5/2$ occurs at higher energy, and the 3/2 at lower one. The theoretical intensity ratio $3d^{3/2}/3d^{5/2}$, also called branching ratio, is equal 3:2 (given by the ratio of their respective degeneracies). Depth-sensitivity of the measurements is achieved from the escape depth dependence of the photoelectrons on their kinetic energy (for more details see section 4.5).

The Nb 3*d* core-level spectra measured on the the Nb(110) surface after oxidation during 6h in air are presented in Fig. 6.2 for various photon energies (normal emission angle,

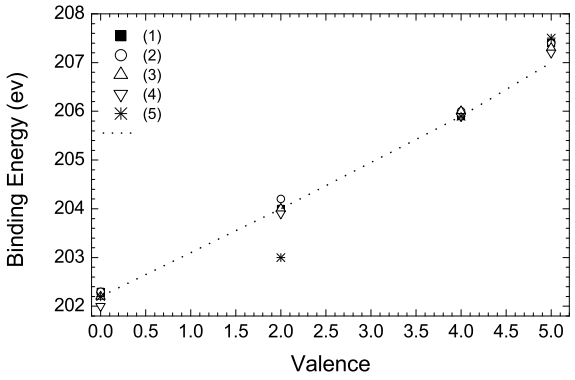

Figure 6.3: Binding energies reported in literature for the Nb$3d_{5/2-3/2}$ doublets of the main niobium oxides. From (1) to (5) : [91, 99, 100, 102, 103].

RT). The individual components have been fitted using Doniach-Sunjic line shapes convoluted with Gaussian functions[4]. The intensity, the binding energy (B.E.), the lineshape parameters (Lorentzian FWHM Γ, Gaussian FWHM σ and the asymmetry parameter α), and the background are free parameters. They should, however, be consistent for all measurements at different depths as well as at different temperatures, which were included in the analysis in order to increase the reliability of the results. The spin-orbit splitting of the Nb $3d$ level is 2.74eV, in good agreement with values reported in literature (see section 4.5). A branching ratio of ~ 0.67 was used and the lifetime width of the $3d^{3/2}$ level was found to be about 0.1-0.2eV bigger than for the $3d^{5/2}$ level [190]. A selection of binding energies reported in literature for the Nb$3d_{5/2-3/2}$ doublets of the main niobium oxides is given in Tab. 4.2 and plotted in Fig. 6.3. The major components of the spectra Fig. 6.2 are assigned to Nb_2O_5, NbO_2, and NbO, located respectively at ∼5.5eV, 4eV and 1.9eV above the niobium metal binding energy[5]. The major component at the surface is, as observed for the XRR results, the Nb_2O_5 component. Additional components P_1 and P_2, with energy shifts with respect to the bulk component inferior to the NbO component, were needed to fully account for the Nb $3d$ line shapes. The interpretation of those components is discussed below. The Nb and NbO components present a non-zero asymmetry parameter characteristic for metals, while an asymmetry parameter equal to zero for the Nb_2O_5 component is consistent with the dielectric nature of Nb_2O_5. The resulting fitting parameters are summarized in Appendix A.

[4]The data were fitted using the FitXPS program developed by D. Adams [183], for more details about the analysis procedure the reader is invited to refer to section 4.5

[5]During our beamtime, problems with the analyzer made the alignment of the data on the Fermi level problematic. All data and the energy shifts are however fully consistent between each other and with what is reported in literature. The spectra have been therefore aligned on the pure metallic Nb peak at 202.2eV

The relative area of the Nb $3d_{5/2}$ components with respect to the niobium bulk component as a function of the photon energy is shown in Fig. 6.2 (b). The escape depth of the photoelectron is increasing from 400eV to 900eV. All oxide components are higher for the photon energies where the surface sensitivity is larger. The strongest decrease is observed for the highest binding energy contribution, attributed to Nb_2O_5, indicating that the photoemitting atoms are located closer to the surface than the other components. This is compatible with a layering of the Nb_2O_5 and NbO_2 oxides, and justifies the model used in the XRR analysis. Note that angle-resolved photoelectron spectroscopy studies show a similar layering for Nb(100) single crystals oxidized in air [21]. The relative decreases of the NbO_2, NbO and P_2 components with increasing the photon energy are similar. However, they are most probably not resolved with the range of energies used here. In contrast, a clear layering of the NbO_2 and NbO oxides is observed after heating (section 6.2.1). The increase observed for the P_1 component with increasing the photon energy, indicates its location at the metal/oxide interface.

From extrapolation of the relationship between the valence of Nb oxide states and the corresponding chemical shifts (see Fig. 6.3), different authors assigned a chemical shift around 1±0.2 eV to the Nb_2O state [19–21, 90, 109]. Arfoui *et al.* [16] attributed chemical shifts of 0.2eV and 0.5eV toward higher binding energies to Nb_6O and Nb_4O compounds, assigned respectively to octahedral and tetrahedral interstitial sites. The P_1 and P_2 components obtained from the deconvolution of the spectra shown in Fig. 6.2 were shifted by ∼0.35eV and ∼0.85eV with respect to the niobium bulk component. However, for the data measured on the natural oxide and after heating at low temperatures (see also next section), the positioning of those weak components could not be determined unambiguously. Further interpretation at this point would be to speculative. In contrast, it will be seen in the next section that at higher temperatures, above 300°C, the P_2 component (assuming the same chemical state) becomes rather important and its energy well resolved. Following the spectroscopic argument mentioned above, it will be assigned to Nb_2O. For further discussion see section 6.2.2.

6.2 Thermal stability of the oxide layer

The progressive dissolution of the natural oxide layer characterized in the previous section, as a function of temperature under UHV conditions, has been investigated by mean of X-ray reflectivity and high-resolution core-level spectroscopy. The surface has been subsequently heated at 145°C, 300°C[6], and 670-800°C. All measurements have been performed after cooling the sample down to a *frozen* state at room temperature (RT) (unless indicated). In the first part of this section, the low-temperature heating treatments, relevant for the rf superconducting cavities, will be presented. Temperature treatments above 300°C will be discussed in the second part of the section. All thermal treatment results will be summarized and discussed together at the end of the section. Additional structural characterization of the oxide layer by grazing incidence X-ray diffraction will be given in section 6.3.

6.2.1 Low-temperature UHV annealing

As mentioned before, the microscopic origin of the remarkable enhancement achieved on the rf accelerating field after a low-temperature annealing (typically 120°C, 12-24h) [1–3], has, despite an increasing interest from the surface science community, remained up to now unclear. Considering the range of temperatures involved, it has been argued that a redistribution of subsurface interstitial oxygen within the penetration depth of the rf field into niobium (typically 500 Å) is involved. This hypothesis will be discussed in detail in chapter 7. However, a complete picture of the near surface region includes, besides the interstitial oxygen, the oxide layer and the metal/oxide interface. Their behavior upon vacuum heating are crucial and will be discussed in this section.

Based on the hypothesis that the oxygen diffusion is involved in the performances achieved on rf cavities, heating at 145°C (3h, UHV) was recently proposed [191] in the superconducting rf community, as faster alternative to the standard baking procedure (120°C,12-24h). This treatment has shown similar improvements in the cavity performances and is therefore a good compromise for us, taking into account the time requirements for synchrotron experiments.

XRR results

Fig. 6.4 (a) shows the X-ray reflectivity data measured after heating the Nb(110) surface at 145°C (5h, UHV). The native oxide data, discussed in the previous section, are shown

[6] An intermediate heating at 200°C for ∼1h (UHV) was systematically applied before heating at 300°C but is not discussed here.

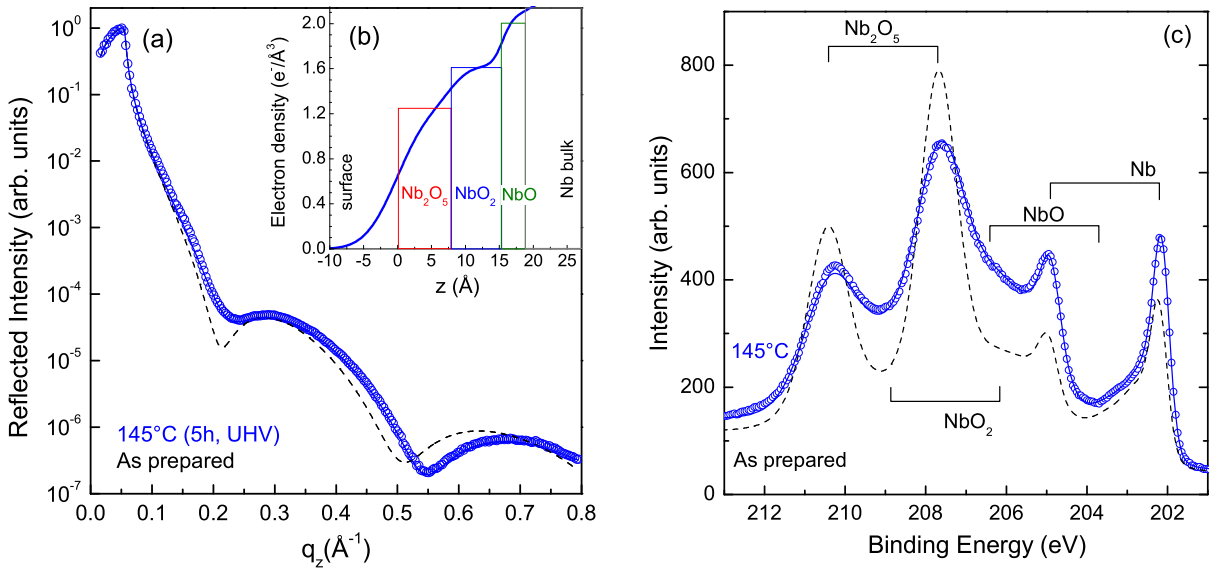

Figure 6.4: (a) X-ray reflectivity data (open circles) and fit (solid line) of the Nb(110) surface after heating at 145°C (5h, UHV), the data measured after atmospheric oxidation are shown for comparison (dashed line). (b) Corresponding electron density profile (see text for details). (c) Core-level Nb $3d_{3/2-5/2}$ spectrum (open circles) with fit (solid line) measured on Nb(110) after 145řC (3h,UHV), the data measured after atmospheric oxidation are plotted for comparison (dashed line) (photon energy = 650eV, normal emission angle, RT).

for comparison. The measurements were recorded after cooling the sample down to RT, freezing the state of the system. The best fit was obtained using a three layer model, as for the native oxide, with a total oxide thickness which slightly decreased from 20.3 Å to 18.8 Å. The corresponding electron density profile is plotted in Fig. 6.4 (b). The main effect of the thermal treatment is the reduction of the Nb_2O_5 thickness by $\sim$ 20% to 7.9 Å, while the NbO_2 layer is slightly thickening to 7.4 Å. Only the NbO layer stays unchanged in comparison with the RT data. All interfacial roughnesses, presented in Tab. 6.1, stay nearly constant. An increase of the Nb_2O_5 electron density by 10 % in comparison with the as-prepared value is observed (see Appendix A).

Core-level results

The Nb 3*d* core-level spectrum measured after heating at 145°C (3h, UHV) is presented in Fig. 6.4 (c), the data for the natural oxide are shown for comparison (normal emission angle, $h\nu = 650$ eV). The decrease in intensity observed for binding energies corresponding to Nb_2O_5 in favor of an increased intensity around the lower binding energies of NbO_2, indicates that the oxide layer reduces progressively from Nb_2O_5 to NbO_2, showing similar behavior as reported on polycrystalline [18,19] and Nb(100) single crystal [21] surfaces, and

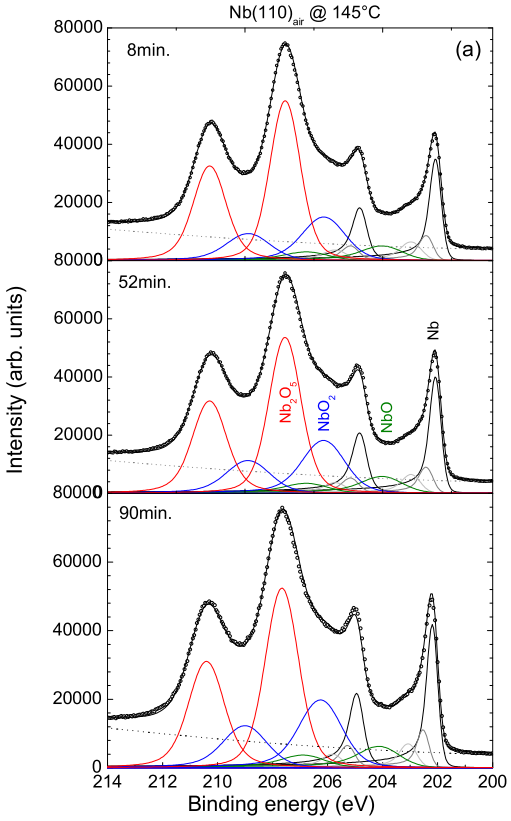

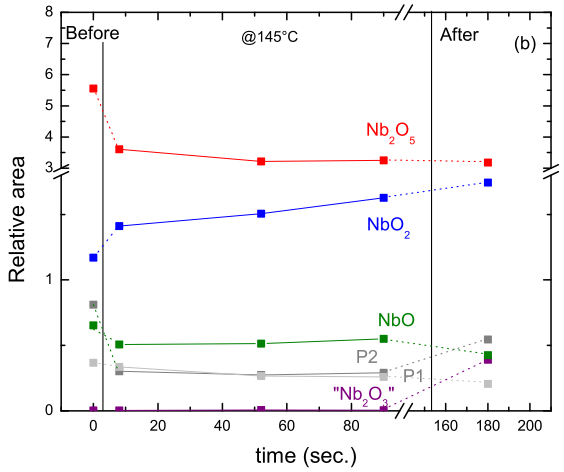

Figure 6.5: (a) Deconvolution of the Nb $3d_{3/2-5/2}$ spectra measured during annealing at 145°C (normal emission angle, $h\nu = 650$ eV). (b) Relative area of the oxygen-induced components with respect with the bulk component as a function of the photon energy. The data measured before and after heating are shown for comparison. The lines are given as eye-guides.

in agreement with the layer transformations observed by the reflectivity measurements.

Spectra recorded *in-situ* during the annealing at 145°C are plotted in Fig. 6.5 (a). The fitting procedure has already been discussed in the previous section. The fitting parameters are given in Appendix A. The different components are identical as for the native oxide layer. The relative area of the main oxide components with respect to the bulk component as a function of the time is shown in Fig. 6.5 (b). The data points corresponding to measurements performed before and after heating (at RT) are plotted for comparison.

Details of the deconvolution of the depth-dependent core-level spectra measured after cooling down to RT are presented in Fig. 6.6. An additional component corresponding to a B.E. shift of 2.7eV (purple) with respect to the pure niobium, was needed to fully account for the Nb 3*d* line shape. One could be tempted to assign it to an interfacial state for the niobium atoms located at the NbO_2/NbO interface, seeing an intermediate bonding state. However, such a component was not necessary for the native oxide, or the data recorded during heating (see below). Ma *et al.* [21] reported the presence of Nb_2O_3 underneath NbO_2 for a Nb(100) single crystal oxidized in air and annealed at 430K. The extrapolation of the average values reported in Fig. 6.3 would yield to the Nb_2O_3 valence.

The relative area of the main Nb $3d_{5/2}$ components with respect to the niobium bulk component as a function of the incident photon energy is shown in Fig. 6.6 (b). The

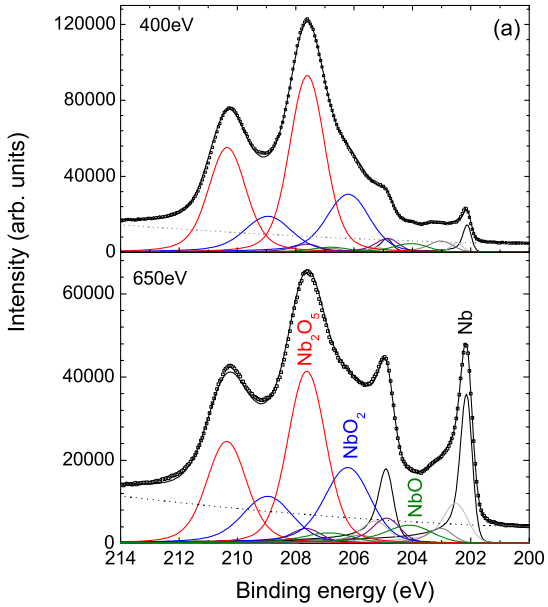

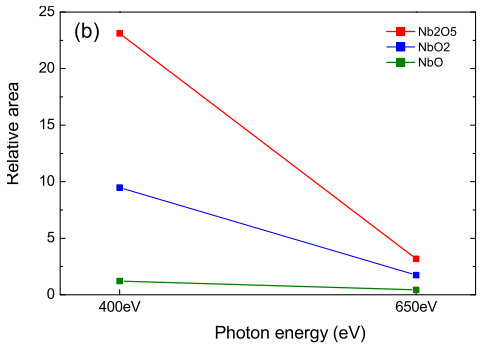

Figure 6.6: (a) Nb $3d_{3/2-5/2}$ spectra (open circles) measured after heating at 145°C (3h,UHV) for $h\nu = 400$ and 650eV (normal emission angle) and fit details (solid lines). (b) Relative area of the main oxide components with respect with the bulk component as a function of the photon energy.

strongest decrease is observed for the Nb_2O_5 component, implying a similar layering of the Nb_2O_5 and NbO_2 components as observed for the native oxide. The decrease of the NbO_2 component is higher than for the NbO component, indicating that the NbO_2 is present on top of NbO and not intermixed with it. This justifies the layered model assumed previously in the XRR analysis.

6.2.2 Vacuum annealing between 300 and 800°C

For vacuum annealing above 300°C, the native oxide characterized by mean of XRR and HRCLS, reduces significantly from Nb_2O_5 and NbO_2, into NbO. This involves a major dissolution of the oxide layer, in contrast with the moderate changes presented in the last section. The existence of a transition temperature between 200-300°C for the reduction of the oxide layer to NbO, was already reported in different studies [18–20]. The thermal treatments discussed in this section, were subsequently applied to the low-temperature heating discussed in the previous section[7].

XRR results

The specular X-ray reflectivity data measured after heating at 300°C (50min., UHV), and at 670°C (5min., HV) are shown in Fig. 6.7 (a). Both spectra have been fitted with a unique NbO layer on the niobium substrate, respectively 8.6 Å and 29 Å thick. The corresponding electron density profiles are shown in Fig. 6.7 (b). Simultaneously to the oxide growth,

[7]The samples were therefore subsequently heated at 145°C (section 6.2.1), 200°C (not discussed), 300°C and higher.

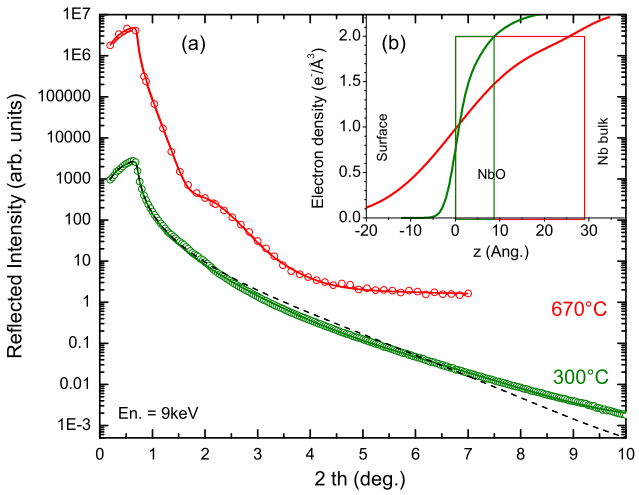

Figure 6.7: (a) X-ray reflectivity data (open circles) and fit (solid lines) after heating at 300°C (5h, UHV), and at 670°C (5min., HV). The data were vertically shifted for clarity. Dashed curve : best fit of the 300°C data without oxide layer, which can not describe the data. (b) Corresponding electron density profile. A single NbO layer model, thicker at higher temperature, was used for both temperatures.

both roughness at the surface and at the NbO/Nb interface increase drastically. The data present few features, especially at 300°C. However, a rough bare substrate alone can not reproduce the curve (dashed line in Fig. 6.7).

Note that for those experiments (and the GIXD discussed in the following chapter), 670°C was the maximum temperature that could be reached with a rather slow heating rate ($>$ 1h). The pressure in the chamber increased simultaneously to 10^{-5}mbar[8].

A stable and passivating NbO layer grown on Nb(110) was reported after oxidation of Nb(110) thin films in pure oxygen atmosphere at 340°C [15]. It is specified that a low oxygen pressure and high temperatures are necessary. Parallel the NbO growth, a consequent roughening of the surface and the metal/oxide interface was observed. We have performed different oxidation experiments on the Nb(110) single crystals in similar conditions, but did not obtain a NbO passivating layer. The oxide grown on the single crystal surfaces oxidized further into NbO_2 and Nb_2O_5 once immersed in air.

Grazing incidence X-ray diffraction measurements discussed in section 6.3, confirm the growth of an NbO epitaxial layer with a strained interface due to the high lattice mismatch between the two crystalline structures. Complementary information is given by the core-level results presented below.

[8]The chamber was not initially baked in order not to affect the sample before the experiment with a "pre-low-temperature" treatment, and residual water can be expected inside the chamber.

HRCLS results

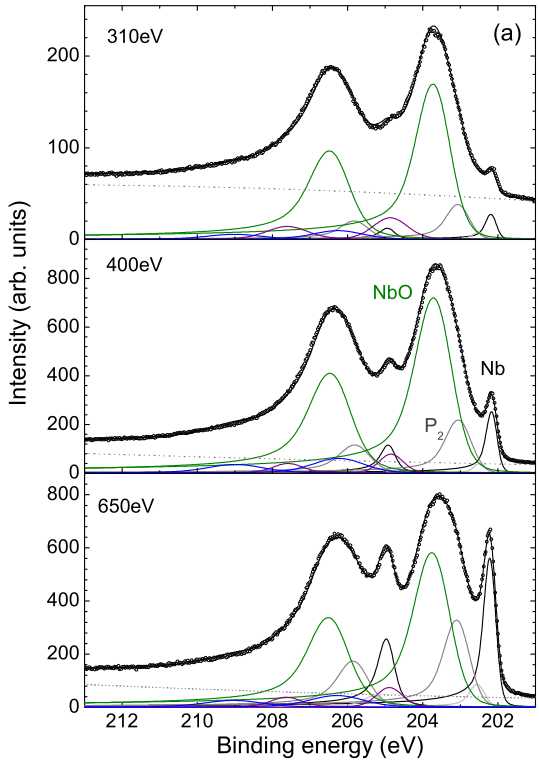

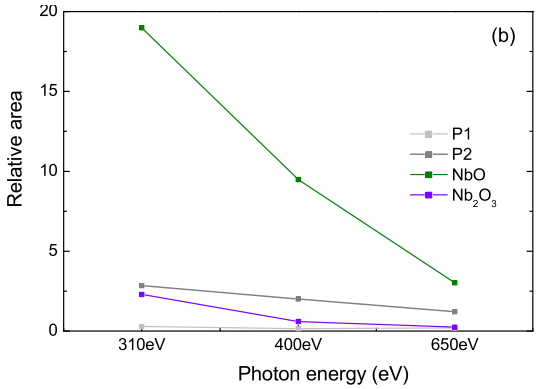

Figure 6.8: (a) Nb $3d_{3/2-5/2}$ spectra (open circles) measured after annealing at 300°C (30min.,UHV) as a function of the incident photon energy (normal emission angle) and fits (solid lines). (b) Relative area of the oxygen-induced components with respect to the bulk component as a function of the photon energy (see text for details).

The depth-dependence of the Nb $3d_{3/2-5/2}$ spectra measured after heating at 300°C (30min., UHV) is shown in Fig. 6.8 (a). The Nb_2O_5 component has completely disappeared (compare with Fig. 6.6), while only slight traces of NbO_2 are still apparent, in agreement with the XRR results. No LEED pattern could be observed (not shown), which is an indication of the disordered state of the surface. The main component, located 1.5 eV above the niobium bulk component, can be assigned to NbO (see Tab. 4.2), although its B.E. is smaller than observed at lower temperatures. Such a shift toward lower binding energy was already mentioned for thin NbO layers [16, 21, 109]. Moreover, the results obtained after heating at 800°C (see below), suggest to split the broad NbO in two components shifted by 1.4 and 1.9 eV with respect to the bulk component. The details of the spectra deconvolution including these two NbO components are given in Appendix A.

Fig. 6.9 (a) shows the spectra and decomposition of the Nb $3d$ core-level measured after annealing at 800°C (5min., UHV)[9] at various photon energies. We have already mentioned that the components shifted by 1.4 and 1.9 eV with respect to the niobium bulk component

[9]In contrast to the XRR measurements at high temperature, the HRCLS measurements were performed under UHV conditions and at fast heating rate.

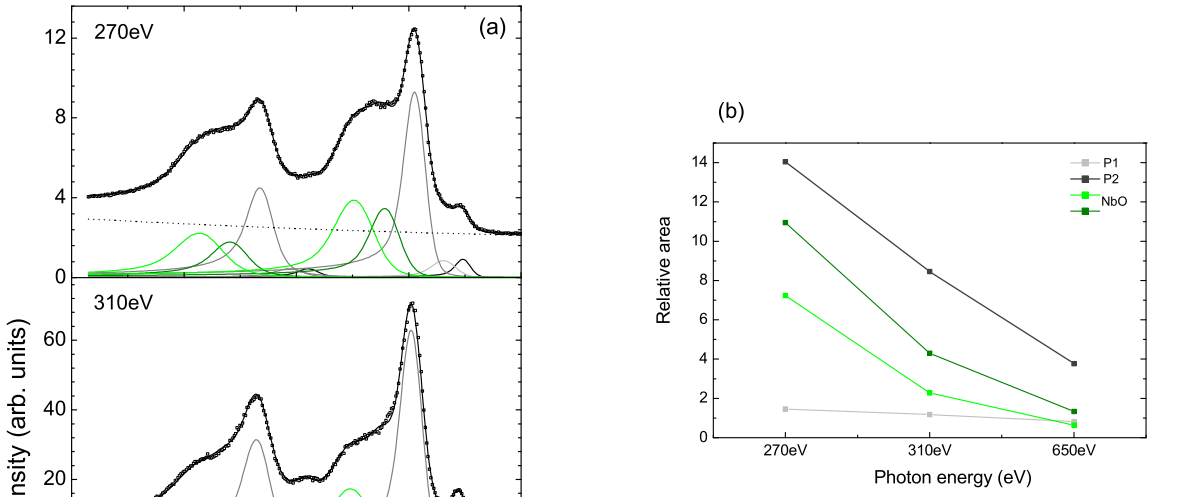

Figure 6.9: (a) Nb $3d_{3/2-5/2}$ spectra (open circles) measured after annealing at 800°C (5min.,UHV) as a function of the incident photon energy (normal emission angle) and fits (solid lines). (b) Relative area of the oxygen-induced components with respect with the bulk component as a function of the photon energy (see text for details).

(green), can be assigned to atoms in a NbO environment. Such a splitting between two components for a thin NbO oxide was already reported [192]. The two components of energy shifts 1.6 eV and 2.1 eV, were assigned to deviation in stoichiometry in the NbO layer, with $NbO_{1\pm\epsilon}$ and $\epsilon \sim 0.2$. The XRR results have shown that the growth of the NbO layer was accompanied by a huge increase of the surface roughness, which implies an enhanced surface area. Since the surface atoms experienced a potential different from the bulk because of a lower coordination number, their core-levels are expected to be shifted. The relative area of the different components with respect to the bulk component as a function of the energy is shown in Fig. 6.9 (b). The strongest decrease is observed for the 1.4 eV shifted NbO component, which is therefore located closer to the surface than the 1.9 eV NbO component. Lower binding energies for surface atoms have been reported for numerous systems[10]. The P_2 component appears below the NbO components and above P_1, which finally occurs at the metal/oxide interface.

[10]The surface state of pure niobium was reported to be shifted toward higher binding energy for the Nb(110) surface [101] and the Nb(001) surface [105].

The P_2 doublet appear to be the main component of the data presented in Fig. 6.9. Its B.E. is shifted by ~ 0.85 eV with respect to the bulk component. A small component at the same B.E. was already introduced in the decomposition of the native oxide spectra, and increased significantly in intensity starting from 300°C. Its magnitude with respect to the other components in Fig. 6.9 (a), indicates a well-defined chemical environment extending over several layers, rather than an interfacial contribution. We already mentioned that by extrapolation of the relationship between the valence of Nb oxide states and the corresponding chemical shifts (see Fig. 6.3), different authors assigned a chemical shift around 1±0.2 eV to the Nb_2O state [19–21, 90, 109]. Ma *et al.* [21] for example, referred to Nb_2O as the remaining species after 20h of vacuum annealing at 250°C of a Nb(100) single crystal initially grown in air. However, no information about the structure of this "phase" is usually given in these studies[11]. A XRD characterization of a so-called Nb_2O structure has been done [142]. The occurrence of a tetragonal phase directly related to the niobium *bcc* lattice was suggested, where oxygen atoms ordered themselves along preferential directions, namely occupying only the x and y interstices (see Fig. 3.8 and section 3.3.6). Other authors [71, 133, 141] refer to this phase as the NbO_x phase. We did not perform yet structural investigations to confirm (or not) the presence of this tetragonal phase. For further discussion see also section 6.5.

6.2.3 Partial summary and discussion

A consistent picture of the natural layered oxide and its dissolution upon heating is achieved thanks to the complementarity of the XRR and HRCLS results. The natural oxide observed on the Nb(110) surface is layered with the following sequence of oxides Nb_2O_5, NbO_2, NbO, from the surface to the metal/oxide interface. It reduces progressively with increasing temperatures, from Nb_2O_5 to NbO_2 at 145°C, and to NbO at 300°C and above, such that one can write

$$Nb_2O_5 \xrightarrow{LT} NbO_2 \xrightarrow{HT} NbO \tag{6.1}$$

where the transition between low temperatures LT and high temperatures LT occurs between 200 and 300°C. The thicknesses and roughnesses of the individual oxide layers obtained from the X-ray reflectivity analysis are summarized in Tab. 6.1. After heating at 145°C, the NbO layer stays unchanged while Nb_2O_5, which possess the lower heat of decomposition of the different niobium oxides (see Tab. 3.5), reduces into NbO_2. The

[11] As exception, the presence of Nb_2O while repeating annealing cycle on a Nb(100) surface at elevated temperatures (from 1700 to 2000°C) was observed simultaneously to (3×1) and (4×1) surface reconstructions in LEED [109]. In a separate work, these divers reconstructions were characterized as arrangement of NbO nanocrystals on Nb(100) [95].

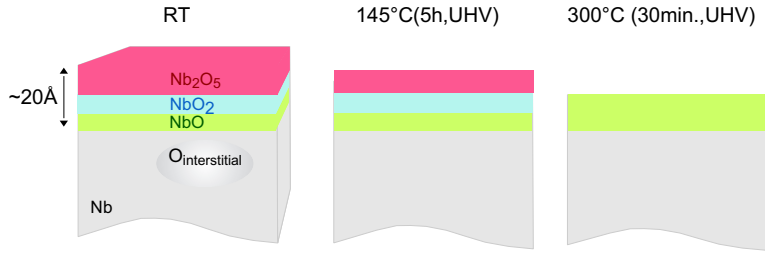

Figure 6.10: Schematic view of the natural layered oxide on Nb(110) single crystals oxidized in air at RT and its progressive dissolution upon vacuum annealing.

Oxide	RT	145 °C	300°C	700°C
Nb_2O_5	10.2 (3.4)	7.9 (3.7)	-	-
NbO_2	6.7 (2.2)	7.4 (2.2)	-	-
NbO	3.4 (0.7)	3.5 (1.1)	8.6 (3.6)	30 (12.5)
Substrate	- (3.7)	- (3.6)	- (3)	- (5.5)
Total thickness	20.3	18.8	8.6	30

Table 6.1: Thicknesses (roughnesses) in Å (error bar of ± 1 Å) of the different niobium oxides observed on Nb(110) surfaces oxidized 10h in air at RT for different thermal treatments. The results are obtained from the X-ray reflectivity analysis described in the text.

depth-resolved core-level measurements confirm a layering of the different oxide species identical to the natural oxide. These results indicate that the progressive reduction of the Nb_2O_5 layer toward NbO_2 occurs at its interface with the NbO_2 layer, in agreement with what is reported in [21], rather then as an homogeneous process inside the Nb_2O_5 layer [18].

Each step of the conversion 6.1 involves oxygen removal. The net amount of oxygen released during the oxide dissolution (and resp. uptake/growth at 670°C) can be calculated from the different oxide densities and the variation of their thickness. The atomic contents in niobium and oxygen atoms for the different niobium oxides are given in Tab. 3.2. The dissolution of the Nb_2O_5 layer at 145°C, from 10.2 Å to 7.9 Å, corresponds to a release of 1.19×10^{15} O at./cm^2 oxygen atoms per surface unit, while the NbO_2 uptake is equal to 3.97×10^{14} O at./cm^2. This gives a total oxygen release of

$$O_i^{release}(RT \rightarrow 145°C) = 8 \times 10^{14}\ O\ at./cm^2 \tag{6.2}$$

For comparison, 1 nm of niobium crystal containing interstitial oxygen atoms with an average concentration of 10 at.% corresponds to an amount of oxygen of 5×10^{14} O at./cm^2. The oxygen release due to the partial oxide reduction at 145°C can also be expressed as

$\sim$ 0.6 Nb(110) monolayer (ML) equivalents. After annealing at 300°C, Nb_2O_5 and NbO_2 are converted almost entirely to NbO, and the overall oxygen release is equal to $\sim$ 5 ML equivalents. Fig. 6.11 illustrates the total amount of niobium and oxygen atoms involved into the oxide layer, summing the contributions of the Nb_2O_5, NbO_2 and NbO layers, as a function of temperature. The release of oxygen increases strongly from 145°C to 300°C, as calculated above. These results are of first importance for the understanding of the interstitial oxygen profiles studied by means of depth-resolved diffuse scattering in chapter 7. The diffuse scattering measurements were realized during the same beamtime and therefore the same conditions than for the XRR results presented here, and thanks to these complementary results, a full picture of the near surface region of a Nb(110) surface oxidized in air will be achieved.

In two different works on polycrystalline materials, the kinetic parameters for the conversion 6.1 have been calculated [18, 193]. The NbO_2 to NbO transition was determined to be the rate-limiting step in the overall reduction [18]. One can calculate, using their parameters, the amount of oxygen produced during annealing at 145°C for 5h. Assuming a frequency factor A of $3 \times 10^9 s^{-1}$ [3] and an activation energy E_a of $135 kJ/mol$ [193], the oxygen release is given by $c(t,T) = c_0(1 - e^{k(T)t})$, where c_0 is the initial oxygen concentration in the oxide. The amount of oxygen obtained is one order of magnitude lower than what we observed. Note that the dissolution of the natural oxide layer depends strongly on the thermal treatment applied, but also the surface preparation, crystal orientation, etc.. Different oxidation conditions of the Nb(110) surface will be discussed in chapter 8.3, while the atmospheric oxide on the Nb(100) surface will be presented in chapter 8.1.

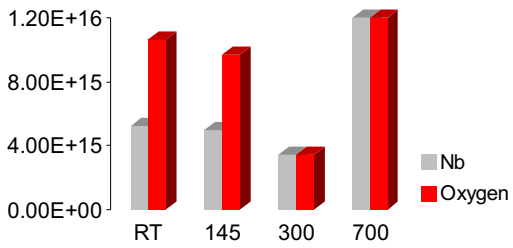

Figure 6.11: Total amounts of niobium and oxygen atoms involved into the oxide layer (including Nb_2O_5, NbO_2 and NbO layers) as a function of the thermal treatments applied (the values are calculated from the thicknesses obtained from the XRR analysis).

Both XRR and HRCLS measurements at higher temperatures (resp. 670°C, HV ; 800°C, UHV) are delicate to compare, because of the temperature difference, but also significant differences in the experimental conditions. Theoretical calculations [113] show that NbO has a very high potential barrier for the incorporation of further oxygen and therefore prevent further ion transport from the surface to the interface or vice versa. The growth of the oxide layer after heating at 670°C in a degraded vacuum would, following

this argument, rather be associated to oxygen segregation from the bulk, than by oxygen incorporation at the surface. In this hypothesis, the NbO growth is limited by kinetics. The total O1s peak area for the core-levels measurements (not shown) shows no significant change between 300°C and 800°C, indicating that the transformation that occurs in the surface region do not release or uptake oxygen into/from the bulk. At both temperature the presence of an intermediate phase between the niobium bulk and NbO is observed and assigned in a first attempt to Nb_2O. For further discussion see also section 6.5.

The niobium monoxide already observed in the natural oxide, was the only remaining oxide component on the Nb(110) surface for temperatures $\geq$ 300°C. In the next section, the XRR and HRCLS results are confirmed by mean of complementary grazing incidence X-ray diffraction measurements, suitable for the characterization of the NbO crystalline structure.

6.3 NbO(111) epitaxial layer on Nb(110)

In the previous sections, we have observed by means of X-ray reflectivity and core-level measurements, the existence of niobium monoxide at the metal/oxide interface, already for the natural oxide. Simultaneously to the reduction of the oxide layer upon heating, NbO was observed to grow, and remained the unique oxide species at the surface for temperatures higher than 300°C. In this section, we investigate its crystalline structure, as well as its epitaxial relationships with respect with the underlying substrate by means of grazing incidence X-ray diffraction (GIXD). GIXD measurements are highly sensitive to the in-plane and out-of-plane structure at the surface and few nanometers below, offering complementary information to the X-ray reflectivity and core-levels results discussed before.

6.3.1 In-plane structure

The grazing incidence X-ray scattering intensity measured over the first Brillouin zones of the Nb(110) surface annealed at 350°C (2h,UHV) after dry oxidation at RT (see Sec. 8.2) is

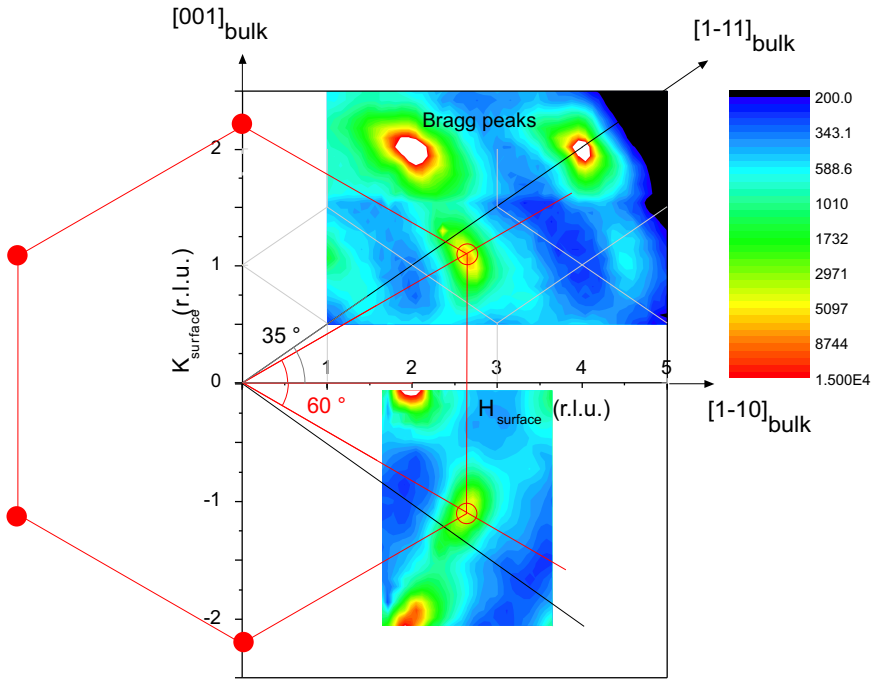

Figure 6.12: Grazing incidence *in-plane* X-ray scattering intensity for the Nb(110) surface measured after annealing at 350°C (2h,UHV) (scattering depth $\sim$ 6nm). Besides the high intensity niobium Bragg reflections (220), (420), (200) and (2$\bar{2}$0) (in surface units), a six-fold symmetry signal corresponding to the (2$\bar{2}$0)-type reflections of an epitaxial NbO(111)/Nb(110) layer is observed (see text for details).

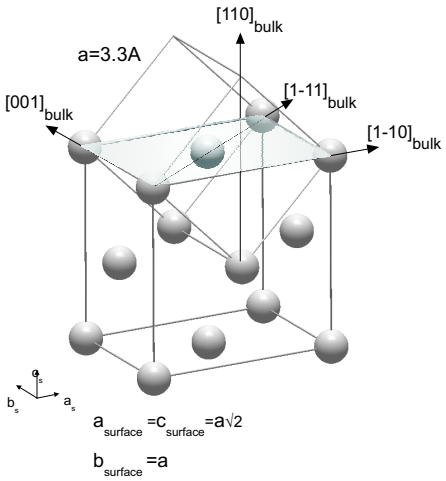

Figure 6.13: Structural unit cell of the Nb(110) surface. The bulk *bcc* unit cell is shown for indication.

shown in Fig. 6.12. The measurements were performed at ESRF, on ID32 (beamtime E1). The incident and exit angles were respectively fixed at 0.2 and 0.6°, which corresponds to a scattering depth of $\sim$ 6nm. The H_{surface} and K_{surface} indexes describe the in-plane momentum transfer expressed in reciprocal lattice units (r.l.u.) in the Nb(110) surface coordinates, as depicted in Fig. 6.13. $H_{\text{surface}} = 1$ corresponds to the reciprocal lattice unit $|\vec{a}^*| = 2\pi/(a\sqrt{2})$ Å^{-1}, and $K_{\text{surface}} = 1$ to $|\vec{c}^*| = 2\pi/a$ Å^{-1}, with $a = 3.3$ Å lattice parameter of the *bcc* unit cell.

In Fig. 6.12, the niobium Bragg reflections (220), (420), (200) and $(2\bar{2}0)$ (in surface units) are visible. In addition, reflections rotated by 60° with an in-plane scattering vector $Q = 4.13$ Å^{-1}, corresponding to a d-spacing of 1.52 Å, are observed. This is compatible with the six-fold symmetry of the NbO(111) planes, where the nearest-neighbor distance is equal to 2.98 Å, see figures 6.13 and 6.21. The two reflections observed in Fig. 6.12 can therefore be attributed to the $(0\bar{2}2)$ and $(20\bar{2})$ reflections of NbO(111)[12] with the in-plane directional relationship Nb[001]||NbO[$1\bar{1}0$], as depicted in Fig.6.14.

For fcc-(111)/bcc-(110) interfaces, we have discussed in section 3.4 that, depending on the geometrical relationship given by the ratio $r = d_{fcc}/d_{bcc}$ of the nearest neighbor distances, the Nishiyama-Wassermann (NW) or Kurdjumov-Sachs (KS) orientations are predicted from rigid-lattice theory, and experimentally observed for many metal-on-metal systems. The directional orientation relationship between the oxide layer and the underlying substrate observed here corresponds to the Nishiyama-Wassermann orientation (see Fig. 3.10).

[12]The mixed *hkl* reflections, such as the $(1\bar{1}0)$, are forbidden for the rock salt structure, while extremely weak for the NbO defective structure. This has its importance, as we will see in the next chapter, to be able to distinguish the NbO reflections from the diffuse scattering induced by the interstitial oxygen atoms dissolved into niobium (see chapter 7).

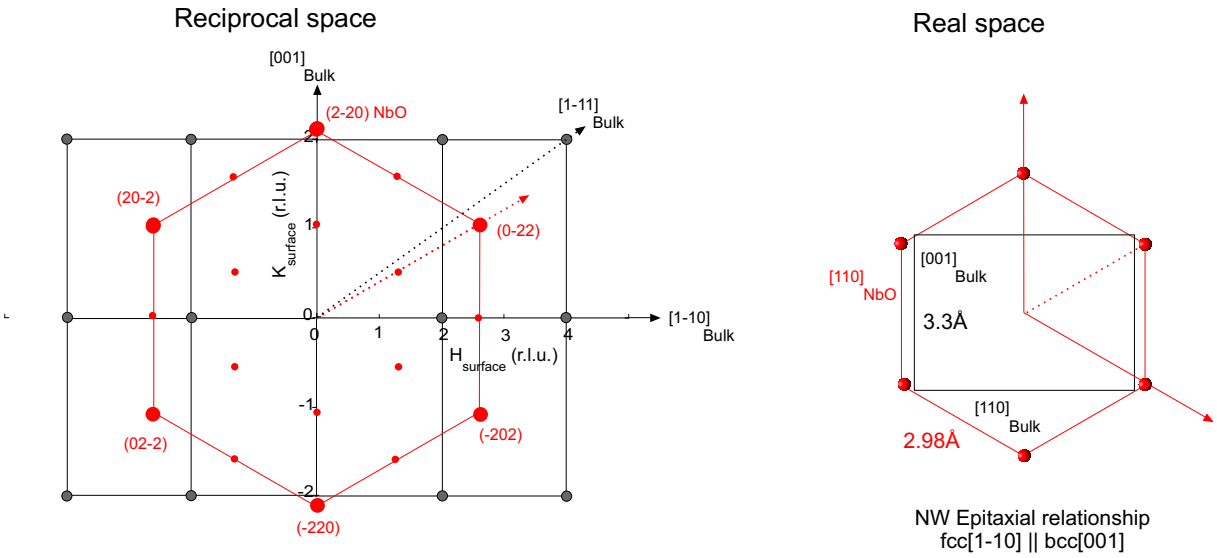

Figure 6.14: In-plane view of the reciprocal and real space of the NbO(111)/Nb(110) interface. The epitaxial orientation relationship at the NbO(111)/Nb(110) interface is determined to be the Nishiyama-Wassermann orientation.

For NbO(111) on Nb(110), the parameter $r = 1.042$ is smaller than the ideal value r_{KS} of 1.0887, but still very different from the optimal values of the NW orientation of 0.9428. A KS orientation would therefore be predicted by the rigid-lattice theory. The NbO/Nb lattice mismatch along their common directions equals 10% for the NW orientation relationship[13], which is relatively high compared to a lattice mismatch of 4% for the KS orientation. A side to side arrangement of NbO(111) nanocrystals with a KS-type epitaxial relationship was reported on Nb(110) single crystals [112], in agreement with the aforementioned prediction. The NW orientation, however, has also been reported in various studies: for NbO(111) on Nb(110) thin films oxidized in dry oxygen atmosphere ($\sim$ 300°C) [116], and on Nb(110) single crystals annealed at high temperatures [69]. As emphasized in [69], the simple rigid-lattice model takes into account only geometrical parameters, neglecting for example the influence on the interfacial energy of the metal-oxide bonding at the interface (and the strong directional bonding between Nb and O). The coexistence of the KS and NW orientation relationships, or transitions in between them depending on film thickness or the growth temperature has been investigated in other fcc(111)/bcc(110) systems [151][14]. Similar transitions have been observed at higher temperatures in this work, as it will be discussed below.

Meshscans measured around the region of interest for the Nb(110) surface oxidized in

[13] NbO[001] (3.3Å) and Nb[1-10] (2.98Å)

[14] The KS orientation is generally preferred at the interface because of the smaller lattice mismatch, resulting in a lower density of interfacial defects and therefore in a lower interfacial energy. In this case, the transition to the NW orientation occurs above a critical thickness where the volume energy is minimized.

air (ANKA beamtime A4), for the different treatments discussed in the previous sections, are shown in Fig. 6.15. The incident and exit angles were respectively fixed at 0.25 and 1°, which corresponds to a scattering depth of ∼ 5nm. The theoretical calculation of the oxygen-induced diffuse scattering discussed in details in the next chapter 7, is shown for indication[15]. The corresponding diffracted intensity measured as a function of the in-plane rotation angle θ for a fixed scattering vector on the $(0\bar{2}2)$ reflection is shown in

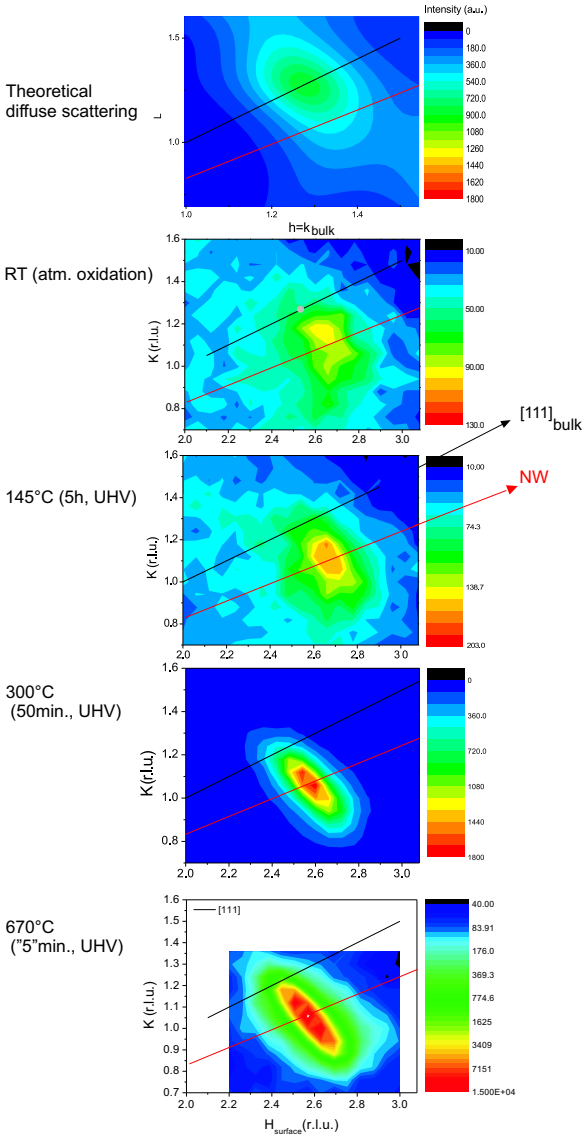

Figure 6.15: *In-plane* meshscans around the NbO $(0\bar{2}2)$ reflection as a function of the temperature for the Nb(110) surface initially oxidized in air (ANKA beamtime A4). The theoretical calculation of the diffuse scattering induced by interstitial oxygens dissolved into the niobium lattice (see chapter 7) is shown for comparison.

[15]The theoretical calculations were performed by R. P. Kurta [164] (section 4.2)

Fig. 6.16 for different temperatures. In all scans the sixfold symmetry of the NbO(111) planes is observed. At low temperature, the NbO $(0\bar{2}2)$ reflection occurs at a position slightly shifted to a smaller angle than the 5.26° expected between the in-plane Nb$[1\bar{1}1]$ and NbO$[1\bar{1}0]$ directions for the NW orientation, indication of a distorted epitaxial oxide. After heating at higher temperatures, the peak moves progressively toward the angle of the NW position, simultaneously to an increase of the $d-$spacing (shift of the maxima toward lower Q values). One knows from the XRR results, and will discuss in the next part of this section, that heating to 670°C induced the growth of the NbO layer. A highly strained interface is expected from the strong mismatch of the NW orientation relationship, which can distort the thin oxide film and explain the progressive shift of the NbO$(0\bar{2}2)$ reflection. One has also to keep in mind the presence of a high concentration of interstitial oxygens at the metal/oxide interface (see chapter 7 and section 6.2.2), strongly correlated to the strain into the niobium lattice and thereby to the epitaxial constraints. Referring to the width of the NbO peaks, the high mismatch yields to small but epitaxially oriented in-plane domains. It is interesting to note that the NbO $(0\bar{2}2)$ reflection occurs in the direct vicinity of the oxygen-induced diffuse X-ray scattering intensity expected at the $\mathbf{Q}^*_{bcc}=\frac{2}{3}(1,1,1)$ (Fig. 6.15 (top)), and is shifted toward it in the initial state of the natural oxide.

The NW orientation has been systematically observed in our measurements for Nb(110) surfaces oxidized under dry oxygen atmosphere or ambient conditions. In the following, two additional set of data are presented.

The first set of data are meshscans measured at ANKA (beamtime A1) on the Nb(110)

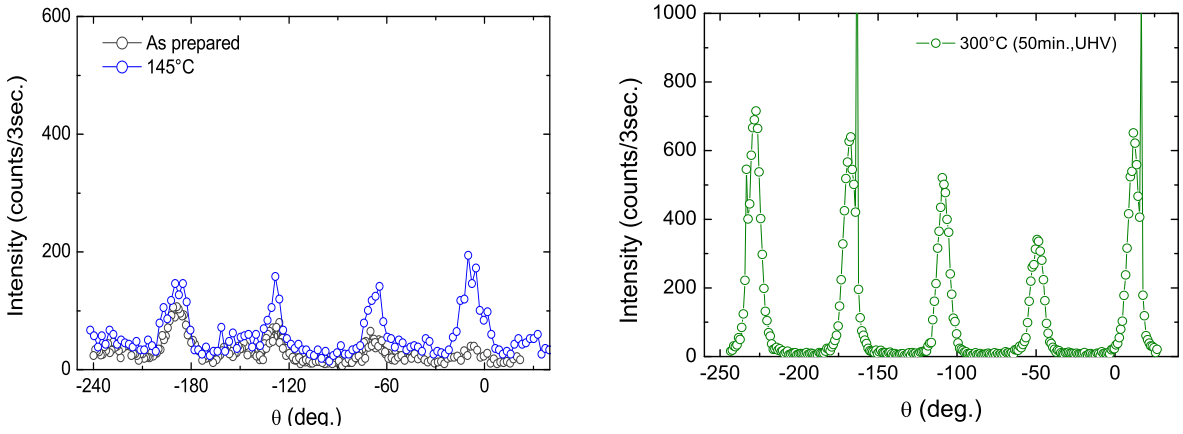

Figure 6.16: Diffracted intensity as a function of the in-plane rotation angle θ for different thermal treatments applied on the Nb(110) initially oxidized in air. The scattering vector is fixed on the NbO$(0\bar{2}2)$ reflection. In all scans the sixfold symmetry of the NbO(111) planes is observed.

surface oxidized in air (6h, RT) as a function of thermal treatments[16], shown in Fig. 6.17. A similar evolution of the peak position is observed for the two first temperatures as described before. For the last thermal treatment (Fig. 6.17 (c)), measured after heating at slightly higher temperature, a shift toward higher Q value is observed, corresponding to a smaller d-spacing and indicating the occurrence of a relaxation process.

In Fig. 6.18, in-plane rocking scans measured on the NbO($2\bar{2}0$) reflection for different high temperature annealings and dry $in-situ$ oxidation applied on the Nb(110) surface initially oxidized 3h in air are presented (beamtime E1, see also section 8.2.1). After heating at 1800°C, the characteristic pattern of the Kurdjumov-Sachs orientation relationship, presenting two domains rotated by $\pm$ 5.26° with respect with the [100] direction of the

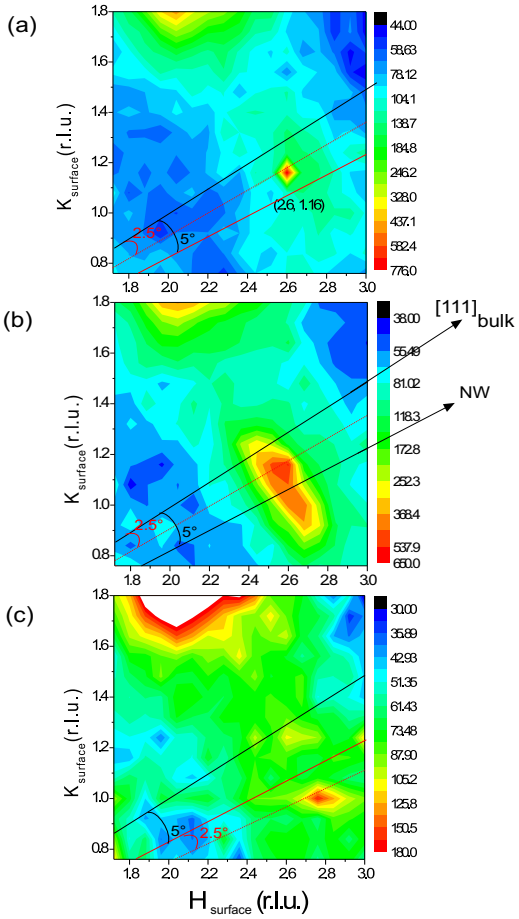

Figure 6.17: *In-plane* meshscans around the NbO ($0\bar{2}2$) reflection as a function of the temperature for the Nb(110) surface initially oxidized in air (ANKA beamtime A1). (a) After heating at 200°C (1h). (b) After heating at 300°C (30min.). (c) After in-situ dry oxidation at 200°C and subsequent heating at 300°C and 700°C (5min.) (see text for details).

[16]The complete sequence of treatments was the following : RT, 200°C (1h,UHV), 300°C (30min., UHV), *in-situ*dry oxygen oxidation at 200°C, 300°C and 700°C (5min.,UHV)

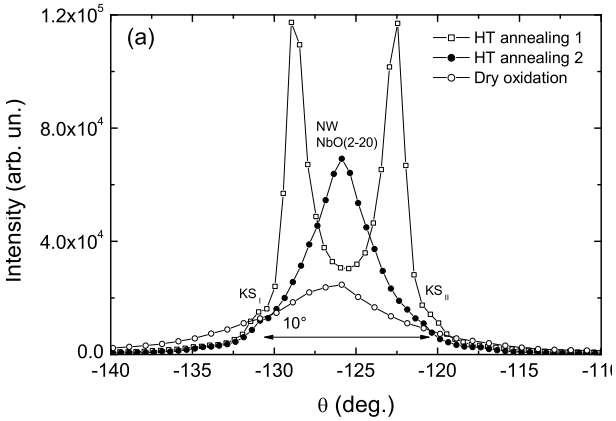

Figure 6.18: In-plane NbO($2\bar{2}0$) rocking scans measured on Nb(110) initially oxidized in air for subsequent high temperature annealings (H1 1800°C), (H2 2000°C), and in-situ RT dry oxidation. A progressive transition between the KS and NW epitaxial orientation relationships is observed.

substrate, was identified. The simultaneous presence of the two KS peaks splitted by 10° (low intensity shoulders), and by an angle inferior to 10° (main component), indicates that a transition between the KS and NW orientations is occurring. The subsequent vacuum annealing at 2000°C presents, as main component, the NW orientation. Small shoulders indicative of traces of the KS orientation are still visible. The decomposition of the lineshape observed after in-situ dry oxidation is shown in Fig. 6.19. The NbO($2\bar{2}0$) peak is fitted with three reflections that allow to identify the coexistence of the NW and KS. The in-plane view of the reciprocal space of the Nb(110)/NbO(111) interface for both NW and KS orientation relationships is shown in Fig. 6.19.

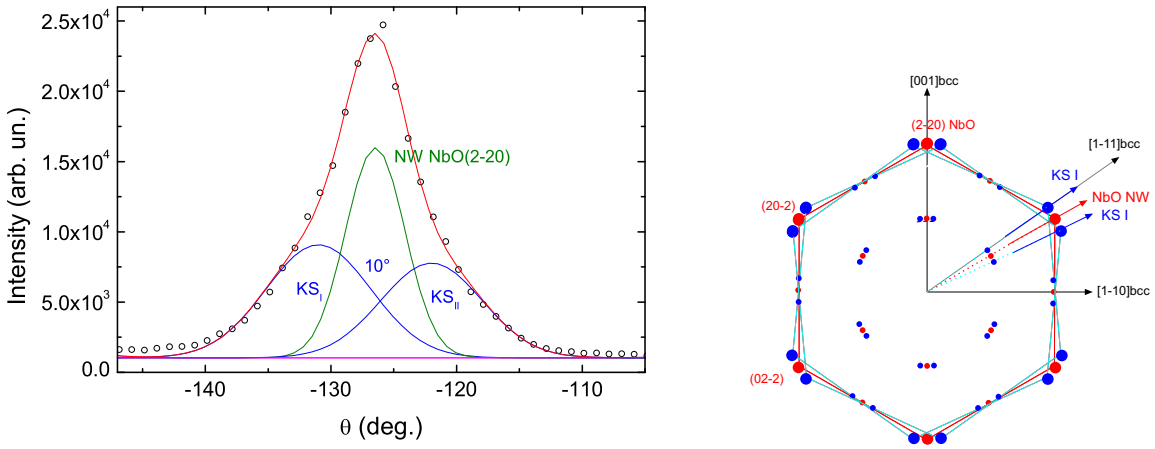

Figure 6.19: Left : In-plane NbO($2\bar{2}0$) rocking scan measured after *in-situ* dry RT oxidation. Right: In-plane view of the reciprocal space of the Nb(110)/NbO(111) interface for both NW and KS orientation relationships.

6.3.2 Out of plane structure

The measurements discussed in the previous section considered only the in-plane structure of the oxide layer with respect to the substrate. In complement to them, out-of-plane measurements have been performed in order to characterize the oxide structure normal to the surface. The out-of-plane reflections arising from the thin oxide layer are schematically shown with respect to the underlying substrate lattice in Fig. 6.20 (a) (only some given directions are plotted). The out-of-plane coordinate L_{NbO} defines the momentum transfer

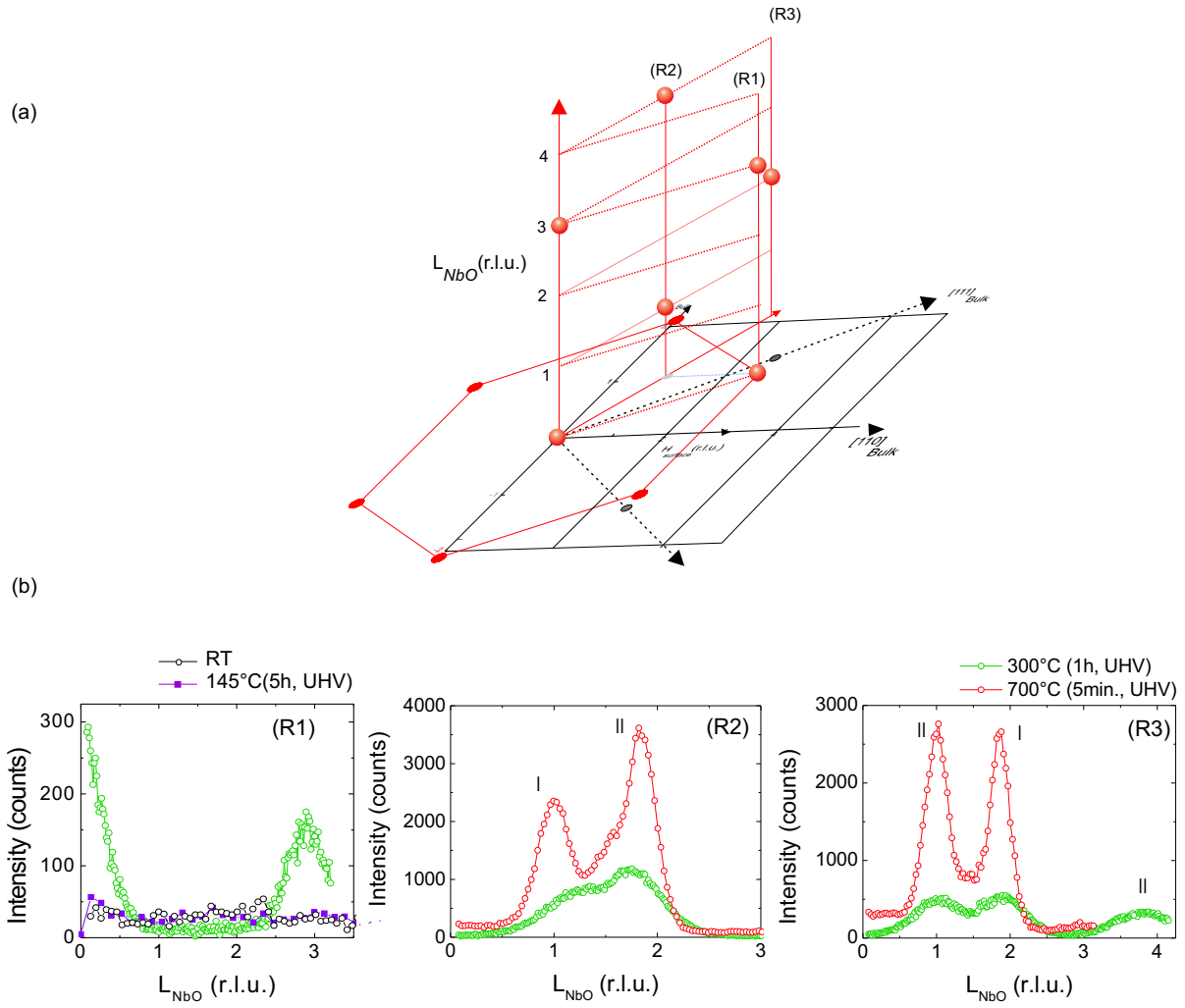

Figure 6.20: (a) Out-of-plane view of the NbO(111) reciprocal lattice (red) (only some given directions are plotted) with respect to the in-plane reciprocal lattice of Nb(110). (b) L-scans along the three NbO reciprocal directions (R1), (R2) and (R3) normal to the surface, as a function of the temperature.

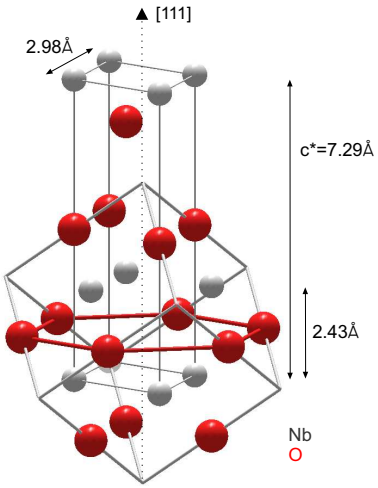

Figure 6.21: NbO(111) plane in both bulk defective rock salt and new surface unit cells.

normal to the surface Q_z in the NbO(111) surface coordinates, as described in Fig. 6.21. $L_{NbO} = 1$ corresponds to the reciprocal lattice unit $|\vec{c}^*_{\mathrm{NbO}}| = 2\pi/c_{\mathrm{NbO}} = 0.86$ Å^{-1}, where $c_{\mathrm{NbO}} = 4.21\ \sqrt{3}$Å$= 7.29$ Å.

In Fig. 6.20 (b), out-of-plane scans measured along three different NbO reciprocal lattice directions normal to the surface are shown. The data have been recorded in the niobium surface coordinates and plotted in Fig. 6.20 and 6.23 in the bulk NbO coordinates. The corresponding rods are illustrated schematically in Fig. 6.20 (a). The data were measured subsequently to the reflectivity measurements discussed in section 6.2 (beamtime A4). The corresponding in-plane meshscans were presented in Fig. 6.15. Along the direction (R1), data are plotted for the atmospheric oxidation of the Nb(110) surface, after heating at 145°C (5h,UHV) and at 300°C (50min.,UHV). It has been shown in the previous section, that the in-plane six-fold symmetry of the thin NbO(111) layer was already visible after

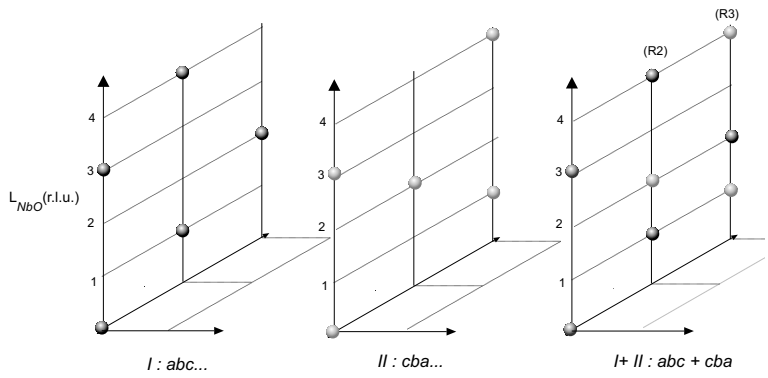

Figure 6.22: Out-of-plane reciprocal NbO lattice. The presence of both reflections in one scan (for example along (R2) or (R3)) is a typical sign for twin formation where domains with abcabc and inverted cbacba stacking sequences laterally coexist.

atmospheric oxidation and after annealing at 145°C (see Fig. 6.16). From the reflectivity analysis, however, one knows that this layer is not thicker than a unit cell.

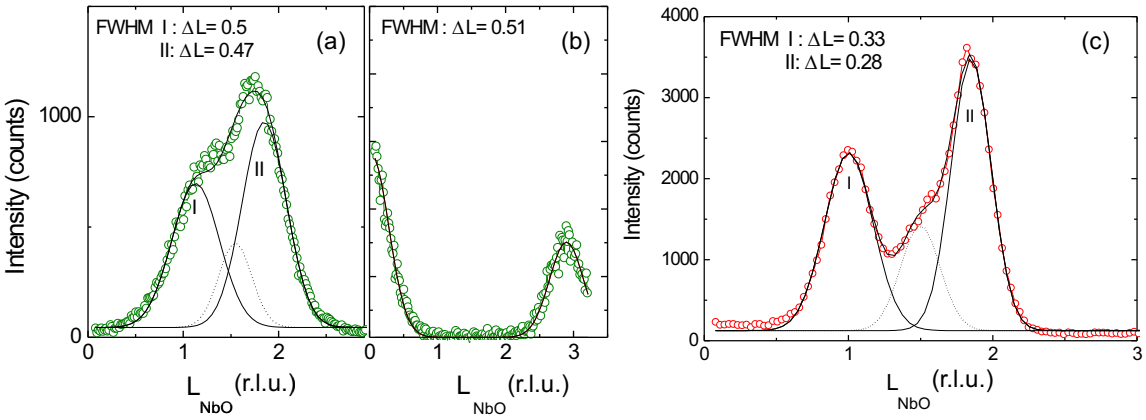

Figure 6.23: (a,b) L-scans measured after heating at 300°C along (R2) and (R1), respectively. (c) L-scan measured along (R2) after heating at 670°C.

Data measured along the (R_2) and (R_3) directions after heating the sample at 300°C (50min.,UHV) and at 670°C (5min.,HV) are presented in Fig. 6.20 (b). In both (R2) and (R3) scans NbO reflections at $L_{\mathrm{NbO}} = 1$ and $L_{\mathrm{NbO}=2}$ are observed, although from the bulk structure factor only the reflections at $L_{\mathrm{NbO}=1}$ should be observed along (R2) and $L_{\mathrm{NbO}=2}$ along (R3), as described in Fig. 6.22. The bulk structure of NbO in the [111] direction consists of alternating niobium and oxygen layers respectively in an hexagonal fcc-like stacking sequence *abcabc*..., see Fig. 6.28. The fcc reciprocal lattice can not be transformed into itself by a rotation of 180° around the [111] axis. This plane is therefore sensitive to the layer stacking and stacking faults in the subsequent layers. The presence of both reflections in one scan is a typical sign for twin formation, where domains with *abcabc*... and inverted *cbacba*... stacking sequences laterally coexist. The reflections assigned I can be attributed to *abcabc*... stacked domains and II corresponds to the *cbacba*... stacked domains.

The decompositions of the scans measured along (R2) and (R1) after heating at 300°C

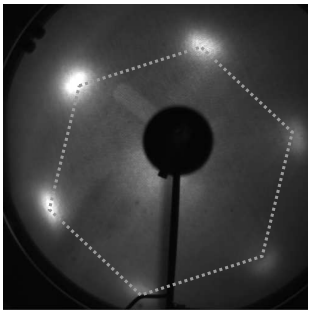

Figure 6.24: LEED pattern taken on the Nb(110) surface after annealing at 800°C for 5min. The six-fold symmetry of an NbO(111) epitaxial layer is visible.

are presented in Fig. 6.23 (a,b). The fit of the data recorded after heating at 670°C is given in Fig. 6.23 (c). Note that, as mentioned above, the data are plotted in the bulk NbO coordinates. An expansion of the lattice parameter of the thin oxide layer with respect to the NbO bulk value would then give rise to a shift toward lower reciprocal values as observed for the peaks in Fig. 6.23 (b). In addition to the two domains peaks I and II, the rod intercepts the tail of the Nb(111) reflection, which gives rise to a contribution around $L_{NbO} = 1.5$. The full width at half maximum (FWHM) of the reflections, ΔL ∼0.5 and ∼0.3 in relative units, correspond to a stacking correlation length D of 14.6 Å and 22-26 Å in real space, using the rough estimate $\Delta L = 2\pi/D$. Those value are comparable with the total film thickness of ∼10 Åand 30 Å obtained in the previous section by means of XRR measurements[17].

The similarities between the NbO and NbC structures, already mentioned in section 3.2, make it difficult to distinguish them. However, the content in carbon impurities reported in niobium is usually much lower than the oxygen, known as the main niobium impurity. The solubility of C in Nb extremely low is comparison with O [79]. Taking into account the repeated purification cycles applied on the samples as described section 5.4, the only carbon contamination of the samples originates from their immersion in air. In addition, at low temperatures, the Nb_2O_5 acts as a diffusion barrier preventing the carbide formation. A small content of NbC of maximum 1ML was reported on niobium polycrystalline samples oxidized 43h in air [19].

As already mentioned, LEED patterns recorded after annealing the sample at 300°C do not show any ordered feature at the surface indicative of a disordered state of the surface. After heating at 800°C, the six-fold symmetry of the NbO(111) epitaxial layer is visible, see Fig. 6.24.

6.4 Oxide/metal interfacial structure

So far, we have discussed the structural details of the thin NbO oxide layer. In this section, the structure of the oxide/metal interface is briefly investigated by means of crystal truncation rods (CTR) measurements (see section 4). In Fig. 6.25, three L-scans along the niobium (20L), (11L) and (02L) CTRs for the Nb(110) surface oxidized in air (6 and 10h, RT) are presented. The reflections are indexed within the Nb(110) surface coordinates[18]. The data were recorded close to the critical angle in order to maximize the signal. The

[17]Note that the XRR data measured after 670°C and presented in Sec. 6.7, can be fitted as well with a two layer model, including a NbO layer of 24 Å and a second layer of intermediate density between NbO and Nb, referring to the Nb_2O phase mentioned in the core-level results (not shown).

[18]See Fig. 6.13 and Sec. 6.3

determination of the interfacial structure at the atomic level can be achieved by fitting a calculated structure factor to the experimental data. This work is currently under progress. Qualitative results, however, can already bring interesting information about the interfacial behavior upon heating.

The interesting observation to make is that for low-temperatures treatments, namely until $< 200°C$ the rods do not present major changes. This corresponds, as seen in section 6.2, to a range of temperatures where only slight rearrangement mainly between the Nb_2O_5 and NbO_2 oxides occur, while the NbO layer, located at the interface with the underlying substrate stays unchanged (see also section 6.3). This is consistent with a constant interfacial structure. At 300°C though, the oxide layer was observed to reduce fully into a NbO layer. Simultaneously, the rods features change drastically. An interference pattern is observed corresponding to a reciprocal distance of $\Delta L = 0.5$ in relative units. In the same range of temperatures, the HRCLS results revealed the occurrence of a intermediate layer, tentatively attributed to Nb_2O phase, accompanied by an interstitial oxygen ordering. Further analysis of the data should resolve the atomistic origin of the (11L) interference patterns, and the full structural changes at the interface.

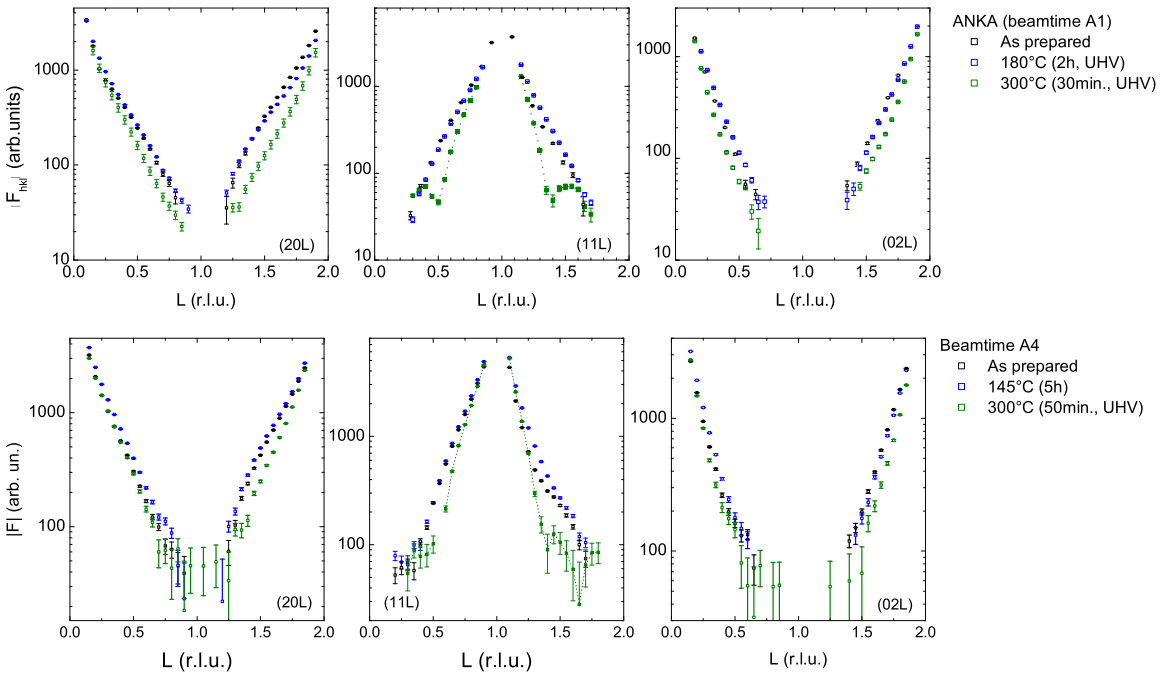

Figure 6.25: Crystal truncation rod scans along the (20L), (11L) and (02L) Nb(110) rods (in reciprocal lattice units of the Nb(110) surface unit cell). Top : after room temperature oxidation during 6h in air, after heating at ∼180°C (2h,UHV) and at 300°C (30min.,UHV). Bottom : after room temperature oxidation during 10h in air, after heating at ∼145°C (5h,UHV) and at 300°C (30min.,UHV).

6.5 From interstitial oxygen to NbO : mechanisms

Niobium monoxide was reported by different authors as the first oxidation step on clean niobium surface exposed to oxygen atmosphere, under dry or atmospheric conditions (see section 3.3.2). In addition, oxygen-induced quasiperiodic structures identified as NbO or NbO precursor have been observed in various works after vacuum annealing at elevated temperatures and attributed to interstitial oxygen segregation to the surface. The role of interstitial oxygen in the oxide formation, often pointed out, is discussed here. In this section, a possible path for the transformation occurring at a critical oxygen concentration from the interstitial oxygen to the NbO oxide is proposed, where the monoxide forms on the base of the distorted niobium environment induced by the interstitial oxygen atoms in the niobium lattice.

As already mentioned, niobium exhibits an intrinsic instability in the [111] direction toward the ω-phase, manifested in the deep minimum of the phonon dispersion curve at $\mathbf{Q}^*_\omega = \frac{2}{3}(1,1,1)(2\pi/a_{bcc})$. The strong oxygen-induced local distortions in niobium couple to this anisotropic softness of the lattice, such that *single* oxygen impurities in niobium are nuclei for the local formation of trigonal ω-phase embryo, embedded into the natural *bcc* lattice [22] (see section 3.2). Fig. 6.26 represents the Nb(110) *bcc* lattice, with both bulk *bcc* and (110) surface unit cells. A series of $(1\bar{1}1)$ planes, normal to the surface are shown (green). The strong local distortions induced by an isolated oxygen atom located on octahedral site, are schematically represented by the Kanzaki forces (arrows), as discussed in section 3.2. The ω phase, as we already described, is obtained by collapsing one pair of (111) planes of the *bcc* lattice to their intermediate position, leaving the next plane unaltered, collapsing the next pair, and so on, as illustrated in Fig. 6.26. For oxygen in niobium the rumpled trigonal ω phase, corresponding to a partial collapse of the planes is observed [22].

Different core-level spectroscopy studies report the existence of the Nb_2O phase from extrapolation of the relationship between the valence of niobium oxide states and the corresponding chemical shift. Nb_2O is reported after prolongated annealing at low temperatures or, as we observed in this chapter, after annealing at elevated temperature (in our case at 300°C and 800°C). However, few information are available in literature about the structure of this "phase". One work from Brauer and Müller [134] has characterized what they called the Nb_2O structure by XRD, suggesting the occurrence of a tetragonal phase directly related to the niobium *bcc* lattice, where oxygen atoms order themselves along preferential directions, namely occupying only the x and y interstices. This structure is illustrated in Fig. 3.8. The presence of the Nb_2O phase, between the niobium bulk and NbO, suggests

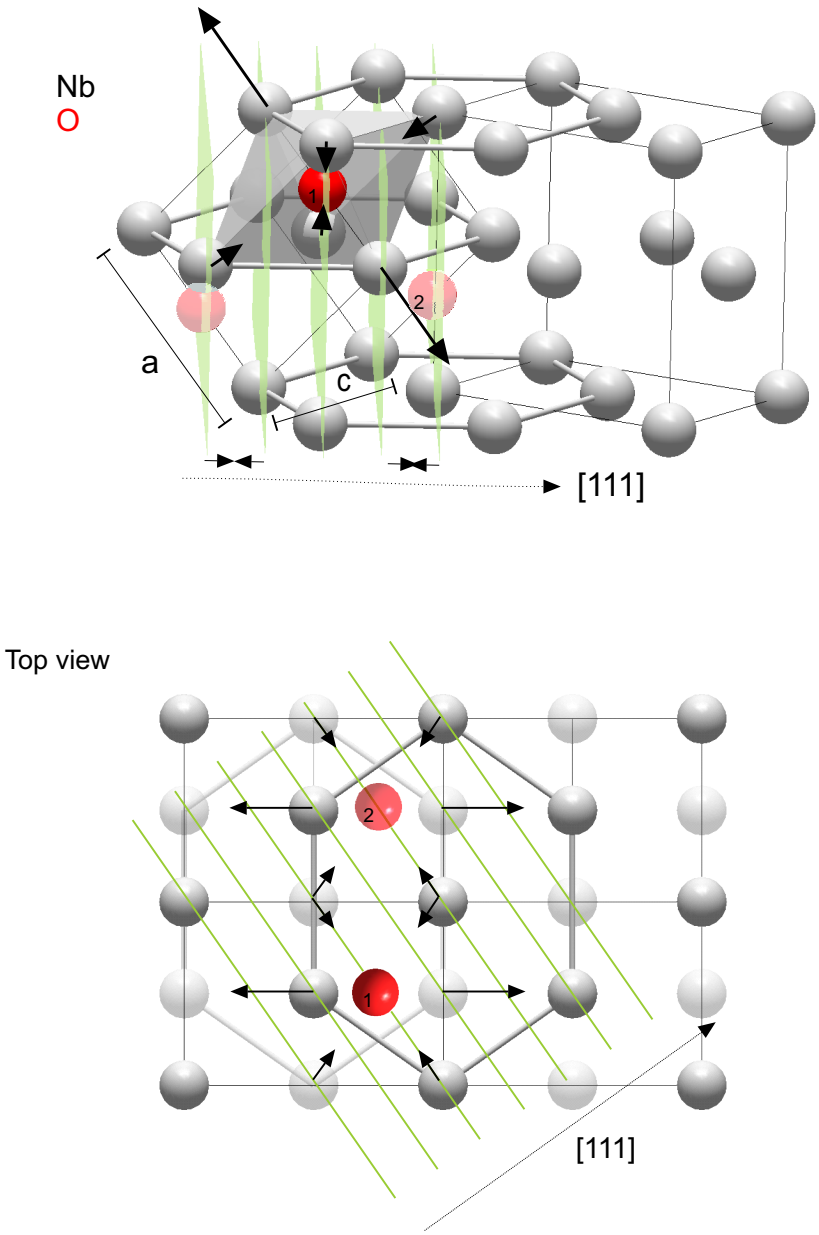

Figure 6.26: Top: Nb(110) surface unit cell and for indication *bcc* niobium unit cell. Lattice distortions in the local neighborhood of an interstitial oxygen located on an octahedral site (red) and Kanzaki forces f_i around it. The oxygen-induced displacements of the $(1\bar{1}1)_{bcc}$ planes (green) along the $[1\bar{1}1]$ direction corresponding to the ω-phase nucleation are indicated. Shaded red atoms : oxygen atoms on x, y octahedral sites suggested for the Nb_2O structure [134] (see text for details). Bottom : Top view of the two first atomic planes of the Nb(110) surface (snd plane in shadow) and the $(111)_{bcc}$ planes (green). The strong local distortions of the niobium lattice around interstitial oxygen atoms are indicated for two oxygen atoms 1 and 2. The relative displacement of two on three $[1\bar{1}1]$ planes along this direction are indicated.

an intermediate state in the oxidation process. In Fig. 6.26, faded oxygen atoms indicate the possible arrangement of one Nb_2O unit cell, with one third of the $x-y$ interstices occupied, as found in the structure of Brauer. Assuming similar distortions as for random defects, a top view of the lattice distortions induced by two oxygen atoms (labeled 1 and 2) located in two subsequent layers is shown in Fig. 6.26 (bottom). The in-plane distortions around the oxygen atoms involve a transformation toward an hexagonal symmetry and similar displacements to those needed to distort the *bcc* niobium lattice into the fcc NbO structure. The epitaxial orientation relationship of NbO with respect with the underlying Nb(110) substrate has been determined in section 6.3 as Nb(110)[001]||NbO(111)[1$\bar{1}$0] for different thermal treatments after atmospheric oxidation. The top view of two subsequent Nb(110) and NbO(111) planes are compared in Fig. 6.27. The displacements of the niobium atoms required to go from one structure to the other one are indicated. This includes lateral enlargement from 4.667 Å to 5.16 Å and an increase in the top and bottom angles from 110° to 120°. The corresponding in-plane displacements along [1$\bar{1}$0] are $\mathbf{u}_1^n \sim 0.56$ Å and $\mathbf{u}_2^n \sim 0.3$ Å. For comparison, the displacements of bulk niobium atoms in the local neighborhood of an oxygen impurity associated to the nucleation of the ω-phase, are given in Tab. 3.1. The projection of $\mathbf{u}_1$ and $\mathbf{u}_2$ in the (110) plane and perpendicular to it are equal to 0.297 Å and 0.09 Å respectively.

The $ABAB\ldots$ stacking sequence observed in Nb(110) bcc and the $ABCABC\ldots$ fcc stacking observed in NbO are presented in Fig. 6.28. Only the niobium atoms are presented for the NbO structure, for clarity reasons. The $d-$spacings between subsequent

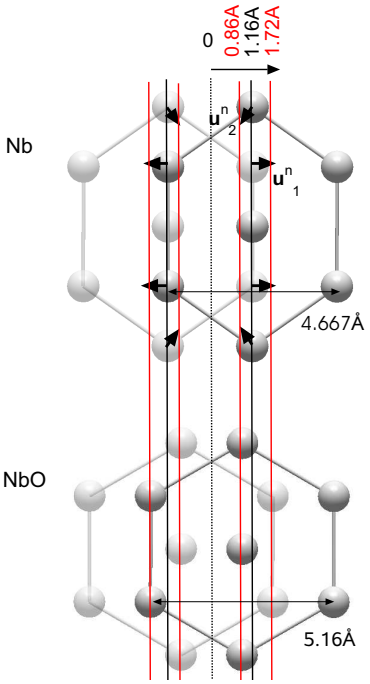

Figure 6.27: Top view of in-plane oxygen-induced deformation from the Nb *bcc* to the NbO hexagonal lattice. The required atomic displacements are indicated by arrows.

niobium planes in the direction normal to the surface are rather similar for Nb(110) and NbO(111), with 2.33 Å and 2.43 Å respectively. The transition between both stacking can be understood as following. Let's assume that two subsequent planes, in blue and red in 6.28 stay unmoved, besides the hexagonal in-plane deformation described above and illustrated in Fig. 6.27. Shearing every third layer in turn, once to the left (P2 plane) and once to the right (P1 plane), from the *bridges* toward the *hollow* sites, reproduces the NbO stacking. This is illustrated in the right panel of Fig. 6.28. The P_2 plane of the NbO structure, shifts from the red *bcc* plane position to the left, from the bridges to the hollow sites. While, the P_1 plane shifts from the blue *bcc* plane position to the right, from the bridges to the hollow sites.

According to [73], the initial incorporation of subsurface O is the "bottleneck" in the oxidation sequence of transition metals, acting as a metastable precursor to the formation

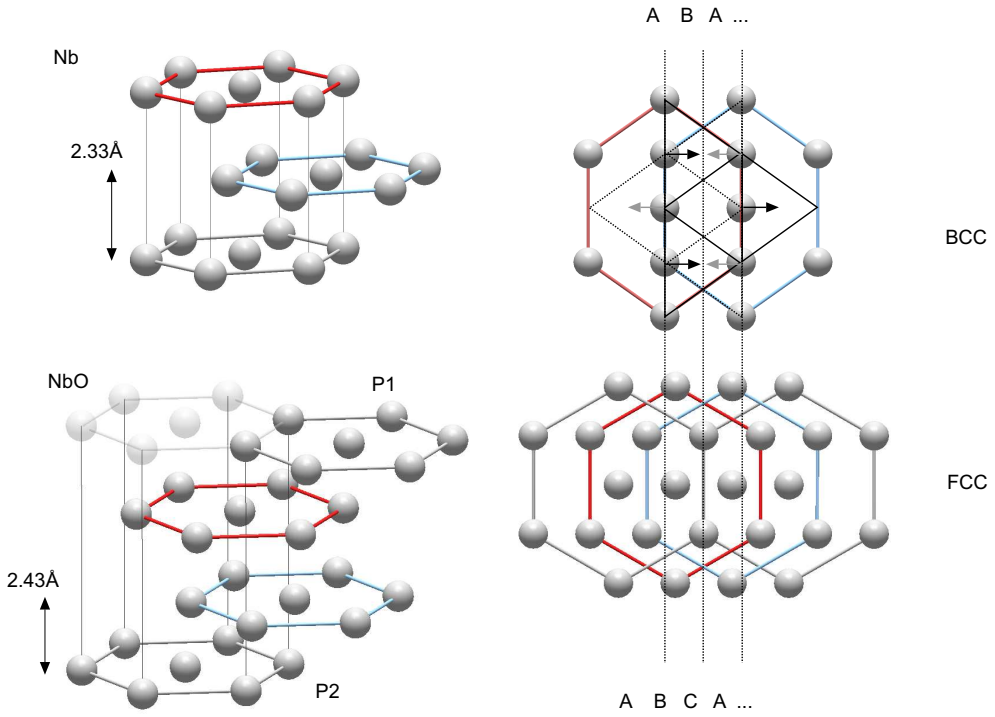

Figure 6.28: Left : Stacking sequences of the niobium atoms in the Nb(110) bcc $ABABA\ldots$ and in the fcc-like NbO(111) $ABCABC\ldots$. The oxygen atom planes, which alternate with the niobium planes, are omitted in the NbO structure for clarity reasons. The corresponding lattice spacings between successive niobium planes normal to the surface are indicated. Right : top view of both stacking sequences. The atomics movements associated to the $P1$ and $P2$ planes along the $[1\bar{1}0]$ direction, for a transition form the bcc to the fcc stacking, are represented by arrows. The in-plane deformation of the red and blue planes are described in Fig. 6.27.

of the final oxide structure. Based on theoretical considerations, the stability of subsurface oxygen was shown to depend strongly on the lattice deformation cost. This implies correlations between the oxidation behavior and properties such as the cohesive energy or bulk modulus.

The process described in this section can be summarized as follows. In the first stage the interstitial oxygen atoms dissolved in small amount into niobium act independently from each other and are randomly distributed on octahedral interstitial sites. Due to the intrinsic instability of the niobium lattice in the [111] direction to which the strong local oxygen-induced distortions couple, each single oxygen impurities are nuclei for the formation of the ω-phase. The atomic displacements around each defect associated to the ω-phase act as precursor for the formation of the hexagonal symmetry of NbO. At some point, as the oxygen concentration increases, the oxygen atoms start to interact with each other, which leads to the formation of ordered oxygen superstructure. The Nb_2O structure proposed by Brauer involves a layering of the oxygen atoms in alternation with niobium atoms in the [110] direction, similar to the one observed in the NbO structure. A chemical shift corresponding to the presence of a Nb_2O species at the interface between NbO and niobium has been observed under different conditions in the high-resolution core-level spectroscopy results discussed in section 6.2. Ordered layering of interstitial oxygen has been reported in Nb(110) films oxidized in air at temperature $\sim$ 300°C by mean of X-ray diffraction (through the shift of the Bragg niobium reflection due to the lattice expansion and superstructure reflections) [15]. The ordered structures observed in niobium thin films present the alternation of niobium and oxygen planes of the Nb_2O and NbO(111) structures. In the final step of the oxidation process described here, the lattice gets saturated at a critical oxygen concentration, and metal-oxygen bounds are formed leading to the appearance of the oxide. The *bcc* to fcc transformation occurs as a combination of shear and strain described in Fig. 6.27 and 6.28. Note that the alternation of niobium and oxygen planes in the $[1\bar{1}0]$ direction is characteristic of the ordered defective rock-salt structure of NbO, which can be seen as a three dimensional network of niobium octahedra with strong metal-metal bonding, and to which the remarkable properties of NbO such as superconducting properties have been attributed [122].

6.6 Summary

In this chapter, the natural oxide layer on Nb(110) single crystals oxidized under RT atmospheric conditions and its progressive dissolution upon vacuum annealing have been investigated by means of X-ray reflectivity (XRR), high-resolution core-level spectroscopy (HRCLS) and grazing incidence X-ray diffraction (GIXD). All measurements have been performed with synchrotron radiation. The XRR and GIXD measurements have been carried out at the MF-MPI beamline at the synchrotron ANKA, Germany. The HRCLS measurements were realized on the beamline I311 at the synchrotron source Max-Lab II, Sweden.

In sections 6.1 and 6.2, XRR and HRCLS results on the natural oxide and its thermal dissolution have been presented. The natural oxide layer formed on Nb(110) single crystals oxidized in air (6-10h, RT) presents a layered structure, constituted of Nb_2O_5, NbO_2 and NbO, from the surface to the interface. After heating at 145°C (3-5h, UHV), minor changes are observed in the total oxide thickness, while the highest oxidation state of niobium Nb_2O_5, predominant in the natural oxide, reduces to NbO_2. The reduction process takes place at the interface between both oxides. The NbO layer, as well as the structure of the metal/oxide interface, stay at this temperature unchanged. Above 300°C, the oxide layer dissolves considerably and both Nb_2O_5 and NbO_2 reduce into the lowest stable oxidation state of niobium, NbO. These results are illustrated in Fig. 6.29. Each step of the conversion from Nb_2O_5 to NbO_2 to NbO involves oxygen removal. The amounts of oxygen released during the dissolution process has been calculated in section 6.2.3.

In section 6.3, in-plane and out-of-plane structural characterizations of the NbO oxide layer by means of grazing incidence X-ray diffraction, and its growth simultaneous to the overall oxide reduction aforementioned, are presented. The NbO layer presents epitaxial relationships with the underlying substrate, where the NbO(111) planes are parallel to the Nb(110) planes, and the in-plane directional relationship Nb[001]||NbO[$1\bar{1}0$] corresponds to the Nishiyma-Wassermann orientation. Evidence for the in-plane epitaxial relationship is observed already in the natural oxide. The thin oxide layer is shown to be highly strained. Coexistence of the Kurdjumov-Sachs and Nishiyma-Wassermann orientations is observed for measurements realized at higher temperatures (1700°C).

A qualitative description of the interfacial structure behavior upon heating is given in section 6.4. The results indicate that the metal/oxide interface stays nearly unchanged for low-temperatures heating (145-180°C,UHV). While, drastic changes are observed at 300°C. A quantitative analysis of the CTR measurements allowing to resolve the atomic interfacial structure is planned in a near future.

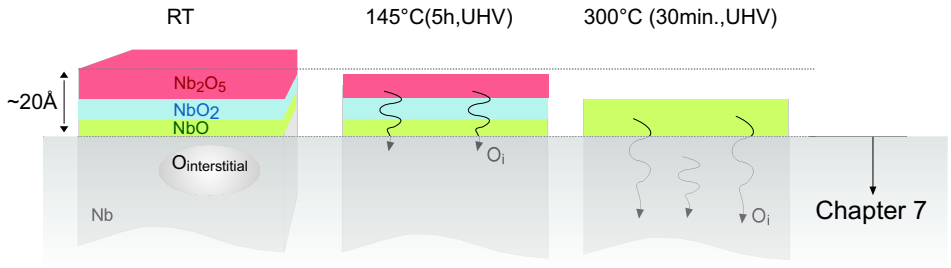

Figure 6.29: In this chapter, the natural oxide layer on Nb(110) single crystals oxidized under RT atmospheric conditions, and its progressive dissolution upon vacuum annealing has been investigated. A depth-resolved analysis of the interstitial oxygen profile below the interface will be presented in chapter 7.

In section 6.5, the transformation that occurs from the oxygen-induced ω-phase observed for randomly distributed defects into niobium, toward the NbO defective rock-salt structure, reported as first oxidation step on niobium surfaces by various authors, is discussed. A transformation path is proposed, involving the precursor role of niobium suboxide species assigned in a first attempt to Nb_2O.

As, it is known that niobium does not release oxygen in UHV below 1600°C [57, 68], oxygen liberated by the oxide dissolution described above necessarily gets dissolved into niobium across the niobium/oxide interface. The depth-resolved analysis of the interstitial oxygen profile below the interface, by mean of grazing incidence X-ray scattering measurements of the oxygen-induced diffuse scattering, will be presented in chapter 7. Therewith, a full picture of the near surface region of the natural oxide grown in air, and its behavior upon vacuum annealing will be completed.

Chapter 7

Depth-resolved oxygen-induced diffuse X-ray scattering in niobium

In this chapter, it is shown how grazing incidence diffuse X-ray scattering measurements offer a non-destructive *in-situ* method to investigate the depth-distribution of *subsurface* interstitial oxygen in niobium and its evolution upon thermal treatments with a nanometer scale resolution. The basis of a comprehensive depth-resolved oxygen-induced diffuse X-ray scattering analysis, together with the fitting routine developed within this work, are presented in section 7.1. In section 7.2, experimental results obtained on Nb(110) single crystals oxidized in air are discussed. The determination of the different contributions to the experimental data lineshape is discussed in 7.2.1. The temperature evolution of the data for a fixed depth, which brings qualitative information about the subsurface interstitial oxygen behavior upon heating, is investigated in section 7.2.2. Finally, the quantitative depth-profiling of the absolute oxygen concentration is reported in 7.2.3. The results are summarized at the end of the chapter.

The diffuse X-ray scattering measurements presented here were performed subsequently to the X-ray reflectivity and grazing incidence X-ray diffraction measurements discussed in chapter 6. A complete picture of the near surface region upon vacuum annealing is therefore achieved combining the respective results of both chapters, the oxidation behavior from chapter 6, and the interstitial oxygen distribution evolution underneath the oxide layer in the present chapter.

The measurements presented in this chapter were carried out at the MPI-MF beamline at the Angstromquelle Karlsruhe (ANKA), Germany [186], at a photon energy of 8.984 keV, on a Nb(110) single crystal oxidized under atmospheric conditions (beamtime A4). The method developed in this work can be generally applied to any further surface preparation. Results obtained under other preparation conditions on Nb(110) and Nb(100) surfaces will be shortly described in chapter 8.

7.1 Depth-resolved grazing incidence diffuse X-ray scattering

For the unambiguous monitoring of subsurface interstitial oxygen one exploits the fact that interstitial oxygen, which occupies octahedral sites in the niobium lattice, gives rise to strong local distortions of the host lattice. These distortions have been shown to couple to the intrinsic instability of the niobium *bcc* lattice toward the ω-structure, thereby producing pronounced maxima of the distortion-mediated diffuse X-ray scattering at $\mathbf{Q}^*_{bcc} = \frac{2}{3}(1,1,1)$. This has been evidenced, as discussed in sections 3.2 and 4.2.1, in a neutron scattering study for dilute solutions of oxygen in niobium *bulk* [22].

In this chapter, it will be demonstrated that the monitoring and quantitative analysis of the aforementioned diffuse maxima at $\mathbf{Q}^*$ by grazing incidence diffuse X-ray scattering provides a detailed picture of the emergence of interstitial oxygen in the *near surface* region of niobium.

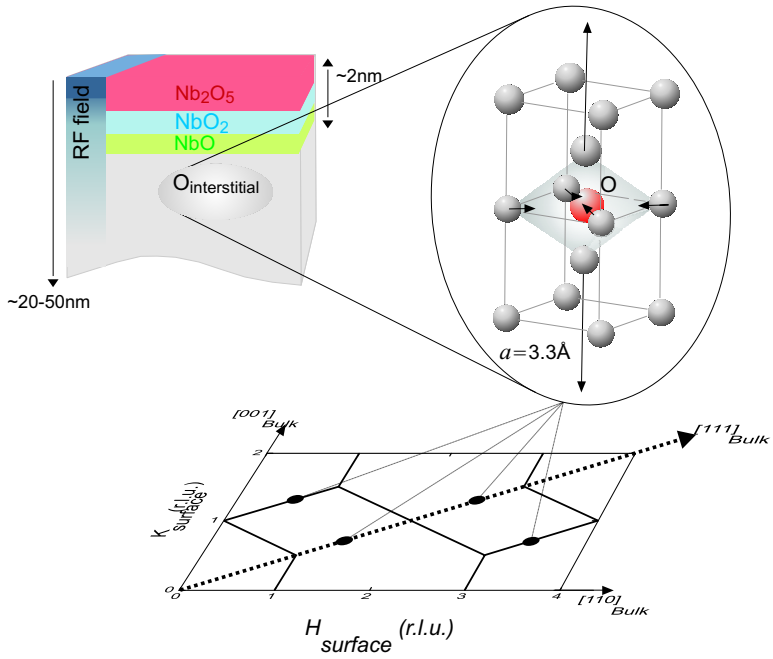

Figure 7.1: Left: Schematic view of the Nb(110) surface oxidized under ambient conditions, its natural layered oxide and subsurface interstitial oxygens. For comparison, the penetration depth of the rf field is shown. Rigth: Strong local distortions of the niobium lattice in the local neighborhood of interstitial oxygen (octahedral site) [22]. Coupled to the common instability of the *bcc* lattices in the [111] direction, these distortions give rise to domains of the trigonal ω-phase, thereby producing pronounced maxima of the distortion-mediated diffuse X-ray scattering at $\mathbf{Q}^*_{bcc} = \frac{2}{3}(1,1,1)$ [22]. Bottom : Reciprocal in-plane map of a Nb(110) surface in surface coordinates, the circles locate the interstitial oxygen-induced diffuse scattering at $\mathbf{Q}^*=\frac{2}{3}(1,1,1)$ and equivalent positions (see text for details).

It is important to stress that using grazing incidence diffuse X-ray scattering to monitor the depth-distribution of subsurface oxygen is definitely a nonstandard technique. A comprehensive method based on the distorted-wave Born approximation (DWBA) formalism[1] and the fitting routine have been developed within this thesis and are presented in the following of this section. The theory and underlying concepts have been introduced in section 4.3.2.

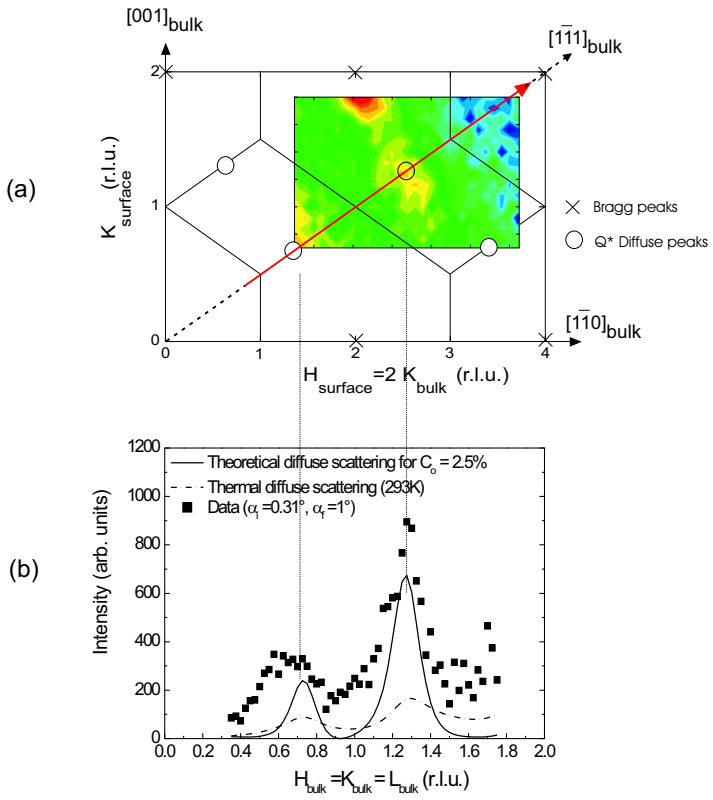

Figure 7.2: (a) Reciprocal *in-plane* map of the Nb(110) surface and location of the theoretically expected oxygen-induced diffuse scattering intensity at $\mathbf{Q}^*_{bcc}=\frac{2}{3}(1,1,1)$ and equivalent positions (open circles). Color map : experimental meshscan of the Nb(110) single crystal oxidized in air taken for a scattering depth $\approx$ 150 nm. (b) Experimental curve measured along the $[1\bar{1}1]$ direction (open squares) for a scattering depth of $\sim$ 10 nm, and theoretical contributions of the oxygen-induced diffuse scattering (solid line) and thermal diffuse scattering (dashed line) (see text for details). The data were corrected for the polarization factor, and the background substracted.

The first experimental *in-plane* meshscan of the diffuse scattering originating from interstitial oxygen dissolved in the near surface region of a Nb(110) single crystal oxidized few hours in air, measured around $\mathbf{Q}^*_{bulk} = \frac{4}{3}(1,1,1)$, is shown in Fig. 7.2. The relevant

[1]Since the niobium crystals are mosaic a kinematic description of the experimental results is applicable here.

information depth for the surface sensitive measurements is the scattering depth Λ, defined in (4.48). The scattering depth is controlled by both the incidence and the exit angle. The data presented in Fig. 7.2 have been measured at an incident angle $\alpha_i = 0.5°$ and $\alpha_f = 0.6°$, which corresponds to a scattering depth of $\sim$ 150 nm. A sketch of the reciprocal *in-plane* map of the Nb(110) surface is illustrated around the meshscan, including the first Brillouin zones and the locations of the oxygen-induced diffuse intensity at the $\mathbf{Q}^*$ equivalent positions. The map is plotted in the Nb(110) surface coordinates described in section 6.3.

One can easily understand the difficulties involved in the determination of an *absolute* oxygen depth-distribution, knowing the complexity of the system under consideration. In chapter 6, the structure of the natural oxide layer on Nb(110) surfaces oxidized in air has been discussed in detail. From these results, one knows that a multilayer system of niobium oxides is present at the surface which has to be fully accounted for in the model developed here. The presence of the oxide layer at the surface has two major implications on the measured intensity. One of them is its influence on the optical properties of the surface, which determines the evanescent wave profile into the material, crucial for the determination of the depth-profile of the interstitial oxygen atoms into the material. This point is discussed later in section 7.1.2. The second concerns the contribution of the oxide structure factor to the total signal.

In this chapter, linescans of the diffuse X-ray scattering intensity measured along the in-plane $[1\bar{1}1]_{bulk}$ direction will be analyzed as illustrated in Fig. 7.2 (b). In this figure the lineshape of an experimental scan is compared to the theoretical curve of the oxygen-induced diffuse X-ray scattering calculated, as described in section 4.2.1, for an arbitrary concentration including the TDS contribution. As mentioned before, the theoretical structure factor of the diffuse scattering has been calculated by R. Kurta in the framework of his PhD thesis [164]. The first remark to do regarding the theoretical and the experimental curves (after correction for the polarization and substraction of a background) in Fig. 7.2 (b), is the remarkable agreement of the main features, i.e. the two oxygen-induced diffuse maxima at $\mathbf{Q}^*_{\mathrm{bcc}} = \frac{2}{3}(1,1,1)$ and $\frac{4}{3}(1,1,1)$. Aside the characteristic footprint of the interstitial oxygen at the $\mathbf{Q}^*$ maxima, however, shoulders occur in the intensity profile at the left side of each maxima. It will be demonstrated in section 7.2.1 that these features are due to the natural oxide layer present at the sample surface.

Another difficulty to stress is related to the determination of the absolute concentration in oxygen, in the absence of clean surface measurements available as reference. In order to deal with this situation, our knowledge on the absolute ratio between the oxygen-induced signal and the TDS signal will be exploited. This is described in section 7.1.1.

7.1.1 Absolute oxygen concentration profile

Any kinematic scattering intensity I_{GIXS} observed near the condition of total external reflection can be expressed from Eq.(4.45) as,

$$I_{\mathrm{GIXS}}(\mathbf{Q}') \propto |T_i|^2 |T_f|^2 \; S(\mathbf{Q}') \tag{7.1}$$

where $T_{i,f}$ are the transmission coefficients for the incident and exit beam, and $S(\mathbf{Q}')$ the structure factor of the scattering process under consideration. The prime designates quantities inside the material. In our case the structure factor $S(\mathbf{Q}')$ includes, as mentioned before, contributions from the oxygen-induced diffuse scattering, the TDS and the oxide structure factors, so that

$$S(\mathbf{Q}') = S_{\mathrm{diff}}(\mathbf{Q}') + S_{\mathrm{TDS}}(\mathbf{Q}') + S_{\mathrm{oxides}}(\mathbf{Q}') \tag{7.2}$$

Taking into account expressions 4.15 and 4.51, and dividing the scattering vector $\mathbf{Q}'$ into the *in-plane* component $Q_{\parallel}$ and the normal component Q'_z, the oxygen-induced diffuse scattering structure factor $S_{\mathrm{diff}}(\mathbf{Q}')$ is given by,

$$S_{\mathrm{diff}}(Q_{\parallel}, Q'_z) \propto S_{\mathrm{D}}(Q_{\parallel}) \int_{0^*}^{\infty} c(z)(1-c(z)) \left| e^{-z/\Lambda} \right|^2 dz \tag{7.3}$$

where $S_{\mathrm{D}}(Q_{\parallel})$ is the in-plane structure factor of a single defect defined in section 4.2, and $c(z)$ the interstitial oxygen concentration profile along the surface normal into the material. The Q_z-dependence of S_{D} has been neglected in expression (7.3) (see discussion below). Within this approximation, the depth-dependence of S_{diff} is directly given by the Laplace transform of the oxygen concentration profile $c(z)$, with respect to the scattering depth Λ. Keeping in mind that the scattered intensity originates from the interstitial oxygen atoms dissolved into the niobium lattice below the oxide layer, the integration has to be performed only from $0^* = ox$, where ox is the total oxide layer thickness.

It is important, while interpreting depth-resolved spectra, to keep in mind the definition of the scattering depth Λ. Relevant length, as mentioned before, describing the grazing incidence intensity, the scattering depth is defined as the depth for which the scattered intensity is reduced to $1/e$, with $\lambda = Im(Q'_z)^{-1}$. Therefore, as shown by Eq. 7.3, the signal measured at a given scattering depth Λ carries much more information than what comes from this depth itself. Oxygen atoms dissolved much deeper into the niobium bulk will, although their contribution is strongly damped by the exponential decay of the wave field, always contribute to a certain extend to the signal measured for a scattering depth close to the metal/oxide interface.

The main DWBA quantities encountered in Eq. 7.1 and 7.3 are illustrated in Fig. 7.3 (a-e) for a niobium surface, as a function of α_i/α_c and different α_f. The real part of the

normal component of the scattering vector within the sample $\mathrm{Re}(Q'_z)$, is plotted in Fig. 7.3 (a). The scattering depth Λ is shown in Fig. 7.3 (b). The totally incoherent scattering, i.e. with no Q-dependence, is illustrated in Fig. 7.3 (d). The Fresnel transmission coefficients for the incident and exit beam $T_{i,f}$ are plotted in Fig. 7.3 (e). These quantities are important and will often be referred to in the following.

The second term of the structure factor in Eq. 7.2 is assigned to the TDS contribution to the signal. If one neglects the Q_z-dependence of the thermal diffuse scattering (see the discussion below), $S_{\mathrm{TDS}}(Q')$ is given from Eq.(4.45) by

$$S_{\mathrm{TDS}}(Q_\parallel, Q'_z) = S_{\mathrm{TDS}}(Q_\parallel) \int_{ox}^{\infty} \left| e^{-z/\Lambda} \right|^2 dz \tag{7.4}$$

$$\propto \Lambda e^{-\frac{2\ ox}{\Lambda}} \tag{7.5}$$

where $S_{\mathrm{TDS}}(Q_\parallel)$ is the in-plane component of the TDS structure factor given in section 4.2.2, and ox the oxide thickness.

The exact oxygen-induced diffuse scattering and TDS structure factors are theoretically calculated as described in section 4.2. Their Q_z-dependence is illustrated in Fig. 7.4. The range of depths under interest for the measurements described in this work is indicated. In a first approximation, one sees that the signal can be considered as constant for small Q_z values. This give rise to the simplified expressions 7.3 and 7.5. The decay associated to the last depth scanned is, however, corrected by a scaling factor in order to account for the strong decrease in intensity and not to lead to a wrong interpretation of the oxygen concentration.

Fig. 7.5 illustrates the *in-plane* components along the $[111]_{bulk}$ direction of the oxygen-induced diffuse scattering structure factor $S_{\mathrm{diff}}(Q_\parallel)$ for different homogeneous oxygen concentrations, and of the room temperature TDS structure factor $S_{\mathrm{TDS}}(Q_\parallel)$. The coordinate of the scan are in bulk units (remember that the $[1\bar{1}1]_{bulk}$ direction lies in the surface plane of the Nb(110) surface). Both contributions are calculated in absolute electron units, and the ratio of their respective intensities is given by

$$R(\Lambda) = \frac{I_{\mathrm{Diff}}}{I_{\mathrm{TDS}}} = c_\Lambda(1 - c_\Lambda) \ \ \frac{S_{\text{Single defect}}(Q_\parallel)}{S_{\mathrm{TDS}}(Q_\parallel)} \tag{7.6}$$

where c_Λ is defined as an average homogeneous oxygen concentration for a given scattering depth Λ.The absolute ratio between the oxygen-induced diffuse scattering and the TDS intensity can therefore be seen as the ratio of their in-plane components, which is known from the theory, multiplied by an average oxygen concentration for the considered depth. This result is of first importance since it will serve to determine the common scaling factor of the diffuse and thermal diffuse scattering between the calculated value in absolute units

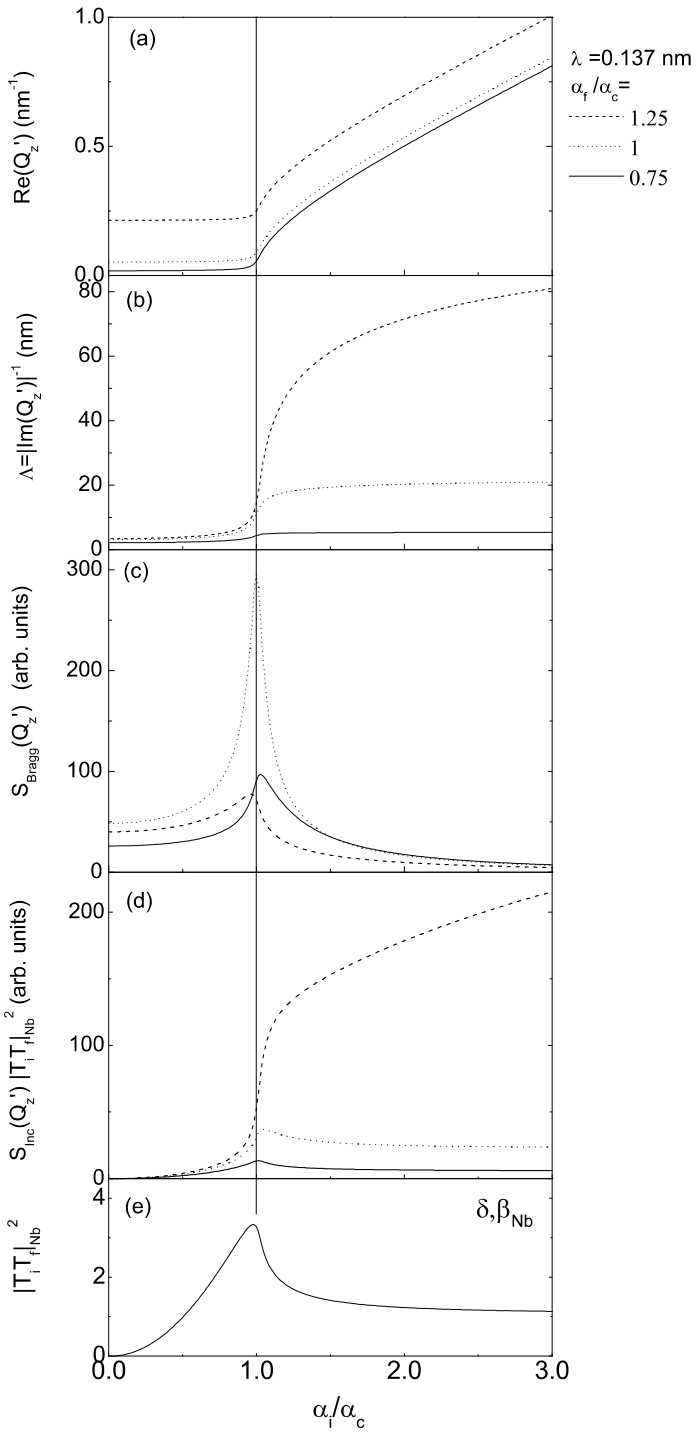

Figure 7.3: DBWA scattering quantities as a function of α_i/α_c for various scattering angle α_f in niobium. (a) Real part $\mathrm{Re}(Q'_z)$ of the z component of the momentum transfer Q'_z within the sample. (b) Scattering depth $\Lambda = |Im(Q'_z)|^{-1}$ in pure niobium (Eq. 4.48). (c) Evanescent Bragg scattering law from the Nb(110) surface (Eq. 4.50). (d) Evanescent incoherent scattering law (Eq. 4.51). (e) Niobium Fresnel transmission coefficients.

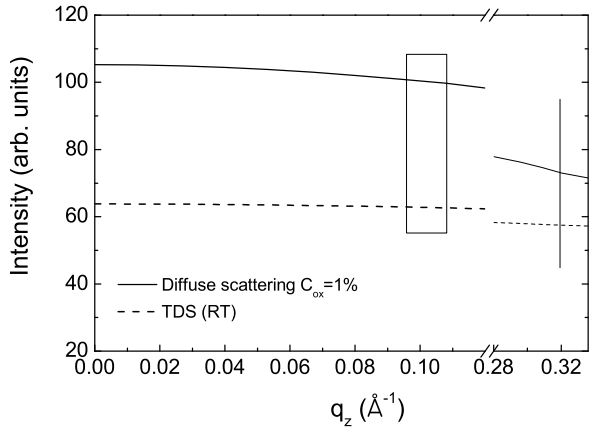

Figure 7.4: Q_z-dependence of the oxygen-induced diffuse scattering for an average oxygen concentration of 1% and of the room temperature TDS (on $Q^* = \frac{4}{3}(1,1,1)$ for the normal direction of a [110] surface). The Q_z range corresponding to the set of data, i.e. of angles, considered in this work is indicated (rectangle for a continuous range, and line for an isolated Q_z value).

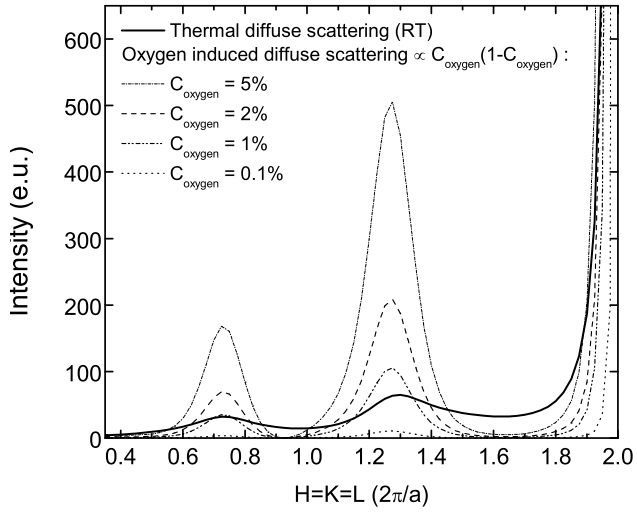

Figure 7.5: Theoretical curves of the oxygen-induced diffuse scattering along the [111] direction for different homogeneous oxygen concentration in the bulk and bulk TDS at room temperature.

and the data point for the fitting procedure, and thereby allowing the determination of the absolute oxygen concentration into niobium.

The surface imperfection and the detector acceptance have to be taken into account for the calculation of the expressions of the depth-dependence of the diffuse intensity and the TDS, this point is discussed in section 7.1.3.

7.1.2 Oxide influence on the optical factors

The presence of different oxide layers at the surface of the sample, with different optical properties, influences the penetration of the evanescent wave into the material, and thereby the scattering depth Λ. For a material m, one has from Eq. 4.48,

$$\Lambda_m(\alpha_{i,f}) = \frac{\lambda}{2\pi(l_{i,m} + l_{f,m})} \tag{7.7}$$

where λ is the wavelength of the incident beam, and

$$(l_{i,f})_m = 2^{-1/2}\left\{\left(2\delta_m - \sin^2\alpha_{i,f}\right) + \left[\left(\sin^2\alpha_{i,f} - 2\delta_m\right)^2 + 4\beta_m^2\right]^{1/2}\right\}^{1/2} \tag{7.8}$$

The dispersion δ_m and absorption parameter β_m of the different niobium oxides are summarized for λ =1.377Å and the different niobium oxides in Tab. 7.1.

Fig. 7.6 (a) illustrates the exponential decays e^{-z/Λ_m} of the evanescent wave into niobium and its different oxides. The higher the oxidation state of niobium is, the higher the corresponding scattering depth is, for given incident and exit angles. Taking into account the different decay lengths into each oxide layers and continuity conditions at the interfaces, one can define an *effective scattering depth* Λ_{Eff}. This is illustrated in Fig. 7.6 (b) in the case of the natural oxide layer observed at Nb(110) surfaces. The effective scattering depth, defined as the depth where the intensity is reduced to $1/e$, is a function of the thicknesses of the different oxide layers. The Laplace transform over the z component in the expression of the scattered intensity in Eq. 4.50 or Eq. 4.51, can be decomposed in

$$\begin{aligned} L(\Lambda_{\text{Eff}}) = &\int_0^{Ox1} f(z)\; e^{-\frac{z}{\Lambda_{Nb_2O_5}}}\; dz + A_1 \int_{Ox1}^{Ox2} f(z)\; e^{-\frac{z}{\Lambda_{NbO_2}}}\; dz \\ &+ A_2 \int_{Ox2}^{Ox3} f(z)\; e^{-\frac{z}{\Lambda_{NbO}}}\; dz + A_3 \int_{Ox3}^{\infty} f(z)\; e^{-\frac{z}{\Lambda_{Nb}}}\; dz \end{aligned} \tag{7.9}$$

where $Ox_{1,2,3}$ are the thicknesses of the Nb_2O_5, NbO_2 and NbO oxide layers respectively, $f(z)$ an arbitrary function, and A_i the scaling factors obtained from the continuity conditions at the respective interfaces. The exponential decay of the evanescent wave into

	δ	β
Nb_2O_5	1.08×10^{-5}	0.38×10^{-6}
NbO_2	1.38×10^{-5}	0.51×10^{-6}
NbO	1.67×10^{-5}	0.72×10^{-6}
Nb	1.9×10^{-5}	0.98×10^{-6}

Table 7.1: Dispersion and absorption parameters, δ and β, for niobium and its oxides for a wavelength $\lambda = 1.377$ Å.

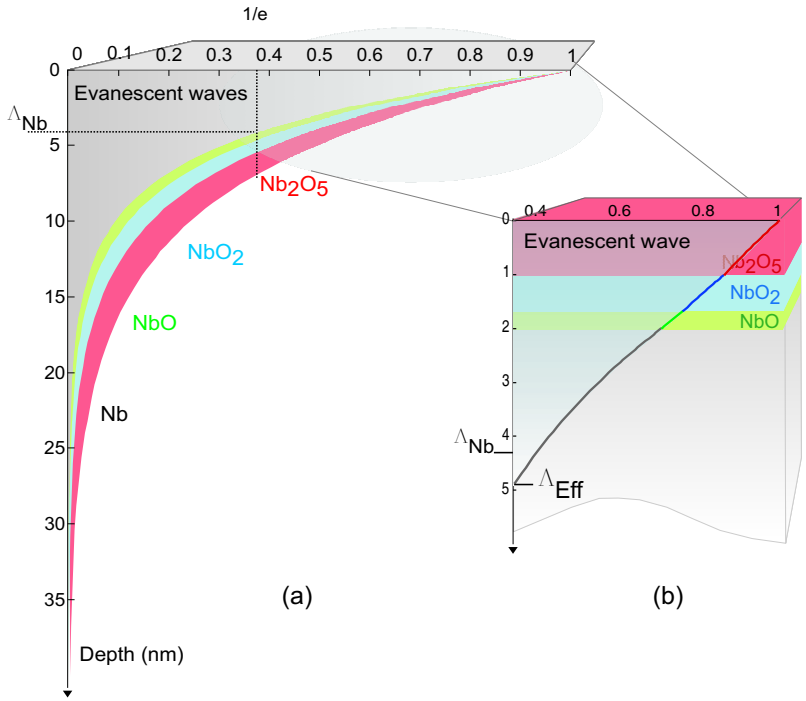

Figure 7.6: (a) Exponential decay of the evanescent wave in niobium and its different oxides for a given incident and exit angle. For given incident and exit angles, the higher the oxidation state of niobium is, the higher the decay length is. (b) Taking into account the different decay lengths in each oxide layer and applying continuity conditions at the interfaces, a new profile is defined as well as a corresponding *effective* scattering depth Λ_{Eff}.

niobium underneath the oxide layer, which is relevant for the interstitial oxygen profile determination can be exactly expressed by $e^{-(z-z_0)/\Lambda_{\mathrm{Nb}}}$, so that

$$L_{\mathrm{oxide}}(\Lambda_{\mathrm{Eff}}) = \int_{ox}^{\infty} f(z)\; e^{-\frac{z-z_0}{\Lambda_{\mathrm{Nb}}}}\; dz \quad \text{for } z \geq ox \tag{7.10}$$

where ox is the total thickness of the oxide layer, and $z_0(\Lambda_{\mathrm{Eff}})$ is determined by the continuity conditions at the different oxide interfaces and the respective thicknesses of the oxides layers, as illustrated in Fig. 7.7. This is important for the data analysis described in section 7.1.4, where an analytical form of the exponential decay of the evanescent wave is required for the fitting function.

In section 7.2.1, the NbO_2 and NbO oxide contribution to the individual lineshape of the diffuse scattering, i.e. the *in-plane* features of the data, will be discussed. The depth-dependence, on the other hand, of these contributions is evaluated here. Each oxide contributes to the expression 7.9 only over the z range corresponding to its thickness, for example NbO_2 is different than zero for $Ox_1 \leq z \leq Ox_2$. If one neglects the Q_z-dependence

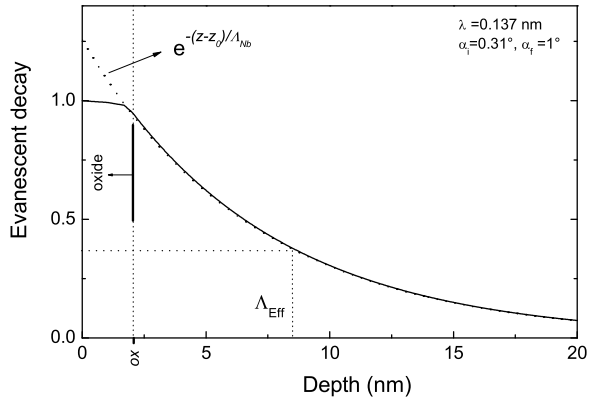

Figure 7.7: Exponential decay of the evanescent wave into niobium below the oxide layer.

of the oxide structure factors, one can write following Eq. 4.51,

$$I_{NbO_2}(\alpha_i) \propto A_1 \; S_{\mathrm{NbO_2}}(Q_\parallel) \int_{Ox1}^{Ox2} \left| e^{-\frac{z}{\Lambda_{\mathrm{NbO_2}}}} \right|^2 dz \tag{7.11}$$

where $S_{\mathrm{NbO_2}}$ is the in-plane component of the structure factor of the oxide. The exponential decay of the evanescent wave through the oxide layer is illustrated for different incident angles and a fixed exit angle in Fig. 7.8. The depth-profile of the NbO_2 and NbO intensity as a function of the incident angle are plotted in Fig. 7.8. Their evolution can be understood qualitatively from the sketch in Fig. 7.8 (b). The intensity of the NbO_2 component is given by the blue area, which increases with the angles until it reaches a saturation plateau above the critical angle. The amount of Nb material contributing to the signal, as for it, is increasing proportionally to the scattering depth Λ_{Eff} plotted for comparison in Fig. 7.8 (b).

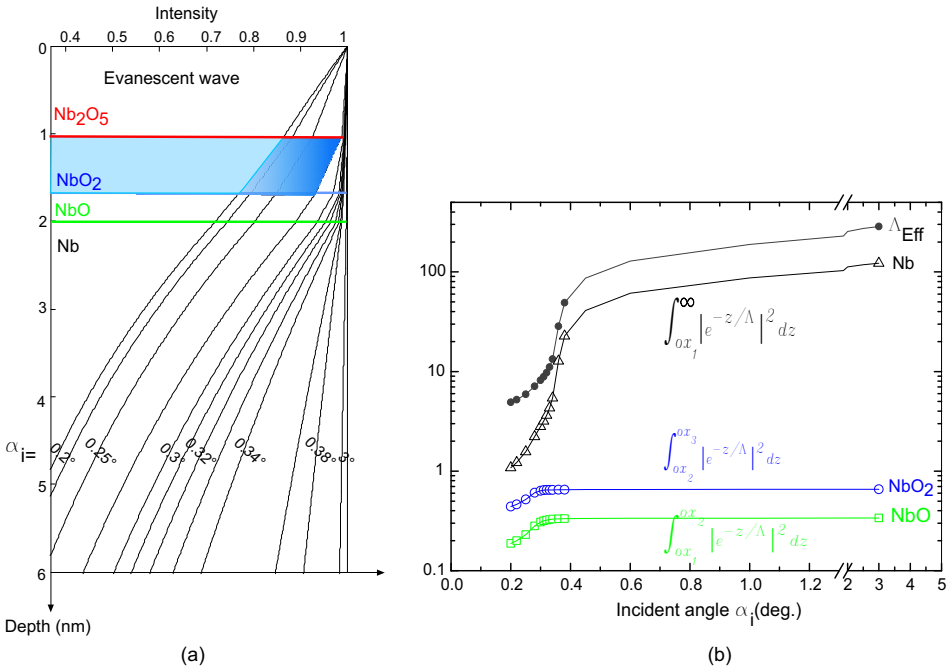

Figure 7.8: (a) Exponential decay of the evanescent wave for different incident angles and a fixed exit angle ($\alpha_f = 1°$). The intensity of the NbO_2 component, as an example, is pictured for a given angle by the blue area. (b) The intensity of the NbO_2 and NbO oxides peaks is increasing with the incident angle before reaching a saturation plateau above the critical angle. The amount of niobium material contribution to the signal as for it, is increasing proportionally to the scattering depth Λ_{Eff}.

7.1.3 Surface waviness and detector acceptance

Depth-controlled grazing incidence scattering studies, as mentioned before, require well-defined incidence and exit angles ($\alpha_{i,f}$). This necessitates that the surface investigated is atomically smooth and macroscopically flat on the scale of the critical depth. The waviness of the surface (deviation from the surface normal) can be checked by the angular width of a rocking scan[2] on the specular reflected beam, as illustrated in Fig. 7.9 for ($\alpha_i = \alpha_f = 0.5°$), and the corresponding waviness Δn_s =0.07°. The alignment of the surface, its structural and optical properties can be checked via grazing incidence Bragg scattering measurements and be used later on for the diffuse scattering analysis.

In the case of kinematic Bragg scattering with a pronounced Q-dependence (remember that one considers the Bragg planes perpendicular to the surface under investigation) the semi-infinite kinematic sum for Bragg scattering is given by Eq. (4.50).

Fig. 7.10 shows the (002) grazing-angle Bragg scattering profile measured at room temperature for the Nb(110) surface oxidized in air at RT during 10h. Note that the (002) Bragg reflection refers to bulk coordinates, and lies in the surface plane of the Nb(110) surface (see Fig. 6.12). The α_i profile of the (002) Bragg intensity was measured at α_f/α_c = 1.25. The asymmetric line shape of the data is characteristic of the evanescent Bragg scattering as shown by the calculated profile of an ideal Nb(110) surface in the DWBA (solid black line) (Eq. (4.45) and (4.50)). The maximum intensity is no longer obtained at $Q_z = 0$ for an inplane bulk Bragg reflection as predicted from simple kinematical theory but shifted to $\alpha_i = \alpha_c$. This is attributed to the action of the transmission function and, partly to the scattering law itself (see Fig. 7.3 (c,e)). For angles $< \alpha_c$, the Bragg condition is fulfilled inside the sample because $Re(Q'_z) \approx 0$. The amount of layers in (4.50) contributing

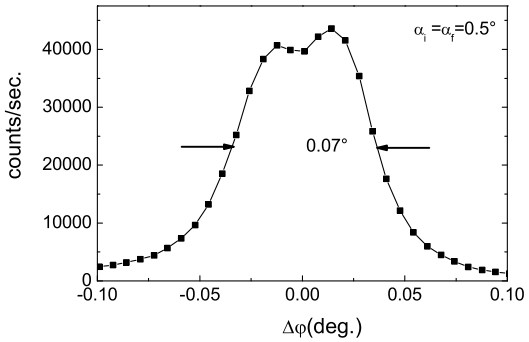

Figure 7.9: Rocking scan measured at $\alpha_i = \alpha_f = 0.5°$. The width of the curve gives the waviness of the sample along the illuminated surface.

[2]Rotation of the sample around the y-axis in the in-plane scattering geometry, at a fixed detector position.

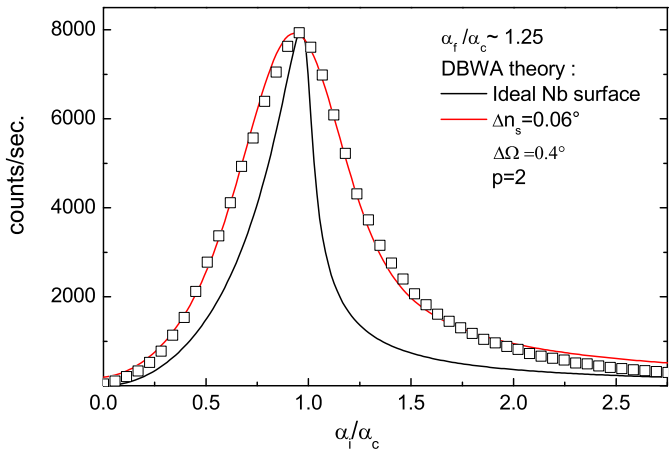

Figure 7.10: Experimental α_i profile of the Bragg scattering at the $(002)_{\text{bulk}}$ reflection (open squares) and theoretical prediction from the DWBA theory for an ideal niobium surface (black line) and including effects of surface waviness Δn_s =0.06°, a detector acceptance $\Delta\Omega$ of 0.4° and p=2 dead surface layers (red line).

to the diffraction is defined by the scattering depth, therefore small at those angles and increasing with the angle. When α_i is increased above the critical angle however, $Re(Q'_z)$ (see Fig. 7.3) becomes finite and the Bragg condition is no longer fulfilled.

The discrepancy observed between the measured and calculated intensity profiles can be explained by the structural properties of the real surface such as the microscopic roughness, dead-layers, misalignment of the Bragg peaks and the macroscopic waviness of the surface Δn_s. To take into account these factors, the scattering intensity has to be averaged over the associated variations of the incidence and exit angles $\Delta\alpha_{i,f}$, such that

$$I_{\text{Bragg}}(\alpha_i) \propto \left\langle |T_i|^2 |T_f|^2 \frac{e^{-2pa/\Lambda}}{|1 - e^{iQ'_z a_z}|^2} \right\rangle_{\alpha i,f} \tag{7.12}$$

where $\langle\rangle_{\alpha i,f}$ expresses the convolution over the adequate α_i and α_f distributions

$$I(\alpha_{i0}, \alpha_{f0}) = \int\int I(\alpha_{i0} - \alpha_i, \alpha_{f0} - \alpha_f) w(\Delta\alpha_i) w(\Delta\alpha_f) d\alpha_i d\alpha_f \tag{7.13}$$

where $w(\alpha_{i,f})$ are weight functions [173].

In Fig. 7.10, the calculated curve taking into account the modified expression from Eq. (7.12) is shown (red solid line) for surface waviness Δn_s =0.06°, p=2 dead surface layers (which can be attributed to the oxide layers at the surface), but also the detector acceptance $\Delta\Omega$ = 0.4°, the agreement is good. Taking into account those parameters is crucial for the diffuse scattering analysis discussed in the following. Indeed, the depth-dependence of key parameters such as the transmission coefficients or the scattering depth

is strongly affected by the convolution expressed in Eq. (7.12). Fig. 7.11 illustrates the convoluted transmissivity of a niobium surface and the parameters aforementioned[3]. The dashed curve represents the convoluted function, and the open squares indicate the data points, i.e. the incident angles, at which the measurements presented in this work have been performed.

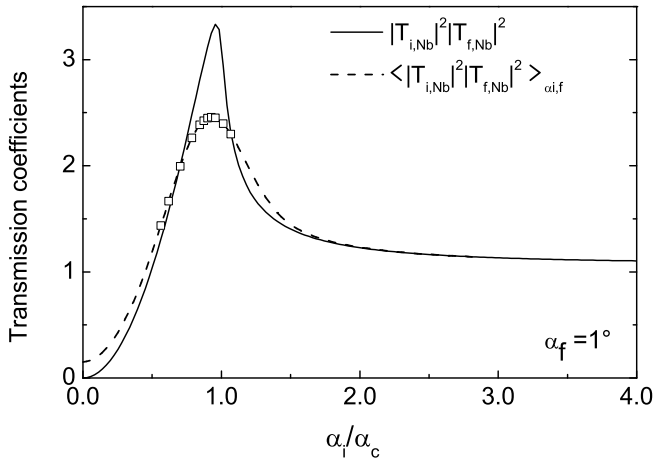

Figure 7.11: Transmission coefficients $|T_i|^2\,|T_f|^2$ as a function of α_i/α_c with $\alpha_f = 1°$, for an ideal niobium surface (solid line) and calculated for a surface waviness of Δn_s =0.06° and a detector acceptance $\Delta\Omega = 0.4°$ (dashed line).

7.1.4 Fitting procedure

The diffuse X-ray scattering data are modeled by a function $f_j(\mathbf{x})$ that accepts the parameters vector $\mathbf{x}$, expressed from Eq. (7.1-7.12) as,

$$\begin{aligned} f_j(\mathbf{x}) = x_0 &+ x_1 \,.\, DW_{\mathrm{Nb}} \,.\, S_{\mathrm{Diff}}(Q_\parallel).\, \left\langle |T_i|^2|T_f|^2 \int_{ox}^{\infty} c(z,\mathbf{x})(1-c(z,\mathbf{x}))\left|e^{-z/\Lambda}\right|^2 dz \right\rangle_{(\alpha_{i,f})_j} \\ &+ x_1 \,.\, DW_{\mathrm{Nb}} \,.\, S_{\mathrm{TDS}}(Q_\parallel).\, S_{\mathrm{Inc,j}} \\ &+ x_2 \,.\, DW_{\mathrm{NbO_2}} \,.\, S_{\mathrm{NbO_2}}(Q_\parallel).S_{\mathrm{Inc,j}} \\ &+ x_3 \,.\, DW_{\mathrm{NbO}} \,.\, S_{\mathrm{NbO}}(Q_\parallel).S_{\mathrm{Inc,j}} \\ &+ x_1 \,.\, S_{\mathrm{Compton}}(Q_\parallel).\, S_{\mathrm{Inc,j}} \end{aligned} \tag{7.14}$$

with

$$S_{\mathrm{Inc,j}}(\Lambda) = \left\langle |T_i|^2|T_f|^2 \int_{ox}^{\infty} \left|e^{-z/\Lambda}\right|^2 dz \right\rangle_{(\alpha_{i,f})_j} \tag{7.15}$$

[3]The convoluted function has been normalized. The transmission profile converges to 1 at high incident angles and high exit angles. For $\alpha_f = 1°$, however, this value is slightly superior to 1.

$f_j(\mathbf{x})$ is function of the scattering depth, through a set of incident and exit angles $(\alpha_{i,f})_j$. The first term of the sum in (7.14) describes the oxygen-induced diffuse scattering, the second the TDS, and the next terms two oxide contributions from NbO_2 and NbO (see section 7.2.1). x_0 is the background and DW represents the Debye-Waller factor (section 4.2.2). The Compton scattering (section 4.4) $S_{\text{Compton}}(Q_\parallel)$ has been included as material dependent with the same incoherent Q_z-dependence as the TDS and the oxide layers, given by Eq. (7.15). The scaling parameter x_1 is unique for the calculated oxygen-induced diffuse scattering, the TDS and the Compton (section 7.1.1).

In order to extract the depth-profile of the interstitial oxygen from the grazing incidence diffuse X-ray scattering, the whole set of data, i.e. including all spectra measured at different incident angles, has to be fitted *at once*. The data are corrected for the polarization and the active area factors (see section 4.4). The least-squares curve fitting is performed by minimizing the function $F(\mathbf{x})$ with respect to the parameter vector $\mathbf{x}$, with

$$\min_{\mathbf{x}} \|F\|^2 = \min_{\mathbf{x}} \sum_j (f_j(\mathbf{x}) - ydata(\alpha_{(i,f)_j}))^2 \tag{7.16}$$

where $f_j(\mathbf{x})$ is given by (7.14), and the summation performed on the incident angle $(\alpha_i)_j$ at which each individual linescan $ydata(\alpha_{i(j)})$ has been measured.

It is important to emphasize that the different contributions to the signal have to be fitted at once for the relevance of the absolute oxygen concentration extracted from the data. Indeed, a linescan at high angle ($\alpha_i = 3°$) (see Fig. 7.20) is dominated, as it will be demonstrated later, by the feature of the TDS. The data measured at $\alpha_i = 3°$ alone would not be sensitive enough to the diffuse contribution from the oxygen. However, they provide a key information as they determine the scaling factor x_1 in Eq. (7.14). And vice versa the data measured at small incident angle are much more sensitive to the oxygen-induced diffuse scattering contribution. This is illustrated in Fig. 7.12, where the maximum intensity of the diffuse scattering data measured on the Nb(110) surface after atmospheric oxidation are presented, as a function of α_i/α_c (section 7.2). The oxygen-induced diffuse scattering intensity calculated for an arbitrary exponential concentration profile, and the TDS contributions are shown. They are convoluted over the surface waviness Δn_s =0.06° and the detector acceptance $\Delta\Omega$ of 0.4°.

In this model the optical factors, namely the transmission functions and the scattering depth of a clean niobium surface, have been used. The influence of the oxide layer at the surface on the optical factors has been discussed in section 7.1.2. In the expression of the evanescent field in Eq. (7.14) z has to be replaced by $z^* = z - z_0$. Note that z_0 is a function of the incident and exit angles. The convolution in (7.14) is performed on the angular distribution corresponding to a surface waviness $\Delta n_s = 0.06°$ as well as a detector

acceptance $\Delta\Omega = 0.4°$, as determined by the GIXD measurements (section 7.1.3). The concentration profile for the subsurface interstitial oxygen atoms is assumed to follow a general exponential decay form:

$$c(z, \mathbf{x}) = x_4 + x_5 e^{-(z-x_6)/x_7} + x_8 e^{-(z-x_9)/x_{10}} \tag{7.17}$$

where x_{4-10} are parameters to be fitted, x_4 represents the bulk concentration. An effective decay length can be defined as the length where the concentration is reduced to $1/e$.

In order to get an *analytical* expression of the oxygen-induced diffuse contribution in (7.14) necessary for the first version of the fitting program, the oxygen-induced diffuse scattering contribution in (7.14) was approximated by

$$\left\langle |T_i|^2 |T_f|^2 \right\rangle_{\alpha_{i,f}} \int_{ox}^{\infty} c(z, \mathbf{x})(1 - c(z, \mathbf{x})) \left| e^{-z^*/\Lambda} \right|^2 dz \tag{7.18}$$

The fitting parameters of the model presented here are reduced for the whole set of data, i.e. minimum *12* depth-dependent spectra, to only: the scaling factors (3 parameters), the width and positions of the oxide peaks (4 parameters), the oxygen concentration profile (6 parameters) and a background. The non-linear least-squares fitting was realized using the *lsqnonlin* function under Matlab [194]. *lsqnonlin* uses a large-scale algorithm which is

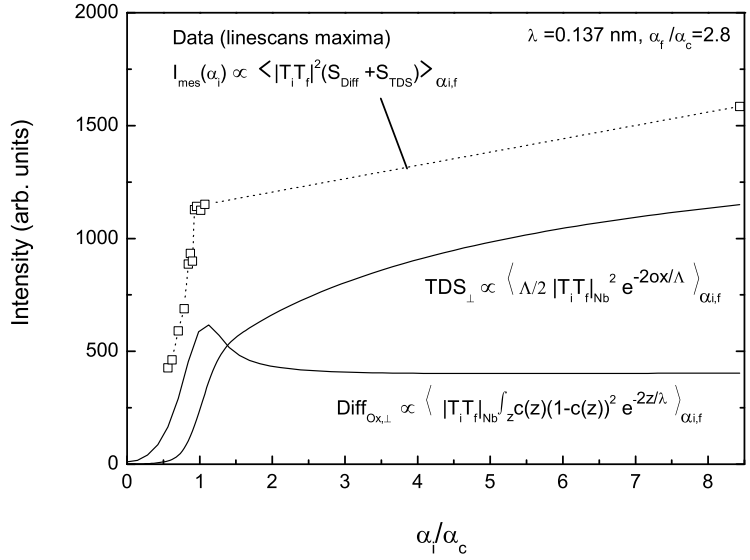

Figure 7.12: Depth-profile of the maximum intensity of the diffuse scattering data measured on the Nb(110) surface after oxidation 10h in air (RT), as a function of α_i/α_c. The oxygen-induced diffuse scattering intensity calculated for an arbitrary exponential concentration profile, and the TDS contributions are shown. They are convoluted over the surface waviness Δn_s =0.06° and the detector acceptance $\Delta\Omega$ of 0.4° (see text for details).

a subspace trust region method based on the interior-reflective Newton method described in [195, 196]. Each iteration involves the approximate solution of a large linear system using the method of preconditioned conjugate gradients.

7.2 Results and discussion

Depth-resolved diffuse scattering intensities have been measured along the in-plane $[1\bar{1}1]_{bulk}$ direction, for the Nb(110) surface oxidized in air (10h, RT), after heating at 145°C (5h, UHV) and at 300°C (50min., UHV) (beamtime A4). All measurements were performed after cooling the sample down to room temperature (RT). The scattering depth was controlled by tuning the incident angle α_i, keeping the exit angle fixed at $\alpha_f = 1°$, as schematically plotted in figure 7.13 (a). A selection of diffuse X-ray scattering data is presented in Fig. 7.13 (b).

Even though the scattering depth Λ can be controlled, as mentioned before, either by tuning the incident angle α_i either the exit angle α_f, which is in theory strictly equivalent (see section 4.3.2), the experimental conditions make an important difference. Since the depth probed depends sensitively on the angle which is scanned, this parameter has to be well defined. The low scattering cross-section of the broad diffuse scattering makes it necessary to open the detector vertical slits to 6 mm. The corresponding angular acceptance at the detector is too large to get any reasonable resolution from an exit angle scan. The incident beam on the contrary is well defined with a divergence inferior to 10^{-2}mradians. The incident angle is defined to an accuracy better than 0.01 degree. We therefore probed the depth in our measurements scanning α_i. The exit angle was set at $\alpha_f = 1°$ where the transmission function is nearly constant. The vertical entrance slits were open to 0.3 mm. The scattering depth can be varied from a minimum value which is only material dependent $\Lambda_{min} \sim \lambda/4\pi\alpha_c$ and a maximum value that is basically determined by photoelectric absorption and increases with α_i up to several hundred of angstroms. For niobium Λ_{min} is approximately 2 nm. For an exit angle $\alpha_f = 1°$, and the angular range of α_i probed in this work, scattering depths between 4 nm and 300 nm are investigated, as illustrated in Fig. 7.13 (a).

The following of this section is organized as follows. A comprehensive description of the *individual lineshape* of the data is first established in section 7.2.1. Additional components to the diffuse scattering, assigned to oxides contributions, are identified. Their temperature dependence and a *qualitative* description of the subsurface interstitial oxygen evolution upon heating is discussed in section 7.2.2, for a fixed scattering depth. At the end of this section 7.2.3, the absolute interstitial oxygen concentration profiles will be extracted from the sets of data presented in Fig. 7.13, for the data measured after atmospheric oxidation, and after heating at 145°C. The least-square curve fitting is performed exploiting the method and fitting routine described in the previous section.

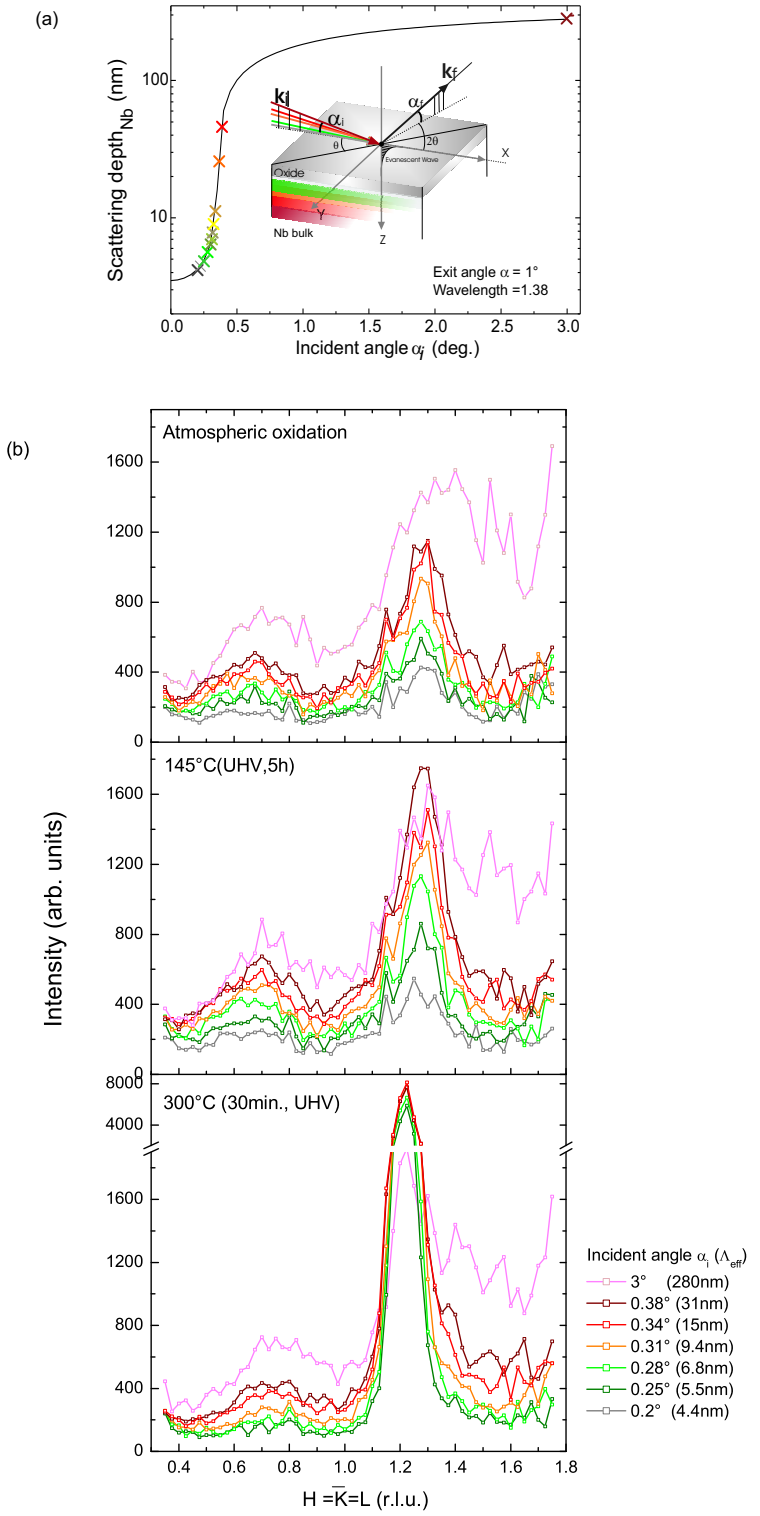

Figure 7.13: (a) Scattering depth Λ as a function of the incident angle α_i, for a fixed exit angle $\alpha_f = 1°$ and a wavelength $\lambda = 0.137$ nm. Schematic view of the penetration depth into the material as a function of α_i in the grazing incidence geometry. (b) Grazing incidence diffuse X-ray scattering data for selected scattering depths after atmospheric oxidation of the Nb(110) single crystal, after heating at 145°C (5h,UHV) and at 300°C (30min.,UHV). The incident angle is varied, the exit angle is fixed at 1° (wavelength = 0.137 nm). The data have been corrected for the polarization factor (see text for details).

7.2.1 Oxide contributions to the individual lineshape

All diffuse scattering data plotted in Fig. 7.13 (b) exhibit two characteristic maxima at $\mathbf{Q}^*_{bcc}=\frac{2}{3}(1,1,1)$ and $\frac{4}{3}(1,1,1)$, signature of the emergence of interstitial oxygen in the near surface region of niobium. In order to fully account for the lineshape of the individual spectra it is however obvious that additional contributions to the oxygen-induced diffuse structure factor, and to the room temperature TDS, are needed. Two shoulders around $H = 0.55$ and $H = 1.1$ (r.l.u.), are visible. In this section, these contributions are shown to be assigned to the natural oxide layer present on the Nb(110) surface. Their influence on the determination of the oxygen depth-profile, discussed at the end of this chapter, is clarified.

Fig. 7.14 shows the decomposition of the diffuse scattering intensity measured on the Nb(110) surface after atmospheric oxidation for incident and exit angles $\alpha_i = 0.31°$ and $\alpha_f = 1°$, which corresponds to a fixed scattering depth of ∼10 nm. All data presented hereafter are corrected for the polarization factor. The in-plane data have been fitted using the calculated structure factors for randomly distributed oxygen interstitials and thermal diffuse scattering, described in section 4.2. The absolute oxygen concentration determines the ratio in between these two contributions. This point has been discussed in detail in section 7.2.3. The fitting function includes the thermal Debye Waller factor, the Compton scattering (see section 4.4), and, three additional components reproducing the shoulders at $H = n \times 0.55$ (2 π/a) with $n = 1, 2, 3$. For $n = 1$, $Q = 1.82$ Å^{-1} corresponds to a $d-$spacing of 3.45 Å. This is compatible with the NbO_2 (400) reflections of the low-temperature distorted rutile structure of NbO_2 described in section 3.3.4. The two first order NbO_2(400) and (800) reflections are needed to fully reproduce the lineshape of the spectrum. However, the data are not sensitive to the third order (12 0 0) reflection. The respective intensities of the NbO_2 reflections are taken from the calculated structure factor given in [129], attenuated by the NbO_2 thermal Debye Waller factor.

The natural oxide layer on the Nb(110) surface oxidized under atmospheric conditions has been characterized in chapter 6, together with its behavior upon thermal treatments. The attribution of the signal observed around $Q = 1.8$ Å^{-1} to NbO_2 reflections is consistent with what has been observed after heating the sample at 300°C (see section 6.2.3), i.e. the dissolution of the NbO_2 layer. Fig. 7.15, shows the decomposition of the diffuse scattering intensity measured after heating at 300°C, for identical incident and exit angles as above, $\alpha_i = 0.31°$ and $\alpha_f = 1°$. In section 6.2.3, the reduction of the oxide layer after heating at 300°C into NbO was observed. In agreement with this observation, one can see in Fig. 7.15 and 7.16, that the intensity around $H = 0.55$ (r.l.u) clearly vanishes after heating at 300°C. Complementary measurements of other NbO_2 reflections as well as an out of plane

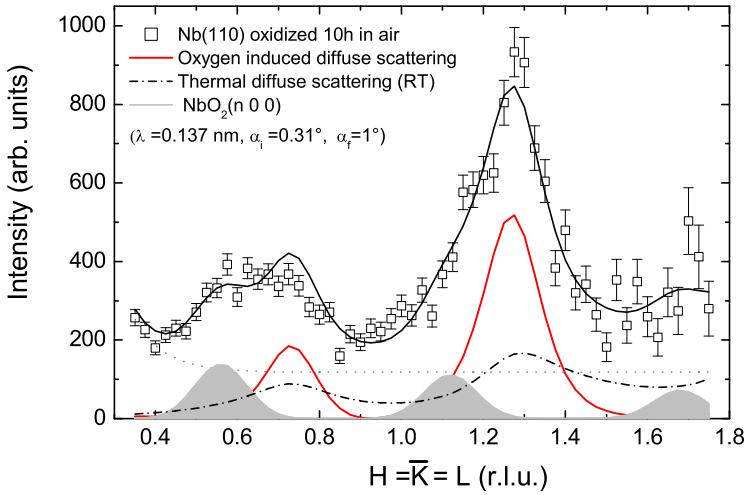

Figure 7.14: Grazing incidence diffuse scattering data measured along the $[1\bar{1}1]$ direction for the Nb(110) surface oxidized 10h under atmospheric conditions at a scattering depth of $\sim$ 10 nm (open squares) and fit (solid line). The data were corrected for the polarization. The fitting function includes : oxygen-induced diffuse scattering at the $\mathbf{Q}^*_{bcc}=\frac{2}{3}(1,1,1)$ and $\frac{4}{3}(1,1,1)$ positions, thermal diffuse scattering, and components attributed to the NbO_2 (400) and (800) and (1200) reflections (filled curves) (see text for details).

characterization would be appropriate in order to determine the structural relationship of the NbO_2 with respect to the underlying substrate but have not been performed yet.

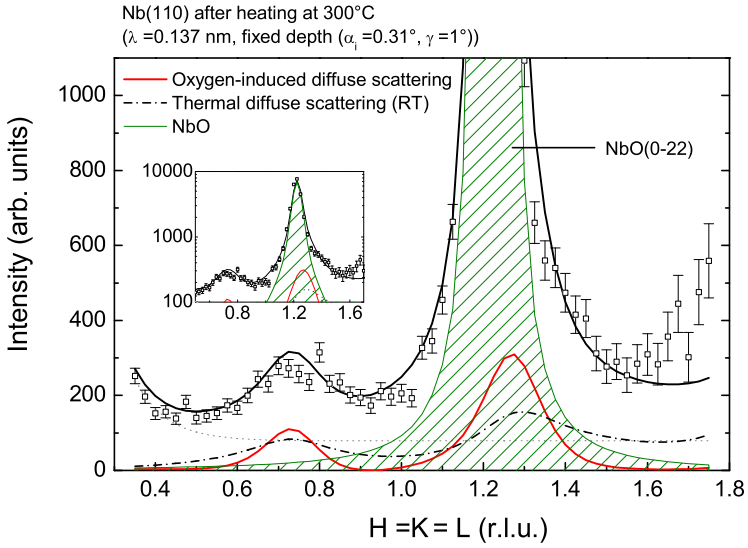

Figure 7.15: Grazing incidence diffuse scattering data measured at RT after heating at 300°C (50min.,UHV) (open squares) and fit (solid line). The data were corrected for the polarization. The sharp contribution that dominates the profile, besides the oxygen induced diffuse scattering and the thermal diffuse scattering, is attributed to the $(0\bar{2}2)$ reflection of an epitaxial $NbO_{fcc}(111)/Nb_{bcc}(110)$ layer (filled curves) (see text for details).

Simultaneously to the dissolution of the NbO_2 layer at 300°C, and the vanishing of the corresponding shoulders in the signal, a new sharp contribution appears in the scan at $H = 1.22$ (r.l.u). The crystalline structure of the remaining oxide at this temperature, NbO, and its epitaxial relationships with the underlying niobium substrate, have been characterized in detail in section 6.3. The sharp component observed in Fig. 7.15 is accordingly to those results assigned to the tail of the $(0\bar{2}2)$ NbO reflection (see also Fig. 6.14). Note that even though the existence of a thin NbO layer at low temperatures has been mentioned in the last chapter, the corresponding reflection is too weak to contribute significantly to the diffuse scattering intensity.

As already mentioned, mixed *hkl* reflections, such as the NbO$(0\bar{1}1)$, are forbidden for the rock salt structure. This allows us, to distinguish the NbO reflections from the oxygen-induced diffuse scattering, and to fit the intensity of the latter on the $\mathbf{Q}^*_{bcc}=\frac{2}{3}(1,1,1)$ peak, as illustrated in Fig. 7.15.

All necessary components needed to describe the individual lineshape of the data presented in Fig. 7.13 have now been identified. The influence of the oxide layers at the surface, and the depth-dependence of their contribution to the diffuse scattering data has been discussed in section 7.1.2.

7.2.2 Temperature evolution at a given depth

In the previous section, the influence of the oxide layer at the Nb(110) surface on the individual lineshape of the diffuse scattering data has been discussed. One more point will be examined before proceeding to the depth-resolved data analysis, and extract the absolute oxygen concentration profile (section 7.2.3). The evolution of the diffuse scattering data, at a *fixed* depth, upon heating is discussed in this section. Constraints on the evolution of the different fitting parameters upon the thermal treatments are discussed. The *relative* evolution of the average concentration of subsurface oxygen over the probed depth upon heating is determined.

Fig. 7.16 shows the temperature evolution of the diffuse scattering data measured a fixed $\alpha_i = 0.31°$ and $\alpha_f = 1°$, which correspond to a scattering depth ~ 10 nm. The measurements were performed after oxidation 10h in air at RT, after heating at 145°C (5h,UHV) and at 300°C (50min.,UHV). The oxide layer for identical treatments was investigated by means of X-ray reflectivity and core-levels measurements in the previous chapter (section 6.2).

The details of the fit decomposition include the oxygen-induced diffuse scattering intensity, the oxide components and the thermal diffuse scattering (TDS), shown in Fig. 7.16 (b,c,d) respectively. The evolution of each of these contributions as function of the

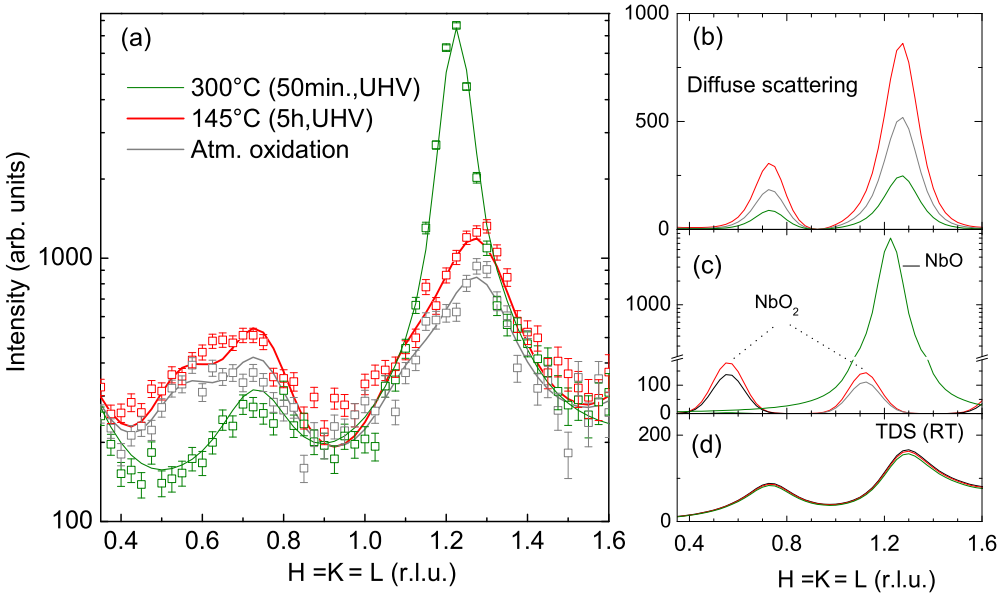

Figure 7.16: (a) Temperature evolution of the grazing incidence diffuse scattering intensity data (open squares) and fits (solid line) measured along the $[1\bar{1}1]$ direction with $\alpha_i = 0.31°$ and $\alpha_f = 1°$ (scattering depth $\sim$ 10 nm) for the near surface of Nb(110). After oxidation 10h in air at RT, after heating at 145°C (5h,UHV) and at 300°C (50min.,UHV). (b) Temperature evolution of the oxygen-induced diffuse scattering contribution. (c) Temperature evolution of the $NbO_2(400)$, $NbO_2(800)$, and $NbO(0\bar{2}2)$ contributions. (d) Thermal diffuse scattering contribution (all measurements were performed at room temperature).

thermal treatments is not arbitrary, and from its proper evaluation depends the correct determination of the oxygen-induced diffuse intensity. The oxide peaks, shown in Fig. 7.16(c), evolve in agreement with the reflectivity results described in section 6.2. The NbO_2 components increase after heating at 145°C, before vanishing at 300°C, where the NbO becomes predominant. This confirms the interpretation given in the previous section and the assignment of these features to the oxides. As all measurements were taken at room temperature, the thermal diffuse signal is only proportional to the amount of niobium material probed below the oxide layer. This amount of material can be evaluated as follows. From our X-ray reflectivity results (section 6.2), we know the thickness of the each oxide layer, for the three states of the surface discussed here. The decay of the evanescent field below the surface can therefore be calculated as discussed in section 7.1.2.

Fig. 7.17 illustrates the evanescent field decay for the three different states of the Nb(110) surface under interest. The corresponding effective scattering depths Λ_{Eff} are indicated. After RT oxidation in air, and after heating at 145°C, both Λ_{Eff} are similar and $\sim$1 nm larger than after heating at 300°C. This compensates for the different thicknesses of the total oxide layer for the different states of the surface, i.e. $\sim$2 nm (RT, 145°C) versus

∼1 nm (300°C). However, the field decay through the oxide layers is higher through the NbO oxide for the data measured after heating at 300°C by ∼ 6%, as shown in Fig. 7.17. The weight of the information that originates from the first nanometers below the surface is slightly inferior at 300°C than at lower temperatures. In conclusion, the amount of niobium atoms probed, and therefore contributing to the oxygen-induced diffuse scattering and the TDS signals, is strictly constant for the two first states of the surface (after oxidation and after heating at 145°C), and can be in first approximation[4] considered as constant for the third treatment (after heating at 300°C). This is illustrated for the TDS contribution to the fits, calculated for 297K (see section 4.2), in Fig. 7.16(d).

As mentioned before, the ratio between the oxygen-induced diffuse scattering and the TDS is dermined by the absolute oxygen concentration, one unique scaling factor is then necessary to fit the calculated values to the data. This point has been discussed in details in section 7.1.1. In the present section, only the relative evolution of the diffuse signal is considered.

In what follows the interstitial oxygen behavior is discussed. The intensity of the oxygen-induced diffuse signal doubles after heating at 145°C. Note that this is observed for every single depth considered (not shown here). From the X-ray reflectivity results discussed in section 6.2, one knows that the NbO_2 and NbO oxide layers, and therefore their

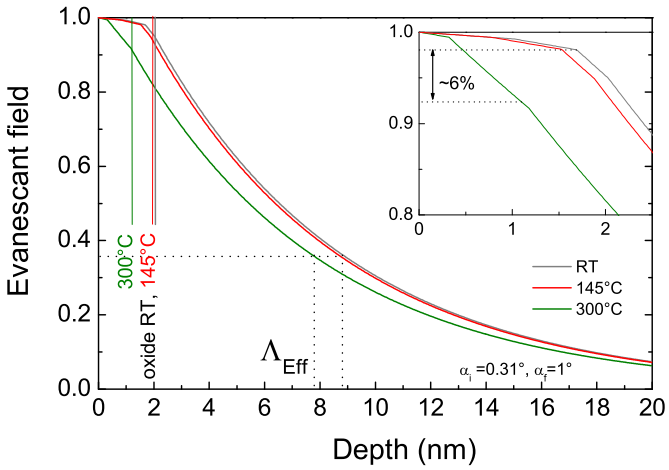

Figure 7.17: Evanescent field decay below the Nb(110) surface for a given incident and exit angle $\alpha_{i,f}$. After RT oxidation in air and after heating at 145°C, the effective scattering depth Λ_{Eff} is similar, and ∼ 1 nm larger than after heating at 300°C. This compensates directly for the difference in oxide thickness and the amount of niobium atoms probed and contributing to the signals is therefore considered as constant for the three different treatments. However, the field decay through the oxide layers is higher by ∼ 6% for NbO.

[4]The maximal error has been estimated above.

contributions to the spectra, are not considerably changing after heating at 145°C. From this, one can intuitively deduce that the average amount of oxygen is roughly doubling. This means that, at this temperature and for this amount of time, the net result of oxygen release from the oxide decomposition, oxygen diffusion into niobium, and/or its segregation to the interface, is an oxygen enrichment within the first 10 nm below the surface, as we discussed in [197]. At 300°C, even though a consequent amount of oxygen is released from the oxide dissolution (section 6.2.3), the diffusion length of oxygen in niobium [60] is in 50 min above 1000 nm, namely two orders of magnitude higher than at 145°C in 5h ($\sim$ 35 nm). The oxygen diffuses therefore much deeper into the bulk and the diffuse signal in the first 10 nm decreases significantly compared to its initial value.

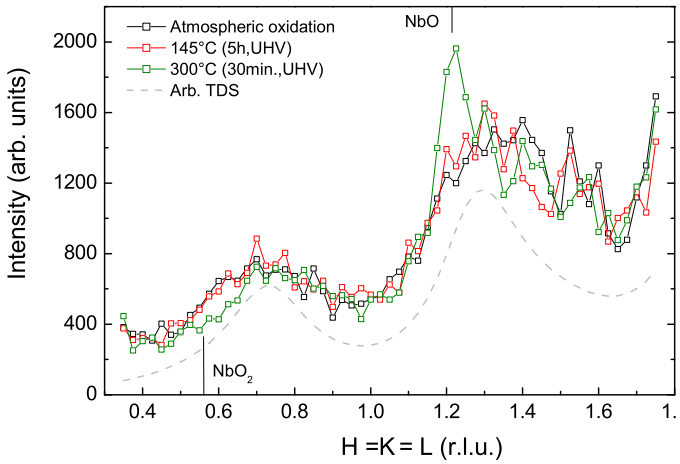

Figure 7.18: Temperature evolution of the diffuse intensity data measured at high incident angle $\alpha_i = 3°$ and $\alpha_f = 1°$ (scattering depth $\sim$ 280nm). Dashed curve : TDS contribution of arbitrary amplitude for comparison. The signals are comparable for the three different states, as "bulk like" and dominated by the TDS. Oxide signals, NbO_2 at RT and 145°C and NbO at 300°C are still visible.

Fig. 7.18 shows a second example of temperature evolution of the diffuse scattering data measured this time at fixed $\alpha_i = 3°$ and $\alpha_f = 1°$, which correspond to a deeper scattering depth $\sim$ 300 nm. The measurements were performed for the same three different treatments as discussed above. The signals are comparable for the three different states. As "bulk-like", they are dominated by the TDS, as this one increases proportionally to the scattering depth (see also section 7.2.3). The TDS scaled to an arbitrary amplitude is plotted for comparison. Oxide signals, NbO_2 after oxidation and after heating at 145°C, and NbO after heating at 300°C are still visible.

7.2.3 Depth-profiling of interstitial oxygen

The depth-resolved diffuse scattering data analyzed in this section, have been presented in Fig. 7.13. The lineshape decomposition of each individual spectra measured along the in-plane $[1\bar{1}1]$ direction has been discussed in section 7.2.1. In addition to the diffuse scattering due to interstitial oxygen and thermal diffuse scattering, oxides contributions have been identified. The depth and temperature dependences of the different contributions have been discussed in detail in sections 7.1 and 7.2.2 respectively. In this section, the absolute interstitial oxygen concentration profile underneath the oxide layer is determined for the Nb(110) surface oxidized in air, and after heating at 145°C, exploiting the comprehensive method and fitting routine described in section 7.1.4.

Atmospheric oxidation

The best fit of the diffuse scattering data measured on the Nb(110) surface after oxidation 10h in air, was found for the interstitial oxygen concentration profile, $c_o(z)$, plotted in Fig. 7.19. The fit decomposition is shown in Fig. 7.20, and the fitting parameters are summarized in Appendix B. The agreement between the model and the experiment is remarkably good. The relative intensity of the TDS with respect to the oxygen-induced diffuse scattering, directly proportional to $c_o(1 - c_o)$ (see section 7.1.1), increases as the average oxygen concentration over the depth probed decreases. At $\alpha_i = 3°$, the data are *bulk-like* and the TDS dominates nearly exclusively the lineshape of the spectra. The

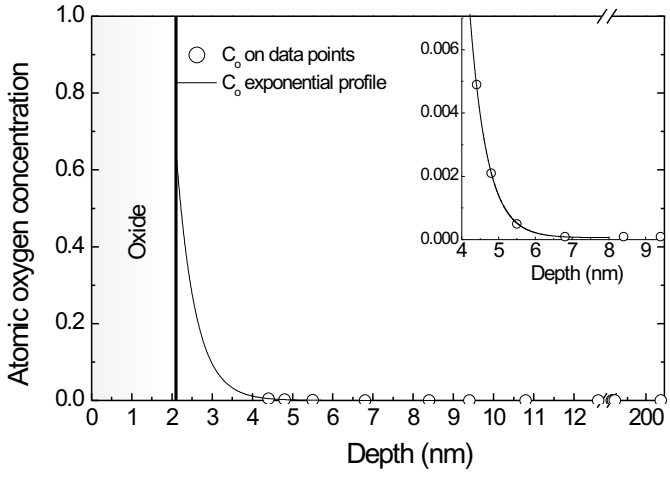

Figure 7.19: Exponential atomic oxygen concentration profile as a function of the depth into niobium below the oxide layer as obtained from the best fit of the diffuse scattering data measured on the Nb(110) surface after oxidation 10h in air, and zoom (see text for details).

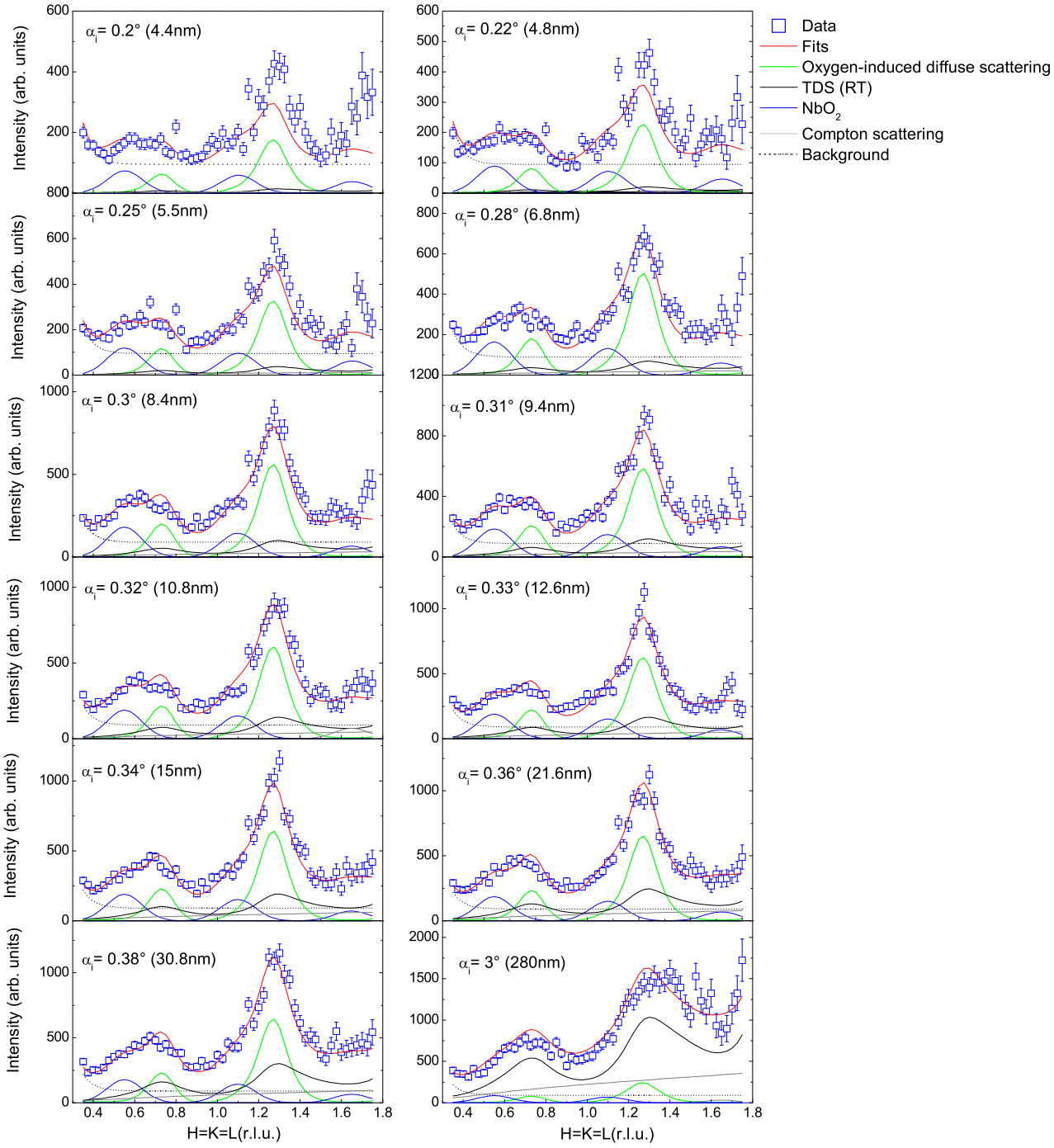

Figure 7.20: Best fit (red solid line) for the diffuse scattering data measured on the Nb(110) surface oxidized 10h in air (RT) (open squares). The data were corrected for the polarization and active area. All data were fitted whit a unique depth-dependent function including the oxygen-induced diffuse scattering (green line) associated to an exponential profile, the thermal diffuse scattering (black line), oxides contributions (blue solid lines), background (dotted line) and Compton scattering (grey line) (see text for details about the fitting procedure).

depth-profile of the measured intensity and the fit value at $Q^* = \frac{4}{3}(1, \bar{1}, 1)$ are plotted in Fig. 7.21 with respect to the scattering depth. The contributions of the oxygen-induced diffuse scattering and the TDS are illustrated. Note that this includes the transmission factors, etc., as described in Eq. (7.14).

The effective exponential decay length of the oxygen concentration profile shown in 7.19, is equal to ~ 0.5 nm, indicating that most of the interstitial oxygen is located in the direct vicinity of the oxide/niobium interface. It is important to keep in mind that, even though no data were recorded for scattering depths below 4 nm, every measured intensity is given by the Laplace transform of the complete concentration profile, as a function of the scattering depth (see expression 7.3). Information about the oxygen concentration for the region between the oxide interface and 4 nm is therefore carried by the measured data. The atomic oxygen concentration decreases gradually from the oxide content to a bulk concentration $\leq 0.01\%$. This is in line with the interstitial oxygen concentration generally equal to a few ppm observed at the end of the annealing cycles performed previously to the sample oxidation (section 5.4). The integration of the oxygen profile over the first 10 nm is equivalent to an average oxygen concentration equal to

$$\langle O_i \rangle_{10nm} = 3.6 \text{ at.}\% \tag{7.19}$$

A concentration value superior to the 50% concentration of the oxygen in NbO (shown in chapter 6 to be the oxide species present at the interface between the oxide layer and

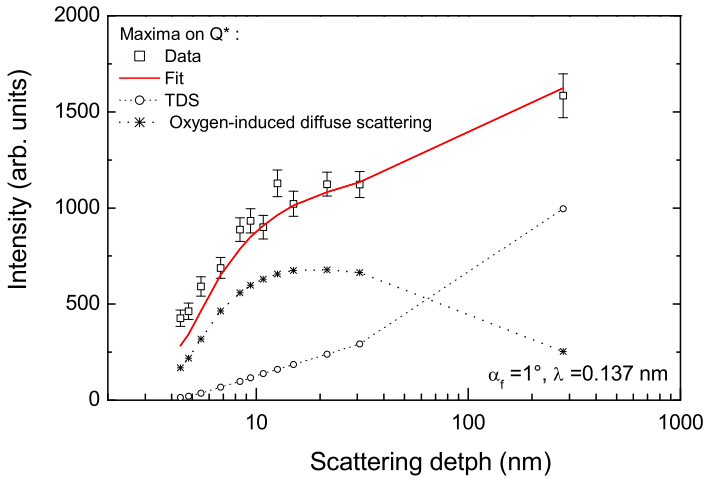

Figure 7.21: Depth-profile of the maximal intensity at $Q* = \frac{4}{3}(1, \bar{1}, 1)$ for the data measured on the Nb(110) surface oxidized 10h in air (RT) (open squares) and fits (red). The depth-profile of the oxygen-induced diffuse scattering (stars) and the TDS contributions are plotted (see text for details). The fit was calculated for the data points, lines are eye-guides (see text for details).

niobium), is observed in the direct vicinity of the interface. This can be explained as an artefact due to the hypothesis made in 7.17 of an exponential shape of the profile. A step-like profile in the direct vicinity of the interface can not be excluded. The amount of intersitial oxygen involved then, could not be accommodated by a exponential profile without an overestimated concentration at the interface. The sensitivity of the model parameters and the degree to which different fits of the same set of data scatter can be used to estimate the error bars of the fit parameters. An error of $\pm \sim 1$ at.% can be estimated on the value given in (7.19).

Note that the agreement between the data measured at very small angle and the model is not perfect (see Fig. 7.20). The explanation for this most probably lies in some of the approximation made in the model (section 7.1). For example, interfacial effects associated to a highly strained interface as observed between the NbO and niobium in chapter 6. The theoretical calculation of the diffuse scattering has been performed using bulk properties of niobium, neglecting interfacial effects, which probably locally affects the elastic constants of the material. These are open questions and would require further investigations. In the case of the oxygen-diffuse scattering calculation, surface effects have been investigated performing calculation within the slab geometry [164]. From this *free* surface, effects are shown to be confined in the very first atomic layers.

After heating at 145°C (5h, UHV)

The best fit of the diffuse scattering data measured on the Nb(110) surface after heating at 145°C (5h,UHV) was found for the interstitial oxygen concentration profile plotted in Fig. 7.22. The concentration profile for the surface after oxidation in air is shown for comparison. The fit decomposition is shown in Fig. 7.23, and the fitting parameters are summarized in Appendix B. Considerations described in section 7.2.2 on the constrains that applied on the fitting parameters with respect to the temperature evolution have been accounted for in the fitting procedure. The agreement between the model and the experiment is remarkably good. The depth-profiles of the measured intensity and the fit value at $Q^* = \frac{4}{3}(1, \bar{1}, 1)$ are plotted in Fig. 7.23 with respect to the scattering depth. The contributions of the oxygen-induced diffuse scattering and the TDS are illustrated.

The effective exponential decay length of the oxygen concentration profile is ~ 0.9nm, indicating that most of the interstitial oxygen is located in the direct vicinity of the oxide/niobium interface, as observed for the surface after oxidation in air. The atomic oxygen concentration decreases gradually from the oxide content to a bulk concentration $\leq 0.01\%$. The integration of the oxygen profile over the first 10 nm corresponds to an average oxygen

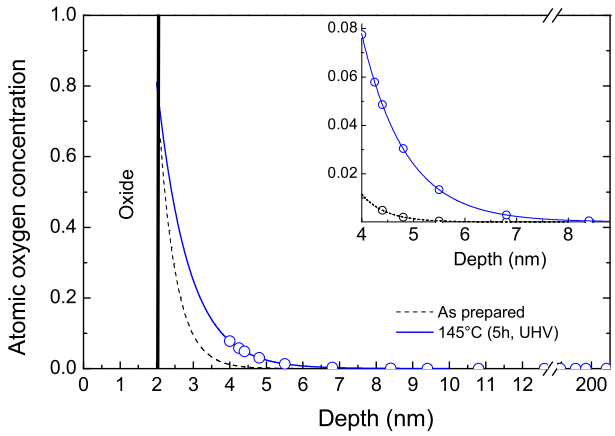

Figure 7.22: Exponential atomic oxygen concentration profile as a function of the depth into niobium below the oxide layer as obtained from the best fit of the diffuse scattering data measured on the Nb(110) surface after heating at 145°C (5h,UHV), and zoom. Dashed line: profile after oxidation 10h in air for comparison (see text for details).

concentration equal to

$$\langle O_i \rangle_{10nm} = 7.6 \text{ at.}\% \tag{7.20}$$

A net enrichment in interstitial oxygen is observed underneath the metal/oxide interface after heating at 145°C. The average concentration in the first 10 nm is doubling after the low temperature treatment. This corresponds to an average increase of 4% of the oxygen concentration in the first 10 nm. This increase can be directly compared to the oxygen released from the oxide dissolution after heating at 145°C, determined from the X-ray reflectivity analysis described in section 6.2.3. An amount of 8^{14} at./cm^2 oxygen atoms was shown to be liberated, which corresponds to an average increase of the oxygen concentration of $\sim 1.5\%$ over 10 nm. Within the error bars, these results show a surprisingly good agreement.

Discussion

High concentrations of subsurface interstitial oxygen are observed in the direct vicinity of the niobium/oxide interface of the Nb(110) surface after atmospheric oxidation. This observation is in agreement with previous studies on Nb(100) single crystals [62], on Nb(110) films oxidized above 100°C in air [15], on Nb(110) single crystal after high temperature UHV annealing [16], and for polycrystalline high residual resistivity ratio samples investigated in a recent atom probe tomography study [17]. The concentration profiles of both set of data discussed here decay rapidly, i.e. with a decay length of ∼1 nm below the interface, from the oxide layer concentration to the low concentration of the bulk. A previous study on the segregation of oxygen at interfaces by means of Auger Electron Spectroscopy com-

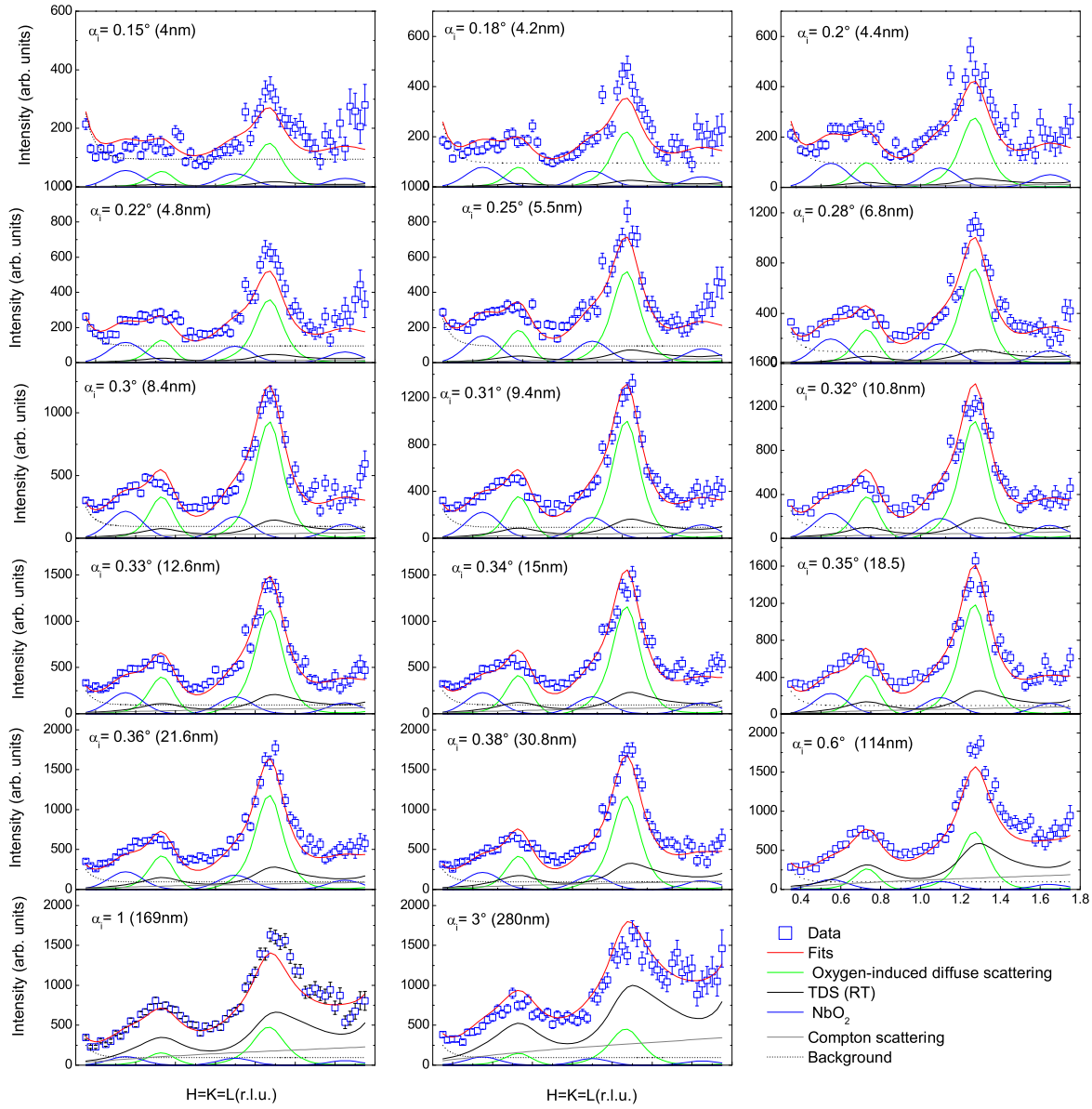

Figure 7.23: Best fit (red solid line) for the diffuse scattering data measured on the Nb(110) surface after heating at 145°C (5h, UHV) (open squares). The data were corrected for the polarization and the active area. All data were fitted whit a unique depth-dependent function including the oxygen-induced diffuse scattering (green line) associated to an exponential profile, the thermal diffuse scattering (black line), oxides contributions (blue solid lines), background (dotted line) and Compton scattering (grey line) (see text for details about the fitting procedure).

bined to ion sputtering [64] has shown that the segregation of oxygen of annealed surfaces is extremely localized (1-1.5 nm).

After heating at 145°C (5h, UHV) no depletion, but an increase in the oxygen concentration is observed in the direct neighborhood of the metal/oxide interface. Interstitial oxygen originates from the dissolution of the oxide layer, and does not diffuse further in

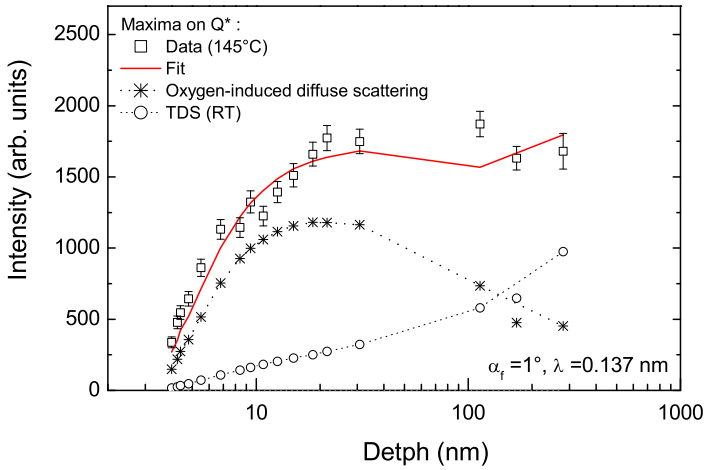

Figure 7.24: Depth-profile of the maximal intensity at $Q* = \frac{4}{3}(1, \bar{1}, 1)$ for the data measured on the Nb(110) surface after heating at 145řC (5h, UHV) (open squares), fits (red), oxygen-induced diffuse scattering (stars), and TDS contributions. The fit was calculated for the data points, lines are guides for the eye (see text for details).

the niobium bulk than the first nanometers underneath the interface although the bulk concentration is well below its saturation value. Different arguments can be proposed to explain this observation. On one hand, the oxygen released from the oxide dissolution, which takes place as discussed in section 6.2.3 at the Nb_2O_5/NbO_2 interface, has to cross the NbO_2 oxide layer and the diffusion barrier formed by the NbO at the interface with niobium [113]. On the other hand, as mentioned before, several studies performed under ultra high vacuum have underlined the oxygen segregation at the niobium surface after annealing at temperatures above already 300°C [61–66]. These studies showed that oxygen in niobium prefers to segregate toward the crystal surface in relatively high concentration although the solubility limit in the bulk is not reached. This is in line with what has been determined in this section.

7.3 Summary

In this chapter, the unambiguous monitoring of subsurface interstitial oxygen in niobium and its evolution upon heating have been presented. A non-destructive *in-situ* method to determine the absolute oxygen concentration profile has been developed, exploiting the diffuse X-ray scattering from the characteristic local lattice distortions occurring around interstitial oxygen defects in niobium.

The observation of the weak diffuse scattering intensity in combination with total external reflection is only feasible exploiting the highly brilliant synchrotron radiation. The grazing incidence X-ray diffuse scattering measurements on the the Nb(110) surface oxidized in air have been performed at the MF-MPI beamline at the synchrotron ANKA, Germany.

A first insight into the interplay between the oxide formation/dissolution and the emergence of subsurface oxygen has been given. Since niobium does not release oxygen to the surrounding environment below 1600°C [57, 67, 68], the oxygen liberated from the oxide dissolution discussed in chapter 6, gets dissolved into niobium (see Fig. 7.25). For its unambiguous detection, the diffuse X-ray scattering maxima at the $\mathbf{Q}^*_{bcc} = \frac{2}{3}(1,1,1)$ positions are used as quantitative fingerprints.

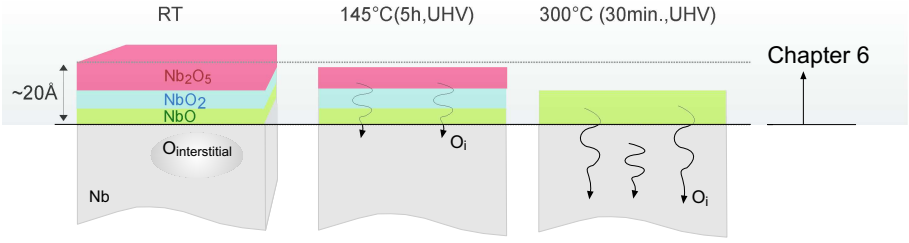

Figure 7.25: From the results given in chapter 6 and 7, a first insight into the interplay between oxide formation/dissolution and the occurrence of interstitial oxygen has been given.

The lineshape decomposition of each individual spectra measured along the in-plane $[1\bar{1}1]_{bulk}$ direction has been discussed in section 7.2.1. In addition to the oxygen-induced diffuse scattering and the thermal diffuse scattering, oxides contributions have been identified. The depth and temperature dependences of the different components have been discussed in sections 7.1 and 7.2.2 respectively.

The depth-distribution of interstitial oxygen below the natural oxide layer of the Nb(110) surface initially oxidized in air, and its evolution after heating at 145°C (5h, UHV), has been established. Assuming an exponential profile, the decay length of the interstitial oxygen below the oxide layer was found to be inferior to 1 nm, indicating that most of

the oxygen is located in the direct vicinity of the oxide/niobium interface. Large amounts of subsurface interstitial oxygen are observed underneath the interface even though the concentration in the bulk is far below the solubility limit.

A clear subsurface interstitial oxygen enrichment within the first 10 nm is observed after heating at 145°C (5h, UHV). The average concentration over the first 10 nm increases by 4%, which is of the same order of magnitude as the amount of oxygen released by the oxide dissolution (section 7.2.3).

Important observations have been made by consideration of single data curve, i.e. at a fixed scattering depth, measured after heating at 300°C. The NbO_2 signal vanishes, while the NbO$(2\bar{2}0)$ Bragg contribution gets very pronounced, both in agreement with the reflectivity and core level results discussed in the previous chapter. In parallel, the diffuse scattering signal from interstitial oxygen decreases drastically, although a consequent amount of oxygen is released from the oxide dissolution. This can be explain by an enhanced diffusion of oxygen toward the niobium bulk.

One can conclude from these results that the oxygen distribution and its chemical/physical state in the surface and subsurface regime of niobium is highly sensitive to low thermal treatments. The amount of subsurface interstitial oxygen is a sensitive balance between the oxygen release from the oxide dissolution and the oxygen diffusion into the niobium bulk. A convenient X-ray technique has been presented that can be applied for further investigation of samples prepared e.g. under production conditions of niobium rf cavities.

Chapter 8

Complementary experimental results

The oxidation of niobium surfaces, and metals in general, is sensitive to various parameters such as the surface orientation or the oxidation active environment. The reactivity of oxygen with surfaces, as well as the mass transport through the oxide are often increased by the presence of water, encountered in various steps of the preparation of superconducting niobium rf cavities.

In this chapter, complementary experimental results are presented on three different systems. In section 8.1, the less dense Nb(100) surfaces oxidized in air and the evolution of their near surface region upon thermal treatments are investigated by mean of x-ray reflectivity and grazing-incidence diffuse x-ray scattering. In section 8.2, $in-situ$ measurements of the diffuse scattering intensity recorded during vacuum annealing of the Nb(110) surface oxidized in dry oxygen atmosphere are presented. In section 8.3, the Nb(110) surface oxidized in clean water is investigated by means of x-ray reflectivity and high-resolution core-level spectroscopy measurements.

The different methods and experimental details have been discussed in chapters 4 and 5, and their exploitation in the two previous chapters of experimental results.

8.1 Experimental results on Nb(100)

In this section, the experimental results on the natural oxide on Nb(100) single crystals oxidized in air and the evolution of the near surface region upon vacuum annealing are presented. The results are organized as follows: in the first part of the section, the oxide layer and its thermal stability are investigated by mean of x-ray reflectivity measurements. In the second part, the behavior of interstitial oxygen below the oxide layer is discussed on the basis of grazing-incidence diffuse x-ray scattering measurements.

A Nb(100) single crystal with a diameter of 13.7 mm and a thickness of 2mm was polished and purified as described in section 5.4. The sample was subsequently oxidized in air

during 14 days at room temperature and then mounted in the portable UHV x-ray diffraction chamber. The x-ray reflectivity and grazing incidence x-ray scattering experiments have been performed at the MPI-MF beamline at the Ångstrømquelle Karlsruhe ANKA, at a photon energy of 10keV. The following sequence of thermal treatments were applied on the oxidized surface under high vacuum conditions[1]: room temperature (RT), 120°C (4h30), 200°C (6h), and 300°C (45min.). All measurements were performed after cooling down the sample in a *frozen* state to RT.

8.1.1 XRR results

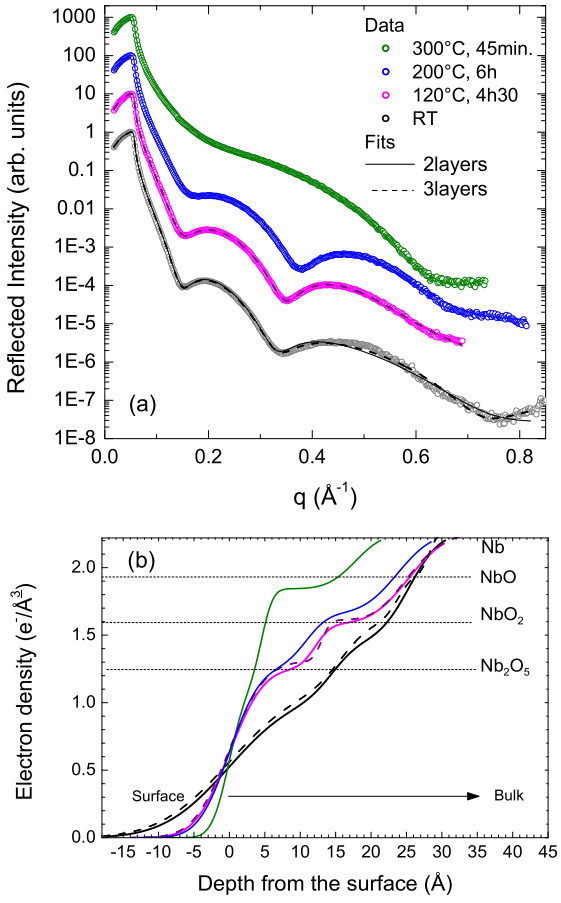

Figure 8.1: (a) X-ray reflectivity data measured on a Nb(100) single crystal oxidized in air at RT during 14 days for different mild thermal treatments (open circles) and fits assuming a two layer model (solid lines), and a three layer model (dashed lines) in the Parratt formalism. The curves were vertically shifted for clarity. (b) Electron density profiles along the surface normal obtained from the fits (see text for details).

[1] 1-5× 10^{-7}mbar.

The X-ray reflectivity spectra measured on the Nb(100) surface after atmospheric oxidation at room temperature, and after heating at 120°C (4h30, HV), at 200°C (6h, HV), and at 300°C (45min., HV) are shown in Fig. 8.1 (a). The data have first been fitted assuming a two layer model in the Parratt formalism. The thickness of the layers, the roughness of the surface and of the interfaces, as well as the density parameters of the oxides were free, the electron density profiles obtained from the fit are presented in Fig. 8.1 (b) (see also Appendix A). The best fit, however, was obtained with a three layer model for the native oxide layer and the subsequent heating at 120°C. This model is discussed subsequently to the two layer model. Both are illustrated in Fig. 8.1 (a,b). The thicknesses and roughnesses for all different treatments discussed above are summarized in Tab. 8.1.

After 14 days in air, the Nb(100) single crystal has, following our model, a total oxide thickness of 25±1 Å. The outermost oxide layer is the thickest one with 14.7±1 Å and can be identified as Nb_2O_5, highest and more stable oxidation state of Nb. The inner layer has a lower electron density close to NbO_2 with a thickness of 10.7±1 Å. The corresponding roughnesses are high with respectively 7 Å, 3 Å and 4 Å for the metal/oxide interface. After heating at 120°C the total thickness of the oxide layer stays nearly unchanged and only a rearrangement between the two oxide layers is observed, corresponding to the dissolution of the higher oxidation state Nb_2O_5 layer together with at thickening of NbO_2. Simultaneously, a drastic decrease of the roughness at the surface, but also at the interface between those two layer is observed (see Figure 8.1). After heating at 200°C, the Nb_2O_5 layer continue its progressive dissolution, and NbO_2 stops to grow. At higher temperature, i.e. $300°C$, both Nb_2O_5 and NbO_2 oxide layers reduce. The total thickness decreases by 30% and the second layer has an electron density close to the one of NbO, lower oxidation state of Nb. The reason why this value is slightly inferior to the electron density of NbO bulk, i.e. smaller atomic density, can be either the existence of a mixture of NbO and residual NbO_2, or a defective NbO structure. The reflectivity results do not allow to distinguish between these two cases.

Although the two layer model offers a reasonable fit to the data, the best fit for the native oxide curve in terms of chi-square was obtained assuming a three layer model compatible with the following sequence of oxide layers: Nb_2O_5, NbO_2 and NbO, from the surface to the metal/oxide interface. The total thickness of the oxide layer is consistent with the one obtained from the two layer model. The individual thicknesses are 16Å, 7.8Å and 4.3Å (error bar ± 1Å). The respective roughnesses are 7.8Å, 3.2Å, 2.8Å and 2Å for the interface. All results are summarized in Tab. 8.1. The introduction of the third NbO layer is accompanied by a decrease of the interfacial roughness compare to the one observed for the two layer model. This can be understood by the fact that the presence of a thin NbO

Oxide	RT		120 °C (4h30)		200°C (6h)	300°C (45min.)
	2 layers	3 layers	2 layers	3 layers	2 layers	2 layers
Nb_2O_5	14.7 (7.2)	*16 (7.8)*	12.1 (3.8)	*13 (4)*	10 (3.4)	4.6 (1.9)
NbO_2	10.7 (2.9)	*7.8 (3.2)*	13.1 (1.7)	*10.5 (1)*	12.8 (2.4)	-
NbO	-	*4.3 (2.8)*	-	*4.3 (3.4)*	-	13.2(1.3)
Substrate	(3.4)	*(2)*	(4.2)	*(3.4)*	(3.8)	(3.1)
Total (Å)	25.4	*25.4*	25.2	*25.2*	22.8	17.8

Table 8.1: Thicknesses (roughnesses) in Å (error bar of ± 1Å) of the different niobium oxides obtained from the X-ray reflectivity analysis for different thermal treatments, for a two and a *three* layer model in the Parratt formalism.

layer of intermediate electron density between NbO_2 and Nb can be seen as a roughness of their interface. As a result, both electron density profiles are rather similar, as can be seen in Fig. 8.1.

As it has been shown in different studies and already discussed in the results on the Nb(110) surfaces, niobium does not release oxygen below 1600°C. The oxygen liberated during the oxide dissolution is therefore assumed to get dissolved into the Nb bulk below the Nb/oxide interface. This result is in agreement with the observations made on the oxygen-induced X-ray diffuse scattering measurements discussed in the next section.

The total amount of niobium and oxygen atoms involved into the oxide layer, summing the contributions of the Nb_2O_5, NbO_2 and/or NbO layers in the two-layer model, as a function of temperature, is illustrated in Fig. 8.2. It is interesting to note that after the low-temperature treatment, namely at 120°C, the oxide reduction that occurs from Nb_2O_5 to NbO_2 does not release any oxygen. Indeed, the net amount of oxygen liberated from the Nb_2O_5 dissolution with respect to the NbO_2 growth can be calculated in the same way

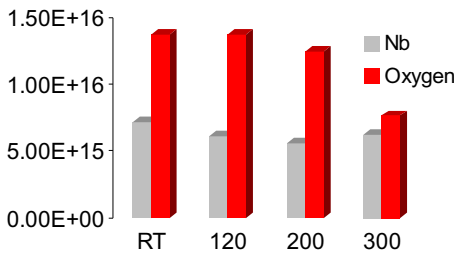

Figure 8.2: Temperature evolution of the total amount of niobium and oxygen atoms involved in the oxide layer summing the contributions of the Nb_2O_5, NbO_2 and/or NbO layers assuming a two-layer model (see text for details).

as described in section 6.2.3. A decrease of the Nb_2O_5 thickness by 2.6Å in the case of the two layer model corresponds to 1.35×10^{15} O at./cm^2 which is equivalent to the amount of oxygen necessary to an increase of the NbO_2 thickness by 2.4Å. In the same way a decrease of the Nb_2O_5 thickness by 3Å for the three layer model corresponds to $\sim 1.5\times10^{15}$ O at./cm^2 which is equivalent to the amount of oxygen necessary to increase the thickness of NbO_2 by 2.66Å. This observation is of primary importance for the understanding of the diffuse scattering results discussed hereafter. After heating at 200°C and 300°C, the amount of oxygen liberated from the oxide dissolution is equal respectively to 1.26×10^{15} O at./cm^2 and 4.7×10^{15} O at./cm^2.

8.1.2 Grazing incidence diffuse X-ray scattering

In parallel to the oxide dissolution characterized in the previous part, the behavior of the interstitial oxygen atoms dissolved below the oxide layer upon vacuum annealing, is investigated by mean of grazing incidence X-ray diffuse scattering. The temperature evolution of the oxygen-induced diffuse X-ray scattering measured around $\mathbf{Q}^* = 4/3(1,1,1)$ along the [111] direction is shown in Fig. 8.4 and 8.5 for two different incident angles $\alpha_i = 0.3°$ and $\alpha_i = 0.5°$, which corresponds to scattering depths of ∼10 nm and ∼200 nm respectively. The data have been corrected for the polarization factor.

Before discussing these results one should precise that the [111] direction, along which the oxygen-induced diffuse X-ray scattering is measured, does not lie in the Nb(100) surface plane, in contrast to Nb(110) surfaces (see section 7). Both surface orientations are represented in Fig. 8.3. A linescan along the [111] direction implies therefore for the Nb(100) surface a continuous change in the z-component of the momentum transfer Q_z, achieved by a continuous change in the exit angle. For incident angles below the critical angle $\alpha_c \sim$

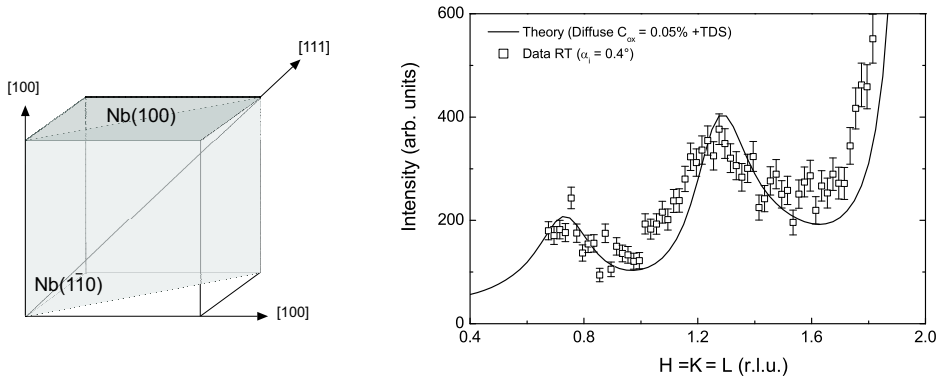

Figure 8.3: Left : Scanning direction along the [111] for the Nb(100) surface. Rigth : Comparison between data and theoretical sum of the diffuse scattering for an average oxygen concentration ($C_o = 0.05\%$) and the TDS.

0.32°, the scattering depth is constant for increasing exit angles above α_c (see Fig. 4.10). In this case, the probed depth does not depend on the exit angle, always above α_c for the given scan. For incident angles above the critical angles however, the scattering depth increases with increasing exit angles. This effect can explain the systematic discrepancy observed in Fig. 8.3 between the data corrected for the polarization and the calculated diffuse scattering (average oxygen concentration of 0.05% and including the thermal diffuse scattering). This complicates the determination of an absolute interstitial oxygen depth-profile in comparison with Nb(110) surfaces. In this section, numerous qualitative information are gained from the data presented, for which this effect can be neglected. The scattering depths were calculated for the exit angle corresponding to $\mathbf{Q}^* = 4/3(1,1,1)$ (r.l.u.).

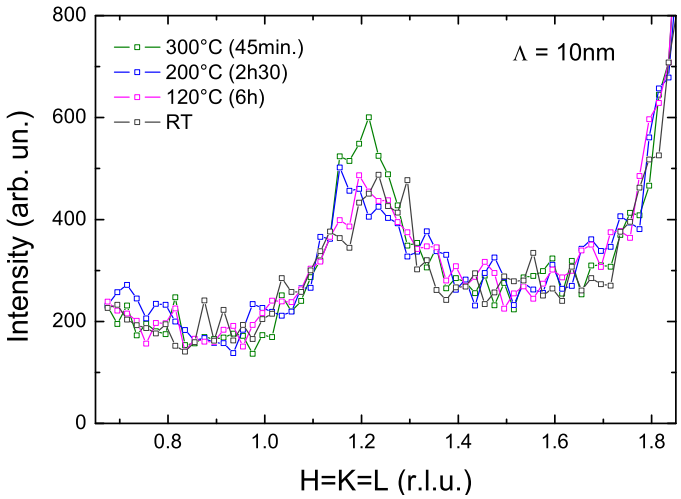

Figure 8.4: Diffuse Scattering data measured along the [111] direction for different thermal treatments at an incident angle $\alpha_i = 0.3°$ (scattering depth $\sim$ 10 nm). The measurements were done after cooling the sample to RT.

As already mentioned before, niobium does not release oxygen in UHV below 1600°C [57,68], and the oxygen liberated by the oxide reduction described in the previous section, necessarily gets dissolved into niobium across the niobium/oxide interface. The diffuse intensity measured after heating at 120°C (6h, high vacuum), does not show any changes neither in the first 10 nm or 200 nm (see Fig. 8.4 and 8.5). This observation is in agreement with the reflectivity results which showed that for these conditions, no oxygen was released from the oxide reduction, the dissolution of Nb_2O_5 being exactly balanced by growth of NbO_2. This also means that, after the low-temperature treatment, no depletion (neither segregation) of oxygen initially present interstitially below the metal/oxide interface is observed into those regions. This observation contradicts the proposed explanation for the

effect of the low-temperature treatment on the performances of niobium rf cavities [4, 29].

After heating at 200°C, a large oxygen release from the oxide dissolution has been calculated in section 8.1.1. The diffuse intensity, however, does not show significant increase in the first 10 nm below the metal/oxide interface. This can be explained by an enhanced oxygen diffusion into niobium at this temperature. The diffusion length of oxygen in niobium is indeed at 200°C during 6h equal to $\sim$ 260 nm, nearly 7 times more then at 145°C during 5h (see Eq. (3.1)). Up to this temperature, the oxygen atoms seem therefore to maintain an equilibrium concentration profile in the near surrounding of the metal/oxide interface. The intensity measured at a higher incident angle $\alpha_i = 0.5°$ (scattering depth of $\sim$200 nm), however, shows a net increase of the signal. This highlights the emergence of a diffusion front of interstitial oxygen, propagating from the metal/oxide interface toward the niobium bulk. The net increase of the diffuse intensity is associated to an enrichment in the "average" amount of interstitial oxygen in the region between 10 nm and 200 nm below the interface.

After heating at 300°C (45min., high vacuum), the maximum of the diffuse intensity is clearly increasing for both scattering depths considered in Fig. 8.4 and 8.5, indicating a net oxygen enrichment in the near surface region in parallel to the oxygen release from the oxide dissolution. This shows a different behavior than the one observed on the Nb(110) surface for similar conditions, for which the oxygen had fully diffused into the bulk. Another difference is the amount of niobium atoms contributing the oxide layers (Fig. 8.2), which is increasing for the Nb(100), while it was decreasing for the Nb(110) surface. This is probably linked to the growth of the oxide, namely the NbO oxide, stable under Nb atoms

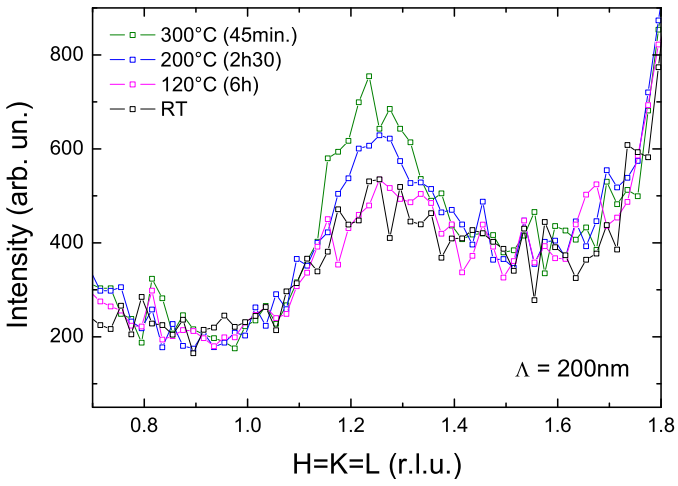

Figure 8.5: Diffuse scattering data measured along the [111] direction for different thermal treatments at $\alpha_i = 0.5°$ (scattering depth $\sim$ 200 nm). The measurements were all done after cooling the sample to RT.

excess. It is interesting to see that for the same conditions the XRR results indicate much faster NbO growth for the (100) surface as for the (110).

8.1.3 Discussion

In this section, the natural oxide on a Nb(100) single crystal oxidized under room temperature atmospheric conditions, and its progressive dissolution upon vacuum annealing have been investigated by mean of X-ray reflectivity (XRR). The simultaneous behavior of interstitial oxygen dissolved below the oxide layer has been characterized by grazing incidence diffuse X-ray scattering (GIDXS).

The natural oxide layer formed on the Nb(100) surface oxidized in air (14 days, RT) present a layered structure, constituted of Nb_2O_5, NbO_2 and NbO, from the surface to the metal/oxide interface, similar to the one observed on Nb(110) surfaces oxidized in air (see chapter 6). The Nb(100) oxide layer (25 Å) is only slightly thicker than the Nb(110) oxidized 10h in air (20Å). This can be explained by the drastic slow down of the atmospheric oxidation of niobium after the formation, in the first hours, of the first 2 nm [89]. The effect was observed by complementary XRR measurements (not shown) on the Nb(110) surfaces exposed to air for 3, 6 and 10 h, forming respectively 15 Å, 18 Å and 21 Å thick oxide, and confirms observations reported on the oxidation of Nb(110) thin films in air [116]. Note however that the uptake of oxygen, as well as the oxidation at 350°C to 450°C, have been shown to strongly depend on the orientation of niobium surfaces, being the fastest for Nb(111) surfaces, followed by Nb(110) surfaces, the slowest being the Nb(100) surface [198].

The stability of the native oxide layer as a function of temperature shows similar behavior for the Nb(110) and Nb(100) surfaces oxidized in air. Below a temperature of 200°C the total thickness of the oxide layers is only slightly changed, by less than 8% at 145°C (5h) on Nb(110) and not all at 120°C (4h30) on Nb(100). The main changes observed after heating is the Nb_2O_5 reduction into the lower oxidation state NbO_2 that increases by 7% for the Nb(110) surface and up to more than 20% for the Nb(100) surface. The dissolution of the Nb_2O_5 oxide layer, occurs therefore on Nb(100) faster and earlier, i.e. at lower temperatures, than on Nb(110). Note that similar observations have been made on HRCLS results on Nb(100) surfaces oxidized in water (not shown). After heating at 300°C, regardless of the duration, the remaining oxide on both surface is mainly the lowest stable oxidation state of niobium, namely NbO. In the case of the Nb(110) surface the NbO layer was shown to present Nishiyama-Wasserman epitaxial orientation relationships with respect to the niobium substrate. In contrast to the results on Nb(110), no GIXD measurements were realized on the Nb(100) surface, such that the existence of an epitaxial oxide layer

on Nb(100) has not been yet investigated. The clean Nb(001) surface and its interaction with oxygen has been studied with valence-band and core-level photoemission [105, 109]. After oxidation at low oxygen pressure, for several hours and subsequent cycles of annealing at high temperatures under high vacuum conditions, two suboxides states were found and assigned to Nb_2O and NbO. In another study, oxygen-induced NbO(100) epitaxial nanocrystals on Nb(100) with $[011]_{fcc} \parallel [010]_{bcc}$ have been observed during cleaning of the surface at elevated temperatures by means of LEED, AES and STM [95]. This confirms the occurrence of NbO as first oxidation step on Nb(100) surfaces and its probable existence at the metal/oxide interface in the natural oxide, as proposed by the three layer model for the XRR results.

An insight into the behavior of the interstitial oxygen dissolved below the oxide layer has been given by mean of grazing incidence diffuse X-ray scattering measurements. No oxygen got released from the oxide reduction process after heating at 120°C, and in parallel, no enrichment or depletion in the average oxygen concentration were observed neither in the first 10 nm, nor in 200 nm below the surface. This contradicts the argument that a depletion in oxygen in the near interface region, due to diffusion toward the bulk during the low-temperature heating, is responsible for the improvement of the cavity properties [26]. However, from the results presented here only the average concentration over the region considered is available. A redistribution of the oxygen within the first 10 nm giving rise to the same average concentration can not be excluded (see also chapter 7). A striking result is the direct observation of the diffusion front of interstitial oxygen from the metal/oxide interface toward niobium bulk. After heating at 200°C indeed, no enrichment is observed in the first 10 nm below the surface, although a considerable amount of oxygen has been liberated from the oxide dissolution. The net increase of the diffuse signal, however, is observed for a scattering depth of 200 nm indicating a clear increase in the average concentration of interstitial oxygen in this region and the diffusion of the released oxygen toward the bulk region. For temperature up to 200°C the distribution of the oxygen at the direct neighborhood of the interface seems to regulate to an equilibrium constant average concentration. At 300°C, however, an general increase in the signal at 10 nm and 200 nm is noticed, in contrast to what was observed on the Nb(110) surface. This is accompanied by a faster growth from the NbO than for Nb(110), which is most probably directly related to the high amount of oxygen at the interface.

8.2 Results on Nb(110) oxidized in dry oxygen

In-situ measurements of the diffuse scattering were performed during annealing of the Nb(110) surface oxidized in *dry oxygen* atmosphere (P_{o2}= 22 mbar). The results are presented in section 8.2.2. Prior to these measurements, the surface was "cleaned" *in-situ* by high temperature annealing ($\sim$ 2000°C) and the surface characterized by means of X-ray reflectivity (section 8.2.1). The X-ray reflectivity and grazing incidence diffuse X-ray scattering measurements were carried out on ID32 at the ESRF (beamtime E1, see 5.1).

8.2.1 High temperature annealing (2000°C)

As mentioned earlier, obtaining a clean niobium surface requires to anneal the sample above 2000°C under UHV conditions [57, 67, 68]. For this purpose, a high-temperature experimental setup for the portable UHV X-ray diffraction chamber was developed within this work (see section 5.2). Temperatures up to 2000°C could be currently reached. The best vacuum that could be maintain in the chamber for few minutes at this temperature is $\sim 5.10^{-7}$mbar.

The Nb(110) single crystal surface was prepared as described in section 5.4, exposed to air for 3h, and then mounted in the UHV chamber. X-ray reflectivity data measured on the Nb(110) surface after repeated annealing cycles (20th) at 2000°C (5min.), and after oxidation in dry oxygen atmosphere are shown in Fig. 8.6. Traces of a residual oxide layer are still visible after 20 cycles of annealing, as demonstrated by the oscillations presented by the spectrum. The characterization of the epitaxial relationships between the NbO

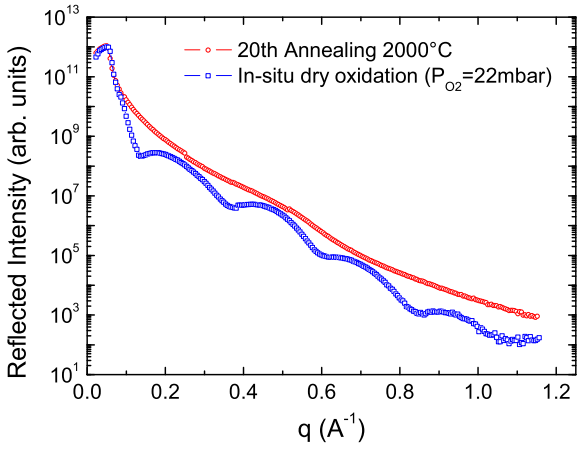

Figure 8.6: X-ray reflectivity data measured on the Nb(110) after 20 annealings cycles ($\sim$ 2000°C, 5 min., HV) and after in-situ dry oxidation (P_{o2}= 22 mbar, RT for $\sim$ 1h).

oxide with respect to the underlying niobium substrate has been discussed in section 6.3.1 (see Fig. 6.18 and 6.19). Oxygen-induced NbO structures on Nb(110) due to surface segregation after high temperature vacuum annealing were reported by different authors ([66, 69, 96, 112]).

After the repeated annealing cycles, the sample was oxidized in dry atmosphere (P_o=22mbar, RT, $\sim$ 1h). A rough estimation indicates the presence of $\sim$25 Å thick oxide layer, which is considerably thicker than what is observed for a comparable amount of time in air, but similar to the thickness observed after 10h in air. Note that a faster oxidation of Nb(110) thin films in pure oxygen atmosphere than in air has been reported [15].

8.2.2 Grazing incidence diffuse X-ray scattering

Fig. 8.7 shows the evolution during annealing of the diffuse scattering signal measured along the [1$\bar{1}$1] direction at fixed incident $\alpha_i = 0.6°$ and exit angle $\alpha_f = 0.2°$, which corresponds to a scattering depth of $\sim$ 6 nm. The data have been corrected for the polarization factor. Measurements were recorded at 200°C (30 min.), 300°C (30 min.) and 350°C (2h30) (HV). The sample was realigned at each given temperature. After the dry oxidation and while heating at 200°C, the linescans present a similar lineshape characteristic of the presence of the NbO_2 oxide at the surface, as discussed in detail in section 7.2.1 for the Nb(110) surface oxidized in air. The oxygen-induced diffuse signal at

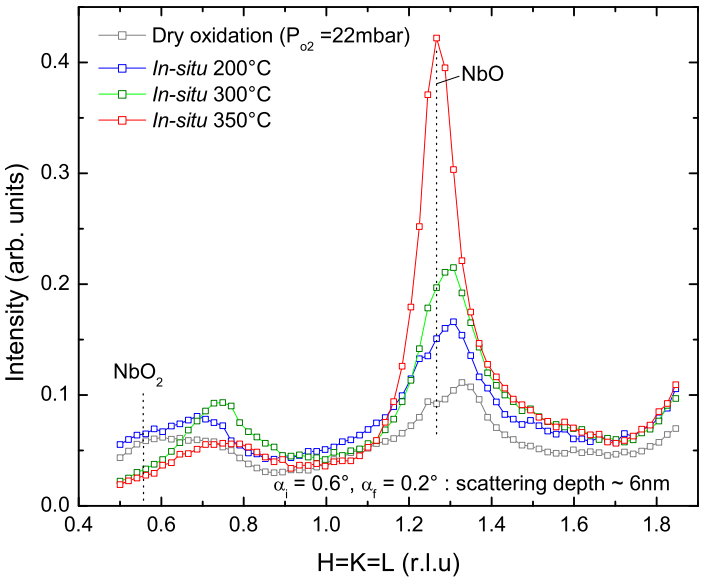

Figure 8.7: *In-situ* diffuse scattering data measured on a Nb(110) surface oxidized in dry oxygen atmosphere (P_{o2}=22mbar) upon annealing, at fixed incident angle $\alpha_i = 0.6°$ and exit angle $\alpha_f = 0.2°$ (scattering depth $\sim$ 6 nm).

$\mathbf{Q}^* = \frac{2}{3}(1,\bar{1},1)$ and $\frac{4}{3}(1,\bar{1},1)$ increases, indicating an enrichment in subsurface interstitial oxygen in the near surface region probed, in agreement with what was observed before for heating at T$\leq$ 200°C. At 300°C, in the same way, the NbO_2 contributions vanish. However, the interstitial oxygen contribution continues to increase in contrary to what was observed for the Nb(110) surface oxidized in air after cooling the sample down to room temperature. Fig. 8.8 compares the experimental data taken at 300°C with the theoretical structure factor of the oxygen-induced diffuse scattering (arbitrary concentration) and the thermal diffuse scattering. The agreement between both curves is surprisingly good. The data do not show any evidence of the presence of a layer of NbO at the surface yet. At 350°C (P = 5$\times$ 10^{-8}mbar), the epitaxial NbO layer is clearly visible in detriment to the interstitial oxygen signal.

From X-ray reflectivity measurements described in the previous section, the thickness of the oxide layer can be estimated at $\sim$ 25 Å, which is similar to the oxide layer thickness observed after the atmospheric oxidation conditions (6.1). During the heating process up to 300°C, the oxide layer dissolves progressively, releasing oxygen into the niobium bulk across the metal/oxide interface in a similar way as described before (6.2.3). At 350°C, the formation of the epitaxial NbO layer seems to be energetically favorable and the NbO layer grows. This important observation suggests that the oxide dissolution occurring at $T \geq 300°C$, proceeds via dissolution of the NbO_2 oxide into Nb and interstitial oxygens, followed by the growth of NbO at higher temperature, rather than as a direct transformation from NbO_2 into NbO.

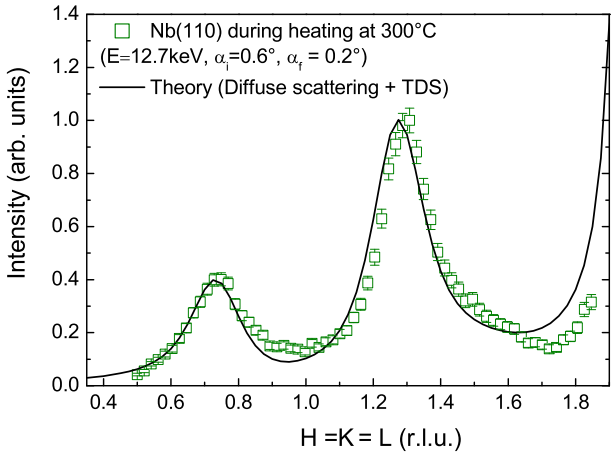

Figure 8.8: Experimental curve of the diffuse scattering after correction of the polarization and substraction of the background (open squares). Normalized theoretical curves for the diffuse scattering for an arbitrary oxygen concentration and thermal diffuse scattering (solid line).

8.3 Results on Nb(110) oxidized in water

In this section the oxidation of Nb(110) single crystals in pure water, and the thermal stability of the oxide layer are investigated by means of X-ray reflectivity and core-level spectroscopy measurements.

Nb(110) single crystals with a diameter 11 mm diameter and a thickness of 3 mm were oriented better than 0.1°, polished and purified as described in section 5.4. The samples were exposed to air for 10h (RT) prior to their oxidation in pure water during 10h at RT, and then mounted in the UHV chambers. The X-ray reflectivity measurements have been performed at the MPI-MF beamline (ANKA), at a photon energy of 10keV (beamtime A3). The core-level experiments were carried out at the beamline I311 at MAX-Lab.

8.3.1 XRR results

The X-ray reflectivity data measured on the Nb(110) single crystal oxidized in pure water, after heating at 300°C (1, UHV), and at 2000°C (5min., HV) are shown in Fig. 8.9(a). All measurements were performed after cooling down the sample in a *frozen* state to RT. The data have been fitted using the Parratt formalism in the same way as described in previous sections. The electron density profiles obtained from the fit are presented in Fig. 8.9 (b) and the fitting parameters are summarized in Appendix A.

After having seen air for 10h and clean water for 10 more hours, the Nb(110) single crystal has an oxide layer of total thickness equal to 44±1 Å. The data at RT can be fitted reasonably well using a three layer model with the following sequence of niobium oxide: Nb_2O_5, NbO_2 and NbO, from the surface to the interface with the metal, as previously observed for Nb(110) (section 6.1) and Nb(100) surfaces (previous section) oxidized in air. Note that the best fit is obtained assuming a fourth thin and rough layer on top of the Nb_2O_5, that can be understood as due to a Nb-OHHOH complex at the surface, as reported in previous studies on the oxidation of niobium in H_2O [89,199]. The individual thicknesses and roughnesses of the different layers are summarized in Tab. 8.2. Attempts assuming a three layer model, including the same sequence of oxide but no overlayer is illustrated in Fig. 8.9(a,b) (dashed line).

After heating at 300°C (30min.,HV)[2] the oxide layer reduces nearly completely into a 19 Å thick NbO layer. The subsequent annealing of the sample at 2000°C (5min.) leads to the dissolution by $\sim$ 25% of this NbO layer. Traces of a thin remaining NbO oxide layer

[2]Intermediate heating at 135°C (4h, HV), and the baking of the chamber (120°C, 24h) was performed before heating at 300°C (not shown). Note that these treatments had only small effects on the total thickness of the oxide layer.

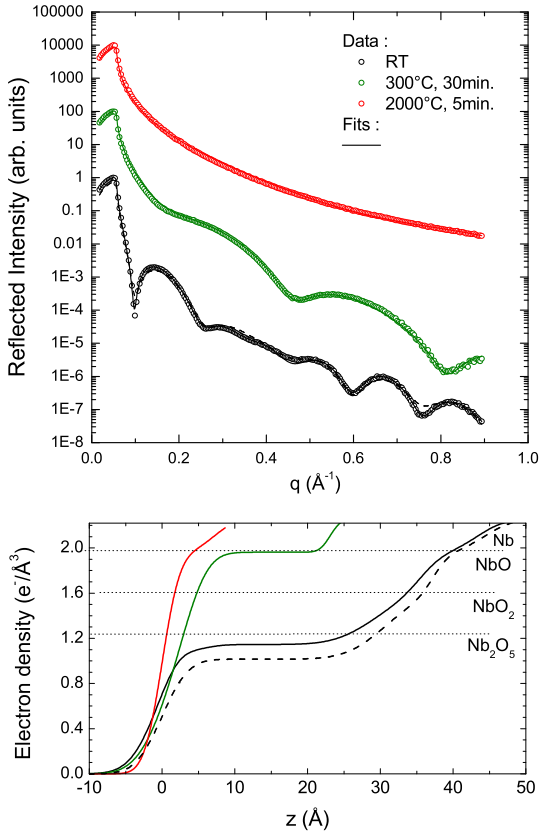

Figure 8.9: (a) Reflectivity data (open circles) and fits (solid lines) measured on a Nb(110) single crystal oxidized in clean water for different thermal treatments. Dashed lines : attempt using a three layer model instead of the fourth layers model in the Parratt formalism. The curves were vertically shifted for clarity. (b) Electron density profiles for the best fits (see text for details).

Oxide	RT		300°C (30min.)	2000°C (5min.)
	4 layers	3 layers		
Overlayer	*3.2 (3.3)*	-	-	-
Nb_2O_5	*26.9 (2)*	30.8 (2.8)	3.7 (3.2)	-
NbO_2	*6.5 (4.4)*	6.6 (4.3)	-	-
NbO	*7.7 (2.5)*	7 (1.7)	19.4 (2.5)	5.3 (1.9)
Substrate	*(2.9)*	(3)	(1.2)	(2.3)
Total (Å)	44.3	44.4	23.1	5.3

Table 8.2: Thicknesses (roughnesses) in Å (error bar of ± 1Å) of the different niobium oxides obtained from the X-ray reflectivity analysis for different thermal treatments. Two different models are proposed for the RT data (see text for details).

are observed at the surface even after repeated annealing cycles at this temperature. This can be explained, as already discussed in section 8.2.1, by the degradation of the vacuum inside the chamber to 10^{-5} mbar while heating at 2000°C (see also section 5.2).

8.3.2 Core-level results

Complementary information about the chemical species that form the wet oxide layer and their thermal stability were obtain by core-level spectroscopy measurements.

Room temperature wet oxidation

The depth-dependent Nb 3*d* core-level spectra of the Nb(110) sample after wet oxidation (10h in air +10h in water) are presented in Figure 8.10 (normal emission angle). The photoemission escape depth is tuned by varying the incident beam photon energies in order to get depth-resolved information.

Two straightforward observations can be made from Fig. 8.10. First, as for the atmospheric oxide layer on Nb(110) (see section 6.1), the main component of the wet oxide layer is shifted by 5.5eV toward higher binding energies with respect with the niobium component and can be attributed to Nb_2O_5. Second, the relative intensity of the Nb_2O_5 doublet

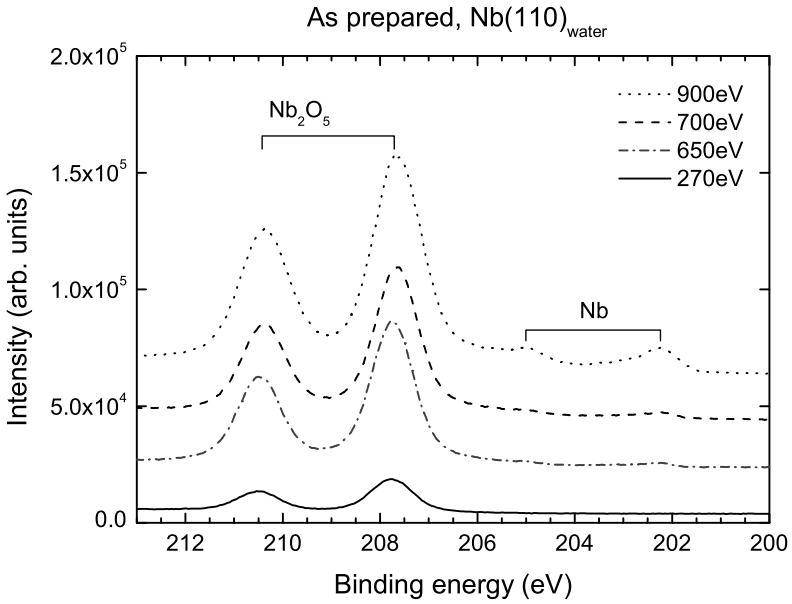

Figure 8.10: Depth-dependence of the Nb 3*d* core-level spectra measured on a Nb(110) single crystal oxidized in clean water during 10h (after having seen the air for 10h at RT) for incident photon energies $h\nu = 270, 650, 700$ and 900eV. The curves are vertically shifted for clarity.

predominates for all incident energies, and the Nb metal component appears only slightly at high photon energy. This indicates a sensibly thicker oxide layer than after atmospheric oxidation at RT, as expected from previous studies [89], and in agreement with the XRR results discussed before.

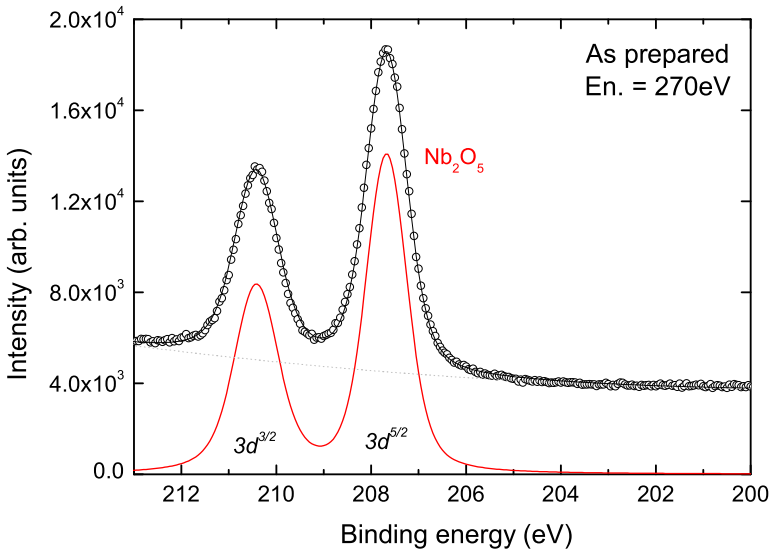

Figure 8.11: Nb 3*d* core-level spectra measured on a Nb(110) single crystal oxidized in clean water during 10h (after having seen the air for 10h) (O) and fit (solid line). The Nb_2O_5 doublet, main component of the oxide layer, is shown.

Fig. 8.11 illustrates the deconvolution of the core-level spectra measured at $h\nu = 270$ eV. The Nb_2O_5 doublet has been fitted using Doniach-Sunjic line shapes convoluted with Gaussian functions [182] (Sec.4.5). A parabolic background was included in the fit. The fitting parameters obtained are summarized in Tab. 8.3. The area ratio between the $3d^{3/2}$ and $3d^{5/2}$ levels follows the theoretical intensity ratio between doublet components ~ 0.67 and the spin-orbit splitting is found to be 2.74 eV, in good agreement with literature

Peaks	BE (eV)	α	Γ (eV)	σ (eV)	Rel. area	FWHM (eV)
$3d^{5/2}$	0	0	0.35	0.82	1	1.02
$3d^{3/2}$	2.74	0	0.48	0.82	0.66	1.11

Table 8.3: Fitting parameters for the Nb 3*d* core-level spectra of the Nb(110) sample after wet oxidation at 270eV.

values (see Appendix A). The lorentzian FWHM of the $3d^{3/2}$ peak is larger then the one of the $3d^{5/2}$ level as reported for the Nb levels [190]. An asymmetry parameter α equal to zero is consistent with the dielectric nature of Nb_2O_5. The decomposition of the data measured at $h\nu = 900$eV reveals the presence of NbO_2, NbO and interfacial components as observed as for the atmospheric oxide layer on Nb(110) (see section 6.1), however, they lie under the background line and will not be discussed further. Previous X-ray photoemission spectroscopy studies on the oxidation of niobium report a chemical shift of about 0.3 eV toward higher binding energies for the Nb_2O_5 component with respect to the Nb component for the oxidation in H_2O in comparison to the dry oxidation [90, 199]. In this work the chemical shift observed for the Nb_2O_5 component with respect to the Nb component was identical after atmospheric and wet oxidation.

Low-temperature UHV thermal treatment

The core-level spectrum measured after heating at 145°C (4h, UHV) is presented in Fig. 8.12, the data on the wet oxide are shown for comparison (normal emission, $h\nu$=650eV). Fig. 8.13 shows the evolution of the Nb $3d$ spectra as a function of the incident photon energy. The decomposition of the spectrum reveals mainly three different components: the niobium metallic doublets (black) and two components shifted by 4eV and 5.5eV toward higher binding energies, respectively attributed to NbO_2 (blue) and Nb_2O_5 (red) doublets

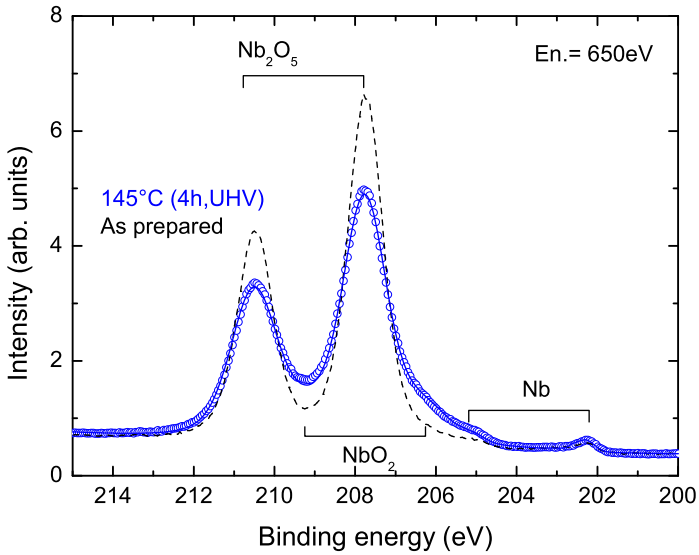

Figure 8.12: Nb $3d$ spectra of the Nb(110) sample oxidized in water after heating at 145řC (4h,UHV) (O) and fit (solid line) for $h\nu = 650eV$, the *as prepared* data are shown for comparison (dashed line). The Nb_2O_5, NbO_2, NbO and Nb doublet energies are indicated.

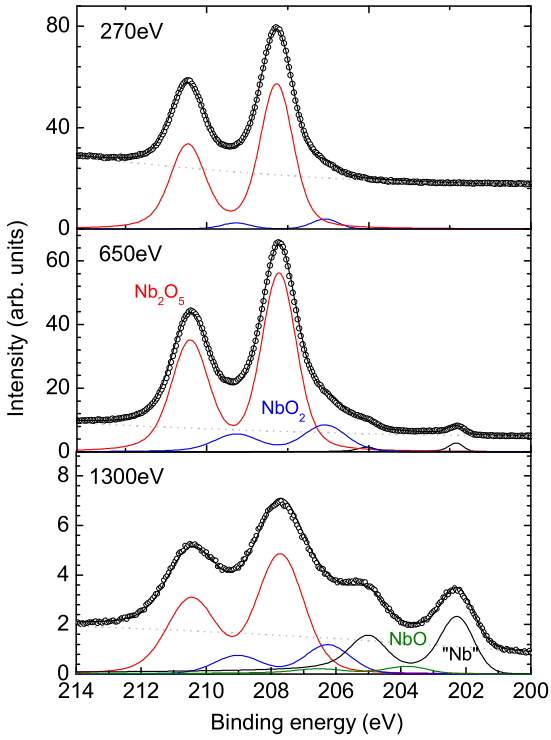

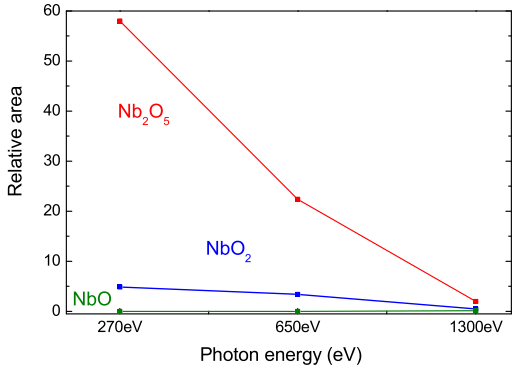

Figure 8.13: (Left) Deconvolution of the Nb 3*d* spectra measured on the Nb(110) sample oxidized in water after heating at 145°C (4h,UHV) (O) and fit (solid line) as a function of the incident photon energy. The Nb_2O_5, NbO_2, NbO and Nb doublets are shown. (Right) Relative area of the different oxide components with respect to the bulk component as a function of the incident photon energy.

(see Tab. 4.2). After heating at 145°C, the wet oxide layer on Nb(110) partially reduces from Nb_2O_5 to NbO_2, showing similar behavior as for the sample oxidized in air as discussed in section 6.2.1.

The relative area of the different oxide Nb $3d^{5/2}$ components with respect to the bulk Nb $3d^{5/2}$ component as a function of the incident photon energy is shown in Fig. 8.13 (b). The most pronounced decrease with increasing the photon energy is observed for the Nb_2O_5 component, indicating that this is the outermost layer, located on top of NbO_2. The NbO component appears only for an incident photon energy of 1300eV, which is sign of its buried location at the metal/oxide interface. This observation is in agreement with the layered model proposed in the XRR analysis.

The temperature evolution of the Nb 3*d* core-level spectra is plotted in Fig. 8.14 for a subsequent vacuum annealing at 300°C (1h), and at 800°C (5min.) (incident photon energy = 650eV). The data were recorded after cooling the sample down to room temperature. After heating at 300°C, the data show the further dissolution of the Nb_2O_5 and NbO_2 toward NbO, which itself dissolves at 800°C, giving rise to similar features at intermediate binding energy between NbO and the metallic peak, as observed for the Nb(110) surface oxidized in air 6.2.2. This component, can be in first attempt assigned by extrapolation of the relationship between the valence of the niobium oxide states and the corresponding

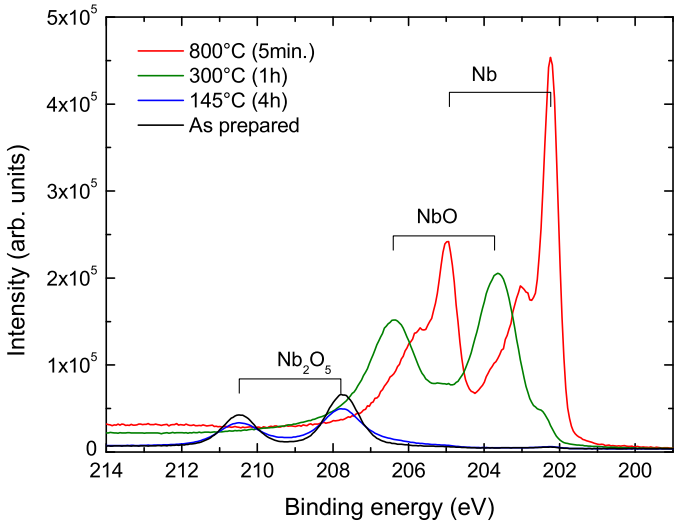

Figure 8.14: Nb 3*d* spectra of the Nb(110) sample oxidized in water after heating at 145°C (4h,UHV), at 300°C (1h), and at 800°C (min.) for $h\nu = 650eV$. The Nb_2O_5, NbO and Nb doublets are shown (see text for details).

chemical shifts, to the suboxide Nb_2O (see also the discussion in 6.2.2).

8.3.3 Discussion

Numerous similarities are observed for the oxidation of Nb(110) single crystals in air and in water at room temperature. The layered system suggested from the XRR analysis on the wet oxide, with Nb_2O_5, NbO_2 and NbO from the surface to the interface, has been confirmed by the HRCLS results recorded after heating at 145°C. Nb_2O_5, highest oxidation state of niobium predominates both oxide layers, and is present as outermost oxide species. The progressive dissolution of the oxide layer from Nb_2O_5 to NbO_2 after heating at 145°C, and to NbO after heating at 300°C show an identical trend as for the Nb(110) and Nb(100) surfaces initially oxidized in air.

The Nb_2O_5 layer, as well as the total wet oxide layer, are however sensibly thicker ($\sim$ 30 Å and $\sim$ 45 Å resp.) than the natural oxide observed after oxidation in air (10h). The amount of oxygen uptake by the surface was shown to be much higher when the surface is exposed to H_2O than when it is exposed to O_2 [118]. In the same way, the oxidation of niobium in H_2O was reported to be much faster compared to dry oxidation [90], with a passivating layer of approximately 50 Å obtained rather fast. The results for the oxidation in air given in this work included data up to only 10h of immersion in air, which can not directly be compared with 10h in air and 10h subsequently in H_2O. However, one knows

that the oxidation rate of niobium in air slows down drastically after the formation of the first 20 Å [15, 89], as already discussed in section 8.1.3. This trends indicates that the Nb(110) surface immersed for 20h in air would not grow much thicker than 20 Å, as observed for the oxidation of Nb(100) in air. The oxidation of Nb(110) can therefore most probably be concluded to be much faster in water than in air, reaching a thickness close to the passivating thickness after 10h already. The predominance of the Nb_2O_5 layer in the wet oxide is in agreement with the observation made in [199], where Nb_2O_5 is continuously growing till about 50 Å, while up to a 20 Å thick oxide the NbO layer stays small ($\sim$ 4 Å) and constant. The Nb_2O_5 surface formed by oxidation in H_2O was reported to be covered by a Nb-OHHOH layer [89,199], which facilitates the incorporation of oxygen ions into the Nb_2O_5 matrix. This is accompanied by a larger defect density in the oxide. In line with this observation, both Nb_2O_5 layers involved in the three and four layer model discussed in section 8.3.1 for wet oxide structure, present a reduced electron density as compared to the bulk density of amorphous Nb_2O_5.

Chapter 9

Summary and conclusions

In this work, the near surface structure of oxidized niobium single crystals and its evolution upon vacuum annealing has been studied by means of complementary non-destructive *in-situ* surface sensitive X-ray techniques. For the first time, the cutting-edge combination of X-ray reflectivity (XRR), grazing incidence X-ray diffraction (GIXD), diffuse X-ray scattering (GIDXS), crystal truncation rods measurements (CTRs), and high-resolution core-level spectroscopy (HRCLS), has enabled the simultaneous characterizations of the oxide layer, and of the depth-distribution of the interstitial oxygen atoms dissolved underneath.

The natural oxide layer formed on Nb(110) single crystals oxidized in air and its evolution with increasing temperature (145-800°C) has been investigated in chapter 6, applying this approach. The natural oxide presents a layered structure, constituted of Nb_2O_5, NbO_2 and NbO, from the surface to the interface. These oxides are unstable for vacuum thermal treatments and their progressive dissolution is initiated by the reduction of Nb_2O_5 to NbO_2. The reduction process takes place at the interface between both oxides. After heating at 145°C (5h, UHV) the NbO_2 layer thickness increases by 7%. At temperatures above 300°C, both Nb_2O_5 and NbO_2 reduce to NbO.

The NbO observed at the metal/oxide interface presents epitaxial orientation relationships with respect to the underlying substrate (see section 6.3). The NbO(111) planes are parallel to the Nb(110) planes, and the in-plane directional relationship Nb[001]||NbO[$1\bar{1}0$] corresponds to the Nishiyma-Wassermann orientation. Evidences of the in-plane epitaxial relationship are already observed in the natural oxide. With increasing temperatures, the epitaxial NbO grows up to a three dimensional thin and highly strained oxide layer. Coexistence of the Kurdjumov-Sachs and Nishiyma-Wassermann orientations has been observed for measurements realized at higher temperatures (1700°C). A qualitative description of the interfacial atomic structure behavior upon heating has been given showing no significant change for low temperatures, while drastic effects are observed after heating at 300°C. This is the first evidence given to our knowledge of the unambiguous presence of NbO_2,

and strained epitaxial NbO oxides in the natural oxide layer on niobium surfaces, between Nb_2O_5 and the metal. This is a crucial observation for technological applications of niobium and especially for the superconducting properties of rf cavities [144, 200]. As niobium does not release oxygen in the surrounding environment below 1600°C, the oxygen liberated from the oxide dissolution gets dissolved into niobium across the metal/oxide interface. The amount of oxygen released has been calculated and could be directly probed.

For the unambiguous monitoring of subsurface interstitial oxygen, the diffuse X-ray scattering from the characteristic strong local lattice distortions occurring around interstitial oxygen defects in the niobium host lattice have been exploited. These distortions couple to the intrinsic instability of the *bcc* niobium lattice toward the ω-structure, thereby producing pronounced maxima of the distortion-mediated diffuse X-ray scattering at $\mathbf{Q}^*=\frac{2}{3}(1,1,1)$. In chapter 7, it has been demonstrated that the monitoring and quantitative analysis of these diffuse maxima by grazing incidence diffuse X-ray scattering provide a detailed picture on the emergence of interstitial oxygen close to the niobium surface. A comprehensive depth-resolved oxygen-induced diffuse scattering analysis has been developed in the DWBA approximation formalism, together with a fitting routine that has been applied successfully to the analysis of various data sets. The depth-distribution of interstitial oxygen below the natural oxide layer of the Nb(110) surface initially oxidized in air, and its evolution after heating at 145°C, has been established. Assuming an exponential profile, the decay length of the interstitial oxygen below the oxide layer is found to be inferior to 1 nm, indicating that most of the oxygen is located in the direct vicinity of the oxide/niobium interface. The net interstitial oxygen enrichment observed in the first 10 nm below the interface after heating is consistent which the amount of oxygen released by the oxide dissolution. From the results given in chapter 6 and 7, a first insight into the interplay between oxide formation/dissolution and the occurrence of interstitial oxygen has been given.

The role of the interstitial oxygen in the oxidation process has often been pointed out in literature. In section 6.5 the particular case of the transformation that occurs from the oxygen-induced ω-phase observed for randomly distributed defects into niobium, toward the NbO defective rock-salt structure, reported as first oxidation step on niobium surfaces by various authors, is discussed. A transformation path is proposed and the precursor role of niobium sub-oxide species assigned in a first attempt to Nb_2O, is discussed.

The oxidation of niobium surfaces, and metals in general, is sensitive to various parameters such as the surface orientation or the oxidation active environment. In chapter 8 complementary results are presented on three different systems. In section 8.1 Nb(100) singles crystals oxidized under atmospheric conditions at room temperature have been studied by mean of XRR and GIDXS. The natural oxide layer observed after 14 days in air

at room temperature, presents a similar sequence of niobium oxides as the one observed on the Nb(110) surface oxidized in air (10h, RT). The total thickness of the oxide is only slightly larger. The oxide layer reduces following the same process with increasing temperature, but faster. At 120°C (4h30), Nb_2O_5 dissolves in profit of the growth of NbO_2 by up to 20%. The total oxide layer thickness stays constant and no interstitial oxygen is liberated from this rearrangement. In absence of oxygen release from the oxide dissolution, no major change of the average concentration of interstitial oxygen was observed (see section 8.1.2), indicating that no depletion or segregation is taking place in average in the first 10 nm and 200 nm below the oxide. After heating at 200°C (6h), the striking observation of a diffusion front from the metal/oxide interface toward the niobium bulk has been made. The NbO layer left on the Nb(100) surface after heating at 300°C, grows faster, and in contrast with the Nb(110) sample, is accompanied by an increase in subsurface oxygen visible up to 200 nm.

In section 8.2, *in-situ* GIDXS measurements performed during annealing of the Nb(110) surface oxidized in dry oxygen atmosphere have been described. The results indicate that the oxide dissolution occurring at temperatures above 300°C proceeds via dissolution of the NbO_2 oxide into Nb and interstitial oxygens, followed by the growth of NbO at higher temperature, rather than as a direct transformation from NbO_2 into NbO.

In section 8.3 the Nb(110) surface oxidized in pure water has been investigated by mean of XRR and HRCLS. As reported in literature, the oxidation process in water is enhanced by the presence of hydrogen, and gives rise to highly defective oxides. The wet oxide observed after 10h in pure water (after 10h in air) observed at the Nb(110) surface is 44 Å thick, which is close to the passivating thickness reported in literature for niobium oxide. The oxide presents a similar sequence of niobium oxide layers as observed for the two previous systems, mainly composed of Nb_2O_5 (30 Å), and similar dissolution with increasing temperature. The epitaxial orientation relationships of the oxide layer with respect to the underlying niobium for the two systems discussed in chapter 8 have not been studied yet.

The overall results demonstrate how sensitive the oxygen distribution and its chemical/physical state in the surface and subsurface regime of niobium is with respect to the the oxidation conditions, the temperature and duration of the thermal treatments applied. The amount of subsurface interstitial oxygen is shown to be a sensible balance between the oxygen release from the oxide reduction and the oxygen diffusion into the niobium bulk.

Recent tests on a superconducting single crystal single-cell niobium cavity [201], show similar improvements in the cavity performances after a low-temperature treatment as observed on polycrystalline niobium cavities. The choice of single crystalline samples made in

this work, which restrained the complexity of the system investigated, from grain boundary effects for example, has been thereby fully comforted.

For the investigation of clean niobium surfaces, high temperature annealing (~ 2000°C) are required. For this purpose a new high-temperature setup has been constructed and implemented in the transportable UHV diffraction chamber allowing *in-situ* experiments 5.2. Temperatures up to 2000°C have been reached successfully for repeated cycles and exploited during various beamtime. The best vacuum that could be maintain in the chamber for few minutes at 2000°C is $\sim 5.10^{-7}$ mbar. Traces of NbO structures that originates from interstitial oxygen segregation from the bulk could not be avoided. Future improvements of the setup are planned.

The weak intensity of the scattering of interest, measured in addition under grazing incidence geometry, or the high-resolution required to distinguish between different chemical states at the niobium surface, require the use of highly brilliant synchrotron radiation sources. The measurements presented in this work have been carried out at the Max Planck Institute for Metals Research beamline at ANKA, Karlsruhe (Germany), on the beamline ID32 at the ESRF, Grenoble (France), and at the I311 beamline of the Max-Lab synchrotron source, Lund (Sweden).

This work has been realized in the framework of a collaboration between the Max Planck Institute for Metals Research, Stuttgart (Germany), and the Département d'Astrophysique, de physique des Particules, de physique Nucléaire et d'Instrumentation Associée, DAPNIA, CEA, Gif-sur-Yvette (France).

The results presented in this work have important implications for technological applications of niobium, in particular for superconducting rf niobium cavities. Some of the open questions mentioned at the beginning of the dissertation have been answered, but some others have been raised. For the understanding of the low-temperature heating effect on the performances achieved on superconducting rf niobium cavities, two crucial results have been pointed out. The first one is that, contrary to prior expectations, no evidence of oxygen depletion below the oxide layer has been noticed for the low temperature thermal treatments and surface preparations investigated in this work. The second one is that the oxide layer reduces from Nb_2O_5 to NbO_2 if the system is annealed at 120°C or 145°C for a few hours. At the time the present manuscript is written, a renewed interest in the role plaid by the oxide species at the surface of niobium cavities has already been stimulated.

Appendix A

XRR fit parameters

Layers	RT	145°C	300°C	700°C
Nb_2O_5	1.91 (0.5)	2.19 (0.5)	-	-
NbO_2	2.82 (1.0)	2.74 (1.1)	-	-
NbO	3.25 (1.2)	3.35 (1.4)	3.37 (1.3)	3.33 (1.7)
Substrate*	3.85 (1.9)	3.85 (1.9)	3.85 (1.9)	3.85 (1.9)

Table A-1: Fit parameters 2δ [10^{-5}] (2β [10^{-6}]) for the results presented in sections 6.1 and 6.2 (photon energy E=9KeV). * fixed parameters.

Oxide	RT 2 layers	RT 3 layers	120°C 2layers	120°C 3layers	200°C 2layers	300°C 2layers
Nb_2O_5	1.45 (5.3)	1.55 (6.0)	1.73 (5.0)	1.80 (4.0)	1.75 (5.0)	1.57 (5.3)
NbO_2	2.01 (5.3)	2.22 (6.8)	2.17 (7.5)	2.22 (6.8)	2.28 (7.5)	-
NbO	-	2.74 (5.0)	-	2.70 (5.0)	-	2.54 (7.8)
Substrate*	3.11 (13)	3.11 (13)	3.11 (13)	3.11 (13)	3.11 (13)	3.11 (13)

Table A-2: Fit parameters 2δ [10^{-5}] (2β [10^{-7}]) for the results presented in section 8.1.1 (photon energy E=10KeV). * fixed parameters.

Oxide	RT *4 layers*	RT 3 layers	300°C	2000°C
Overlayer	1.98 (5.6)	-	-	-
Nb_2O_5	1.57 (4.0)	1.4 (2.0)	1.51 (6.0)	-
NbO_2	2.22 (6.8)	2.22 (6.8)	2.20 (6.1)	-
NbO	2.81 (9.7)	2.78 (9.6)	2.75 (9.6)	2.78 (9.0)
Substrate*	3.11 (13)	3.11 (13)	3.11 (13)	3.11 (13)

Table A-3: Fit parameters 2δ $[10^{-5}]$ (2β $[10^{-7}]$) for the results presented in section 8.1.1 (photon energy E=10KeV). * fixed parameters.

HRCLS fitting parameters

Peak	BE (eV)	Γ (eV)	α	σ (eV)	Rel. Area	FWHM (eV)
1	202.18	0.05	0.13	0.43	1	0.51
2	204.92	0.25	0.13	0.43	0.68	0.65
3	202.51	0.04	0.14	0.95	0.81	1.10
4	205.25	0.25	0.13	0.95	0.54	1.22
5	203.03	0.06	0.18	0.90	0.37	1.09
6	205.77	0.26	0.18	0.90	0.24	1.24
7	203.55	0.05	0.13	0.47	0.04	0.57
8	206.29	0.25	0.13	0.47	0.02	0.71
9	204.03	0.25	0.15	1.5	0.61	1.86
10	206.77	0.45	0.15	1.5	0.40	2.01
11	206.24	0.36	0.04	1.42	1.17	1.68
12	208.99	0.42	0.04	1.42	0.74	1.71
13	207.68	0.36	0	0.92	5.54	1.13
14	210.42	0.54	0	0.92	3.70	1.24

Table A-4: Fit parameters for the Nb 3d spectrum shown in Fig. 6.2 (middle panel : En. = 650eV).

Peak	BE (eV)	Γ (eV)	α	σ (eV)	Rel. Area	FWHM (eV)
1	202.14	0.06	0.15	0.28	1	0.36
2	204.88	0.26	0.14	0.27	0.64	0.52
3	202.47	0.06	0.14	0.27	0.15	0.35
4	205.22	0.26	0.15	0.26	0.10	0.51
5	202.99	0.06	0.15	0.72	1.99	0.85
6	205.73	0.26	0.15	0.76	1.32	1.05
7	203.62	0.15	0.15	0.99	9.48	1.22
8	206.37	0.40	0.15	1.01	6.39	1.43
9	204.84	0.22	0.00	0.63	0.59	0.76
10	207.58	0.46	0.00	0.67	0.40	0.96
11	206.20	0.40	0.04	1.35	1.01	1.62
12	208.95	0.65	0.04	1.38	0.68	1.83

Table A-5: Fit parameters for the Nb 3d spectrum shown in Fig. 6.8 (middle panel : En. = 400eV).

Appendix B

GIXDS fit parameters

Parameter	RT	145°C
Background	94	95
Oxide:		
FWHM (r.l.u.)	0.2	0.2
Position (r.l.u.)	0.55	0.55
Exponential decay :		
Bulk concentration	1.7E-5	1E-5
Amplitude	1.59	1.58
Shift	1.57	1.43
Decay length (nm)	0.51	0.85

Table B-1: Fit parameters for the depth-resolved grazing incidence diffuse X-ray data shown in Fig. 7.20 and 7.23.

List of acronyms

AES	Auger Electron Spectroscopy
ANKA	Ånstromquelle Karlsruhe
BCC	Body Centered Cubic
CTR	Crystal Truncation Rod
CEA	Commissariat a l'Energie Atomique
DC	Direct Current
DWBA	Distorted Wave Born Approximation
ESRF	European Synchrotron Radiation Facility
FCC	Face Centered Cubic
FWHM	Full Width at Half Maximum
GIDXS	Grazing Incidence Diffuse X-ray Scattering
GIXD	Grazing Incidence X-ray Diffraction
GIXS	Grazing Incidence X-ray Scattering
HRCLS	High Resolution Core Level Spectroscopy
HV	High Vacuum
LEED	Low Energy Electron Diffraction
MF	Metallforschung
MPI	Max Planck Institute
RRR	Residual Resistivity Ratio
RT	Room Temperature
STM	Scanning Tunneling Microscopy
SXRD	Surface X-ray Diffraction
TDS	Thermal Diffuse Scattering

UHV	Ultra High Vacuum
UPS	Ultraviolet Photoelectron Spectroscopy
XPS	X-ray Photoelectron Spectroscopy
XRR	X-ray reflectivity

Bibliography

[1] B. Visentin, J. P. Charrier, B. Coadou, and D. Roudier, in Proceedings of the 9th Workshop on RF Superconductivity, Santa Fe, NM, 1999, edited by F. Krawczyk, (Los Alamos National Laboratory, Santa Fe, NM, 2000) 198 (2000).

[2] P. Kneisel, in Proceedings of the 9th Workshop on RF Superconductivity, Santa Fe, NM, 1999, edited by F. Krawczyk, (Los Alamos National Laboratory, Santa Fe, NM, 2000) 328 (2000).

[3] G. Ciovati, Appl. Phys. Lett. **89**, 022507 (2006).

[4] G. Ciovati, P. Kneisel, and A. Gurevich, Phys. Rev. ST Accel. Beams **10**, 062002 (2007).

[5] C. Koch, J. Scarbrough, and D. M. Kroeger, Phys. Rev. B **9**, 888 (1974).

[6] W. DeSorbo, Phys. Rev. B **132**, 107 (1963).

[7] J. Vedrine, G. Coudurier, A. Ouqour, P. P. de Oliveira, and J. Volta., Catal. Today **28**, 3 (1996).

[8] K. Tanabe, Catal. Today **78**, 65 (2003).

[9] M. Ziolek, Catalysis Today **78**, 47 (2003).

[10] I. Nowak and M. Ziolek, Chem. Rev. **99**, 3603 (1999).

[11] P. A. Burke and E. I. Ko, Journal of Catalysis **129**, 38 (1991).

[12] C. Zai-hu, I. Tokio, and T. Kozo, Chemistry Letters **11**, 1085 (1984).

[13] A. Morikawa, K. Ebitani, and Y. Hirano, Catalysis Today **28**, 91 (1996).

[14] T. Ushikubo, Y. Koike, K. Wada, X. Lei, W. Dezheng, and G. Xiexian, Catalysis Today **28**, 59 (1996).

[15] O. Hellwig, H. Becker, and H. Zabel, Phys. Rev. B **64**, 233404 (2001).

[16] I. Arfaoui, C. Guillot, J. Cousty, and C. Antoine, J. Appl. Phys. **91**, 9319 (2002).

[17] J. Sebastian, D. Seidman, K. Yoon, P. Bauer, T. Reid, C. Boffo, and J. Norem, Physica C **441**, 70 (2006).

[18] B. King, H. Patel, D. Gulino, and B. Tatarchuk, Thin Solid Films **192**, 351 (1990).

[19] Q. Ma and R. A. Rosenberg, Appl. Surf. Sci. **206**, 209 (2003).

[20] E. Palmer, R. Kirby, F.K.King, and E. Garwin, Nuclear Instr. and Methods in Phys. Research **A297**, 321 (1990).

[21] Q. Ma, P. Ryan, J. Freeland, and R. Rosenberg, J. Appl. Phys. **96**, 7675 (2004).

[22] H. Dosch, A. Schwerin, and J. Peisl, Phys. Rev. B **34**, 1654 (1986).

[23] H. Dosch and J. Peisl, Phys. Rev. B **32**, 623 (1985).

[24] *http://hasylab.desy.de.*

[25] H. Padamsee, J. Knobloch, and T. Hays, *RF superconductivity for accelerators* (J. Willey son., Interscience, 1998).

[26] G. Ciovati, J. Appl. Phys. **96**, 1591 (2004).

[27] S. Casalbuoni, E.-A. Knabbe, J. Kotzler, L. Lilje, L. von Sawilski, P. Schmuser, and B. Steffen, Nuclear Instrumentation and Methods in Physical Research A **538**, 45 (2005).

[28] G. Ciovati, Phys Rev ST Accel Beam **9**, 042001 (2006).

[29] C. Antoine, in Pushing the limits of RF superconductivity workshop, ANL, Il, USA, 75 (2004).

[30] A. Gurevich, Physica C **441**, 297 (2006).

[31] F. Palmer, in third workshop on rf (radiofrequency) superconductivity. 1988. Argonne National Lab., IL (USA) .

[32] C. Antoine, in collaboration with Tokyo University, unpublished results .

[33] T. Proslier, J. F. Zasadzinski, L. Cooley, C. Antoine, J. Moore, J. Norem, M. Pellin, and K. E. Gray, Appl. Phys. Lett. **92**, 212505 (2008).

[34] G. Miller, *Metallurgy of the rarer metals -6 : Tantalum and Niobium* (Butterworths, London, 1959).

[35] D. Douglass and F. Kunz, *Columbium metallurgy* (Interscience, ADDRESS, 1960).

[36] D. Finnemore, T. Stromberg, and C. Swenson, Phys. Rev. **149**, 231 (1966).

[37] A. R. Jani, N. E. Brener, and J. Callaway, Phys. Rev. B **38**, 9425 (1988).

[38] E. Lekka, M. J. Mehl, N. Bernstein, and D. A. Papaconstantopoulos, Phys. Rev. B **68**, 035422 (2003).

[39] M. Methfessel, D. Hennig, and M. Scheffler, Phys. Rev. B **46**, 4816 (1992).

[40] M. Brejnak and P. Modrak, Surf. Sci. **310**, L614 (1999).

[41] J. S. Luo and B. Legrand, Phys. Rev. B **38**, 1728 (1988).

[42] D. Lacina and J. L. Erskine, Phys. Rev. B **76**, 104103 (2007).

[43] Y. Li, J. L. Erskine, and A. C. Diebold, Phys. Rev. B **34**, 5951 (1986).

[44] R. J. Smith, Phys. Rev. Lett. **45**, 1277 (1980).

[45] B.-S. Fang, C. A. Ballentine, and J. L. Erskine, Phys. Rev. B **38**, 4299 (1988).

[46] B.-S. Fang, C. A. Ballentine, and J. L. Erskine, Phys. Rev. B **36**, 7360 (1987).

[47] H. Dosch, F. Schmid, P. Wiethoff, and J. Peisl, Phys. Rev. B **46**, 55 (1992).

[48] G. Song, A. Remhof, K. Theis-Brohl, and H. Zabel, Phys. Rev. Lett. **79**, 5062 (1997).

[49] G. Song, A. Remhof, D. Labergerie, C. Sutter, and H. Zabel, J. Alloys and Compounds **293-295**, 476 (1999).

[50] G. Song, M. Geitz, A. Abromeit, and H. Zabel, Phys. Rev. B **54**, 14093 (1996).

[51] H. Dosch, U. Schubert, T. H. Metzger, and J. Peisl, J. Phys. F: Met. Phys. **14**, 2467 (1984).

[52] T. H. Metzger, U. Schubert, and J. Peisl, J. Phys. F: Met. Phys. **15**, 779 (1985).

[53] U. Schubert, H. Metzger, and J. Peisl, J. Phys. F: Met. Phys. **14**, 2457 (1984).

[54] K. Ravi and R. Gibala, Acta Met. **18**, 623 (1970).

[55] R. Elliott, Trans. Amer. Soc. Met. **52**, 990Ű1014 (1960).

[56] A. Seybolt, Journal of Metals 774 (1954).

[57] E. Fromm and E. Gebhardt, *Gase und Kohlenstoff in Metallen* (Springer, Berlin, 1976).

[58] P. Kofstad, *High temperature oxidation of metals* (John Wiley, New York, 1966).

[59] M. Blanter and A. G. Khachaturyan, Metal. Trans. **9A (6)**, 753Ű762 (1978).

[60] R. Powers and M. Doyle, J. Appl. Phys. **30**, 514 (1959).

[61] M. Strongin, H. Farrell, H. Halama, O. Kammerer, and C. Varmazis, Part. Accel. **3**, 209 (1972).

[62] H. H. Farrell, H. S. Isaacs, and M. Strongin, Surf. Sci. **38**, 31 (1973).

[63] R. A. Pasternak and B. Evans, J. Electrochem. Soc. **114**, 452 (1967).

[64] A. Joshi and M. Strongin, Scr. Metall. **8**, 413 (1974).

[65] S. Hofmann, G. Blank, and H. Schultz, Z. Metall. **67**, 189 (1976).

[66] K. Rieder, Applications of Surface Science **4**, 183 (1980).

[67] H. Rovner, A. Drowart, F. Degreve, and J. Drowart, Air Force Materials Laboratory Technical Report **AFML-TR-68-200**, (1968).

[68] K. Schulze and H. Jehn, Z. Metallkde **68**, 645 (1977).

[69] C. Surgers, M. Schock, and H. v. Lohneysen, Surface Sciences **471**, 209 (2001).

[70] M. Ondrejcek, R. S. Appleton, W. Swiech, V. L. Petrova, and C. P. Flynn, Phys. Rev. Lett. **87**, 116102 (2001).

[71] N. Norman, J. Less-Common Met. **4**, 52 (1962).

[72] I. Lindau and W. Spicer, J. Appl. Phys. **45**, 3720 (1974).

[73] M. Todorova, W. X. Li, M. V. Ganduglia-Pirovano, C. Stampfl, K. Reuter, and M. Scheffler, Phys. Rev. Lett. **89**, 096103 (2002).

[74] S. Sikka, Y. Vohra, and R. Chidambaram, Progress in Materials Science **27**, 245 (1982).

[75] B. Hickman, J. Mater. Sci. **4**, 554 (1969).

[76] H. Kanzaki, J. Phys. Chem. Solids **2**, 24 (1957).

[77] O. Hellwig and H. Zabel, Physica B **336**, 90 (2003).

[78] R. Kurta, V. Bugaev, A. Stierle, and H. Dosch, Journal of Physics: Condensed Matter **20**, 275206 (2008).

[79] G. Brauer, H. Renner, and J. Wernet, Z. anorg. chem. **277 (249)**, 557 (1954).

[80] M. Ruda, D. Farkas, and J. Abriata, Scripta Materialia **46**, 349 (2002).

[81] C. Carlisle, T. Fujimoto, W. Sim, and D. King, Surf. Sci. **470**, 15 (2000).

[82] N. Cabrera and N. Mott., Rep. Progr. Phys. **12**, 163 (1949).

[83] A. Fromhold and E. Cook., Phys. Rev. **158**, 600 (1967).

[84] K. R. Lawless, Rep. Progr. Phys. **37**, 231 (1974).

[85] O. Kubaschewski and B. Hopkins, *Oxidation of Metals and Alloys* (Butterworths, London, 1962).

[86] P. Fehlner, *Low-temperature oxidation* (John Wiley, New York, 1986).

[87] G. Samsonov, *The Oxide Handbook* (IFI/Plenum, New York, 1973).

[88] T. Hurlen, J. Inst. Metals. **89**, 273 (1961).

[89] J. Halbritter, Appl. Phys. A **43**, 1 (1987).

[90] M. Grundner and J. Halbritter, J. Appl. Phys. **51**, 397 (1980).

[91] A. Darlinski and J. Halbritter, J. Vac. Sci. Technol. A **5**, 1235 (1986).

[92] J. Sheasby, J. Electrochem. Soc. **115**, 695 (1968).

[93] D. Bridges and W. Fassell., J. Electrochem. Soc. **103**, 326 (1956).

[94] R. Franchy, T. Bartke, and P. Gassmann, Surface Science **366**, 60 (1996).

[95] B. An, S. Fukuyama, K. Yokogawa, and M. Yoshimura, Phys. Rev. B **68**, 115423 (2003).

[96] R. Pantel, M. Bujor, and J. Bardolle, Surface Science **62**, 589 (1977).

[97] P. H. Dawson and W.-C. Tam, Surf. Sci. **81**, 464 (1979).

[98] H. Oechsner, J. Giber, H. J. FüSSer, and A. Darlinski, Thin Solid Films **124**, 199 (1985).

[99] J. M. Sanz and S. Hofmann, J. Less-Common Met. **92**, 317 (1983).

[100] R. Fontaine, R. Caillat, L. Feve, and M. Guittet, J. Electron Spectrosc. Relat. Phenom. **10**, 349 (1977).

[101] F. Strisland, A. Ramstad, C. Berg, and S. Raaen, Phil. Mag. Letters **78**, 271 (1998).

[102] P. Karulkar and J. Nordman, J. Vac. Sci. Technol. **17**, 462 (1980).

[103] M. K. Bahl, J. Chem. Solids **36**, 485 (1975).

[104] Z. P. Hu, Y. P. Li, M. R. Ji, and J. X. Wu, Solid State Commun. **71**, 849 (1989).

[105] W.-S. Lo, T.-S. Chien, C.-C. Tsan, and B.-S. Fang, Phys. Rev. B **51**, 14749 (1995).

[106] A. Dacca, G. Gemme, L. Mattera, and R. Parodi, Appl. Surf. Sci. **126**, 219 (1998).

[107] T. Haas, A. Jackson, and M. Hooker, J. Chem. Phys. **46**, 3025 (1967).

[108] H. H. Farrell and M. Strongin, Surf. Sci. **38**, 18 (1973).

[109] W.-S. Lo, H.-H. Chen, T.-S. Chien, C.-C. Tsan, and B.-S. Fang, Surface Review and Letters **4**, 651 (1997).

[110] Y. Uehara, T. Fujita, M. Iwami, and S. Ushioda, Surf. Sci. **472**, 59 (2001).

[111] Y. Li, B. An, X. Xu, S. Fukuyama, K. Yokogawa, and M. Yoshimura, J. Appl. Phys. **89**, 4772 (2001).

[112] I. Arfaoui, J. Cousty, and H. Safa, Phys. Rev. B **65**, 1 (2002).

[113] M. Ronay and P. Nordlander, Phys. Rev. B **35**, 9403 (1987).

[114] P. Nordlander and M. Ronay, Phys. Rev. B **36**, 4982 (1987).

[115] O. Hellwig and H. Zabel, Physica B **283**, 228 (2000).

[116] O. Hellwig, Ph.D. thesis, Bochum, 2000.

[117] I. Colera, S. Rey, and J. de Segovia, Surf. Sci. **251/252**, 851 (1991).

[118] I. Colera, J. L. de Segovia, P. L. Wincott, R. Casanova, and G. Thornton, Surf. Sci. **292**, 61 (1993).

[119] E.-E. Latta and M. Ronay, Phys. Rev. Lett. **53**, 948 (1984).

[120] J. K. Hulm, C. K. Jones, R. A. Hein, and J. W. Gibson, J. Low Temp. Phys. **7**, 291 (1972).

[121] A. Okaz and P. Keesom, Phys. Rev. B **12**, 4917 (1975).

[122] J. Burdett and T. Hughbanks, J. Am. Chem. Soc. **106**, 3101 (1984).

[123] W. W. Schulz and R. M. Wentzcovitch, Phys. Rev. B **48**, 16986 (1993).

[124] W. Wahnsiedler, J. of Solid State Chemistry **49**, 195 (1983).

[125] T. Sakata, K. Sakata, and I. Nishida, Phys. Status solidi **20**, K155 (1967).

[126] A.K.Cheetham and C. Rao, Acta Cryst. **B32**, 1579 (1976).

[127] G. Thornton, A. F. Orchard, and C. N. R. Rao, Phys. Lett. **54**, 235 (1975).

[128] R. Pynn, J. Axe, and R. Thomas, Phys. Rev. B **13**, 2965 (1976).

[129] B. O. Marinder, Ark. Kemi **19**, 435 (1962).

[130] A. Bolzan, C. Fong, B. Kennedy, and C. Howard, J. Solid State Chem. **113**, 9 (1994).

[131] S. M. Shapiro, J. Axe, G. Shirane, and P. M. Raccah, Solid State Commun. **15**, 377 (1974).

[132] V. Eyert, Europhysics letters **58 (6)**, 851 (2002).

[133] N. Terao, Japanese Journal of Applied Physics **2**, 156 (1963).

[134] G. Brauer, Z. anorg. Chem. **248**, 1 (1941).

[135] E. Crawford and J. Anderson, Phil. Trans. R. Soc. (London) **A 304**, 327 (1982).

[136] B. Meyer and R. Gruehn, J. Less Common Metals **83**, 185 (1982).

[137] F. Holtzberg, A. Reisman, M. Berry, and M. Berkenblit, J. Amer. Chem. Soc. **79**, 2039 (1957).

[138] L. Oliveira, T. Ramalho, M. Goncalves, F. Cereda, K. Carvalho, M. Nazzarro, and K. Sapag, Chemical Physics Letters **446**, 133 (2007).

[139] D. Rosenfeld, P. E. Schmid, S. Szeles, F. Levy, V. Demarne, and A. Grisel, Sensors And Actuators B : Chemical **37**, 83 (1996).

[140] A. Kohli, C. C. Wang, and S. A. Akbar, Sensors And Actuators B: Chemical **56**, 121 (1999).

[141] N. Norman, P. Kofstad, and O. Krudtaa, J. Less-Common Met. **4**, 124 (1962).

[142] G. Brauer and H. Muller, Plansee Proc., Reutte, Austria 257 (1958).

[143] J. Mayer, C. Flynn, and M. R´uhle, Ultramicroscopy **33**, 51 (1990).

[144] Q. Jiang, Y. Xie, W. Zhang, H. Gu, Z. Ye, K. Wu, J. Zhang, C.Y.Li, and D. Yin, J. Phys.: Condens. Matter **2**, 3567 (1990).

[145] Z. Nishiyama, Sci. Rept. Tohoku Univ. **23**, 638 (1934).

[146] G. Wassermann, Arch. Eisenhiittenw. **16**, 647 (1933).

[147] G. Kurdjumov and G. Sachs, Z. Phys. **64**, 325 (1930).

[148] Y. Gotoh and H. Fukuda, Surf. Sci. **223**, 315 (1989).

[149] E. Bauer and J. van der Merwe, Phys. Rev. B **33**, 3657 (1986).

[150] L. Bruce and H. Jaeger, Philos. Mag. A **38**, 223 (1978).

[151] O. Hellwig, K. Theis-Brohl, G. Wilhelmi, A. Stierle, and H. Zabel, Surface Science **398**, 379 (1998).

[152] B. Warren, *X-Ray Diffraction* (Dover, New York, 1990).

[153] A. Guinier, *X-Ray Diffraction: In Crystals, Imperfect Crystals, and Amorphous Bodies* (Dover, New York, 1994).

[154] Als-Nielsen, *Elements of Modern X-ray Physics* (John Wiley Sons, Ltd, West Sussex, England, 2001).

[155] I. K. Robinson, Phys. Rev. B **33**, 3830 (1986).

[156] I. K. Robinson and D. J. Tweet, Rep. Prog. Phys. **55**, 599 (1992).

[157] S. R. Andrews and R. A. Cowley, J. Phys. C **18**, 6427 (1985).

[158] R. Feidenhansl, Surf. Sci. Rep. **10**, 105 (1989).

[159] A. Stierle, Z. Metallkd. **93**, 8 (2002).

[160] G. Renaud, Surf. Sci. Rep. **32**, 1 (1998).

[161] P. Dederichs, J. Phys. F **3**, 471 (1973).

[162] M. Krivoglaz, *X-Ray and Neutron Diffraction in Nonideal Crystals* (Springer, Berlin, 1996).

[163] H. Trinkaus, Phys. Status Solidi B **51**, 307 (1972).

[164] R. P. Kurta, Ph.D. thesis, in preparation.

[165] R. Barabash and M. Krivoglaz, Sov. Phys. Solid State **29 (10)**, 1768 (1987).

[166] M. Born and K. Huang, *Dynamical Theory of Crystal Lattices* ((Clarendon Press), Oxford, 1954).

[167] Y. Nakagawa and A. D. B. Woods, Phys. Rev. Lett. **11**, 271 (1963).

[168] P. Wombacher, Ph.D. thesis, Technische Hochschule Aachen, Federal Republic of Germany, 1972.

[169] K. Huang, Proc. Roy. Soc. **A 109**, 102 (1947).

[170] L. G. Parratt, Phys. Rev. **95**, 359 (1954).

[171] L. Nevot and P. Croce, Rev. Phys. Appl. **15**, 761 (1980).

[172] G. H. Vineyard, Phys. Rev. B **26**, 4146 (1982).

[173] H. Dosch, *Critical Phenomena at Surfaces and Interfaces* (Springer Tracts in Mod. Phys. (Springer), Berlin, 1992), p. 126.

[174] E. Vlieg, J. Appl. Cryst. **30**, 532 (1997).

[175] F. Hajdu, Acta Cryst. **A28**, 250 (1972).

[176] G. Palinkas, Acta Cryst. **A29**, 10 (1973).

[177] H. Balyuzi, Acta Cryst. **A31**, 600 (1975).

[178] K. Siegbahn, C. Nordling, A. Fahlman, R. Nordberg, K. Hamrin, J. Hedman, G. Johansson, T. Bergmark, S. Karlsson, I. Lindgren, and B. Lindberg, (Uppsala: Almqvist and Wiksells) (1967).

[179] W. Egelhoff, Surf. Sci. Rep. **6**, 253 (1986).

[180] J. N. Andersen and C. Almbladh, J. Phys.: Condens. Matter **13 (49)**, 11267 (2001).

[181] D.Briggs and M.P.Seah., *Practical Surface analysis (2nd edition) volume 1* (WILEY, New York, 1990).

[182] S. Doniach and M. Sunjic, J. Phys. C **3**, 285 (1970).

[183] D. Adams and J. Andersen, *FitXPS: a fitting program for core level spectra available from ftp://boopic.ifa.au.dk/pub/fitxps.*

[184] *DESY in Hamburg http://www.desy.de.*

[185] R. Nyholm, J. N. Andersen, U. Johansson, B. N. Jensen, and I. Lindau, Nucl. Instrum. Methods Phys. Res. Sect. A **467**, 520 (2001).

[186] A. Stierle, A. Steinhauser, N. Kasper, R. Weigel, and H. Dosch, Rev. Sci. Instrum. **75**, 5302 (2004).

[187] *http://www.esrf.eu/UsersAndScience/Experiments/SurfaceScience/ID32.*

[188] U. Essman and H. Kiessig, Mat. Res. Bull. **14**, 1139 (1979).

[189] A. Stierle, *FEWLAY code available at e-mail address: stierle@mf.mpg.de.*

[190] N. Martensson and R. Nyholm, Phys. Rev. B **24**, 7121 (1981).

[191] B. Visentin, Y. Gasser, and J. Charrier, Physica C **441**, 66 (2006).

[192] I. Arfaoui, Ph.D. thesis, Ecole Centrale Paris, 2001.

[193] Q. Ma and R. A. Rosenberg, in Proceedings of the 10th Workshop on RF Superconductivity, Tsukuba, Japan, 2001 edited by S. Noguchi et al. (KEK,Tsukuba, Japan, 2003) 368 (2003).

[194] *http://www.mathworks.com/.*

[195] T. Coleman and Y. Li, SIAM Journal on Optimization **6**, 418 (1996).

[196] T. Coleman and Y. Li, Thematical Programming **67**, 189 (1994).

[197] M. Delheusy, A. Stierle, N. Kasper, R. P. Kurta, A. Vlad, H. Dosch, C. Antoine, A. Resta, E. Lundgren, and J. Andersen, Appl. Phys. Lett. **92**, 101911 (2008).

[198] P. Cremery and J. Bardolle, J. Less-Common Metals. **77**, 37 (1981).

[199] M. Grundner and J. Halbritter, Surf. Sci. **136**, 144 (1984).

[200] S. Bu, D. Kim, J. Choi, J. Giencke, E. Hellstrom, D. Larbalestier, S. Patnaik, L. Cooley, C. Eom, J. Lettieri, D. Schlom, W. Tian, and X. Pan, Appl. Phys. Lett. **81**, 1851 (2002).

[201] G. Ciovati and P. Kneisel, Phys. Rev. ST Accel. Beams **9**, 042001 (2006).

Résumé, Zusammenfassung, Abstract

Résumé

Les projets de Collisionneur International Linéaire et de lasers X à électrons libres reposent sur les performances des cavités supraconductrices radiofréquences en niobium pour une accélération efficace des particules. Une remarquable amélioration du champ accélérateur est couramment obtenue après un traitement des cavités à basse température (T<150°C pour plusieurs heures). L'origine microscopique de cet effet est jusqu'à présent indéterminée; cependant, il a été proposé qu'une redistribution de l'oxygène interstitiel au voisinnage de la surface entre en cause. Ce travail présente une étude de surface de monocristaux de niobium oxydés par différentes techniques in-situ et non-destructives aux rayons X: réflectivité des rayons X, diffraction de rayons X en incidence rasante, diffusion diffuse, mesures de tiges de troncature, et spectrométrie photoélectronique X. Un premier aperçu de l'interaction entre la dissolution/formation de l'oxyde et l'apparition d'oxygène interstitiel sous la couche d'oxyde est donné. La couche d'oxyde naturelle sur les surfaces Nb(110) et Nb(100) est constituée de Nb_2O_5, NbO_2 and NbO, de la surface vers l'interface. L'oxyde chauffé sous vide se dissout progressivement de Nb_2O_5 en NbO_2 à basses températures, et finalement en NbO à 300°C. L'interface Nb(110)/NbO(111) vérifie une relation d'épitaxie de type Nishiyma-Wassermann. Le profil de concentration en oxygène interstitiel indique une région riche en oxygène dans le direct voisinage de l'interface niobium/oxyde. Aucun appauvrissement en oxygène interstitiel n'a été observé sous la couche d'oxyde pour les traitements thermiques à basse température et les préparations de surface étudiées.

Mots clés : Diffusion des rayons X en incidence rasante, rayonnement synchrotron, oxygène interstitiel, oxydes de Niobium, réflectivité des rayons X, diffusion diffuse, spectrométrie photoélectronique X.

Zusammenfassung

Röntgenlaser und das zukünftige 'International Linear Collider' Projekt basieren auf der Leistungsfähigkeit von supraleitenden Niob hochfrequenz Kavitäten für effiziente Teilchenbeschleunigung. Eine beachtenswerte Zunahme des hochfrequenz Beschleunigungsfelds

wird normalerweise durch Tempern der Kavitäten bei moderaten Temperaturen erreicht (T $<$ 150°C, mehrere Stunden). Der mikroskopische Ursprung dieses Effekts konnte bis heute nicht geklärt werden, jedoch wurde argumentiert, dass eine Umverteilung der Oberflächennahe Sauerstoff-Zwischengitteratome in Richtung des reinen Niob Kristalls eine wichtige Rolle spielt. In dieser Arbeit wurde die Struktur von oxidierten Niob Einkristallen nahe der Oberfläche und deren Entwicklung nach dem Tempern im Vakuum mittels zerstörungsfreier oberflächensensitiven in situ Röntgenmethoden (Röntgenreflektivität, Röntgenstreuung unter streifendem Einfall, diffuse Streuung, Crystal Truncation Rods und hochauflösende Rumpfniveauphotoelectronen Spektroskopie) untersucht. Ein erster Einblick in den Zusammenhang der Oxidschicht Bildung/Auflösung und dem Auftreten der oberflächennahen Sauerstoff-Zwischengitteratome wurde gegeben. Die natürliche Oxidschicht auf Nb(110) und Nb(100) Kristalloberflächen besteht aus Nb_2O_5, NbO_2 und NbO, (in dieser Reihenfolge von der Oberfläche zu der Niob-Einkristall Grenzfläche). Die Oxidschicht wird durch Heizen sukzessive reduziert, von Nb_2O_5 zu NbO_2 bei moderaten Temperaturen und zu NbO bei 300°C. Die Nb(110)/NbO(111) Grenzfläche weisst eine epitaktische Nishiyama-Wassermann Orientierungsbeziehung auf. Die Tiefenverteilung der Sauerstoff-Zwischengitteratome konnte ermittelt werden, die grösste Konzentration an Sauerstoff liegt demnach an der Grenzfläche des Oxids zum Niobkristall. Es konnte kein Abnahme von Sauerstoff unterhalb der Oxidschicht nach dem Tempern bei moderaten Temperaturen und bei den untersuchten Oberflächenpräparierungen festgestellt werden.

Stichwörter : Röntgenstreuung unter streifendem Einfall, Synchrotronstrahlung, Oberflächennahe Sauerstoff-Zwischengitteratome, Niob Oxide, Röntgenreflektivität, Diffuse Streuung, hochauflösende Rumpfniveauphotoelectronen Spektroskopie.

Abstract

X-ray free electron lasers and the future International Linear Collider project are based on the performance of niobium superconducting rf cavities for efficient particle acceleration. A remarkable increase of the rf accelerating field is usually achieved by low-temperature annealing of the cavities (T$<$150°C, several hours). The microscopic origin of this effect has remained unclear; however, it has been argued that a redistribution of subsurface interstitial oxygen into niobium is involved. In this study, the near surface structure of oxidized niobium single crystals and its evolution upon vacuum annealing has been studied by means of non-destructive in-situ surface sensitive x-ray techniques: x-ray reflectivity (XRR), grazing incidence x-ray diffraction (GIXD), diffuse scattering (GIDXS), crystal truncation rods measurements (CTRs), and high-resolution core-level spectroscopy (HRCLS). A first insight into the interplay between the oxide formation/dissolution and the occurrence of

subsurface interstitial oxygen has been given. The natural oxide on Nb(110) and Nb(100) surfaces is constituted of Nb_2O_5, NbO_2 and NbO, from the surface to the interface. It reduces progressively upon heating from Nb_2O_5 to NbO_2 at low temperatures, and to NbO at 300°C. The Nb(110)/NbO(111) interface presents a Nishiyma-Wassermann epitaxial orientation relationship. The depth-distribution of interstitial oxygen has been established indicating that most of the oxygen is located in the direct vicinity of the oxide/niobium interface. No evidence of oxygen depletion below the oxide layer has been observed for the low temperature thermal treatments and surface preparations investigated in this study.

Keywords : Grazing incidence X-ray scattering, synchrotron radiation, subsurface interstitial oxygen, niobium oxides, X-ray reflectivity, diffuse scattering, high-resolution core-level spectroscopy.

Acknowledgements

The last lines of this manuscript should be words of gratitude to all those who helped to make this PhD thesis possible.

First of all, I want to thank **Prof. Dr. Helmut Dosch** for welcoming me in his department at the Max Planck Institute for Metals Research, for many fruitful discussions, for his contagious enthusiasm, and his constant support. I thank him for giving me the opportunity of experiencing such a rich scientific environment, at the institute, on beamtimes, as well as during international conferences and workshops. A special thanks goes to my daily supervisor **Dr. Andreas Stierle** for leading me through the discovery of experimental surface science, for his precious help, his support, and for being always available for discussions. This work would not have been possible without the input of my second supervisor **Dr. Claire Antoine**. I thank her for offering me this opportunity, for her constant encouragements in good and bad times, and for welcoming me warmly at each of my stays in Paris. I am grateful to **Prof. Dr. Louisette Priester** for accepting to be my thesis director in Paris, for the fruitful discussions we had during these years, and the external look that she brought on my work. A special thanks is addressed to **Prof. Dr. David Seidman** and **Prof. Dr. Herbert Over** for being referees of this PhD thesis.

Ce travail fut subsidié trois ans par une bourse de Contrat de Formation par la Recherche (CFR) du Commissariat à l'énergie Atomique (CEA). Je remercie le Service des Accélérateurs, Cryogénie et Magnétisme (SACM, CEA / Saclay) de m'avoir acceuillie dans leur équipe, et en particulier **Prof. Dr. Jean Zinn-Justin, Dr. Antoine Daël, et Dr. Stéphane Chel**. Merci à **Stéphane Berry, Bernard Visentin, Pierre Bosland, Fabien Eozenou**, et les autres, pour leur accueil chaleureux à chacun de mes passages par Paris.

This work would not have been possible without the precious help of **Ralf Weigel**, for all beamtimes at ANKA ; of my night shifts accomplices **Dr. Alina Vlad** and **Dr. Nikolai Kasper** ; and of **Annette Weisshardt, Rolf Henes, Arnold Weible** and **Franck Adams** for the sample preparation and technical help. I thank **Dr. Andrea Resta** and **Dr. Edwin Lundgren** for the beamtime at Max-Lab in Lund, **Dr. Franck**

Renner and **Dr. Jörg Zegenhagen** for their support on ID32 at ESRF.

I am grateful to **Dr. Alejandro Diaz-Ortiz** and **Dr. Ingo Ramsteiner** for proof-reading the introduction and the conclusion of this manuscript.

I especially want to thank the happy crew of the department Dosch for the great time I have had during all these years at the Institute. Thank you to **Alina Vlad, Alexander Udyansky, Ayse Turak, Dimas Garcia de Oteyza, Esther Barrena, Heiko Schröder, Ingo Ramsteiner, Ioan Costina, Nikolai Kasper, Oleg Shchlygo, Paulien Stall, Reinhard Streitel, Ruslan Kurta, Sandrine Dourdain, Ulrich Gebhardt, Vedran Vonk**, and all the others. I wish you all the best for the future, and hope that our roads will cross again.

Enfin, je tiens tout particulièrement à remercier **mes parents** et **grand-parents** pour leur inconditionnel soutien, et leurs affectueux encouragements, me permettant d'aller au bout de ces longues études.

A special thanks goes to **Max**, for his love, his support and his enduring patience during this PhD period.